NANOSCALE FUNCTIONALIZATION OF ION-BEAM FABRICATED SELF-ORGANIZED NANOSTRUCTURES ON SILICON SURFACES

By

MAHESH SAINI

PHYS07201304009
INSTITUTE OF PHYSICS, BHUBANESWAR

A thesis submitted to the

Board of studies in physical sciences

In partial fulfilment of requirements

For the degree of

DOCTOR OF PHILOSOPHY

of

HOMI BHABHA NATIONAL INSTITUTE

JULY, 2019

Homi Bhabha National Institute

Recommendations of the Viva Voce Committee

As members of the Viva Voce Committee, we certify that we have read the dissertation prepared by Mr. Mahesh Saini entitled "Nanoscale functionalization of ion-beam fabricated self-organized nanostructures on silicon surfaces", and recommend that it may be accepted as fulfilling the dissertation requirement for the Degree of Doctor of Philosophy.

Chairman - PANKAJ AGRAWAL Date: 22/1/20

Guide /Convener - TAPOBRATA SOM Date: 22/01/2020

Co-guide (if any) Date:

Examiner - Anirban Mitra. Date: 22/1/20.

Member 1 - Date: 22.1.20

Member 2 - Pratap Date: 22/01/2020

Final approval and acceptance of this thesis is contingent upon the candidate's submission of the final copies of the dissertation to HBNI.

I/We hereby certify that I/we have read this thesis prepared under my/our direction and recommend that it may be accepted as fulfilling the thesis requirement.

Date: 22/01/2020

Place: IOP, Bhubaneswar

Co-guide (if applicable) **Guide** 22/01/2020

STATEMENT BY AUTHOR

This dissertation has been submitted in partial fulfilment of requirements for an advanced degree at Homi Bhabha National Institute (HBNI) and is deposited in the Library to be made available to borrowers under rules of the HBNI.

Brief quotations from this dissertation are allowable without special permission, provided that accurate acknowledgement of source is made. Requests for permission for extended quotation from or reproduction of this manuscript in whole or in part may be granted by the Competent Authority of HBNI when in his or her judgment the proposed use of the material is in the interests of scholarship. In all other instances, however, permission must be obtained from the author.

Mahesh Saini

MAHESH SAINI

DECLARATION

I, hereby declare that the investigation presented in the thesis has been carried out by me. The work is original and has not been submitted earlier as a whole or in part for a degree / diploma at this or any other Institution / University.

Mahesh Saini

MAHESH SAINI

List of Publications arising from the thesis

Journal

1. "Broadband antireflection property of conformally grown zinc tin oxide thin films on nanorippled- and nanofaceted-Si substrates", **M. Saini**, R. Singh, S. K. Srivastava, and T. Som, Journal of Physics D: Applied Physics, **2018**, 51, 275305-275315.
2. "Enhanced cold cathode electron emission efficacy of gold nanoparticle-decorated self-organized silicon nanofacets", **M. Saini**, R. Singh, Sooraj K. P., M. Ranjan, S. K. Srivastava, and T. Som, ACS Applied Materials and Interfaces, **2019** (Communicated).
3. "In-plane optical anisotropy and SERS detection efficiency of self-organized gold nanoparticles on silicon nanoripples: Roles of growth angle and postgrowth annealing", **M. Saini**, S. Augustine, M. Ranjan, and T. Som, Applied Surface Science, **2019** (Under review).

Conference/Symposium

1. **M. Saini**, R. Singh, S. K. Srivastava, and T. Som ─ "Broadband anti-reflection property of conformally grown ZTO thin films on nanofaceted- and nanorippled-Si substrates" **ORAL**: 4th International Conference on Nanoscience and Nanotechnology (ICONN-2017), at SRM University, Kattankulathur (Chennai) on August 11, 2017.
2. **M. Saini**, R. Singh, S. K. Srivastava, and T. Som ─ "Broadband antireflection property of conformally grown Sn-doped ZnO thin films on nanofaceted- and nanorippled-Si substrates" **POSTER**: 4th International Conference on Nano-structuring by Ion Beams (ICNIB 2017), at Devi Ahilya Vishwavidyalya, Indore (Madhya Pradesh) on October 12, 2017.
3. **M. Saini**, M. Ranjan, and T. Som ─ "Plasmonic anisotropy of self-organized gold nanoparticles on nanofaceted silicon surfaces" **POSTER**: International Conference on Microscopes & XXXIX Annual meeting of Electron Microscope Society of India", at Mayfair convection center, Bhubaneswar, Odisha on July 19, 2018.
4. **M. Saini**, R. Singh, Sooraj K. P., M. Ranjan, S. K. Srivastava, and T. Som ─ "Field emission efficacy of self-assembled gold nanoparticles on self-organized nanofaceted silicon surfaces" **POSTER**: 5th international conference on ion beams in materials engineering and characterizations (IBMEC 2018), at Inter-University Accelerator centre, New Delhi on October 10, 2018.

Mahesh Saini

MAHESH SAINI

To my grandfather,
my mother, and my wife

ACKNOWLEDGEMENTS

The journey of Ph.D. life and all the achievements that I have accomplished during my stay at Institute of Physics, Bhubaneswar won’t be possible without the support, help, and guidance of my supervisor, Prof. T. Som. I take this opportunity to express my sincere gratitude to him for his constant encouragement, support, and invaluable guidance throughout my research period. His innovative ways of looking into the problems with an admixture of professionalism and perfectionism will remain as assets for the rest of my life. I sincerely thank him and his family for their care and hospitality which provided home-like environment during my stay in IOP. It has been truly a life time privilege for me to work under his guidance.

I would like to thank Prof. P. V. Satyam from IOP Bhubaneswar, Dr. S. K. Srivastava from IIT Kharagpur, and Dr. B. Satpati from SINP for extending their facilities towards my research work. My special thanks to Dr. M. Ranjan from FCIPT, IPR Gandhinagar for extending their facilities for experiments and precious time to discuss with me at various points of time.

I would also like to acknowledge my senior group members Dr. D. P. Datta, Dr. S. A. Mollick, Dr. S. K. Garg, Dr. T. Basu, and Dr. M. Kumar and for our valuable discussion and providing me a chance to work with them. I would like to thank my other lab mates, Dr. Sudheer, Dr. Ranveer Singh, Mr. Alapan Datta, Ms. Dilruba Hasina, Mr. Rupam Mandal for their constant help in every aspects of my life.

I thank all my teachers who taught me during the pre-doctoral course work and all the experimental condensed matter group faculties of IOP, Bhubaneswar for their generous support. I also thank to scientific staff of IOP, especially Mr. S. K. Choudhury and Mr. Arun Dash for making themselves available wherever their expertise was required for the lab. In fact, I have learnt a lot about various experimental and technical aspects of a system from Mr. S. K. Choudhury.

I am grateful to the former director Prof. A. M. Srivastava, and the present director, Prof. S. Panda, members of my Doctoral committee: Prof. Pankaj Agrawal, Dean HBNI at IOP, Prof. B. R. Sekhar, and Prof. P. K. Sahoo from NISER, Bhubaneswar and other members of the Institute (academic and non-academic) for their timely help, cooperation, and support whenever I needed the same.

A special acknowledgement goes to my batch mates who have celebrated every occasions of happiness with me during these PhD days. Thanks to all the seniors and junior scholars of IOP for their direct or indirect assistance on many occasions during my stay at IOP. I would also like to thank Department of Atomic Energy and IOP for providing financial support to pursue my research work.

Most importantly, I have always been fortunate in being able to count on continuous support from my parents, brother, relatives, specially my grandfather, my mother, and my wife, Babita. They have always believed in me and their love and affection has kept me going during all these years. I owe my deepest sense of affection to my late father Shri Kailash Chandra Saini. Today, you are not with me, but your blessings will always be with me and show me the path to achieve my goals. In particular, I am indebted to my parents for providing me with their love, education, and it is because of them that I was able to become the person I am today.

Date: 25/07/2019

Mahesh Saini

Place: Bhubaneswar

MAHESH SAINI

CONTENTS

Summary

In summary, nanoscale functionalization of 500 eV Ar ion-beam fabricated self-organized nanoscale patterned-Si [viz. nanorippled (NR)- and nanofaceted (NF)] substrates is carried out by decorating them with gold nanoparticles (Au-NPs) and sputter-grown conformal zinc tin oxide (ZTO) films for viable technological applications like substrate morphology-induced in-plane plasmonic anisotropy, surface-enhanced Raman scattering, hitherto unseen fascinating low threshold turn-on field for cold cathode electron emission, and broadband antireflection. The templated-growth of e-beam evaporated Au-NPs at various oblique angles of incidence (65°-85°) leads to the self-organization of Au-NPs on NF- and NR-Si substrates. Interestingly, for NR-Si substrates, the growth of Au-NPs take place along the ripple patterns, resulting in the formation of Au-NP arrays. In the present case, tunability in the size and interparticle gap of Au-NPs is achieved by altering the growth angle. Therefore, optical reflection and ellipsometric studies confirm the anisotropic morphology-driven in-plane plasmonic anisotropy exhibited by arrays of Au-NPs which is further utilized for the SERS-based detection of crystal violet (CV) dye. On the other hand, the self-organized growth of Au-NPs on NF-Si selectively occur at the apexes and/or sidewalls of the same depending upon their growth angle. In the present case, growth angle is the key parameter to tune the decoration of Au-NPs on Si-NFs in a fascinating way to reveal hitherto unseen ultralow threshold fields in the range of (0.27-0.6 V μm^{-1}) for cold cathode electron emission with excellent stability in tunneling current. Kelvin probe force microscopy (KPFM) measurements reveal the decreasing work function with increasing growth angle. Dual pass tunneling current microscopy (DPTCM) measurements manifest the origin of tunneling current from the sites of Au-NPs on Si-NFs. Finite element method (FEM)-based electrostatic field simulations confirm that the field enhancement takes place mostly at the apexes of Si-NFs which further improves after their decoration with Au-NPs. In addition to this, sputter-grown ZTO films (60 nm-thick) conformally grown on NR- and NF-Si substrates exhibit superior broadband antireflection. Thus, functionalization of low energy ion-beam patterned Si substrates by decorating them with Au-NPs offers potential applications in plasmonics, SERS-based sensing of chemical and biological complexes, and low-power field emitters. Likewise, fabrication of ZTO films on patterned-Si substrates leads to AR coatings for solar cells.

List of figures

List of tables

CHAPTER 1

Introduction

1.1 Preamble

Nanotechnology is the fabrication and engineering of functional materials, devices and systems by controlling the dimension of matter at nanoscale leading to out of the box, novel, and fascinating physical, chemical, and biological properties. Nanotechnology includes the synthesis, characterization, exploration, and utilization of nanostructured materials not only for fundamental research, but also for practical and futuristic applications [1,2].

Way back in 1959, Richard P. Feynman in his famous lecture [3], "There's plenty of room at the bottom", pointed out that control of matter at nanometer length scale could emerge to very exciting phenomena that might revolutionize the understanding of science and unleash new horizon in materials research to provide new insights to the world of technology [1,4]. Thereafter, the journey of technology miniaturization started from bulk macroscopic to nanoscale world in terms of functional nanostructures. During last 50 years, the nanostructured materials with tailorable functional properties have been extensively explored and currently a multitude of nanoscale devices are available in the market [5].

There are two basic approaches for fabrication of surface nanostructures and useful devices on various substrates including metals, semiconductors, and insulators in a controlled and repeatable manner namely, the 'top-down' and 'bottom-up' techniques [6]. Top-down approach refers to slicing or successively cutting of bulk materials into nanoscale objects, however, bottom-up approach is the build-up of material from scratch, i.e. adding atom by atom or molecule by molecule. Among all commonly known top-down strategies surface nanostructuring is essentially the removal of atoms from the surface of materials which results in the evolution of surface nanostructures with the aid of a multitude of atomistic processes. This is inherently a non-equilibrium stochastic phenomenon and is governed by a competition between inherent thermodynamic and externally activated kinetic characteristics of materials systems. This stochastic erosion process of flat surfaces towards fabrication of nanostructures is widely known as ‘self-organization’. Special attention has been paid to understand the self-organization phenomenon of nanostructures for their extraordinary and directional properties [2].

A lot of top-down approaches are available for the fabrication of surface nanostructures, e.g. chemical lithography [7–10] or electron-beam lithography [11–13]. Among these ion-beam induced self-organized pattern formation has drawn a lot of attention due to its high throughput and large area (wafer scale) production and relative cost-effectiveness. Ion-beam sputtering (IBS) is the ejection of material from the solid surfaces through the impact of energetic particles [14] which essentially gives rise to a gamut of nanoscale periodic patterns on surfaces. This technique has found important applications not only in basic research but also in potential applications due to a superior control over energy and spatial distribution of the ion species.

In the context of ion-solid interaction, the energy range of ions can be classified into three broad regimes: Low energy ions (0.5−10 keV), medium energy ions (10−500 keV), and high energy ions (> 500 keV) [15].

1.2 Self-organized nanoscale pattern formation

Back in the 1960s, Navez *et al.* bombarded glass surfaces with a 4 keV ion beam of air and found that in the course of sputtering, periodic structures (with their wavelength in nanometer regime) appeared on flat surfaces [16]. It took more than three decades for this novel phenomenon to boost up as a research interest when it was realized that there might be a plenty of scopes for using such nanoscale patterns for potential technological applications. Hence, intensive research started in this field to fabricate a gamut of exotic patterns on a wide class of materials including metals, semiconductors, and insulators. Subsequently, it became important to develop a good theoretical understanding on ion-beam induced pattern formation. As a result, lot of theoretical models were developed to explain the experimental results and it was found that the evolution of the surface morphology during ion-beam sputtering is a complex phenomenon and various factors are involved behind the same. Ion-beam induced self-organized patterns are fabricated under the dynamic balance of both roughening and smoothening processes where incident ion beam randomly roughens the surface, whereas smoothing works simultaneously towards annealing out very small perturbations.

It is noteworthy that ion-beam induced surface nanostructuring depends a lot on various experimental parameters like ion-incident angle, -energy, -flux, -mass, -fluence, substrate temperature, and composition of the substrate. Hence, patterns evolution by varying these parameters has been widely explored by many researchers [14,17–20]. For example, Basu *et al.* [20] have reported that due to 500 eV Ar-ion bombardment on Si surface, there is no pattern formation in the angular window of 0º–50º, albeit, parallel ripples start to evolve at 51º and they get more prominent in the angular window of 60º–65º. However, broken ripples start to appear at 67º which leads to nanoscale facet formation in a very small angular window of 70º–73º. At grazing incidence of 80º perpendicular-mode ripples are observed. On the other hand, Facsko *et al.* have reported the evolution of hexagonally arranged nanoscale dot structures on GaSb substrates for normal incident Ar-ions [21]. Ou *et al.* have observed checkerboard-like patterns on Ge surfaces upon ion irradiation at elevated temperatures [22]. In fact, as stated earlier, ion induced ripple formation has been widely explored for different kinds of materials like semiconductors [19–27], insulators [19,28–30], metals [31,32], and polymers [33].

Fabrication of ion induced patterned surfaces is not only fascinating from fundamental physics point of view, but also important for a number of intriguing applications. For instance, nanostructured surfaces with a high aspect ratio may exhibit antireflection property due to graded refractive index [34–37] which can be useful for enhancing the photoconversion efficiency of solar cells [38,39]. Likewise, arrays of vertically oriented pillars can be used in fabrication of self-cleaning surfaces [40,41], optoelectronic devices [41,42], thermoelectric generators [43], and field emitting devices [44,45]. On the other hand, ripple-like sinusoidal sculpting of surfaces have their own set of applications. For example, Ranjan *et al.* have shown that ripples are capable of growing self-organized Ag nanoparticles which leads to a tunable in-plane optical anisotropy [46,47]. In addition, Sooraj *et al.* have reported blood-glucose detection using surface-enhanced Raman scattering (SERS) of Ag nanoparticles deposited on rippled substrates [48]. In another work, Bhatnagar *et al.* have demonstrated the self-organization of silver nanoparticles on low energy ion-beam fabricated GaSb-nanodots for broadband antireflection properties [49]. In a fascinating report, Teschome *et al*. have aligned Au nanoparticles on DNA origami nanotubes grown on rippled-Si substrates for arrays of parallel nanoparticle chains [50]. Further, Mollick *et al.* have shown strong uniaxial magnetic anisotropy in deposited Co films on grating-like Ge patterns [26]. All these reports clearly indicate that ion-beam patterned surfaces are potential candidates for improving the photovoltaic, optoelectronic, plasmonics, field emission, nanoscale magnetism, and biological applications. Thus, it becomes obvious that a lot more can be done by using self-organized patterned substrates as templates for fabrication of modern architecture-based nanoscale devices.

In the present thesis, we have carried out nanoscale functionalization of ion-beam patterned silicon templates by decorating them with self-organized gold nanoparticles. A brief introduction on the growth processes of thin films and self-organization of nanoparticles is provided in the following section.

1.3 Growth of thin films and self-organized nanoparticles

The physical properties of a bulk material change drastically upon forming the assembly of atoms and molecules in a confined region due to quantum confinement effects [51,52]. For example C is a non-metal but when it is considered at the nanoscale, graphene is a good electrical conductor. When a bulk material is successively sliced along its dimensions then it leads to the formation of thin films, nanowires, and nanoparticles (or nanodots) which are essentially the 2D, 1D, and 0D counterparts of the original material, respectively. Quantum confinement imposes a restriction on the motion of randomly moving electrons, leading to their motion in discrete and specific energy levels and hence, quantum mechanics reflects the atomic realm of particles. It is interesting to note that density of states of semiconductors is strongly influenced by the quantum confinement [53]. As depicted in Fig. 1.1, by continuously slicing down the bulk material into smaller pieces, the density of states alter its dependence on energy as E, E^0, $E^{-1/2}$, and $E^{-3/2}$ corresponding to bulk (3D), thin films (2D), nanowires (1D), and nanodots (0D), respectively.

The bottom-up approach is necessarily the fabrication of nanomaterials by successive assembly of particles together to make a larger structure. It is further classified into two broad categories namely physical vapour deposition (PVD) [54–57] and chemical vapour deposition (CVD) [58–60]. As the name suggests, PVD is a set of techniques, which uses primarily the physical means to deposit a thin layer of material. In fact, a solid precursor material is gasified through the use of high-power electricity or intense laser pulses or low energy plasma jets and these gasified atoms are allowed to condense on a substrate. On the other hand, CVD technique involves the mixing of source materials with one or more volatile precursors which work as carriers.

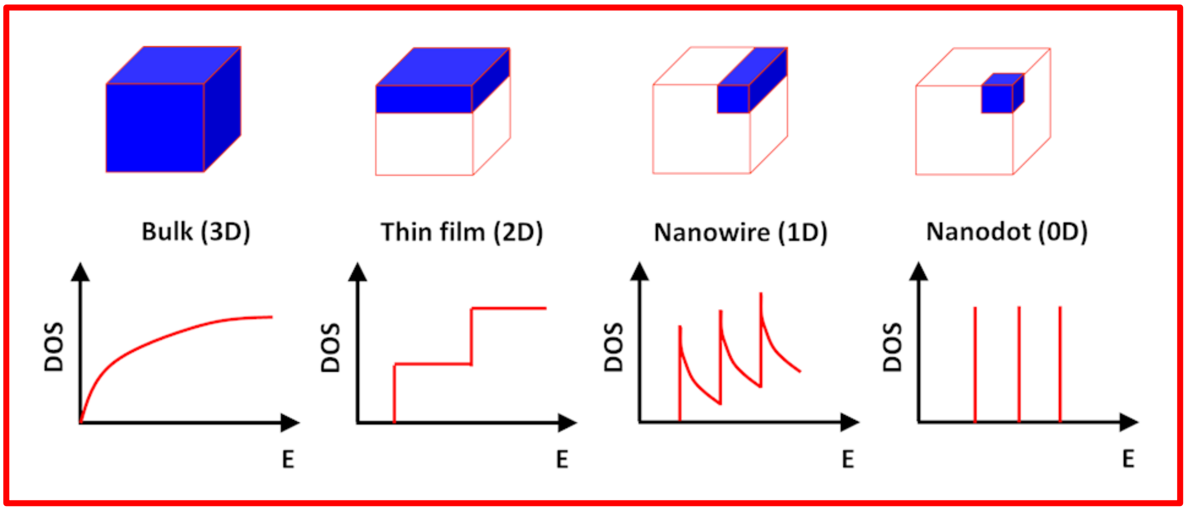

Figure 1.1: The density of states of bulk (3D), thin films (2D), nanowires (1D), and nanodots (0D).

Growth of thin films and nanostructures have enabled a wide range of technological breakthroughs in areas such as energy generation (thin film based solar cells) [61–63] and their storage (thin-film batteries, super-capacitors) [64–67], magnetic and electrical recording media [68–75], semiconductor devices [76–79], optical coatings [80–85] including antireflective coatings, hard coatings on machineries, and cutting tools etc. In addition to this, nanowires and nanoparticles are also being used in various promising technological applications such as photodetectors [86–88], field induced electron emitting sources [89–93], plasmonic solar cells [94–97], magnetic memories [98,99], surface-enhanced Raman scattering (SERS)-based molecular level detection [48,100–102], etc.

In this thesis, we have used the top-down and bottom-up approaches to demonstrate a set of novel applications based on nanostructured Si surfaces. First, we have used ion-beam sputtering technique (top-down approach) for fabrication of self-organized silicon nanostructures. Here, the achieved self-organization of these nanostructures is a special feature of ion-beams [14]. Further to this, bottom-up approach is used to functionalize silicon nanopatterned (prepared by top-down approach) substrates by depositing metal nanoparticles on the same. The self-organization of nanoparticles on the same patterned substrates is of prime interest.

Self-organization

Self-organization is a process of non-random ordering of spatially distributed entities into predictable patterns or structures without any management from an outside source [103]. The self-organization is governed by the normal processes of nucleation and growth [103] where ultimate driving force is the energy minimization via weak intermolecular interactions. For a self-organizing system to reach the minimum free energy configuration, there has to be enough thermal energy to allow the mass transport of the self-organizing atoms/molecules [103]. Hence, kinetic effects and surface defects can also play a very strong role. Small assemblies are formed because of the attractive interactions between the components.

Nanoscale functionalization of ion-beam patterned templates via deposition of thin films and/or nanoparticles have potential importance in various technological applications. A set of novel applications of nanofunctionalized ion-beam patterned silicon templates (presented in this thesis) are briefly introduced in the subsequent sections.

1.4 Cold cathode electron emission

The phenomenon of electron field emission is associated with the quantum mechanical tunneling process whereby electrons tunnel through the potential barrier from a metal or a semiconductor surface into vacuum under the influence of an applied electrostatic field [104–107]. The applied electric field helps in deforming and narrowing the potential barrier for the electrons at the emitter surface and allows to tunnel electrons through it. It is termed as cold cathode electron emission since there is no role of temperature in electron emission process and it can take place at RT.

There is a growing interest in research field emission process due to its ability of dealing with high voltage, high current density, high speed, temperature insensitive, and radiation hardened applications. Now-a-days, field emission is the most commonly used source of vacuum breakdown and electrical discharge phenomena which provides fantastic applications such as flat panel displays, bright electron sources for high-resolution electron microscopes, microwave power amplifiers, space applications, as well as gas and mass sensors [105–113]. In 1897, R. W. Wood observed electron field emission for the first time while performing some experiments on a discharge tube [114]. The emission mechanism is a complete reduction of the potential barrier up to the Fermi level which was first explained by Schottky [114]. Later on, Gossling proposed that the electron field emission process is independent up to 1500 K [115] and therefore, he suggested that there might be quantum mechanical tunneling mechanism responsible for this type of electron emission. The complete theory was formulated by Ralph H. Fowler and Lothar W. Nordheim [116] using modern wave mechanical formulation of quantum mechanics in 1928. The derived equation was named as Fowler-Nordheim (F-N) equation after them. This quantum mechanical tunneling process is an important mechanism of electron transfer through thin barrier existing in metal-vacuum junction. The F-N theory is based on the following assumptions:

- The temperature of the metal emitter is 0 K.
- There are free electrons in metals and free electron model is valid.
- The emitter surface is smooth and the work function is uniform across the emitting surface which is not affected by externally applied electric field.
- The potential barrier close to the surface consists of an applied electric field induced potential in the vacuum region and its image force potential.

The field emission process is governed by Fowler-Nordheim tunneling [116] as expressed by the equation:

$$J = A\left(\frac{\beta^2 E^2}{\phi}\right)\exp\left(\frac{-B\phi^{3/2}}{\beta E}\right),$$

where J is the electron emission current density (A m^{-2}) and E is the electric field at the emitting surface (V µm^{-1}). A and B are constants having values 1.56×10^{-10} A V^{-2} eV and 6.83×10^{3} V eV$^{-1.5}$ µm^{-1}, respectively [116,117]. The enhancement factor, β, is defined by the ratio of local to the applied electric field which depends on the geometry of field emitting structures such as composition, tip diameter, and the aspect ratio. The other parameter is the work function (ϕ) of field emitting material which is realized as the potential barrier at material-vacuum interface. Hence, the FE characteristics can be improved by tailoring the geometry in terms of morphology, tip size, aspect ratio, etc. and/or by reducing the work function via modification of the electronic structure [91,93,107,118–120].

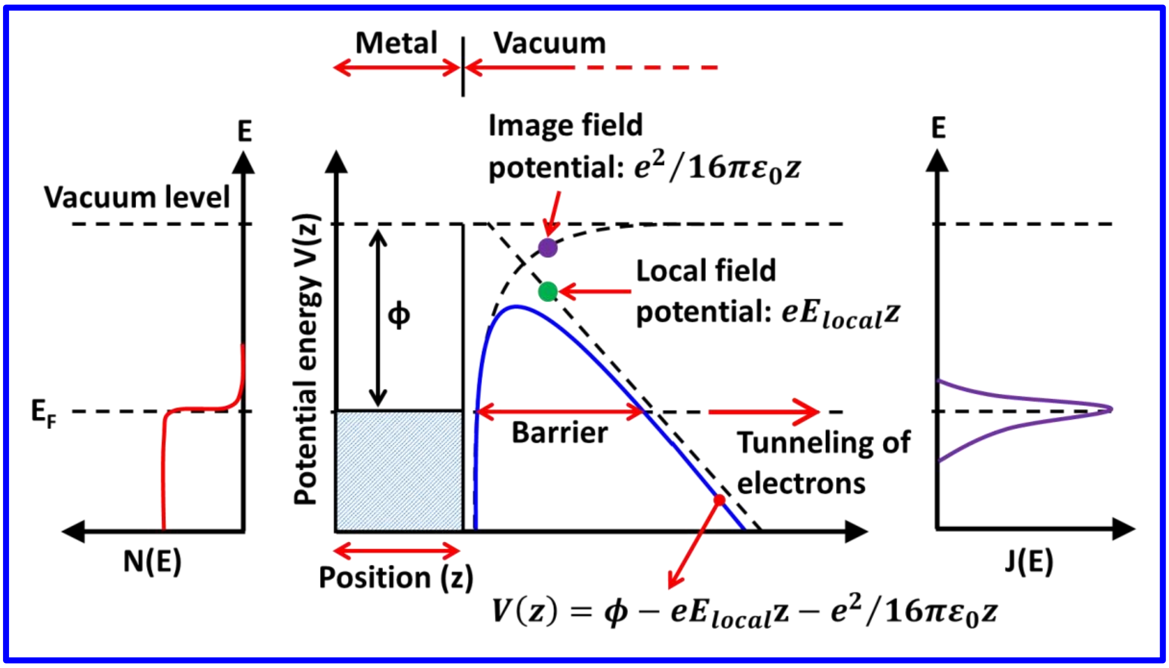

Figure 1.2: The Fermi-Dirac distribution of electrons in metals (left) at some finite temperature, one dimensional potential energy $V(z)$ experienced by an electron as a function of its distance z from the surface of the metal under the influence of an applied electric field (center), and the electron current density $J(E)$ distribution (right).

In this thesis, we demonstrate the growth angle-dependent self-organization of Au nanoparticles on low energy ion-beam fabricated nanofaceted-Si structures and their fascinating low threshold, tunable field emission property using bulk field emission measurements. Since it is not possible to probe the emission sites of tunneling electrons, AFM-based dual pass tunneling current microscopy (DPTCM) technique is employed to probe the same.

1.5 Surface-enhanced Raman spectroscopy

Surface-enhanced Raman spectroscopy (SERS) is a powerful vibrational spectroscopy-based technique which is used for highly sensitive structural detection of low concentration analytes through the amplification of electromagnetic fields generated predominantly by the excitation of localized surface plasmons and to a lesser extent by chemical effects (charge transfer) [121,122]. Standard Raman spectroscopy is limited to the detection of very high concentrations due to much lower scattering cross-section (10^{-30} cm^2). However, metal nanostructures/nanoparticles provide a large increase in the scattering cross-section ($> 10^{-16}$ cm^2) makes SERS a superior method for molecular sensing [123,124]. Hence, SERS has emerged as a useful technique for single molecule level detection and molecular sensing [121,122]. In the case of SERS, when a laser beam is incident on two metal nanoparticles (separated by a few nanometer gap) in a particular orientation, there is a strong focusing of optical energy (near field enhancement) in the gap between two nanoparticles due to their dipolar interaction which is called as *hotspot*. A molecule present in this hotspot will get an enormous energy to make a transition from its ground state to an excited state (Stokes scattering) or jump down from an excited state to the ground state (anti-stokes scattering) giving a vibrational signal of that particular molecule. This technique of molecular detection is known as surface-enhanced Raman spectroscopy. According to electromagnetic theory, SERS is the result of double resonant phenomenon as the incident and Raman scattered fields (stokes and anti-stokes lines) are resonantly enhanced by the surface plasmons. In fact, the metal nanoparticles can scatter light at the Raman shifted wavelength. Hence, the intensity of Raman scattering by molecules close to nanoparticle surface is enhanced by a factor of $|E_{local}(\omega_{exc})/E_{incident}(\omega_{exc})|^4$ [125,126] where ω_{exc} is the excitation frequency.

The field of molecular detection by SERS has grown in multitude of directions. During the last few decades, there are a number of applications in the field of chemical, material, and particular life sciences is rapidly increasing [121,122,127–129]. However, it was predicted theoretically that in an array (chain) of nanoparticles the field enhancement is even larger compared to two nanoparticles [130,131]. Recently, Arya *et al.* have simulated near-field mapping of ripple pattern supported metal nanoparticles arrays and shown that the interparticle gap and ordering of nanoparticles play an important role in calculated and the measured SERS response where a high intensity Raman signal is obtained for arrays of ordered elongated nanoparticles compared to non-ordered and the aligned configuration of spherical nanoparticles on the rippled surface [132]. Bhatnagar *et al.* have shown that ion-beam fabricated GaSb nanodots can be used for templates for silver nanoparticles growth and shown a LSPR-boosted binary platform for broadband light harvesting and SERS property [49]. Recently, Sooraj *et al.* have used 1D arrays of self-organized Ag nanoparticles on rippled-Si substrates and demonstrated the detection of glucose with lower concentration than blood glucose level [48].

In this thesis, we have investigated the efficacy of self-organized Au nanoparticles on rippled-Si substrates as an effective SERS substrate for the detection of crystal violet dye. From our experiments, the effect of Au nanoparticles size and their growth direction on rippled-Si substrates are systematically studied. To check the effect of ordering of nanoparticles, SERS of Au nanoparticles on as-obtained Si substrates are also examined and compared.

1.6 Motivation

Aforementioned ion-beam induced pattern formation on a semiconductor surface is a self-organization process having nanoscale features. The formation of these patterns is theoretically explained by taking into account mainly two competing processes, viz. roughening due to curvature-dependent sputtering and impact-induced mass redistribution as well as surface relaxation processes like ion-induced effective diffusion [133–138]. On the other hand, from last few decades, a lot of experiments are performed in the quest of different exotic patterns on metals, insulators, semiconductors, and polymers with their tunability based on ion-matter interactions [20,22,25,27,29,31,33]. These self-organized patterns are very useful as templates for various applications, viz. antireflection surfaces, solar cells, magnetic/optical anisotropy, magnetic memories etc. Our motivation behind the present thesis is to fabricate and make use of these self-organized patterns as templates and demonstrate their efficacy for a set of novel applications.

Importance of Si as a target: Silicon is chosen as the base material for the experimental work carried out under the scope of the present thesis. It is a mono-elemental target whose physical properties are well-known, second abundant material in the earth's crust (28%), mature fabrication and device manufacturing techniques, and the ease in forming oxide used for insulators in microelectronic circuits. In addition, it is the easily amorphizable upon ion irradiation. Thus, due to its popularity in microelectronics and device fabrication technologies, study of ion-beam induced patterns is well studied in literature [14,139]. Hence, it becomes further important to explore the futuristic and more innovative applications using silicon-based ion-beam patterns as templates/building blocks. Argon ions are chosen here due to its inert nature.

Angle-dependent growth of gold nanoparticles (Au-NPs): The nucleation and growth of nanoparticles is mainly affected by the surface free energies of nanoparticles and the host material surfaces. Moreover, the presence of surface defects can also alter the wettability of surfaces for incident material flux. In addition, the growth of nanoparticles on patterned surfaces can drastically change their interaction with surfaces and of course their self-organization. Hence, the growth kinetics of nanoparticles is of special interest on patterned surfaces. In the present thesis, we have made an attempt to study the growth angle-dependent properties of Au-NPs on ion-beam patterned silicon surfaces.

Optical anisotropy of self-organized Au-NPs on nanopatterned-Si: The optical anisotropy is a phenomenon which is observed when the speed of light in a medium depends upon the polarization plane of the electromagnetic wave. On the basis of material-dependent property (i.e. dielectric tensor), optical anisotropy is classified into two broad categories: the one where the uniaxial anisotropy is defined as $\mathcal{E}_x = \mathcal{E}_y \neq \mathcal{E}_z$ and the biaxial anisotropy is the case for $\mathcal{E}_x \neq \mathcal{E}_y \neq \mathcal{E}_z$. Besides the birefringent crystals, the anisotropy in optical properties of a host matrix can be tailored by incorporating optically-active foreign material in an ordered manner. In this context, the role of patterned substrates in creating the ordered or self-assembled materials come into picture. In fact, uniaxial and biaxial anisotropies can be tailored by oblique angle deposition of a material on rotationally and two fold symmetric patterns, respectively.

In the present thesis, the optical anisotropy induced by oblique angle, self-organized growth of Au-NPs on ion-beam patterned nanoscale rippled- and faceted-Si substrates are of prime interest. However, interpretation of experimentally observed optical anisotropy using spectroscopic ellipsometry and further fitting an adequate physical model for comparing the best fit of computed optical parameters with experimentally observed ones are of interest and are studied in the present thesis.

SERS detection of crystal violet dye: Surface-enhanced Raman spectroscopy is a vibrational spectroscopy technique predominantly based on electromagnetic field enhancement by the excitation of localized surface plasmons of metal nanostructures, which is used for detection of Raman active molecules at low concentrations. The self-organized arrays of Au-NPs on nanorippled-Si substrates exhibit a fascinating local surface plasmon resonance. In particular, oblique angle growth of Au-NPs leads to different sizes of nanoparticles along with their tunable coverage area which is quite interesting to explore in the framework of SERS detection of crystal violet dye.

Cold cathode field electron emission from self-organized Au-NPs on nanofaceted-Si: Field electron emission has drawn a lot of attention because of its possible applications as a fascinatingly low and efficient point electron source in electron microscopes, x-ray sources, flat panel displays, space applications, and microwave amplifiers. It has been reported by our group that ion-beam fabricated smaller facets leads to a lower turn-on threshold field since more native oxide coverage is observed on relatively bigger facets [108]. Therefore, it will be important to revisit and optimize the fabrication process to further lower down the threshold field for cold cathode electron emission from Si-NFs. In this thesis we demonstrate that the lowest threshold field is achieved for Si-NFs fabricated at an incident ion angle of 71º and having low oxide coverage. The aim of the present study is to further lower down the threshold turn-on field for electron emission. It is quite motivating from the literature that field emission can be further enhanced by deposition of metal nanoparticles on top of the silicon nanostructures [140,141]. Therefore, Au-NPs are deposited on nanofaceted-Si substrates in an angular window of 65° to 85° and fascinating field electron emission characteristics are observed corresponding to a growth angle of 70º where the turn-on field is extremely low (e.g. 0.27 V μm^{-1}). Thus, the present study suggests that ion-beam fabricated Si-NFs having low aspect ratios may be good field emitters.

Antireflection of ZTO films on nanostructured-Si: As the name suggests, antireflection (AR) coating is a type of optical coating to reduce the reflection losses by destructive interference of incident and reflected light from an interface. In this context, silicon is a poor absorber of light due to its indirect band gap. As a matter of fact, more than 35% of the incident light is lost through Fresnel reflection due to a large and abrupt change in the refractive index at the interface of Si (n_{Si}~3.4) and air (n_{air}=1). An efficient AR coating, preferably in the form of a transparent conducting oxide (e.g. sputter-grown $ZnO:SnO_2$ (or ZTO) thin films in the present case), is required to improve the performance of a silicon solar cell via an increased light absorption. It is important to note that a single layer TCO coating on a flat-Si substrate can work as antireflection coating for a single wavelength, however the same coating on mirco/nano-patterned surfaces can efficiently reduce the reflection losses over a broad spectral range [36,37]. This is the fact, which motivated us to study the efficacy of thickness-dependent AR in case of ZTO films grown on ion-beam patterned Si substrates.

1.7 Outlines of the thesis

This thesis presents nanoscale functionalization of low energy Ar-ion beam fabricated nanoscale patterned-Si substrates as templates for a set of important applications. For this purpose, we have optimized the angle-dependent growth of Au-NPs on rippled-and faceted-Si substrates. It is interesting to note that the self-organized Au-NPs on rippled-Si substrates exhibit in-plane optical anisotropy, as investigated by spectroscopic ellipsometry measurements and fitting the data using physical models. We have achieved fascinating low threshold turn-on fields and highly stable cold cathode electron emission from self-organized Au-NPs on nanofaceted-Si substrates. We attempt to demonstrate SERS efficacy of 2D arrays of self-organized Au-NPs on rippled-Si substrates towards sensing the of crystal violet dye. In addition to this, we have demonstrated the film thickness-dependent broadband antireflection from the conformally-grown ZTO films on nanoscale rippled- and faceted-Si substrates using sputter deposition technique. The thesis is organized in the following manner:

Chapter 1: In this chapter, a brief review on ion-beam induced fabrication of silicon patterns is provided. It also deals with the growth of thin films and self-organized nanoparticles. A thorough literature survey is also provided as the functionalization of ion irradiation induced self-organized patterned surfaces. In this chapter, we have also incorporated the motivation behind the present thesis work.

Chapter 2: This chapter describes the experimental techniques employed for carrying out the studies presented in this thesis.

Chapter 3: In this chapter, we first introduce the statistical methods for characterization of surfaces. Afterwards, a brief introduction on ion-solid interaction and continuum theory-based models are provided to describe the evolution of surface morphology on Si substrates. A detail discussion on the simulation codes (SRIM, TRIDYN, and SDTrimSP) on ion-solid interaction are provided and are compared the results of simulation obtained for 500 eV Ar-ion bombardment in Si. Growth kinetics of thin films, nucleation, and coalescence of metallic thin films are also discussed in this chapter.

Chapter 4: This chapter describes the nanoscale functionalization of nanorippled-Si substrates. In doing so, the angle-dependent growth of Au-NPs on nanopatterned silicon substrates is discussed in terms of morphological and compositional aspects. For Au-NPs grown on rippled-Si substrates, we have used the spectroscopic ellipsometry technique to investigate the growth angle-dependent in-plane anisotropy using *p*-polarized light and optical models are used to fit the experimental data to reveal the complex dielectric constants. In addition, the SERS detection of crystal violet dye is also demonstrated by using local surface plasmon resonance of 2D arrays of Au-NPs on self-assembled rippled-Si substrates.

Chapter 5: This chapter demonstrates the nanoscale functionalization of nanofaceted-Si substrates. In the quest of achieving highly stable and efficient cold cathode electron emission (with low threshold turn-on field) from these nanostructures, the process of nanoscale facets formation is optimized. Further, we have studied the growth angle-dependence of Au-NPs to achieve tunable field emission (FE) from nanofaceted-Si substrates. The turn-on field of nanofaceted-Si substrates has been significantly lowered down by Au-NPs decoration. We measure the turn-on field, enhancement factor, and the stability of FE from the bulk current-voltage characteristics. However, bulk measurements cannot reveal the regions which mostly contribute to the field induced electron emission from these Si-NFs. In order to overcome this problem, atomic force microscope-based dual pass tunneling current microscopy (DPTCM) in conjunction with Kelvin probe force microscopy (KPFM) are employed. These measurements clearly show that both apexes and sidewalls of nanofaceted-Si contribute to the field induced electron emission when they are decorated with Au-NPs in contrast to bare Si-NFs where the sidewalls and valleys (but not the apexes) contribute to the FE process.

Chapter 6: In this chapter, antireflection efficacy of conformally-grown ZTO thin films on nanorippled- and nanofaceted-Si substrates are investigated. Antireflection property of the nanopatterned-Si substrates is characterized using UV-Vis-NIR spectrophotometer. A significant reduction in the reflectance is observed for as-prepared nanorippled- and nanofaceted-Si substrates compared to *flat*-Si due to multiple reflection of light among the neighbouring facets. Interestingly, the sputter-grown ZTO overlayers demonstrate excellent AR property, albeit, upon depositing them on patterned surfaces (particularly on Si-NFs) exhibit a tunable AR coating over a broad range of optical spectrum.

Chapter 7: In this chapter, we have summarized the outcome of the present thesis work. Further, we have outlined the future scope of experimental studies based on our findings and their importance towards a deeper understanding of ion induced pattern formation and their possible applications.

Bibliography

[1] C. Binns, *"Introduction to Nanoscience and Nanotechnology"*, John Wiley & Sons, Inc., Hoboken, NJ, USA, 2010.

[2] A. Nouailhat, *"An Introduction to Nanoscience and Nanotechnology"*, ISTE, London, UK, 2008.

[3] R.P. Feynman, Eng. Sci. 23 (1960) 22.

[4] B. Bhushan, D. Luo, S.R. Schricker, W. Sigmund, S. Zauscher, eds., *"Handbook of*

Nanomaterials Properties", Springer Berlin Heidelberg, Berlin, Heidelberg, 2014.

[5] A.D. Maynard, R.J. Aitken, T. Butz, V. Colvin, K. Donaldson, G. Oberdörster, M.A. Philbert, J. Ryan, A. Seaton, V. Stone, S.S. Tinkle, L. Tran, N.J. Walker, D.B. Warheit, Nature 444 (2006) 267.

[6] P. Iqbal, J.A. Preece, P.M. Mendes, in: Supramol. Chem., John Wiley & Sons, Ltd, Chichester, UK, 2012.

[7] P. Colson, C. Henrist, R. Cloots, J. Nanomater. 2013 (2013) 1.

[8] R. Zhang, T. Chen, A. Bunting, R. Cheung, Microelectron. Eng. 154 (2016) 62.

[9] A. Pimpin, W. Srituravanich, Eng. J. 16 (2012) 37.

[10] R.M.M. Hasan, X. Luo, Nanomanufacturing Metrol. 1 (2018) 67.

[11] Y. Chen, Microelectron. Eng. 135 (2015) 57.

[12] A.S. Gangnaik, Y.M. Georgiev, J.D. Holmes, Chem. Mater. 29 (2017) 1898.

[13] A.A. Tseng, K. Chen, C.D. Chen, K.J. Ma, IEEE Trans. Electron. Packag. Manuf. 26 (2003) 141.

[14] T. Som and D. Kanjilal, eds., *"Nanofabrication by ion-beam sputtering: From fundamentals to applications"*, CRC Press, 2012.

[15] L. Hanley, S.B. Sinnott, Surf. Sci. 500 (2002) 500.

[16] M. Navez, C. Sella, D. Chaperot, CR Académie Des Sci. . Paris. 254 (1962) 240.

[17] R. Gago, L. Vázquez, R. Cuerno, M. Varela, C. Ballesteros, J.M. Albella, Nanotechnology 13 (2002) 304.

[18] C.S. Madi, B. Davidovitch, H.B. George, S.A. Norris, M.P. Brenner, M.J. Aziz, Phys. Rev. Lett. 101 (2008) 10.

[19] M. Teichmann, J. Lorbeer, F. Frost, B. Rauschenbach, Nanoscale Res. Lett. 9 (2014) 1.

[20] T. Basu, J.R. Mohanty, T. Som, Appl. Surf. Sci. 258 (2012) 9944.

[21] S. Facsko, Science 285 (1999) 1551.

[22] X. Ou, A. Keller, M. Helm, J. Fassbender, S. Facsko, Phys. Rev. Lett. 111 (2013) 1.

[23] M. Teichmann, J. Lorbeer, B. Ziberi, F. Frost, B. Rauschenbach, New J. Phys. 15 (2013) 103029.

[24] O. El-Atwani, S.A. Norris, K. Ludwig, S. Gonderman, J.P. Allain, Sci. Rep. 5 (2015) 1.

[25] S.A. Mollick, M. Kumar, R. Singh, B. Satpati, D. Ghose, T. Som, Nanotechnology 27 (2016) 435302.

[26] S.A. Mollick, R. Singh, M. Kumar, S. Bhattacharyya, T. Som, Nanotechnology 29 (2018) 125302.

[27] D. Chowdhury, D. Ghose, S.A. Mollick, B. Satpati, S.R. Bhattacharyya, Phys. Status Solidi Basic Res. 252 (2015) 811.

[28] Y. Liu, D. Hirsch, R. Fechner, Y. Hong, S. Fu, F. Frost, B. Rauschenbach, Appl. Phys. A Mater. Sci. Process. 124 (2018) 73.

[29] M. Kumar, D.P. Datta, T. Basu, S.K. Garg, H. Hofsäss, T. Som, J. Phys. Condens. Matter 30 (2018) 334001.

[30] T. Bolse, H. Paulus, W. Bolse, Nucl. Instruments Methods Phys. Res. Sect. B Beam Interact. with Mater. Atoms 245 (2006) 264.

[31] T. Škereň, K. Temst, W. Vandervorst, A. Vantomme, New J. Phys. 15 (2013) 093047.

[32] S.P. Kim, H.B. Chew, E. Chason, V.B. Shenoy, K.S. Kim, Proc. R. Soc. A Math. Phys. Eng. Sci. 468 (2012) 2550.

[33] L. Xue, J. Zhang, Y. Han, Prog. Polym. Sci. 37 (2012) 564.

[34] J.Q. Xi, M.F. Schubert, J.K. Kim, E.F. Schubert, M. Chen, S.Y. Lin, W. Liu, J.A. Smart, Nat. Photonics 1 (2007) 176.

[35] S.J. Wilson, M.C. Hutley, Opt. Acta (Lond). 29 (1982) 993.

[36] C. Martella, D. Chiappe, P. Delli Veneri, L. V. Mercaldo, I. Usatii, F. Buatier De Mongeot, Nanotechnology 24 (2013) 225201.

[37] T. Basu, M. Kumar, P. Sahoo, A. Kanjilal, T. Som, Nanoscale Res. Lett. 9 (2014) 192.

[38] C.H. Sun, P. Jiang, B. Jiang, Appl. Phys. Lett. 92 (2008) 061112.

[39] S.-H. Hong, B.-J. Bae, K.-S. Han, E.-J. Hong, H. Lee, K.-W. Choi, Electron. Mater. Lett. 5 (2009) 39.

[40] S. Ji, J. Park, H. Lim, Nanoscale 4 (2012) 4603.

[41] B. Kiraly, S. Yang, T.J. Huang, Nanotechnology 24 (2013) 245704.

[42] C. Martella, D. Chiappe, C. Mennucci, F.B. De Mongeot, J. Appl. Phys. 115 (2014) 194308.

[43] Ü. Sökmen, A. Stranz, S. Fündling, S. Merzsch, R. Neumann, H.-H. Wehmann, E. Peiner, A. Waag, Microsyst. Technol. 16 (2010) 863.

[44] M. Hajra, C.E. Hunt, M. Ding, O. Auciello, J. Carlisle, D.M. Gruen, J. Appl. Phys. 94 (2003) 4079.

[45] P.D. Kichambare, F.G. Tarntair, L.C. Chen, K.H. Chen, H.C. Cheng, J. Vac. Sci. Technol. B Microelectron. Nanom. Struct. 18 (2000) 2722.

[46] M. Ranjan, M. Bhatnagar, S. Mukherjee, J. Appl. Phys. 117 (2015) 103106.

[47] M. Ranjan, S. Facsko, M. Fritzsche, S. Mukherjee, Microelectron. Eng. 102 (2013) 44.

[48] K.P. Sooraj, M. Ranjan, R. Rao, S. Mukherjee, Appl. Surf. Sci. 447 (2018) 576.

[49] M. Bhatnagar, M. Ranjan, S. Mukherjee, J. Nanoparticle Res. 17 (2015) 1.

[50] B. Teschome, S. Facsko, K. V. Gothelf, A. Keller, Langmuir 31 (2015) 12823.

[51] S.E. Hunyadi Murph, G.K. Larsen, K.J. Coopersmith, eds., *"Anisotropic and Shape-Selective Nanomaterials"*, Springer International Publishing, Cham, 2017.

[52] F. Priolo, T. Gregorkiewicz, M. Galli, T.F. Krauss, Nat. Nanotechnol. 9 (2014) 19.

[53] L.-W. Wang, Comput. Phys. Commun. 133 (2002) 137.

[54] N. Selvakumar, H.C. Barshilia, Sol. Energy Mater. Sol. Cells 98 (2012) 1.

[55] S. Shahidi, B. Moazzenchi, M. Ghoranneviss, Eur. Phys. J. Appl. Phys. 71 (2015) 31302.

[56] S.M. Rossnagel, J. Vac. Sci. Technol. A Vacuum, Surfaces, Film. 21 (2003) S74.

[57] R.F. Bunshah, C. V. Deshpandey, J. Vac. Sci. Technol. A Vacuum, Surfaces, Film. 3 (2002) 553.

[58] G. Malandrino, *"Chemical Vapour Deposition: Precursors, Processes and Applications"*, Angew. Chemie Int. Ed. 48 (2009) 7478.

[59] Y. Xu, X.-T. Yan, *"Chemical Vapour Deposition Systems Design"*, Springer London, London, 2010.

[60] Z. Cai, B. Liu, X. Zou, H.M. Cheng, Chem. Rev. 118 (2018) 6091.

[61] J.S. Park, S. Kim, Z. Xie, A. Walsh, Nat. Rev. Mater. 3 (2018) 194.

[62] T.D. Lee, A.U. Ebong, Renew. Sustain. Energy Rev. 70 (2017) 1286.

[63] M.A. Green, J. Mater. Sci. Mater. Electron. 18 (2007) 15.

[64] J.F.M. Oudenhoven, L. Baggetto, P.H.L. Notten, Adv. Energy Mater. 1 (2011) 10.

[65] J. Li, Q. Jiang, N. Yuan, J. Tang, Materials (Basel). 11 (2018) 2280.

[66] K. Kerman, A. Luntz, V. Viswanathan, Y.-M. Chiang, Z. Chen, J. Electrochem. Soc. 164 (2017) A1731.

[67] S. Oukassi, L. Baggetto, C. Dubarry, L. Le Van-Jodin, S. Poncet, R. Salot, ACS Appl. Mater. Interfaces 11 (2019) 683.

[68] R.E. Fontana, S.R. Hetzler, J. Appl. Phys. 99 (2006) 08N902.

[69] C.F. Taylor, J.D. Blades, F.G. Hewitt, J. Appl. Phys. 42 (1971) 1755.

[70] L.D. Stevens, IBM J. Res. Dev. 25 (2010) 663.

[71] A. Chung, J. Deen, J.-S. Lee, M. Meyyappan, Nanotechnology 21 (2010) 412001.

[72] T.W. Kim, Y. Yang, F. Li, W.L. Kwan, NPG Asia Mater. 4 (2012) e18.

[73] D. Ielmini, H.S.P. Wong, Nat. Electron. 1 (2018) 333.

[74] D. Ielmini, Semicond. Sci. Technol. 31 (2016) 063002.

[75] Y. Wu, J. Liang, S. Yu, X. Guan, H.S.P. Wong, IEEE Int. Integr. Reliab. Work. Final Rep.

(2012) 16.

[76] S. Yngvesson , *"Microw. Semicond. Devices"*, Springer US, Boston, MA, 2011.

[77] J.L. Hudgins, Microelectronics J. 24 (1993) 41.

[78] A. Kamiŝalić, I. Fister, M. Turkanović, S. Karakatiĉ, Sensors (Switzerland) 18 (2018) 1714.

[79] R.A. Yotter, D.M. Wilson, IEEE Sens. J. 3 (2003) 288.

[80] G. Abadias, E. Chason, J. Keckes, M. Sebastiani, G.B. Thompson, E. Barthel, G.L. Doll, C.E. Murray, C.H. Stoessel, L. Martinu, J. Vac. Sci. Technol. A Vacuum, Surfaces, Film. 36 (2018) 020801.

[81] S. Guldin, P. Kohn, M. Stefik, J. Song, G. Divitini, F. Ecarla, C. Ducati, U. Wiesner, U. Steiner, Nano Lett. 13 (2013) 5329.

[82] H.K. Raut, V.A. Ganesh, A.S. Nair, S. Ramakrishna, Energy Environ. Sci. 4 (2011) 3779.

[83] B.M. Phillips, P. Jiang, "*Biomimetic Antireflection Surfaces"*, Elsevier, 2013.

[84] H.A. Macleod, Appl. Opt. 20 (2008) 82.

[85] J. Moghal, J. Kobler, J. Sauer, J. Best, M. Gardener, A.A.R. Watt, G. Wakefield, ACS Appl. Mater. Interfaces 4 (2012) 854.

[86] M. Kumar, M. Patel, H.S. Kim, J. Kim, J. Yi, ACS Appl. Mater. Interfaces 9 (2017) 38824.

[87] S. Abbas, M. Kumar, D. Kim, J. Kim, Small (2019) 1804346.

[88] Z. Li, K. Xu, F. Wei, Nanotechnol. Rev. 7 (2018) 393.

[89] S.A. Guerrera, A.I. Akinwande, Nanotechnology 27 (2016) 295302.

[90] B. Liu, Y. Bando, C. Tang, F. Xu, J. Hu, D. Golberg, J. Phys. Chem. B 109 (2005) 17082.

[91] A. Ghosh, P. Guha, R. Thapa, S. Selvaraj, M. Kumar, B. Rakshit, T. Dash, R. Bar, S.K. Ray, P.V. Satyam, Nanotechnology 27 (2016) 125701.

[92] F. Zhao, G. an Cheng, R. ting Zheng, D. dan Zhao, S. long Wu, J. hua Deng, Nanoscale Res. Lett. 6 (2011) 176.

[93] A. Singh, K. Senapati, M. Kumar, T. Som, A.K. Sinha, P.K. Sahoo, Appl. Surf. Sci. 411 (2017) 117.

[94] P. Mandal, S. Sharma, Renew. Sustain. Energy Rev. 65 (2016) 537.

[95] Y.H. Jang, Y.J. Jang, S. Kim, L.N. Quan, K. Chung, D.H. Kim, Chem. Rev. 116 (2016) 14982.

[96] F. Liu, D. Qu, Q. Xu, W. Xie, Y. Huang, *"Plasmonic core-shell nanoparticle-based thin film solar cells"*, 22nd Congr. Int. Comm. Opt. Light Dev. World, 2011.

[97] K. Ueno, T. Oshikiri, Q. Sun, X. Shi, H. Misawa, Chem. Rev. 118 (2018) 2955.

[98] H. Al-Bustami, G. Koplovitz, D. Primc, S. Yochelis, E. Capua, D. Porath, R. Naaman, Y. Paltiel, Small 14 (2018) 1801249.

[99] P. Cui, S. Seo, J. Lee, L. Wang, E. Lee, M. Min, H. Lee, ACS Nano 5 (2011) 6826.

[100] S. Pang, T. Yang, L. He, TrAC - Trends Anal. Chem. 85 (2016) 73.

[101] B. Sharma, R.R. Frontiera, A. Henry, E. Ringe, R.P. Van Duyne, Mater. Today 15 (2012) 16.

[102] H. Zhou, D. Yang, N.P. Ivleva, N.E. Mircescu, R. Niessner, C. Haisch, Anal. Chem. 86 (2014) 1525.

[103] J.R. Nitschke, Angew. Chemie Int. Ed. 47 (2008) 6108.

[104] A.B. El-Kareh, J.C. Wolfe, J.E. Wolfe, J. Appl. Phys. 48 (1977) 4749.

[105] A.A. Talin, K.A. Dean, J.E. Jaskie, Solid. State. Electron. 45 (2001) 963.

[106] S. Nandy, R. Thapa, M. Kumar, T. Som, N. Bundaleski, O.M.N.D. Teodoro, R. Martins, E. Fortunato, Adv. Funct. Mater. 25 (2015) 947.

[107] T. Basu, M. Kumar, M. Saini, J. Ghatak, B. Satpati, T. Som, ACS Appl. Mater. Interfaces 9 (2017) 38931.

[108] N. Egorov, E. Sheshin, *"Field emission cathode-based devices and equipment"*, Springer International Publishing, Cham 2017.

[109] Y. Fan, M. Rose, *"Field emission displays (FEDs)"*, Springer Berlin Heidelberg, Berlin, Heidelberg, 2012.

[110] A. Basu, M.E. Swanwick, A.A. Fomani, L.F. Velásquez-García, J. Phys. D. Appl. Phys. 48 (2015) 225501.

[111] S. Cheng, F.A. Hill, E. V Heubel, L.F.V. Quez-García, J. Phys. Conf. Ser. 476 (2013) 012016.

[112] A.A. Fomani, A.I. Akinwande, L.F. Velásquez-García, J. Phys. Conf. Ser. 476 (2013) 012014.

[113] J. Ximen, P.S.D. Lin, J.B. Pawley, M. Schippert, Rev. Sci. Instrum. 64 (1993) 2905.

[114] G.N. Fursey, Field Emission in Vacuum Micro-Electronics, Springer US, Boston, MA, 2003.

[115] T.E. Stern, B.S. Gossling, R.H. Fowler, Proc. R. Soc. A Math. Phys. Eng. Sci. 124 (2006) 699.

[116] R.H. Fowler, L. Nordheim, Proceedings of the Royal Society A: Mathematical, Physical and Engineering Sciences, 119 (1928) 683.

[117] X. Fang, Y. Bando, U.K. Gautam, C. Ye, D. Golberg, J. Mater. Chem. 18 (2008) 509.

[118] P. Guha, A. Ghosh, R. Thapa, E.M. Kumar, S. Kirishwaran, R. Singh, P. V. Satyam, Nanotechnology 28 (2017) 415602.

[119] M. Choueib, R. Martel, C.S. Cojocaru, A. Ayari, P. Vincent, S.T. Purcell, ACS Nano 6 (2012) 7463.

[120] S. Sridhar, C. Tiwary, S. Vinod, J.J. Taha-Tijerina, S. Sridhar, K. Kalaga, B. Sirota, A.H.C. Hart, S. Ozden, R.K. Sinha, Harsh, R. Vajtai, W. Choi, K. Kordás, P.M. Ajayan, ACS Nano 8 (2014) 7763.

[121] B. Sharma, R.R. Frontiera, A.I. Henry, E. Ringe, R.P. Van Duyne, Mater. Today 15 (2012) 16.

[122] S. Schlücker, Angew. Chemie - Int. Ed. 53 (2014) 4756.

[123] K. Kneipp, Y. Wang, H. Kneipp, L.T. Perelman, I. Itzkan, R.R. Dasari, M.S. Feld, Phys. Rev. Lett. 78 (1997) 1667.

[124] K. Kneipp, H. Kneipp, R. Manoharan, I. Itzkan, R.R. Dasari, M.S. Feld, Bioimaging 6 (1998) 104.

[125] M. Moskovits, J. Raman Spectrosc. 36 (2005) 485.

[126] K.D. Alexander, M.J. Hampton, S. Zhang, A. Dhawan, H. Xu, R. Lopez, J. Raman Spectrosc. 40 (2009) 2171.

[127] C. Muehlethaler, M. Leona, J.R. Lombardi, Anal. Chem. 88 (2016) 152.

[128] M.F. Cardinal, E. Vander Ende, R.A. Hackler, M.O. McAnally, P.C. Stair, G.C. Schatz, R.P. Van Duyne, Chem. Soc. Rev. 46 (2017) 3886.

[129] Y. Kitahama, T. Itoh, P. Pienpinijtham, S. Ekgasit, X.X. Han, Y. Ozaki, in: ACS Symp. Ser., (2012) 181.

[130] S. Enoch, R. Quidant, G. Badenes, Opt. Express 12 (2004) 3422.

[131] R.L. Chern, X.X. Liu, C.C. Chang, Phys. Rev. E - Stat. Nonlinear, Soft Matter Phys. 76 (2007) 016609.

[132] M. Arya, M. Bhatnagar, M. Ranjan, S. Mukherjee, R. Nath, A. Mitra, J. Phys. D. Appl. Phys. 50 (2017) 455603.

[133] G. Carter, V. Vishnyakov, Phys. Rev. B. Condens. Matter 54 (1996) 17647.

[134] C.S. Madi, E. Anzenberg, K.F. Ludwig, M.J. Aziz, Phys. Rev. Lett. 106 (2011) 1.

[135] C. Herring, J. Appl. Phys. 21 (1950) 301.

[136] W.W. Mullins, J. Appl. Phys. 30 (1959) 77.

[137] M.A. Makeev, A.L. Barabási, Appl. Phys. Lett. 71 (1997) 2800.

[138] R.M. Bradley, J.M.E. Harper, J. Vac. Sci. Technol. A Vacuum, Surfaces, Film. 6 (1988) 2390.

[139] R.A. Levy, ed., *"Novel silicon based technologies"*, Springer Netherlands, Dordrecht, 2012.

[140] Y.M. Chang, M.L. Lin, T.Y. Lai, H.Y. Lee, C.M. Lin, Y.C.S. Wu, J.Y. Juang, ACS Appl. Mater. Interfaces 4 (2012) 6676.

[141] C. Ye, Y. Bando, X. Fang, G. Shen, D. Golberg, J. Phys. Chem. C 111 (2007) 12673.

CHAPTER 2

Experimental techniques

The experimental studies presented in this thesis cover the fabrication of self-organized nanoscale patterns on silicon surfaces by bombardment of 500 eV energy Ar-ions at different oblique angles and demonstrate the usefulness of these patterned-substrates as templates for antireflection coatings, SERS substrates, and field emission devices. During the course of this study, an electron cyclotron resonance (ECR) based low energy (0−2 keV) broad beam (2 in. diameter) gaseous ion source was used for ion bombardment. It is noteworthy that two distinct type of patterns were fabricated on silicon surface by simply varying the incident angle of ions. These patterned-Si substrates were used as templates for the growth of zinc tin oxide (ZTO) thin films by using RF sputtering technique towards studying their antireflection property.

In addition, patterned-Si substrates were functionalized by deposition of gold nanoparticles (NPs) at various oblique angles using electron beam evaporation technique. For instance, Au-NPs decorated patterned-Si substrates were used for SERS and cold cathode electron emission. In this chapter, we briefly introduce the basic working principles of these experimental techniques and their instruments.

2.1 Low energy ion-source integrated molecular beam epitaxy system

As the name suggests, molecular beam epitaxy (MBE) is a sophisticated ultra-high vacuum technique to grow epitaxial thin films (far from thermodynamic equilibrium) with extreme regularity in layer thickness and composition, arising from precisely controlled deposition rates [1,2]. The term epitaxy comes from the Greek root “epi” and “taxis” which correspond to “above” and “an ordered manner”, respectively. In other words, the epitaxy is the arrangement of one or more thermal atomic and/or molecular species atop a heated and ordered crystalline substrate to form a thin layer whose crystallinity matches that of the substrate even though the composition of the materials may differ, e.g. GaAs/InGaAs, GaAs/AlGaAs, InP/InAlAs/InGaAs etc. Again, the term beam refers to the unidirectional kinematic flow of evaporated atoms and/or molecules with no mutual interaction before impinging on the substrate due to their long mean free paths involved in the deposition process.

The advancement of MBE started after the discovery of MBE process discovered in the late 1960s at Bell laboratories by J. R. Arthur and Y. Alfred [3,4]. An important aspect of III–V compounds, like non-congruent evaporation of GaAs due to much higher partial pressure of group-V species than group-III ones. As a solution, two crucibles configuration was used by Collins *et al*. (1956) to evaporate and maintain a suitable beam flux ratio of the group-III and group-V species for deposition of stoichiometric films [5]. In this attempt, they were successful in depositing polycrystalline GaSb layers on glass substrates. In 1961, Guenther *et al.* proposed to use a heated substrate holder along with two crucibles for the constituent species (Ga and As) [5]. The crucibles were set to the temperatures for certain beam fluxes, whereas the substrate was kept at sufficiently high temperature to help re-evaporating the surplus amount of group-V species on the glass substrate. However, good quality single crystals of GaAs and InSb were grown by using crystalline substrates which were cleaned using ion bombardment under UHV conditions [5]. Subsequently, to study the substrate cleaning procedures and early growth stages of epitaxial layers, MBE chambers are equipped with Auger electron spectrometry (AES) and reflection high-energy electron diffraction (RHEED) techniques.

The UHV conditions are an integral part of an MBE system, since the surface contaminations and incorporation of unintentional species greatly affect the growth kinetics. Thus, we recall the kinetic theory of gases to understand the necessity of UHV conditions [1,2,5]. According to kinetic theory of gases, the number of atoms hitting a surface per unit surface area and per unit time can be expressed as: $\phi = P/\sqrt{2\pi m K_B T}$, where P is the background pressure, m is the atomic mass of impinging gas atoms, K_B is Boltzmann's constant, and T is the absolute temperature of the gas. The mean free path of gas species can be defined as the average path length travelled by gaseous species before their mutual collisions as: $\lambda = 1/\left(n\pi d^2\sqrt{2}\right)$ where n and d are the number density and diameter of the gaseous atoms, respectively.

Degree of vacuum	Pressure (mbar)	Mean free path (meter)
Atmospheric	1000	5.9×10^{-8}
HV	1×10^{-6}	59
UHV	1×10^{-10}	5.9×10^{5}

Table 2.1 Relation between degree of vacuum and their corresponding mean free path of nitrogen molecule at 273.15 K.

The mean free path values calculated for a nitrogen molecule at 273.15 K and is presented in Table 2.1. Thus, at atmospheric pressure, a nitrogen molecule therefore travels a distance of merely 59 nm between two collisions, while at UHV (< 10^{-10} mbar) it travels a distance of several kilometers. In other words, if the background pressure is higher than UHV conditions and sticking coefficient is considered to be one, it takes a few seconds to form a monolayer (ML) of residual gases. Need of high purity epitaxial layers poses another constraint to have UHV conditions in MBE. Since there is an excellent control over the growth rates of epitaxial layers (< 1 ML/s) in MBE systems, a background pressure of < 1×10^{-10} mbar can reduce the impurity level to less than one part per million, which is the requirement for most of the applications.

Our MBE system (as shown in Fig. 2.1) has a special feature of making use of both bottom-up as well as top-down approaches towards functionalization of materials by sculpting them and depositing materials in the form of thin films and nanostructures towards studying their useful properties. Integration of a low energy ion-source with the MBE system (Prevac, Poland) [6] which opens up a new horizon for the fabrication of self-organized patterns on different substrates including semiconductors, metals, insulators, and thereafter deposition of materials towards their functionalization. This system consists of four stainless-steel chambers separated by gate-valves which are briefly described in following manner:

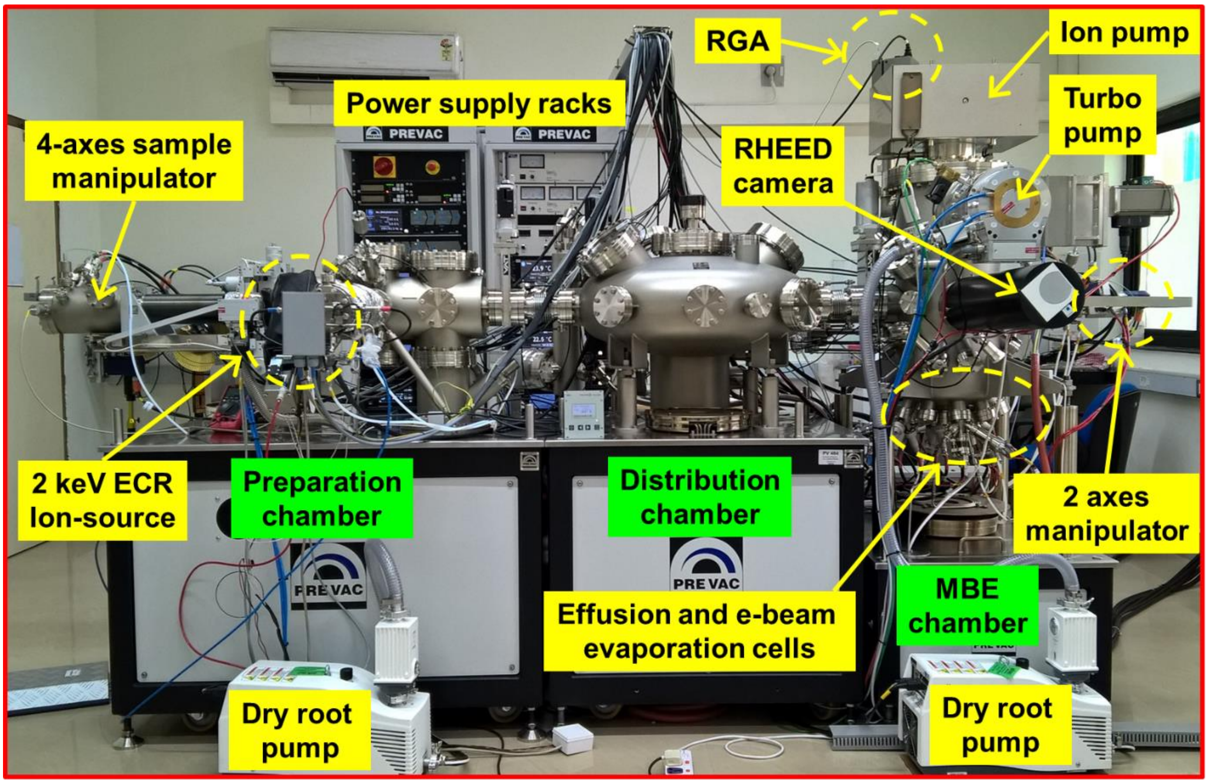

Figure 2.1: Picture of 2 keV ECR-based broad beam ion-source integrated MBE system at NanoAFM laboratory, advanced material processing laboratory (AMPL) complex.

Load lock chamber: The first and smallest volume chamber is load lock (LL) chamber, which is equipped with resistive heating up to 1000°C and halogen heating along with turbo molecular pump (Hi-Pace 300) backed by dry root pump (ACP-15). This chamber have three samples storage capacity at a time. As the name suggests, it works as a bridge for a sample to be transferred from ambient to UHV and vice-versa. Additionally, it offers the sample heating for removal of surface contamination, native oxide layer, and heating-induced improvement in the crystallinity of the sample. The small volume of the chamber allows it to pump down (or restore the vacuum during sample heating) a 1×10^{-8} mbar vacuum in merely 1-2 hours.

Distribution chamber: This chamber is used to transfer samples from load lock chamber to other chambers. It is interesting to note that it has six numbers of blank 40CF ports (stations) to add up different UHV based techniques. A thumb wheel at the top of this chamber is mechanically attached to a metallic arm inside the chamber, which has a special mechanical arrangement to select the station for sample transfer by rotating it clockwise. However, its anti-clockwise rotation at the station enables the linear motion of the arm to put the sample on sample holder in any connected chamber. This chamber is kept at $<1\times10^{-10}$ mbar with the help of ion-pump (Gamma vacuum). In addition, Ti-sublimation pump is also provided to maintain the vacuum during the baking of the system.

Preparation chamber: This chamber is used to prepare the sample before the deposition in the MBE chamber. It maintains a UHV ($<1\times10^{-10}$ mbar) with the help of an ion-pump (Gamma Vacuum) and a turbo molecular pump (Pfeiffer) backed up by a dry root pump (Adixen). Moreover, Ti-sublimation pump is also provided to maintain the vacuum during the baking of the system. In addition, this chamber has an in-built liquid nitrogen cryopanel to cool down the residual gas species present inside the chamber. This chamber is equipped with 2 keV ECR-based broad beam ion source (Gen-II, Tectra GmbH) for fabrication of different self-organized patterns on materials. A turbo molecular pump (HiPace 300, Pfeiffer Vacuum) is also equipped with the ion source as a differential pumping unit to maintain the required vacuum during its operation.

It is interesting to note that a gamut of self-organized patterns can be fabricated on a single material by changing the incidence angle of ions. Hence, to take the advantage of angle-dependent pattern formation, a 4-axes automated manipulator is equipped with this chamber. This manipulator can make precise translational motion in *X*-, *Y*-, and *Z*-directions along with the sample rotation (R1). This chamber provides an extra speciality to study the temperature-dependent fabrication of surface patterns in the temperature range of 78 K (liquid nitrogen) to 1273 K.

MBE chamber: This chamber is the most important chamber of the system, which is equipped with all the accessories required for a typical molecular beam epitaxy system. As described for preparation chamber, this chamber is also equipped with Ti-sublimation pump, ion-pump, and turbo molecular pump backed by dry root pump to achieve $<1\times10^{-10}$ mbar vacuum. However, pressure can be further lowered down to 2×10^{-11} mbar by using in-built liquid N_2 cooled cryopanel. The entire vacuum system is bakeable up to 523 K (for extended periods of time) to minimize outgassing from the internal walls during the evaporation material loading or troubleshooting. The sample receiving stage is connected to a 2-axes fully automated manipulator, which can have the R1 (out of sample plane) and R2 (in plane) rotation. The temperature of the substrate can be set up to 1000°C.

In the next sub-sections, the essential components of low energy ECR-based ion-source integrated MBE system are briefly described. However, pattern formation by low energy ECR-based ion-source and further growth of Au-NPs by e-beam evaporation technique used in the present thesis are explained in detail.

2.1.1 Quartz crystal micro-balance

Quartz micro-balance [7] is a tool for measuring *in-situ* deposition rate on the basis of well-known piezoelectric effect. The natural oscillation frequency of a quartz crystal can be written as: $f_0 = \sqrt{\mu_q/\rho_q}/2t_q$, where $\mu_q = 2.947\times10^{11}$ g cm^{-1} s^{-2}, $\rho_q = 2.648$ g cm^{-2}, and t_q is the crystal thickness. The quality factor is defined as:$Q = frequency/bandwidth = f_c/\Delta f_{FWHM}$. The typical value of resonance frequency for a quartz crystal is 8-15 MHz and quality factor is 10^6. Hence, it accounts for a variation in the mass per unit area by measuring the change in the resonance frequency of a quartz crystal. The resonance is disturbed by the addition of a small mass due to film deposition at the surface of the acoustic resonator. The frequency corresponding to disturbed resonance can be easily measured to a high precision using the piezoelectric effect.

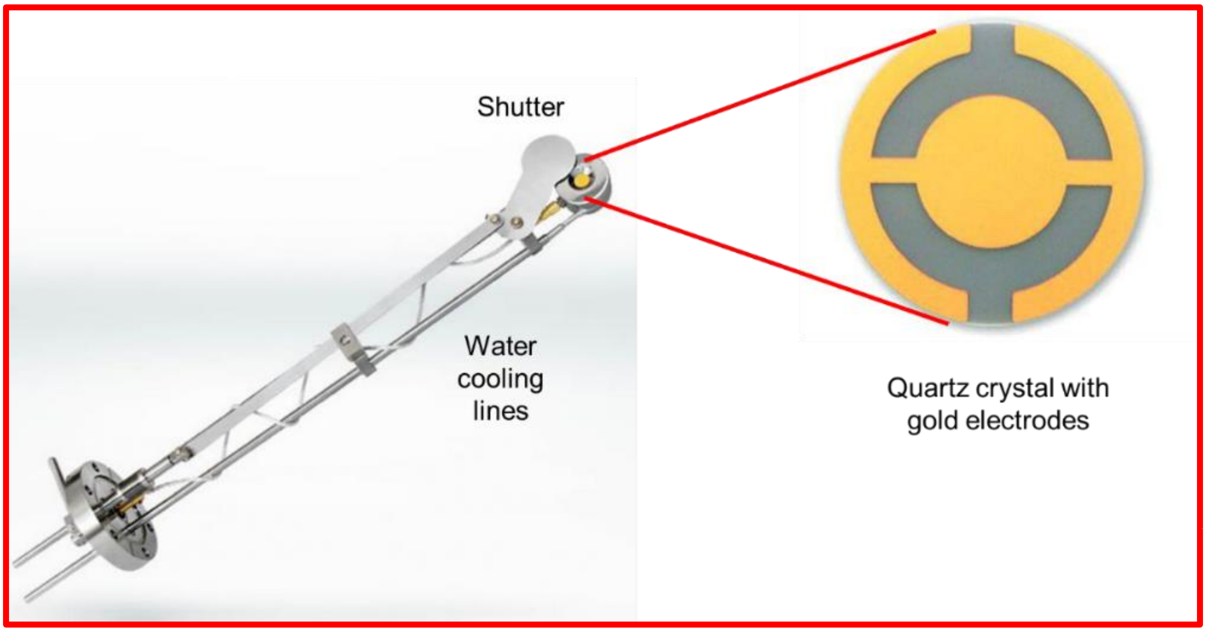

Figure 2.2: Typical look of a quartz crystal balance and the quartz crystal.

In this process, two electrodes are made by evaporation of gold onto back side of a piezoelectric plate. Upon applying an AC voltage across these electrodes, a shear deformation is induced in the piezoelectric plate. Hence, the electromechanical coupling provides a simple way to detect an acoustic resonance by electrical means. Therefore, it is easy to measure mass densities and further, the mass densities are converted to deposition rate in units of thickness per seconds. Figure 2.2 shows a typical image of quartz micro balance and the quartz crystal.

2.1.2 Residual gas analyzer (RGA)

RGA is a spectrometer [8] that effectively measures the chemical composition of the residual gases present in UHV systems. It actually ionizes the residual gases to create various ions and then determines the mass-to-charge ratios. RGA is important to have a mass versus partial pressure spectra of residual gases present in the chamber. In addition, it is capable of leak detection in UHV systems by creating helium gas environment close to the suspected area and simultaneously observing the change in the partial pressure corresponding to helium. Figure 2.3 shows the RGA module (RGA 200) and its schematic diagram.

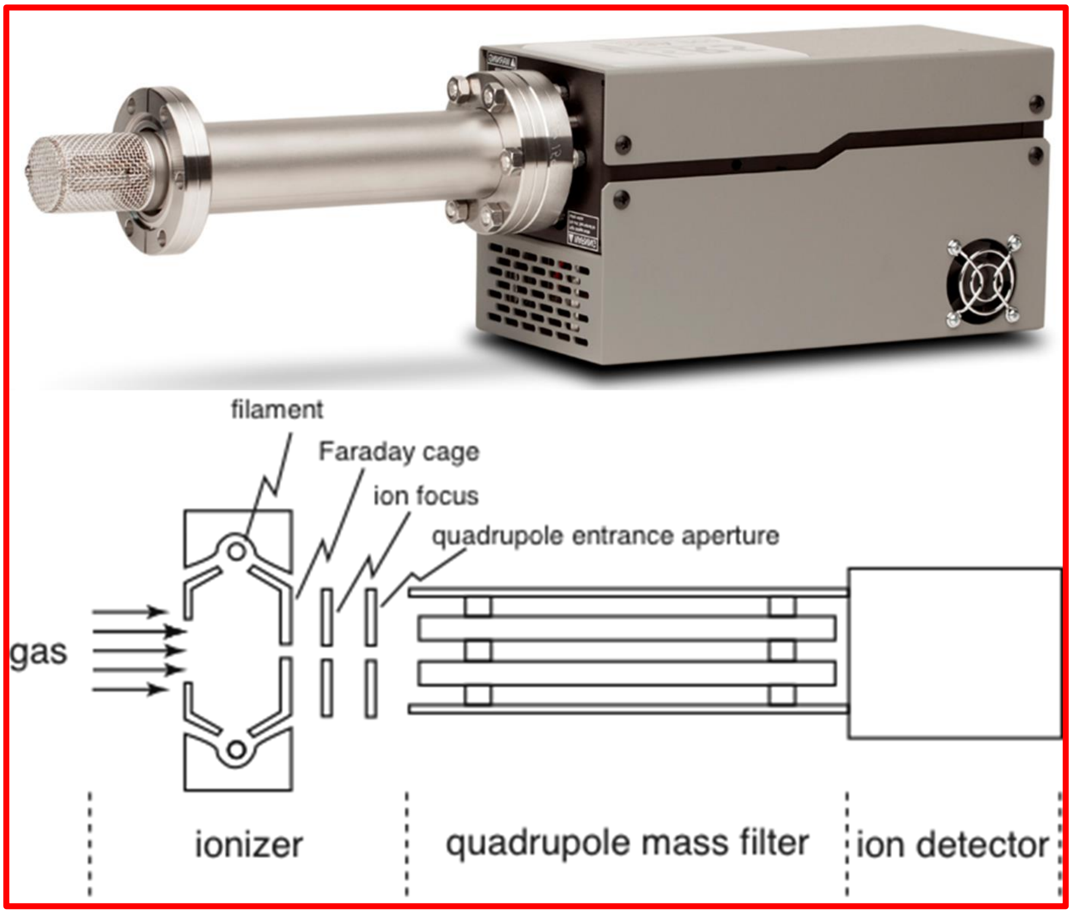

Figure 2.3: RGA200 module (up) and its schematic diagram (down).

The RGA is made of ionizer, electrostatic lens, mass analyzer and filters, and ion detector. In the ionizer, the neutral gas atoms or molecules are converted into positive ions. There are two filaments to emit electrons by thermionic emission, which are covered by a source grid (electrostatic wire mesh) kept at a constant electrostatic potential inside the ionization region. There is also a grounded basket-shaped Faraday shield to nullify the effect of external electrostatic potential inside the ionization region.

The atoms or molecules present in the vicinity of ionizer, collides with energetic electrons and get ionized. These positively charged ions are further focused and accelerated by an assembly of electrostatic lens and form an ion-beam with 10-20 eV of ion-energy. A mass analyzer is used to pass a desired mass to charge ratio using electric and/or magnetic fields. These mass to charge ratio filtered ions are detected by an ion detector system and the ion current is measured either an extended secondary electron multiplier (channeltron) or a Faraday cup. Figure 2.4 shows the typical mass spectrum (analog mode) and helium leak detection (Leak test mode) spectra.

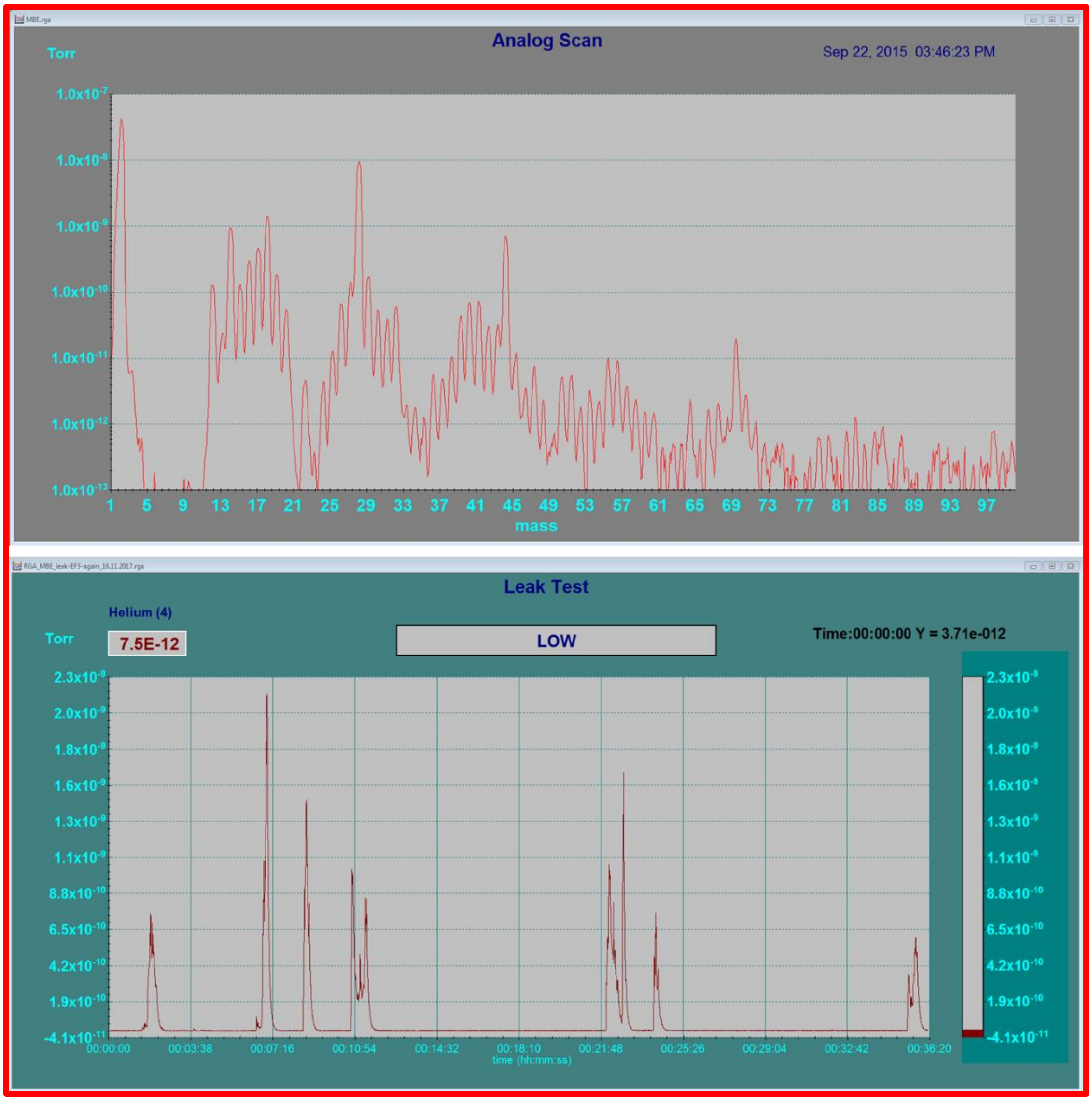

Figure 2.4: Mass spectrum in analog mode (up) and helium leak detection spectrum (down).

2.1.3 Reflection high energy electron diffraction (RHEED)

RHEED is a surface-sensitive technique used to characterize the crystallinity and symmetry of surfaces [9–11]. It uses high energetic electrons (10–100 keV) at grazing angles of incidence to limit the penetration to surfaces only and hence, forward scattered diffraction patterns are observed. The surface sensitivity is obtained by adopting a configuration in grazing incidence. However, in low energy electron diffraction (LEED) technique, low energy (50–100 eV) electrons are used, which are essentially needed to be incident close to the normal to probe the crystallinity of surfaces and hence, backward scattered diffraction patterns are recorded. In both the techniques, the main difference is the energy of electrons, which is proportional to their penetration depth inside the sample and it reduces with increasing angle of incidence of electron beam with respect to the sample normal.

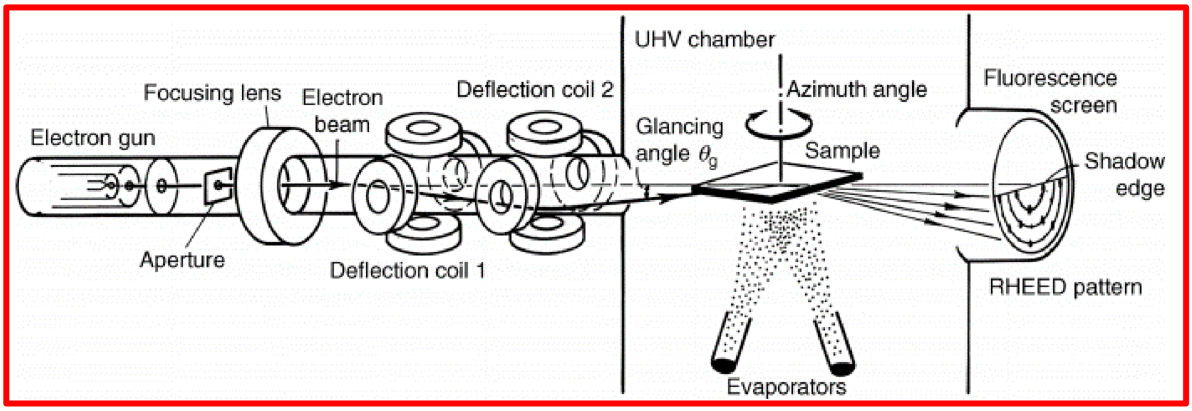

Figure 2.5: Schematic representation of typical RHEED technique [12].

A RHEED system requires an electron gun with aperture and focusing lens to get a well collimated electron beam. Two deflection coils are used to provide fine adjustment of inclination angle with respect to sample surface. One photoluminescent detector screen is required to visualize the diffracted electron patterns and further, a CCD camera is used to capture the high quality images of the photoluminescent detector.

An intense beam of electrons (generated by electron gun) is allowed to hit the sample surface at a very glancing angle (<5°) with respect to the sample surface. These incident electrons are diffracted from the surface atoms and interfere constructively at certain angles to form a regular patterns on the detector (generally, a fluorescent screen). Figure 2.5 shows the schematic diagram of a RHEED system and the kind of RHEED patterns generated for various substrate morphologies are depicted in Fig. 2.6.

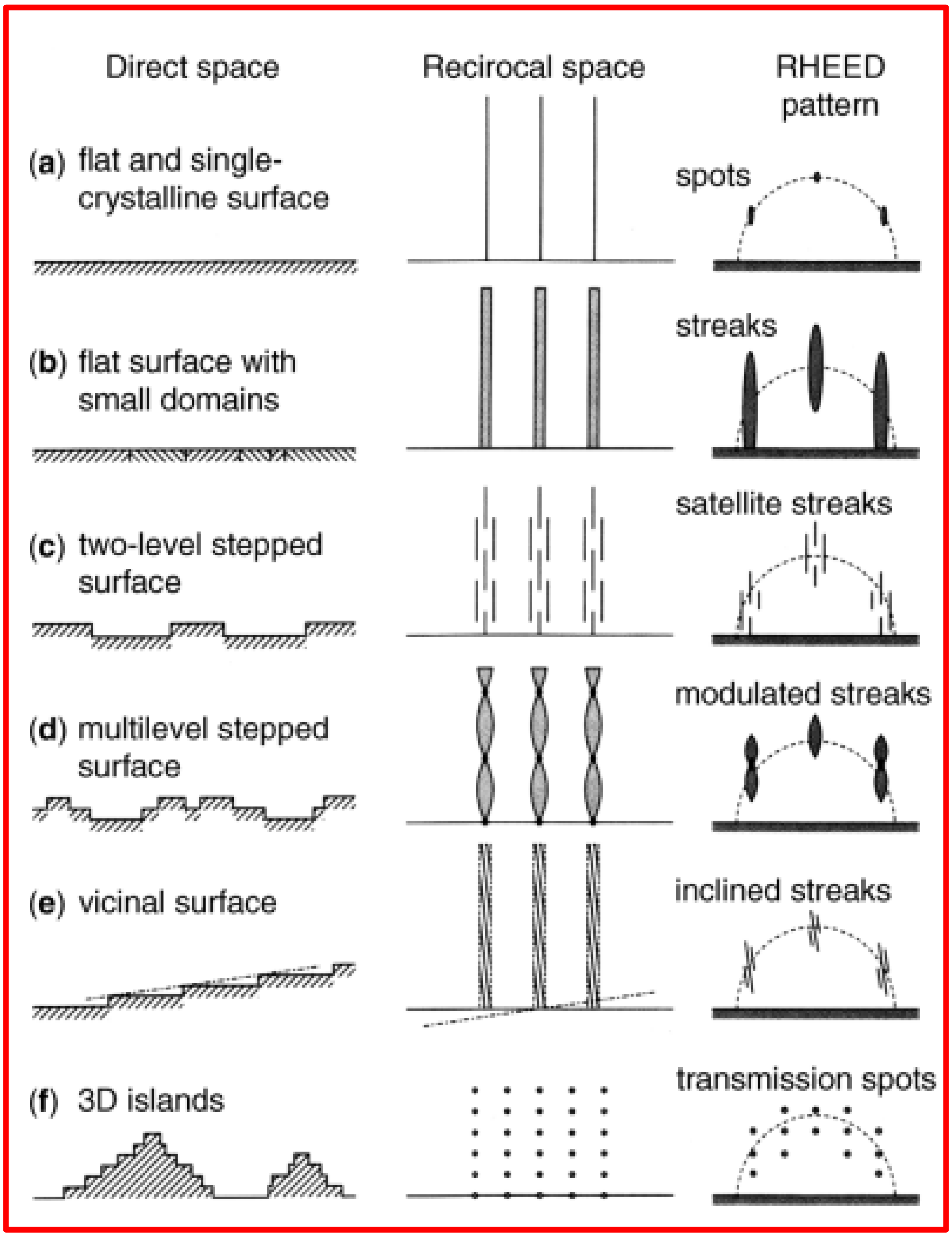

Figure 2.6: Schematics of various kinds of realistic surfaces, in real-space morphology, reciprocal space, and their RHEED patterns (courtesy by Yoshimi Horio).

2.1.4 Effusion cells

An effusion cell is the source of a molecular beam and is a key component of an MBE system [13,14]. As the name suggests effusion cells are based on effusion process, according to which, evaporated molecules are allowed to pass from high evaporant partial pressure to relatively very low pressure region through an orifice of diameter considerably smaller than the mean free path of the molecules. It was Martin Knudsen, who developed the first ever effusion cell [3]. Hence, after his name, effusion cells are also known as Knudsen cells.

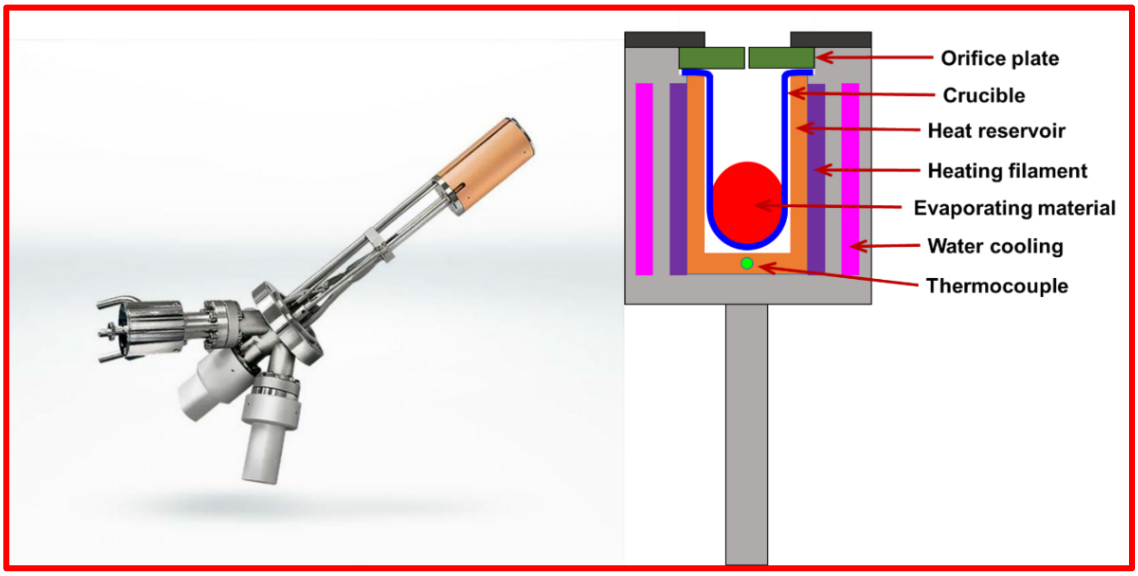

Figure 2.7: Effusion cell (EF40C1) and its schematic diagram (right).

A typical effusion cell includes a crucible (made of quartz, tungsten, pyrolytic boron nitride, or graphite), tantalum heating filaments, heat shields, an orifice plate with shutter, and water cooling system. A source material is filled inside a crucible and a resistive heating source is used for radiative heating of the same. The solid source material sublimates under elevated temperatures and under UHV conditions. The beam intensity within the substrate chamber depends on the pressure of the effusion cell and it can be maintained by controlling the current supply to resistive heating filament. Figure 2.7 shows the effusion cell (EF40C1) installed with MBE system and its schematic diagram.

2.1.5 Electron beam evaporation cell

Electron beam evaporation cell is an important part of a molecular beam epitaxy system, in which materials are heated and evaporated by hitting thermal electrons generated from a glowing filament [15]. The filament current is the key to control the population of thermal electrons used for evaporation. An e-beam evaporator provides a precise control over the depositing material flux and can operate at a relatively lower pressure ($<1\times10^{-9}$ mbar in our work) unlike sputter deposition [16].

In this thesis, electron beam evaporation is used for the growth of metal nanoparticles on ion-beam induced patterned silicon templates and we have compared the growth of metal thin films and nanoparticles by both the techniques since the growth kinetics strongly depend on the incident atom flux.

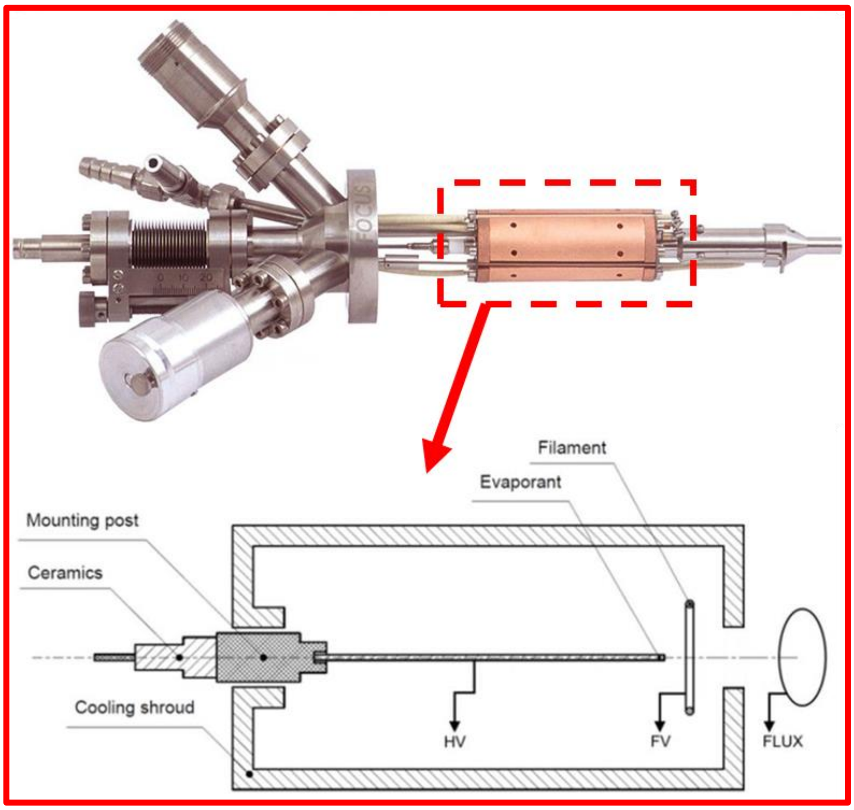

Figure 2.8: The schematic diagram of an e-beam evaporation (up) and its internal layout of components (down).

Deposition of Au-NPs are carried out using a commercially available e-beam evaporator [6] for which schematic diagram and system images are shown in Fig. 2.8. A rod of evaporating material is loaded inside a crucible attached with a metal shaft to be kept at high voltage (600-1000 V). There is a thoriated tungsten filament in front of the crucible, which used to emit thermal electrons. Under operating conditions, the filament glows and emits electrons which are attracted towards positively biased crucible and hence, the heating of crucible takes place. The evaporating material inside the crucible gets evaporated due to a sufficient temperature rise via electron heating [16]. Some fraction of evaporated material is ionised which is used to monitor the material flux by collecting those ions to an electrode connected close to the exit.

In fact, the choice of a proper crucible is very important since the crucible should have evaporating or melting temperature much higher than the evaporating material. Generally, Mo crucibles are used for noble metal deposition (silver, gold), however, reactive materials like Co, Mn, etc. need some special type of Mo crucibles, having an Al_2O_3 coating at the core. The optimized flux of 35 µA is achieved for evaporation of gold for a beam energy of 800 V and the filament current of 2.1 A.

2.1.6 Low energy ECR based ion-source

A low energy electron cyclotron resonance (ECR)-based broad beam, filament-less, gaseous ion etching setup (Tectra, Gen II, Germany) [17] equipped with an ultra-high vacuum (UHV) compatible chamber, along with a 5-axes sample manipulator (Prevac, Poland) [6] was used to perform all the patterning experiments. The chamber base pressure was $<1\times10^{-10}$ mbar and the working pressure was maintained at $\sim3\times10^{-4}$ mbar (required for plasma generation) by using a differential pumping unit. Different components of this experimental setup are briefly described below.

ECR source: The basic idea of an ECR ion source is microwave heating of electrons in a plasma by electron cyclotron resonance process [18]. A radial magnetic field is produced using a permanent magnetic quadrupole to confine the plasma (minimum-B-structure) and gyrate the electrons around the magnetic field lines inside confined plasma with cyclotron frequency: $\omega_c = \frac{e}{m}B$. For a microwave based ECR ion-source, injected (microwaves) can resonantly heat the electrons if the cyclotron frequency matches with the microwave frequency. The resonant magnetic field is 0.088 T corresponding to an ECR ion source working at a microwave frequency of 2.45 GHz. While passing through the resonance region, an electron can achieve 1-2 keV energy for further impact ionization processes. However, ions are not accelerated due to their relatively heavy masses and confined by the electronic space charge region. Some brief introduction on the ion-source is provided in the following sections.

Ion source setup

The ECR-based ion source setup can produce 50 eV to 2 keV ions with high ion beam currents from any gaseous species (including reactive gases). The cross-section of the ion-source is shown in Fig. 2.9. Plasma is generated in an alumina cup, which is coupled with 2.45 GHz magnetron source via a metallic rod used as an antenna for near field coupling of the microwave to the plasma inside the cup. It is surrounded by four water-cooled NdFeB magnets (outside vacuum) which produce ECR zones in a multicasp field. The working gas is fed into the discharge cup through a metallic capillary ended with a BN tube to prevent the plasma from "seeing" the metal at ground potential. The outside view of the source is shown in Fig. 2.10.

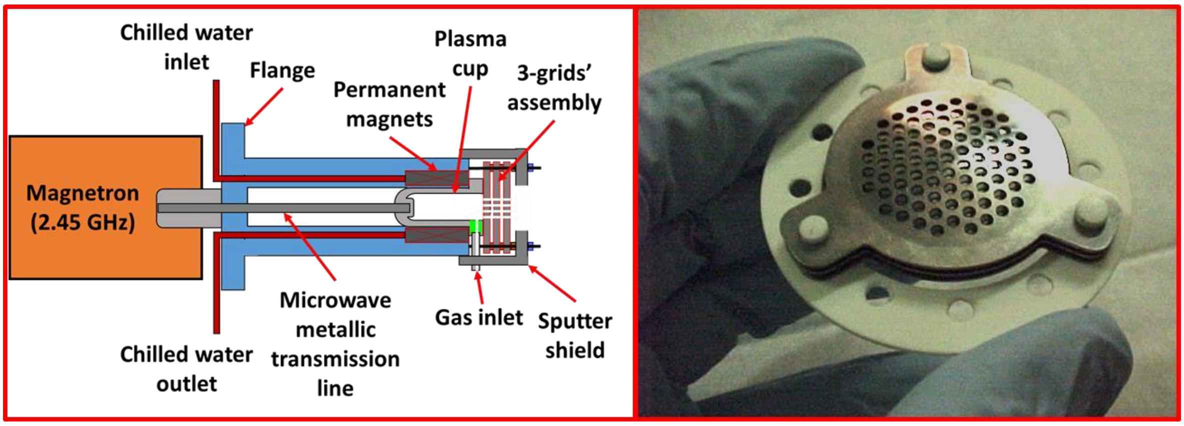

Figure 2.9: Cross-sectional view of the low energy ion source and three-grid assembly.

Plasma density inside the ceramic cup is improved by ECR process and the gyration of electrons is sustained by the resonantly fed microwave from the magnetron. Further, ions are extracted through multiple grid assemblies. In particular, the studies presented in this thesis are based on three-grid system containing 32 holes of diameter 3 mm each, which are collimated to from 32 einzel lenses. Grids are mutually isolated (2 mm separation) with the help of ceramic beads as shown in Fig. 2.9.

Potential at the grids: As shown in Fig. 2.9, three Mo grids are kept fixed on an annular alumina disk by maintaining 2 mm separation among grids using ceramic beads for their electrical isolation.

Grid 1 (Anode): This grid remains in contact of the plasma with some positive bias to shift the plasma potential to the applied potential which works as low cut-off energy thresholding of positively charged ions from the plasma.

Grid 2 (Extractor): This grid is kept at some negative bias to accelerate the ions (due to the potential difference between anode and extractor grids) and control their divergence.

Grid 3 (Ground): This grid is kept at ground potential to create field-free region inside the experimental chamber to avoid field-induced unwanted bending of ions.

Figure 2.10: The outside view of the Tectra-made Gen II ECR-based ion-source.

This ion source can be operated in four different modes namely atom source, downstream plasma source, broad beam ion source, and hybrid source. Out of these four modes, this thesis is based on the broad beam mode of the ion source, which is described below:

Broad beam ion source: A set of two or three metallic grid electrodes electrically isolated by a mutual separation of 2 mm and having holes in the grid electrons of 2 mm diameter are used to produce the broad beam of ions in this mode. This mode of the ion-source was used for the ion irradiation experiments presented in this thesis.

2.2 RF magnetron sputtering

Sputter deposition is a commonly used popular physical vapour deposition (PVD) process where a negatively charged target material is sputtered out by the collisions with positively charged gas ions and the sputtered target atoms get condensed on a substrate surface [19]. In addition, a closed magnetic field is used to trap electrons during magnetron sputter deposition. Hence, the initial ionization efficiency gets enhanced due reduced ion-electron recombination [20].

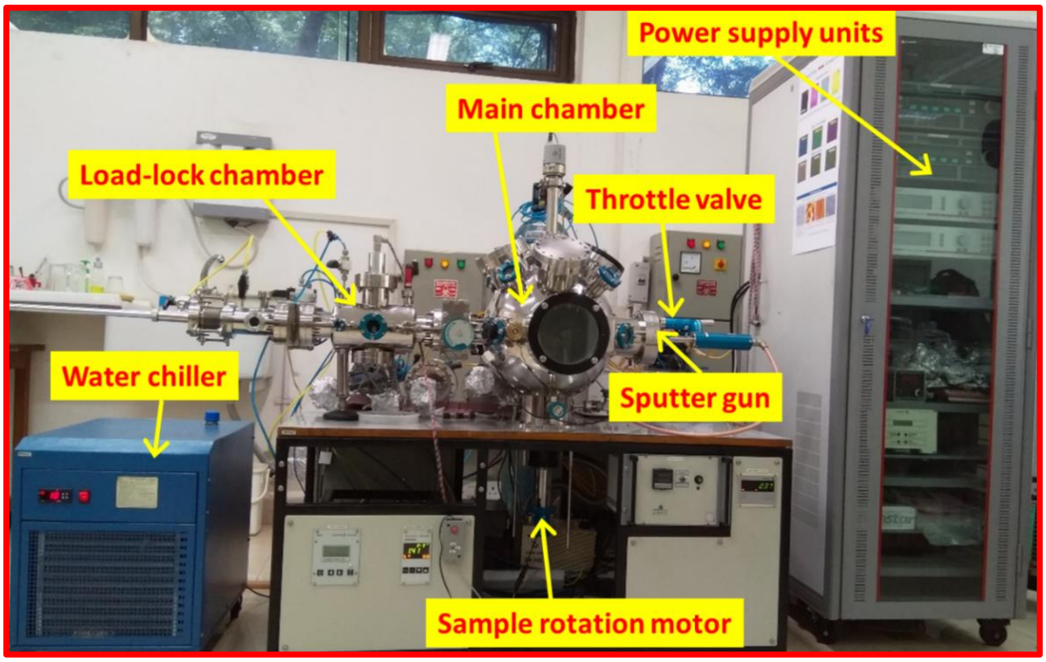

Figure 2.11: The pulsed DC/RF sputtering setup at SUNAG Laboratory.

In the process, the plasma is generated at lower pressures which helps in reducing both the incorporation of background gases in the growing film and energy loss of the sputtered atom through the collisions with background gases. Figure 2.11 shows the pulsed DC/RF magnetron sputtering setup used in the present thesis, where different parts of the setup are highlighted in yellow colour. It has a spherical high vacuum compatible chamber (Excel Instruments, India) equipped with a turbo molecular pump (Varian, USA) backed by a rotary pump are used to maintain the high vacuum condition. Mass flow controllers are used for controlled injection of argon gas inside the main chamber for plasma generation. There are four sputter guns equipped with target materials which can be simultaneously operated for co-deposition of different materials. Substrates are loaded on a sample manipulator having a rotation arrangement to grow materials at oblique angles of incidence with respect to the incoming flux. To ensure the uniformity in the deposited film thickness, substrate azimuthal rotation is also present. In addition, the temperature of the permanent magnets used in sputter guns is kept constant by using a continuous chilled water flow. This setup is equipped with two pulsed DC (Advanced Energy, Pinnacle Plus, USA) and two RF (13.56 MHz; CESAR RF generator, Advanced energy, USA) power supplies to perform confocal sputtering using both the modes.

All the ZTO films (presented in this thesis) were prepared using an RF (13.56 MHz) power of 100 W with this setup at room temperature. Argon gas was used for the sputtering of the target and the deposition was performed under normal incidence using a constant substrate rotation of 3 rpm. For the sake of comparison, besides the patterned-Si substrates, ZTO thin films were simultaneously grown on pristine-Si substrates. In addition to this, deposition of gold on patterned-Si substrates was carried out using an RF power of 100 W for 10 s at oblique angles in the range of 65º-85º with respect to the sample normal. In the present case, no substrate rotation was provided to preserve the substrate morphology-dependent growth of Au-NPs on patterned-Si substrates.

2.3 Stylus profilometry

Surface profilometry is used for measuring the film thickness. In a surface profilometer, a diamond stylus (like a modern ball pen) is moved across the surface to measure the vertical displacement corresponding to the step height. This process involves some mechanical and electronic devices in order to perform the conversion [21]. The sample is mounted on a stage which have precise and controlled movement in *X*- and *Y*- directions. The measurement of the height or *Z*-axis is done by the stylus in contact with the surface.

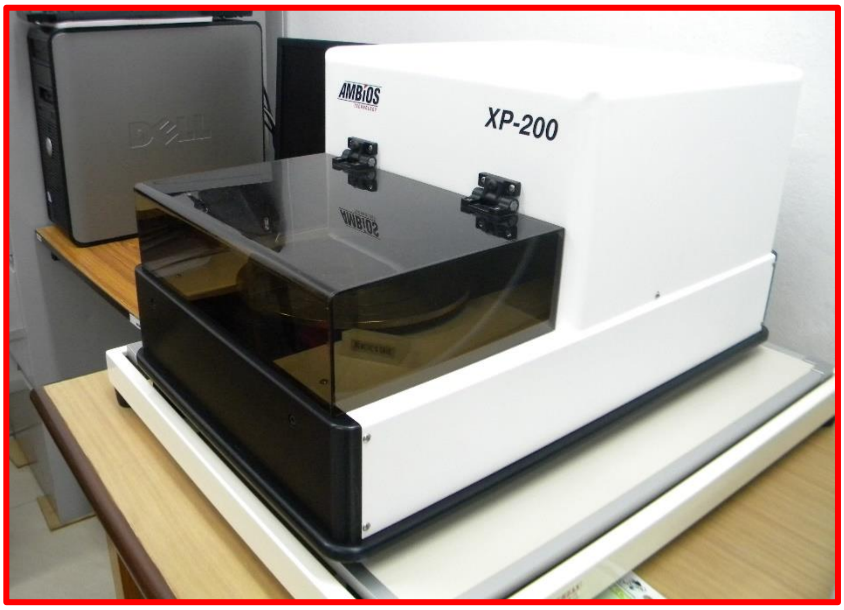

Figure 2.12: Surface profilometer setup at SUNAG Laboratory.

Thickness measurement of the deposited films was carried out by using a stylus-based profilometer (Ambios XP-200, USA) (Fig. 2.12). The stylus is housed in an acoustic isolation hood to reduce vibrational noise during scanning and placed on a large vibration damped sandstone block. The vertical range of the profilometer is 400 μm and its vertical resolution is 0.1 nm at a 10 μm scan length, 1.5 nm at 100 μm scan length, and 6.2 nm at 400 μm scan length [22]. The stylus provided with XP-200 profilometer is a diamond coated tip with radius of 2.0 ± 0.1 μm having an adjustable force range between 0.05–10 mg. The XP-200 profilometer can also calculate surface roughness and waviness besides performing stress analysis on thin films [23]. The film thickness is measured with respect to the substrate where a portion of the substrate is masked prior to the film growth. This helps to get a reasonably good step height during thickness measurement.

2.4 Atomic force microscopy (AFM)

Scanning probe microscopy (SPM) has a gamut of techniques to study the morphology and various nanoscale physical properties [24,25]. During the surface topography scan, a probe moves mechanically over the surface and records the interaction of the probe with the surface under consideration as a function of spatial coordinates [25,26]. The modes of SPM are defined on the basis of the interaction, e.g. inter-atomic, tunnelling current, magnetic, electrical, frictional forces etc. [25,26]. AFM is the most important among the SPM based techniques which can be used for all types of materials including insulators, semiconductors as well as conductors and it can operate in vacuum or ambient condition [24,25]. When an AFM tip attached to the end of a cantilever, approaches to the close proximity of a surface, the nanoscale variation in the surface morphology is measured by the deflection of the tip (10-30 nm in diameter). The working principle of AFM is depicted in a schematic diagram shown in Fig. 2.13. There is a highly reflective region of a cantilever, on which laser beam is focused to reflect the light back onto a position-sensitive photodetector.

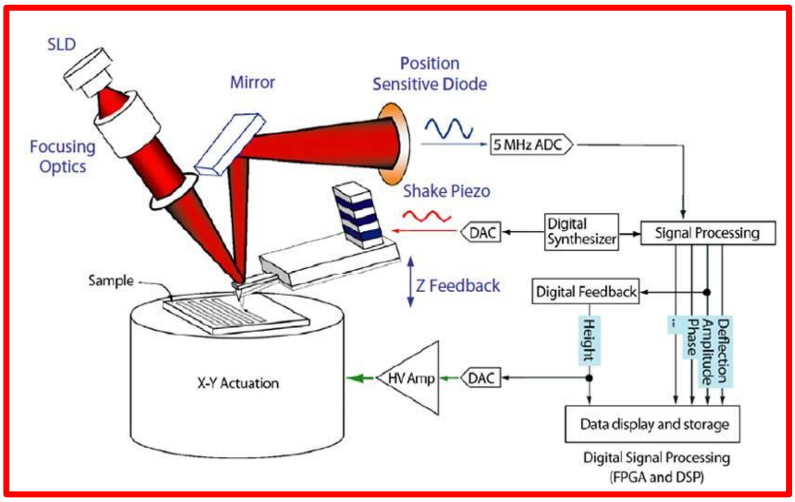

Figure 2.13: Schematic of AFM-setup [26].

A piezoelectric scanner made of PZT (lead zirconium titanate) is used to scan the sample underneath the tip. However, on the basis of feedback loop, there are mainly two modes of operation, one is the constant deflection (contact mode) and other one is the oscillatory amplitude (tapping mode). In these cases, inter-atomic Van der Waals force acts between the tip and the sample during scanning. The applicability and validity of the Van der Waals forces upon the tip-sample distance is shown in Fig. 2.14, where three distinct regimes of tip-surface distance are identified as the contact, non-contact, and the tapping regime.

Contact (repulsive) mode: In this mode, an AFM tip approaches very close to a surface and makes soft physical contact with the sample [25,27]. For this mode, an AFM-tip is attached to a cantilever having a low spring constant. As the tip traces the sample by moving the scanner, the contact force causes the cantilever to bend and these changes are accumulated as the information of topography. This mode is usually applicable for hard crystalline surfaces since strong forces involved in this process may deform the soft surfaces [25,27].

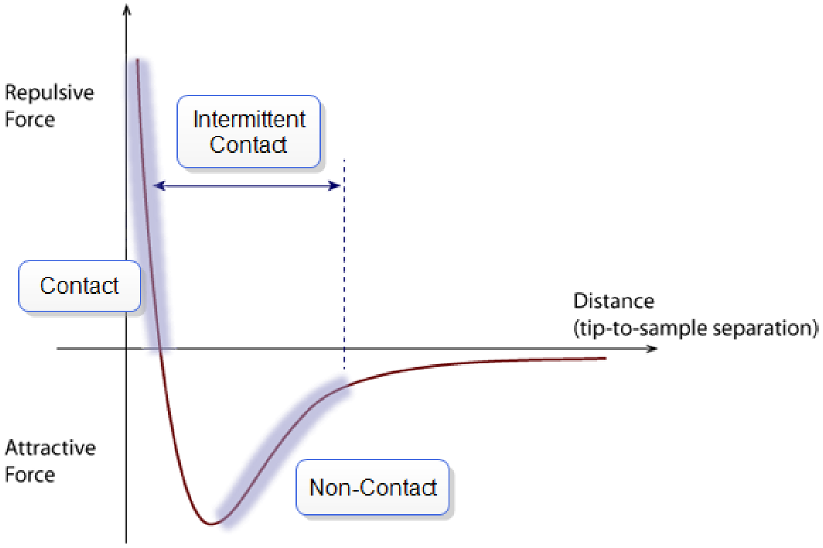

Figure 2.14: Van der Waal’s force as a function of tip to surface distance [25–27].

Non-contact (attractive) mode: There are several AFM-based techniques which rely on non-contact mode of an AFM. In this mode, an oscillating AFM cantilever is brought closer to the sample surface (tens to hundreds of angstroms) and a tip-sample surface induced damping in the cantilever oscillations is recorded [25,27]. The damping of oscillations in terms of change in amplitude and phase are recorded by the lock-in amplifier. In addition to this, a position-sensitive detector also captures the change in the oscillation frequency. These two dataset of information provide the details of the surface. The truly non-invasive character is the major advantage of this mode.

Tapping mode (intermittent-contact): This mode is also known as intermittent-contact mode, since the working principle of this mode is intermittent of both contact and non-contact modes [25]. In this mode, the AFM cantilever is kept under oscillations, closer to its resonance frequency, using a piezoelectric crystal so that the tip remains very close to the sample for a short time and then goes far away for a short time. In this mode, the oscillating cantilever hardly hits or 'taps' the sample upon bringing closer to the sample surface. When this oscillating cantilever is brought closer to the sample surface then the cantilever oscillations are damped due to the tip-surface interaction induced forces. As the oscillating cantilever begins to contact the surface intermittently, the amplitude of oscillation necessarily reduces due to an energy loss caused by the tip in contacting the surface. This damping is recorded using a lock-in amplifier just by comparing the change in the amplitude and phase of the oscillation. In addition, the position-sensitive photodetector also provides the information about the damping.

This mode provides the flexibility to scan soft adsorbates on a substrate (biological samples) with better resolution than in the non-contact mode. Thus, the tapping mode overcomes certain problems associated with conventional AFM scanning method viz. friction, adhesion, electrostatic forces, and other difficulties [25,26].

AFM System and measurements: In the present thesis, AFM images were acquired using an MFP-3D AFM (Oxford instruments, USA) in different modes. The cantilever used for tapping mode has a resonant frequency of around 300 kHz and a spring constant of 42 N m^{-1}. There are many advantages of this AFM system, however, the large area (up to 90×90 µm^2) scanning with high precision is the most important one.

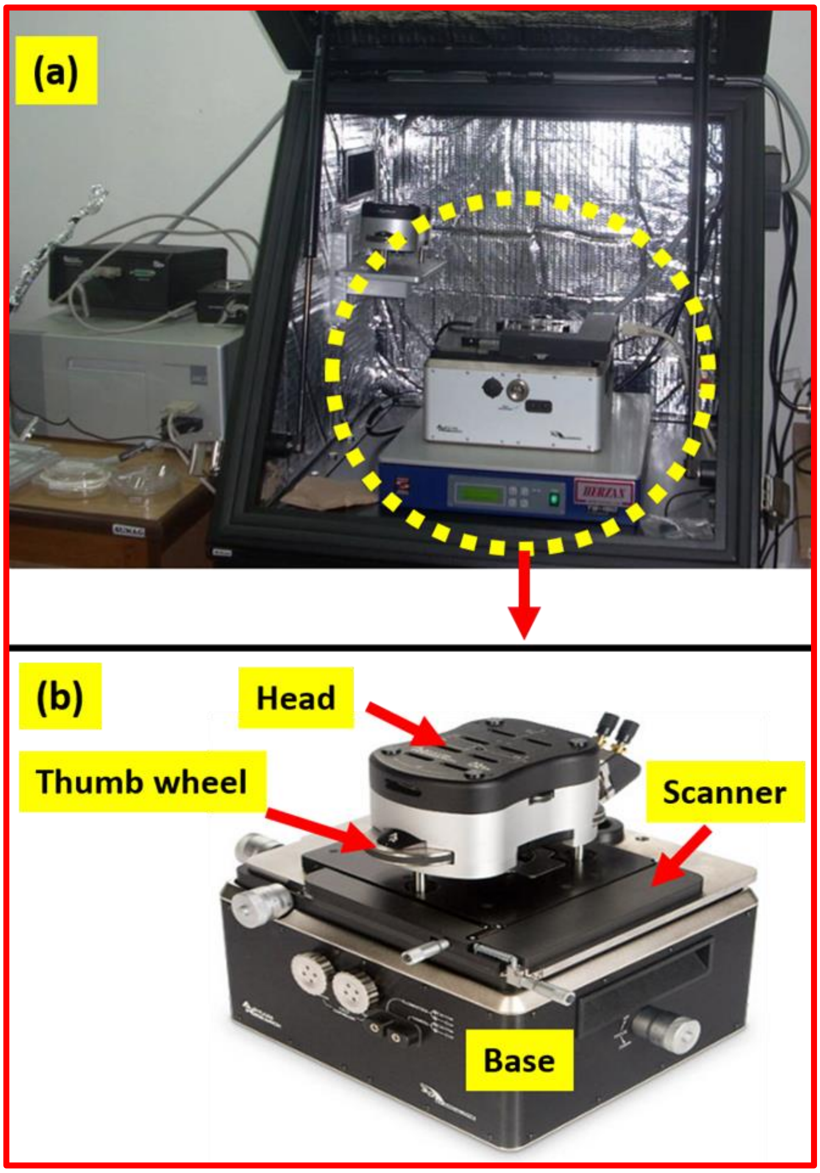

Figure 2.15: MFP-3D AFM setup.

The AFM setup at SUNAG laboratory and its main components, e.g. scanner, head, base, and thumb wheel are shown as Figure 2.15 (a) and (b), respectively. The thumbwheel is used for coarse tuning of the tip-surface distance. During the manual tuning of separation, the close approach to the surface (tip-sample separation remains 80 nm) is controlled by the software to prevent the damage of the tip. A *XY* sample stage with screw-gauge arrangement is attached with the AFM for precise positioning of a sample and testing the large scale uniformity in surface morphology with a translational precision of 10 μm.

2.4.1 Kelvin probe force microscopy (KPFM)

Kelvin probe force microscopy (KPFM) is a technique which is used to measure the potential difference between the tip and the sample [28]. The data collected by the sample represents a combination of three contributing factors: the difference in work function, trapped charge, and applied voltage between the tip and the sample. The technique relies on an AC bias applied to the tip to produce an electric force on the cantilever that is proportional to the potential difference between the tip and the sample [28]. The process of KPFM is shown in Fig. 2.16.

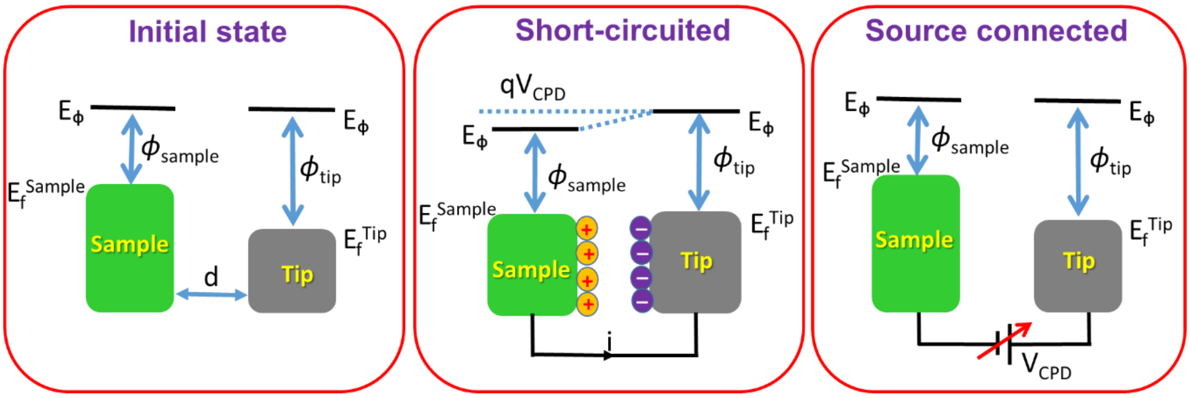

Figure 2.16: Working principle of KPFM technique.

In this mode, the tip is lifted up to a height (>40 nm to overcome the inter-atomic forces) and thus, there is no mechanically induced drive. In fact, now the probe oscillates due to the applied AC bias only. This applied bias between the tip and the sample produces an electrostatic force between them. If they are modelled as a parallel plate capacitor (c), then the force between the two plates is proportional to the square of the applied voltage (V):

$$F = \frac{1}{2}\frac{\partial C}{\partial Z}V^2. \tag{2.1}$$

The total potential difference between the probe and the sample is the sum of the applied AC bias (V_{ac}), the potential difference we are trying to measure (V_{sp}), and DC voltage we apply (V_{dc}).

$$V = V_{\mathrm{sp}} + V_{\mathrm{dc}} + V_{\mathrm{ac}}\sin(\omega t) \quad , \tag{2.2}$$

where, ω is the angular frequency of the applied AC signal.

If we substitute this into Eq. 2.1 and do some rearrangements, we get [28] the following:

$$F = \frac{1}{2}\frac{\partial C}{\partial z}\left([(V_{\mathrm{dc}} - V_{\mathrm{sp}}) + \frac{1}{2}V_{\mathrm{ac}}^2] + 2[(V_{\mathrm{dc}} - V_{\mathrm{sp}})V_{\mathrm{ac}}\sin(\omega t)] - [\frac{1}{2}V_{\mathrm{ac}}^2\cos(2\omega t)]\right). \tag{2.3}$$

Note that there are three force terms here which are summed together. The first force is the static one, meaning it has no frequency dependence, the second occurs at the AC signal drive frequency, while the third force oscillates at twice the drive frequency. The most important term here, as far as the surface potential is concerned, is the second term since this term not only depends on the square of the voltage but also dependent on the potential difference between the tip and the sample and is multiplied by the magnitude of the applied AC voltage. This means that if there is a potential difference between the tip and the sample, there will be an oscillatory force with a certain frequency (ω) of the drive and it will be proportional to the magnitude of the applied voltage and to the potential difference.

The probes used for KPFM measurements are generally conductive or heavily-doped semiconductors. This mode is implemented on the MFP-3D as a two-step technique where the first one is used to determine the topography of the surface and it is exactly done like a standard tapping mode. The second one is used to find the surface potential and the tip is raised above the surface. To do this, '*nap^{TM} mode*' is implemented. During a nap scan, the tip is raised over the surface on a point-by-point basis with active potential feedback loop.

2.4.2 Conductive atomic force microscopy (cAFM)

Conductive atomic force microscopy (cAFM) is a powerful current sensing technique, which can simultaneously map the topography and the current distribution at the contact point of the tip with the sample surface [29]. In fact, this technique is capable of measuring spatial variation in the conductivity of resistive samples in a current range of few picoamperes (pA) to tens of nanoamperes (nA). This technique has been widely used for characterizing various materials including thin dielectric films, ferroelectric films, nanotubes, conductive polymers etc. [30,31]. An ORCA module [32] with the present AFM system consists of a specially-designed cantilever holder and a transimpedance amplifier. The cAFM cantilever holder is designed in such a way that one end of a wire is electrically connected with the conductive cantilever and other end is needed to be connected with the sample to measure the local current by applied fixed bias. This technique of measuring the localized conductivity of a sample, is combined with the contact mode AFM imaging. All electrical images used in this thesis were acquired using the contact mode with a Pt-Ir coated Electro-Lever tip, having a nominal spring constant of 1-2 N m^{-1} and good wear characteristics.

In addition, this system is equipped with the nanopositioning closed loop sensors (NPS™) which make it possible to get the local current-voltage characteristics and also reproduce the position of the cantilever at a point of interest [33]. The tip is positioned at the centre of the coloured circle using the MFP-3D's "pick a point" option available in force curve interface. In fact, the ORCA conductive AFM option for the MFP-3D provides low-noise, flexible transport measurements at the nanoscale. Further, the flexible software environment enables a variety of standard measurements to be made, as well as allowing the researcher to define their own experiments.

2.4.3 Dual pass tunnelling current microscopy (DPTCM)

Dual pass tunnelling current microscopy (DPTCM) is an AFM-based local probe technique to map the local tunneling current emerging sites even at ambient conditions [34]. In this process, a dual pass technique is employed to measure the tunnelling current as shown in the schematic diagram (Fig. 2.17). During the first scan, the tip operates in contact mode and maps the surface topography as it is done exactly in a standard contact mode, whereas in the second scan (which is called lift mode), the tip is elevated at a fixed height above the surface by following the topographic data captured in the first scan [34]. During the second scan the cantilever remains at a constant height with no oscillation and a constant DC voltage is applied to it (with respect to the substrate) which in turn enable the measurement of the tunneling current. Hence, tunneling of electrons occurs from the sample surface to the conductive tip through an air gap equivalent to the provided lift height.

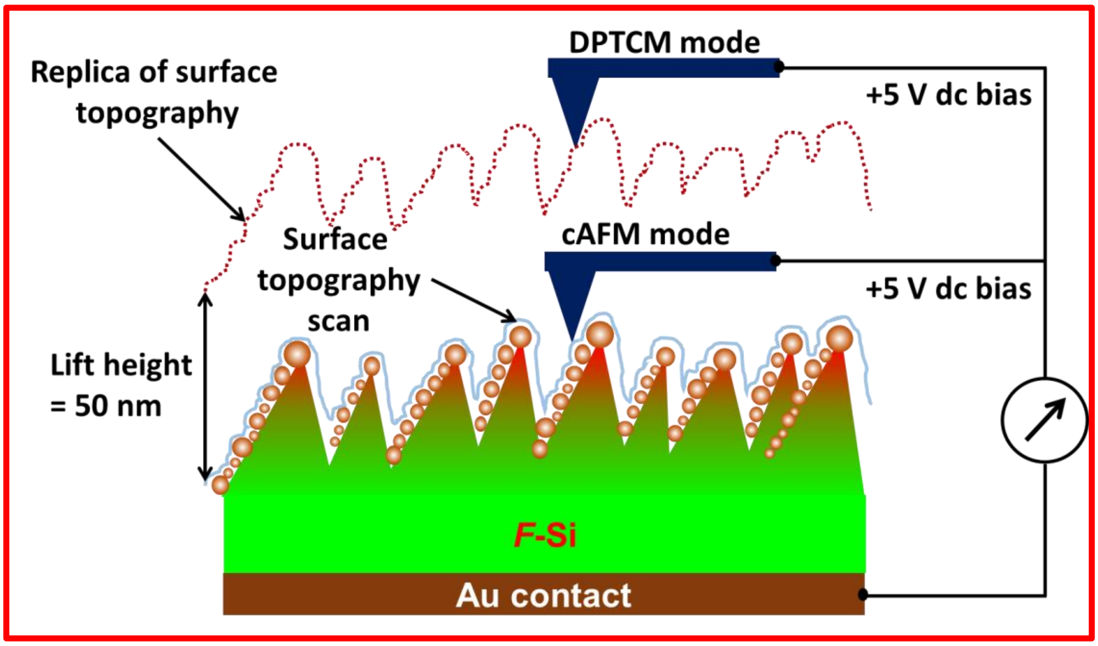

Figure 2.17: Schematic representation of DPTCM technique.

This mode of MFP-3D AFM is termed as dual pass tunneling current microscopy (DPTCM) mode. This process of measuring the tunneling current is similar to the tunneling atomic force microscopy (TUNA) process reported by Chatterjee *et al.* [35]. The special virtue of this technique is that it provides the spatial distribution of the tunneling current on the sample surface along with their corresponding morphological information simultaneously at even ambient pressure. This technique is not a conductive atomic force microscopy (cAFM), however if some potential is also applied during the contact mode scan (first pass) then it can also measure the surface conductivity during first pass besides the tunneling current mapping in the second pass. In the present thesis, we have utilized the DPTCM technique to identify the tunneling current emitting sites on Au-NP decorated NF-Si samples. Throughout the DPTCM measurements, a Pt-coated conductive Si tip is used with a constant lift height of 50 nm from the surface.

2.5 Scanning electron microscopy (SEM)

A SEM is a widely used electron microscope where a focused electron beam scans the sample surface and constructs morphological images of the same [36–38]. The novelty of a SEM system lies in its capability to produce 10-1,00,000 times magnified images. In SEM, a sample surface has to be conductive in order to prevent the electron emission-induced charging effect of the sample. However, for a non-conductive sample surfaces, a very thin gold layer is coated on the sample surface. Moreover, as an alternate, low beam energy and/or high beam spot size and special detectors are used to prevent the surface charging effect.

Upon scanning an energetic electron beam, there are a series of elastic and inelastic scattering events inside a material, which result in backscattering of electrons, production of characteristic x-rays, and emission of secondary electrons, etc. A SEM image with high resolution topographic contrast and large depth of field is obtained using secondary electrons which is the standard imaging mode. The secondary electron coefficient strongly depends on the energy of electrons, however their yield increases with increasing tilt angle. Hence, secondary electrons can be produced more closely to the surface by lowering down the electron energy, and in turn, their higher escape possibility leads to high resolution images.

A SEM contains an electron column for an electron gun and their relevant beam optics. Generally, a field emission based electron gun consists of a very sharp tungsten conical tip which is attached to a hairpin-shaped tungsten wire and is used for electron production. An intense electric field is developed around the tip due to the applied bias to the anode, leading to the emission of electrons. A field emission is highly stable under temperature fluctuations and its gun offers a high electron number density with a beam spot of the order of 20 nm, providing a better resolution in SEM. Various electromagnetic lenses are used to focus the electrons in a nanometer sized beam spot on the sample. Detectors are also mounted inside the sample chamber to detect the emerging electrons and characteristics x-rays from the sample. As per user action, computer-interfaced detectors are able to display the magnified sample image by reconstruction of secondary or backscattered electron mapping. For the SEM studies presented in this thesis, a Carl Zeiss (Germany)-make SEM was used [38] and the microscope was operated at a probe current up to 100 nA and acceleration voltages in the range of 0.2 to 30 kV.

2.6 Transmission electron microscopy (TEM)

Transmission electron microscopy is an indispensable technique to study crystallinity and microstructures along with film thickness, interplanar spacing, and defects in materials [39]. TEM is a powerful technique for microstructural study in terms of its superior resolution and capability of capturing real as well as diffraction images in reciprocal space. Since, this technique relies on transmission of collimated electrons, a TEM specimen should be thin enough to transmit a large portion of the incident electron beam, i.e. a specimen should be electron transparent. For instance, the ideal thickness of a TEM specimen may be below 100 nm for observation under TEM and below 50 nm for high-resolution TEM (HRTEM). The thickness of any material that the electrons can penetrate through is dependent upon the energy of the incident beam and the elemental composition of the material. The sample thinning process involves several steps, especially in case of preparing sample for the cross-sectional observation [40].

To obtain selected area electron diffraction (SAED) patterns of a specimen, an aperture is placed around the selected area of the specimen above the intermediate lens, whereas the SAED aperture is replaced by an objective aperture for the conventional imaging. The schematic diagram of major TEM components, its working principle for imaging in real space and diffraction patterns in reciprocal space are depicted in Fig. 2.18 (from left to right). A lanthanum hexaboride (LaB_6) crystal filament is commonly used for the electron gun in TEMs to produce a stream of energetic electrons [40] and a specimen is kept at the object plane of the objective lens of the TEM. The transmitted electron beam is focused by objective lens and an electron diffraction pattern for the selected area of specimen is formed at the focal plane of the objective lens (Fig. 2.18). A well resolved diffraction pattern can be obtained on the phosphor screen for a specimen which is transparent to electrons. The real space image or electron diffraction patterns can be magnified (100 to more than 1,000,000 times) on the viewing screen by the assembly of intermediate and projector lens. In diffraction mode, first intermediate lens is adjusted in such a way that the back focal plane of the objective lens becomes the object plane of the first intermediate lens.

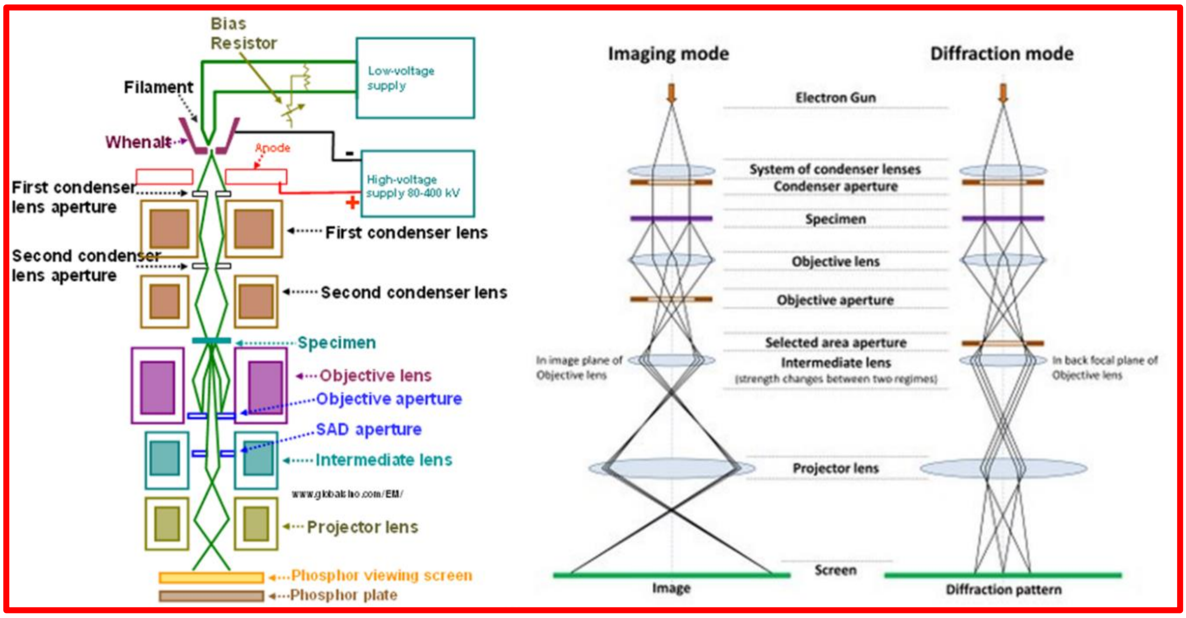

Figure 2.18: Schematic diagram for assembly of major TEM components and their working principle for real space and diffraction pattern imaging in reciprocal space [42].

In this case, an electron diffraction pattern appears on the viewing screen which consists of a bright central spot on the optic axis and other bright spots due to the diffracted electrons. An area of interest on the specimen can be selected from the sample image formed on the first image plane by the selected area aperture. This selected area acts as a virtual source for the intermediate lens assembly so that only electron diffraction from this area can be observed in the viewing screen and is known as selected area electron diffraction [41]. In addition, real space imaging of a specimen can be obtained by adjusting the first intermediate plane so that the first image plane becomes its object plane [Fig. 2.18]. If the central spot on the optic axis is selected for imaging by the objective aperture then it is called bright field imaging, whereas if any diffraction spot is chosen for imaging then it is called dark field imaging.

In the present thesis work, cross-section TEM (XTEM) measurements were carried out using a field emission gun based 300 keV FEI Tecnai G2 S-Twin machine. TEM column was kept at high vacuum ~10^{-8} mbar in order to get a collimated electron beam. The images were recorded in a charge-coupled device (CCD) based detector with 40 ms time resolution and having 4008×2672 pixels (Model 832, Orius CCD detector, Gatan). The pole piece of the objective lens has an ultra-high resolution with a spherical aberration coefficient of 0.5 mm which allows achieving point-to-point resolution of 0.194 nm.

2.7 X-ray diffraction (XRD)

X-ray diffraction is one of the most widely used techniques for evaluating the crystallinity and phase of materials [43]. Since the wavelength of x-rays (sub nanometer) is comparable to interatomic spacing of materials, x-ray waves diffract and scatter upon falling on them.

The scattered waves contain information of the atomic scatterers and their arrangement in materials. Generally, there is no XRD signal from an amorphous sample since upon the incidence of mono energetic x-rays, most of the scattered radiation from randomly distributed atoms lead to a destructive interference. However, in case of crystals, the atoms are arranged in a periodic manner, which leads to constructive interference of scattered x-rays. The condition for a constructive interference is defined by Bragg’s law (Fig. 2.19) given by:

$$2d sin\theta = n\lambda, \tag{2.4}$$

where d is the inter-planar spacing between the planes that cause constructive reinforcement of the beam, θ is half of the angle between the diffracted and the incident x-ray beam direction, and λ is the wavelength of the x-rays.

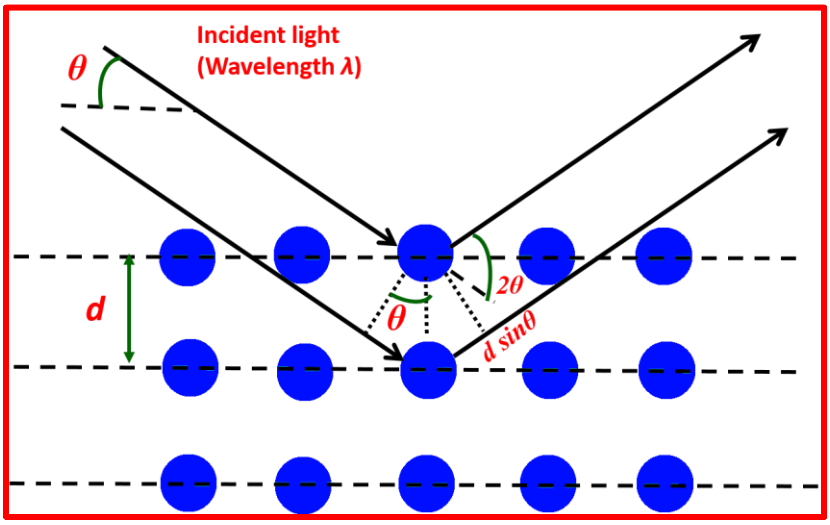

Figure 2.19: Schematic representation of x-ray diffraction from a crystal plane and Bragg's diffraction condition.

The average crystallite size (D) is given by the Scherrer's formula [44]:

$$D = \frac{k\lambda}{\beta\cos\theta}, \tag{2.5}$$

where, β is FWHM of the diffraction peak and k=0.9 is reported in the literature [44]. In addition, the relative lattice strain in polycrystalline materials can also be investigated by measuring the shift in the reflection peak maxima.

In the present thesis, XRD measurements are carried out under Bragg-Brentano geometry and glancing angle modes using a high resolution x-ray diffractometer (Bruker D8 Discover) (Fig. 2.20) with Cu-Kα (1.5418 Å) radiation source has been used. A voltage of 40 kV and 40 mA of current is provided to the X-ray source. Using the Göbel mirror attachment, a parallel beam of x-rays is produced, whereas single bounce Ge (220) monochromator is used for monochromatization of x-rays (removal of Cu-Kα-II and passing only Cu-Kα-I).

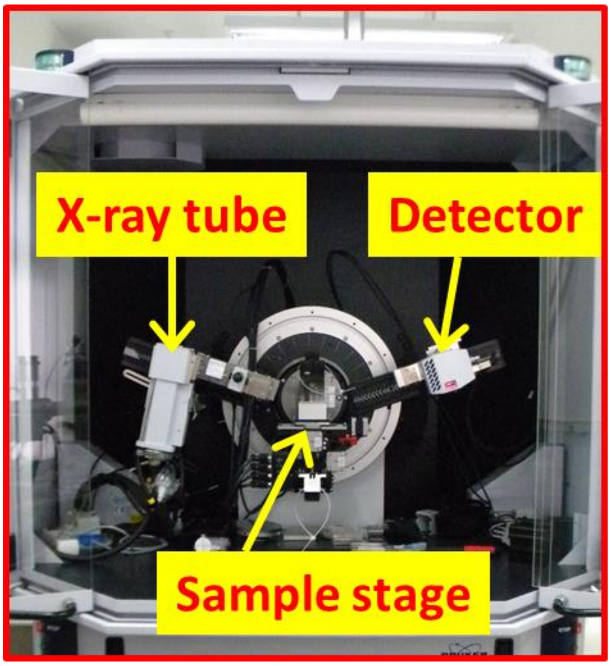

Figure 2.20: High resolution XRD setup at SUNAG Laboratory.

2.8 X-ray photoelectron spectroscopy (XPS)

X-ray photoelectron spectroscopy (XPS) is a surface-sensitive technique used to quantitatively probe the elemental composition, chemical state, and charge state of elements present in a specimen. After the discovery of photoelectric effect by Heinrich Rudolf Hertz in (1887) and its successful explanation by Albert Einstein (1905), photoelectric effect has become the most interesting light-matter interaction process. First ever XPS system was developed by Kai Siegbahn in 1954 and recorded an energy resolved XPS spectrum of cleaved sodium chloride (NaCl) crystal [45]. When an intense beam of monochromatic and known energy X-ray photons are irradiated on a specimen, the solid gets ionized and the emission of inner shell (core) electrons take place from the atoms of the solid. The binding energy of the emitted electrons can be expressed by

$$E_{\text{binding}} = E_{\text{photon}} - (E_{\text{kinetic}} + \varphi), \tag{2.6}$$

where E_{photon} is the energy of the incident x-ray photons, E_{kinetic} is the kinetic energy of the emerging photoelectrons (measured by an electron energy analyzer), and φ is the work function of the material. The electron energy analyzer uses electrostatic and/or magnetic lens to separate out the photoelectrons with a desired narrow band of energies from the wide range of available kinetic energies contained in all other electrons entering the spectrometer. Therefore, the XPS spectrum is basically a plot of photoelectron counts against their kinetic energy. However, there is a requirement of ultra-high vacuum (UHV) conditions to increase the mean free path of photoelectrons and make them capable to reach inside the spectrometer.

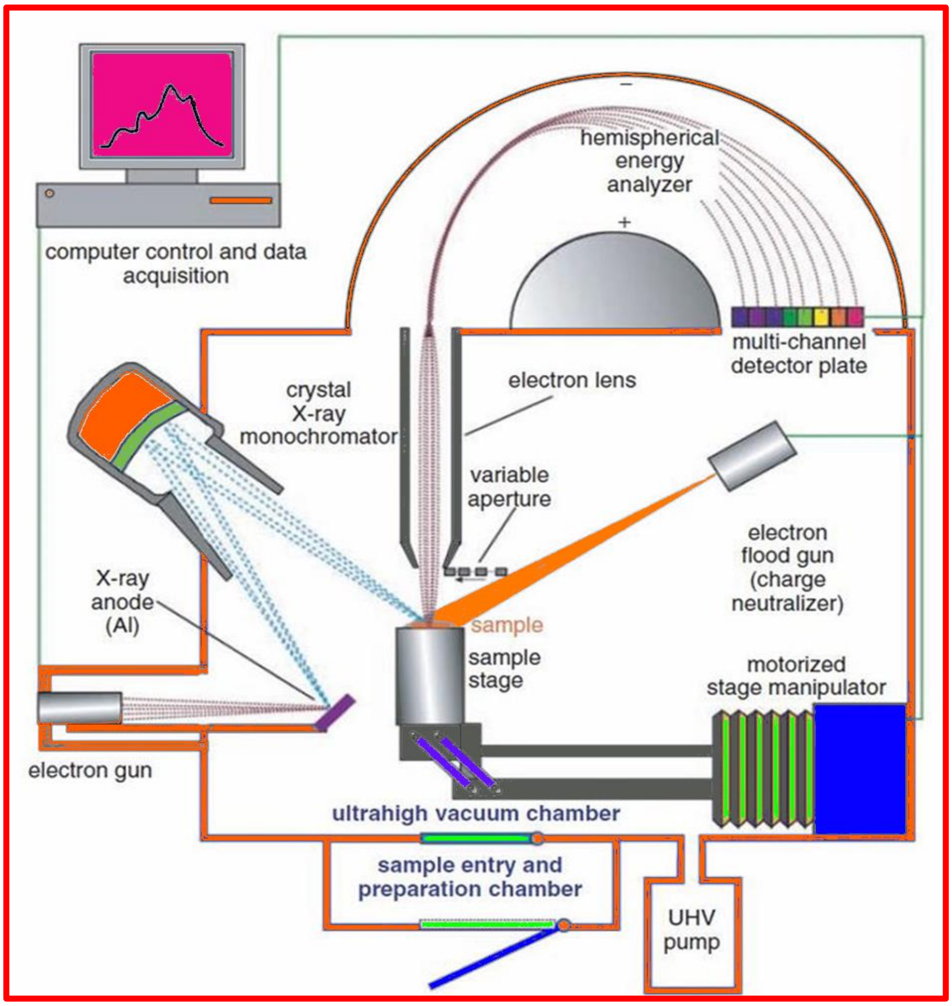

Figure 2.21: Schematic representation of XPS setup and essential components.

The presence of peaks in the XPS spectrum at particular energies are indicative of the presence of a specific element in the sample which corresponds to their binding energy associated with the electrons in each core atomic orbitals, whereas the peak intensity shows the concentration of the element present within the sampled region.

In the present thesis, the XPS experiments were performed using the PHI 5000 Versa Probe II, (ULVAC-PHI, Japan) setup as shown in the schematic diagram in Fig. 2.21. The base pressure of the main chamber is maintained at $<1\times10^{-10}$ mbar. The XPS system is equipped with a microfocused (100 μm, 25 W, 15 KV) monochromatic Al-K_α source ($h\nu$ = 1486.6 eV), a hemispherical analyzer, and a multichannel detector unit.

2.9 Rutherford backscattering spectrometry

Rutherford backscattering spectrometry (RBS) is an important analytical technique which relies on elastic collision of energetic ions with target atomic nuclei and accounts for the number of backscattered ions from the target along with their energy. A collimated beam of He-ions (accelerated using an ion accelerator up to 1-3 MeV) is allowed to impinge on a solid target kept in a high vacuum scattering chamber and a surface barrier detector is placed at a very high angle (≥150°) to detect the backscattered ions. A current integrator is connected to the specimen to measure the ion current and hence, it provides the total number of incident ions on the target. The energy related output signal collected by the detector is transferred to an energy analyzer which finally reaches the multi-channel analyzer through pre-amplifier, amplifier, and analog-to-digital converter. The output data in the form of channel number (or backscattered energy) along x-axis and the number of backscattered ions along y-axis provide the RBS spectrum of a target. RBS data can be fitted with commercially available software [RUMP, SIMNRA] to obtain the elemental depth profiling. RBS is ideally suited for accurate quantitative analysis of composition, thickness of thin films and for depth profiling of heavy elements (C-U) with a good depth and energy resolution in a non-destructive manner. It offers a sensitivity of 10^{11}-10^{15} atoms per cm^2 and an average depth resolution of 5 nm. In the present thesis, RBS technique is employed to probe the growth angle-dependent concentration of Au deposited on *NF*-Si substrates.

2.10 Optical studies

Spectroscopic ellipsometry and specular reflectance measurements were carried out on self-organized gold nanoparticles and sputter-grown ZTO thin films on nanoscale ion-beam patterned silicon substrates presented in this thesis. The working principle of these techniques is described below.

2.10.1 Ellipsometry measurements

Ellipsometry is a versatile technique to measure the optical property of specimen in spectroscopic and generalized modes [46–48]. This technique is based on the polarization of materials under electromagnetic fields and it uses *p*- and *s*-polarized light as a probe incident onto sample at Brewster angle to ensure the maximal difference in the measurement of the reflection coefficients corresponding to *p*- and *s*- polarized light [46–48] and measures a change in polarization state upon reflection or transmission from a material as shown in the schematic diagram in Fig. 2.22. The change in polarization is represented by Ψ and Δ which correspond to the amplitude ratio of reflection coefficients and their phase difference before and after the reflection between *p*- and *s*-polarization, respectively [46–48]. The reflection coefficients are related to (Ψ, Δ) by another parameter ρ, defined as:

$$\rho \equiv tan(\psi)e^{i\Delta} \equiv \frac{r_p}{r_s} \equiv \left(\frac{E_{rp}/E_{ip}}{E_{rs}/E_{is}}\right) \tag{2.7}$$

Where r_p and r_s are the reflection coefficients of *p*- and *s*- polarized light, respectively. Here E_{rp} and E_{ip} denote reflected and incident electric field vectors for *p*-polarized light, respectively. Similarly E_{rs} and E_{is} are reflected and incident electric field vectors for *s*-polarized light wave, respectively. The *p*-polarized component of the incident wave lies in the plane of light incidence whereas the *s*-polarized component lies perpendicular to the plane of incidence [46].

For a homogeneous sample, the refractive index and extinction coefficients can be directly calculated from measured (Ψ, Δ) values by simply using Fresnel's equations [49] as represented here:

$$r_p = \frac{n_t cos\theta_i - n_i cos\theta_t}{n_t cos\theta_i + n_i cos\theta_t}; r_s = \frac{n_i cos\theta_t - n_t cos\theta_t}{n_t cos\theta_i + n_i cos\theta_t}, \tag{2.8}$$

where n_i and n_t are the refractive indices and θ_i and $\theta_t$are the angles of incident and the transmitted light, respectively (with respect to surface normal).

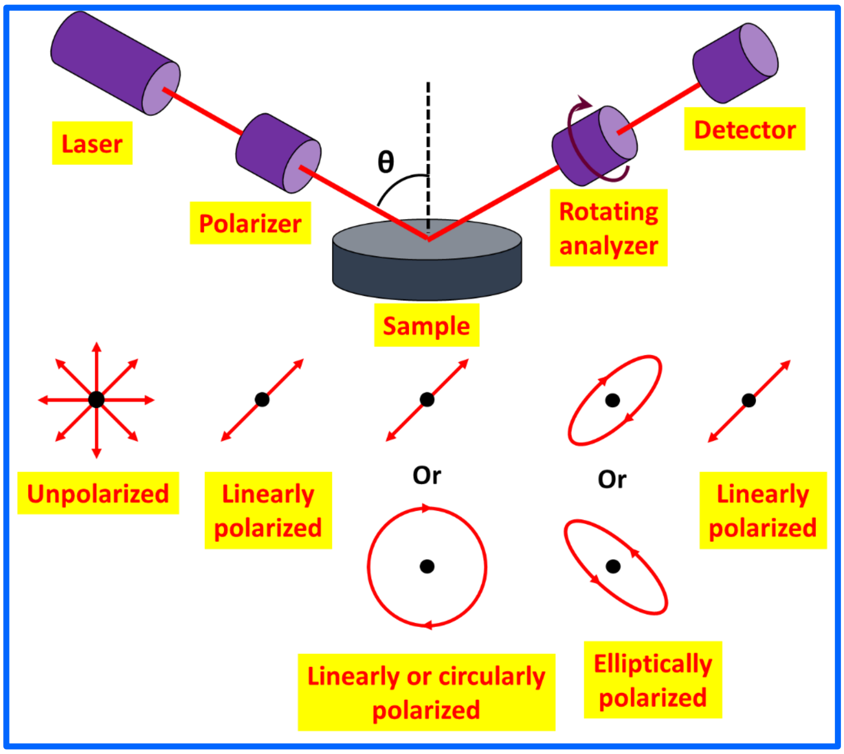

Figure 2.22: Schematic representation of ellipsometry setup and essential components along with their role in polarization of light.

The measured (ψ, Δ) are solely dependent on optical properties, surface roughness, and thickness of individual materials. Thus, ellipsometry is primarily used to determine the thickness and optical constants of the film. However, it can also characterize the composition, crystallinity, roughness, doping concentration, and other material properties which are sensitive to a change in the optical response [46–48].

In order to analyse the measured ellipsometric (ψ, Δ) data, a physical model needs to be defined for the dielectric function ϵ and other physical parameters. The (ψ, Δ) values are calculated with the help of physical model developed by introducing known dielectric functions of bulk counterpart of the materials as the starting point and matched/fitted with the measured (ψ, Δ) values. Fig. 2.23 shows the flow chart and process followed for model fitting of experimentally measured ellipsometry data. The degree of fit between experimentally measured and calculated (ψ, Δ) is defined by a mean squared error (MSE) value from a minimization algorithm (Levenberg Marquardt [50,51]). Upon achieving the best fit (MSE < 10%), optically sensitive parameters like dielectric coefficients, surface roughness, anisotropy etc. can be calculated from the developed physical model.

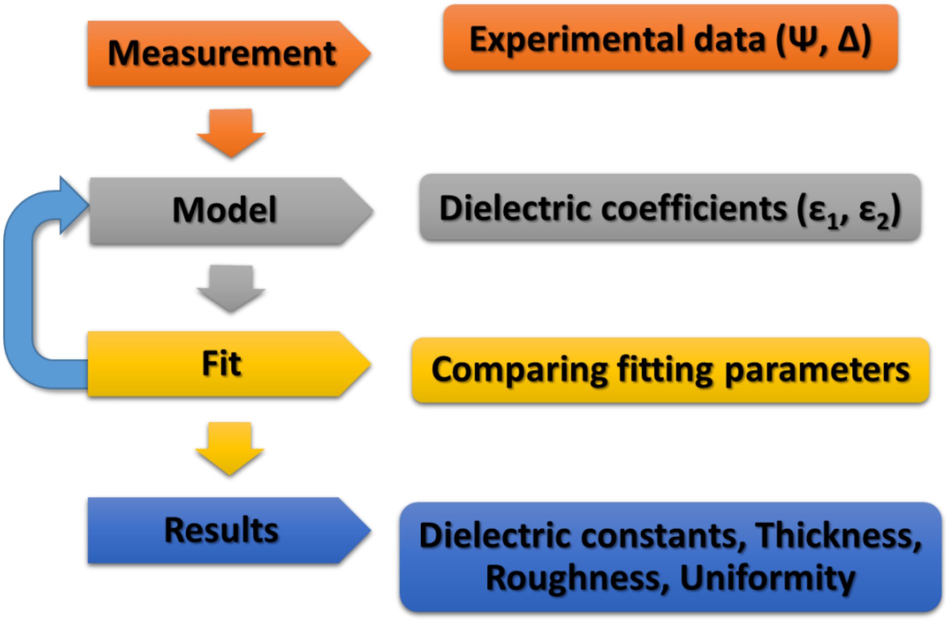

Figure 2.23: Flow chart for the model fitting of ellipsometry measured (ψ, Δ) data and extracting optically sensitive physical parameters of a sample [52].

For a non-homogeneous and isotropic sample, light reflection of a linearly polarized light can be expressed as:

$$\begin{pmatrix}E_{rp}\\E_{rs}\end{pmatrix} = S\begin{pmatrix}E_{ip}\\E_{is}\end{pmatrix} = \begin{bmatrix} r_p & 0\\ 0 & r_s\end{bmatrix}\begin{pmatrix}E_{ip}\\E_{is}\end{pmatrix}. \qquad (2.9)$$

The S-matrix is called Jones matrix [53,54] where the S_{11} and S_{22} components are the purely *p*- and *s*-polarization components of the matrix, while cross-components S_{12} and S_{21} are the flipping of polarization from *p*- to *s*- and *s*- to *p*-polarization state, respectively. It is important to note that the cross-components remain zero for isotropic samples and have non-zero finite values for anisotropic samples. For anisotropic sample the Jones matrix can be redefined as:

$$S = \begin{bmatrix} S_{11} & S_{12} \\ S_{21} & S_{22} \end{bmatrix} = \begin{bmatrix} r_{pp} & r_{ps} \\ r_{sp} & r_{ss} \end{bmatrix} = r_{ss} \begin{bmatrix} \frac{r_{pp}}{r_{ss}} & \frac{r_{ps}}{r_{ss}} \\ \frac{r_{sp}}{r_{ss}} & 1 \end{bmatrix} = r_{ss} \begin{bmatrix} \rho_{pp} & \rho_{ps} \\ \rho_{sp} & 1 \end{bmatrix}. \tag{2.10}$$

Hence,

$$\left.\begin{aligned} \rho_{pp} &= \frac{r_{pp}}{r_{ss}} = tan(\psi_{pp}) e^{i\Delta_{pp}} \\ \rho_{ps} &= \frac{r_{ps}}{r_{ss}} = tan(\psi_{ps}) e^{i\Delta_{ps}} \\ \rho_{sp} &= \frac{r_{sp}}{r_{ss}} = tan(\psi_{sp}) e^{i\Delta_{sp}} \end{aligned}\right\} . \tag{2.11}$$

These expressions show that there are six independent parameters in the Jones matrix to describe an anisotropic material instead of two parameters used for the description of an isotropic sample.

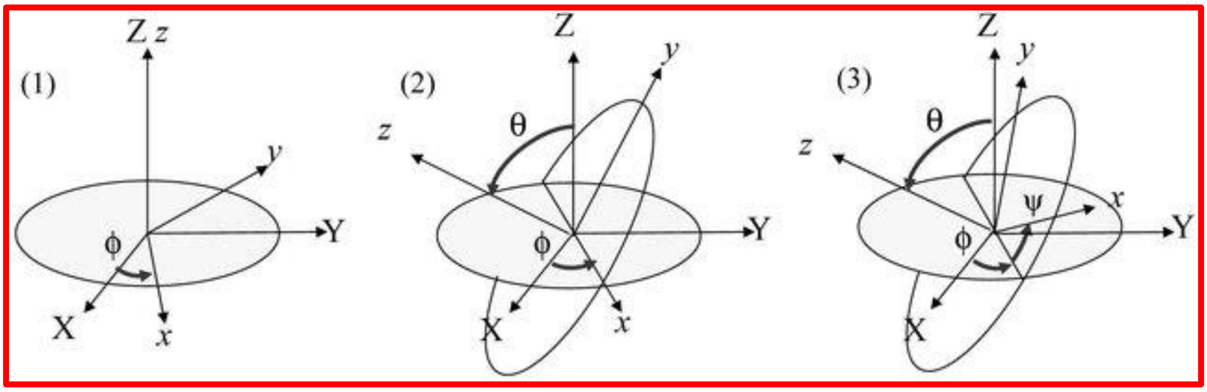

Figure 2.24: Representation of Euler angles [55].

Hence, generalized ellipsometry can be more efficient to explore the polarization states by rotating and analysing various polarisation states for an anisotropic sample, but at the same time, extracting the dielectric functions from the Jones matrix become much more complicated with the inclusion of more parameters. A transfer matrix approach (4×4 matrix method) was developed by Schubert [47,56] to overcome this problem. In this approach deals with the dielectric tensor, which can be directly calculated with the help of a suitable model. A rigorous mathematical treatment converts the 3×3 dielectric tensor matrix into 2×2 Jones matrix of anisotropic samples [46].

Sample orientation and the knowledge of various axis is very important to understand the angular transformations needed for generalized ellipsometry. The rotation angles of a tensor with respect to lab coordinate system are known as Euler angles (ϕ, θ, ψ) [55,57] and these three angles are also considered as the model fit parameters and used to transform random rotation into the lab coordinate system using a transpose matrix. The Euler angles are defined as first rotation is by an angle ϕ about the Z axis. The second rotation is by an angle θ in [0, π] about the former X axis (now x′), and the third rotation is by an angle ψ about the former Z axis (now z′) as shown in Fig. 2.24.

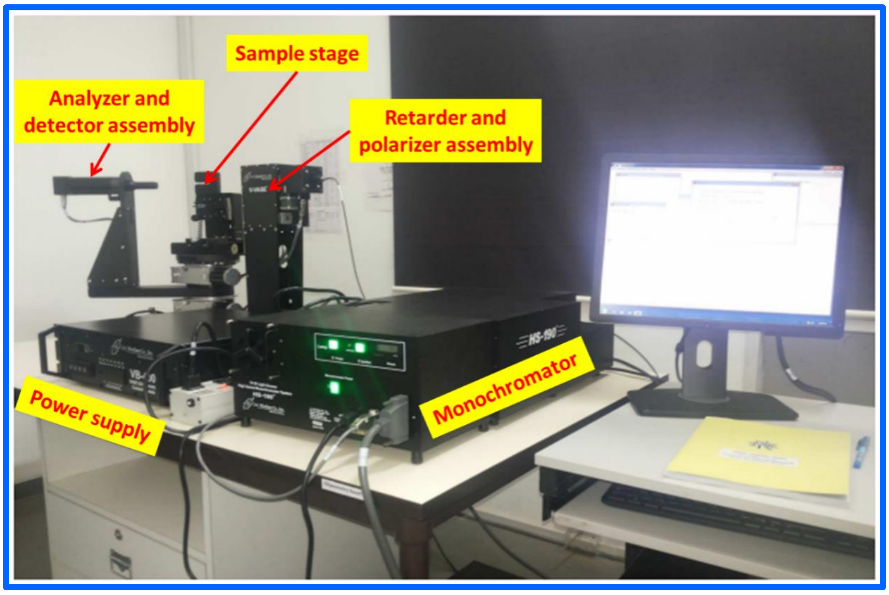

Figure 2.25: Ellipsometry setup at FCIPT, IPR.

We used V-VASE ellipsometer (J. A. Woollam Inc., USA [58]) for the optical characterizations in terms of probing in-plane anisotropy of self-organized Au-NPs on ion-beam patterned nanoscale rippled-Si substrates. As shown in Fig. 2.25, the ellipsometry system is equipped with a high-speed, automated wavelength selection monochromator in the range of 250–1100 nm, fully automated angle of incidence in the range of 15°–90° with an accuracy of 0.01°, rotating analyzer with retarder, and precise *XY* mapping sample stage with vacuum chunk [59].

It is capable of spectroscopic ellipsometry measurements of reflection, transmission, and generalized ellipsometry measurements of anisotropy, Mueller matrices.

2.10.2 Raman spectroscopy

Raman spectroscopy is a vibrational spectroscopic technique based on the frequency shift of photons in monochromatic light upon interaction with the sample. When monochromatic light (usually laser light) falls on a sample electrons get excited to higher energy states by absorbing photons and after attaining the lifetime of that excited state, electrons come back to their ground state by emitting photons.

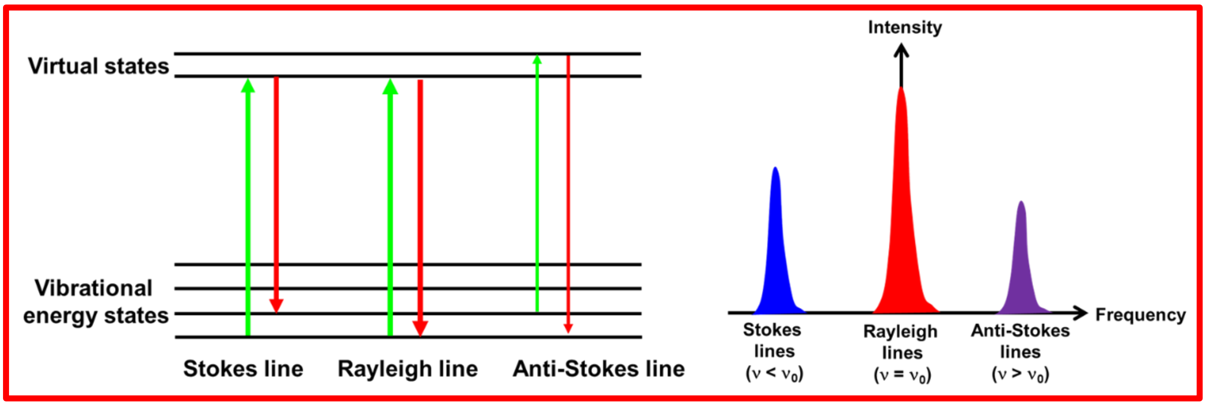

Figure 2.26: Transitions of electrons corresponding to Rayleigh, Stokes, and anti-Stokes lines (left) and their intensities (right).

As shown in Fig. 2.26, a major fraction of photons have the frequency same as the incident photons (elastic scattering: Rayleigh scattering), however, remaining photons either have lower (Stokes lines) or higher (anti-Stokes lines) frequency than the incident photon (inelastic scattering). In fact, the Stokes lines originate due to the excitation of an electron from its ground state, while electrons already in the excited states lead to the anti-Stokes lines. Hence, the intensity of Stokes lines always remains higher than anti-Stokes lines due to higher population of electrons in the ground state. The transitions corresponding to Rayleigh, Stokes, and anti-Stokes lines and their intensities are depicted in Fig. 2.26.

The incident light interacts with the electrons in the molecules which results in its periodic oscillations. The oscillation of electron clouds results in a periodic separation of charges within the molecule that causes an induced dipole moment. The oscillation induced dipole moment is manifested as the source of scattered light or electromagnetic field. This shift provides information about vibrational, rotational, and other low frequency transitions in molecules.

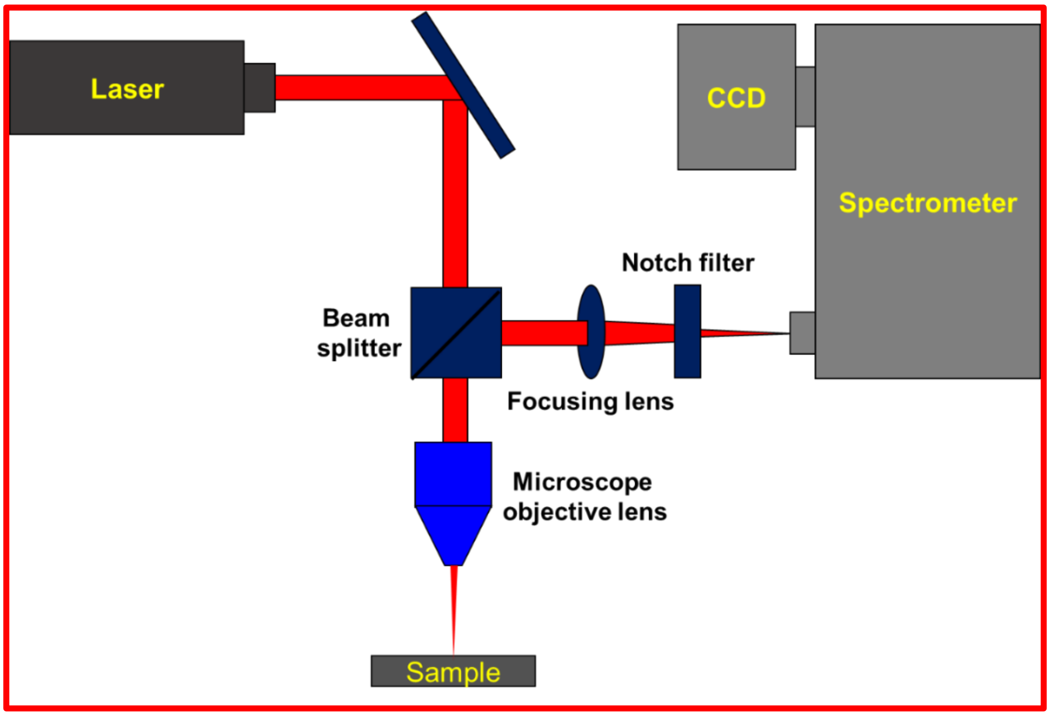

Figure 2.27: Schematic diagram for Raman spectroscopy.

Raman spectroscopy can be used to study solid, liquid, and gaseous samples. A Raman spectrometer is required to have a light source, focusing lenses, and mirrors. Earlier, visible laser excitation was being used for biological applications.

In the succeeding years, this technique has turned out as a major spectroscopic tool for materials characterization as the Raman fingerprints are unique for every molecule. A typical Raman spectrometer used to have visible laser light from helium-neon/argon/krypton ion laser as the source. Raman scattered light is collected by using a collection optics and coupled to a spectrograph. A photomultiplier tube or multichannel optical detector which is located at the end of the spectrograph is used to detect scattered light. A typical schematic diagram of Raman spectroscopy is depicted in Fig. 2.27.

2.10.3 Reflectance measurements

Reflectance is defined as the fraction of incident light which is reflected from a surface [60]. As shown in Fig. 2.28, an ultra-violet-visible-near infrared (UV-Vis-NIR) spectrophotometer (Shimadzu, UV 3101PC) is used for the optical reflectance measurements which is equipped with a specular reflectance measurement accessories.

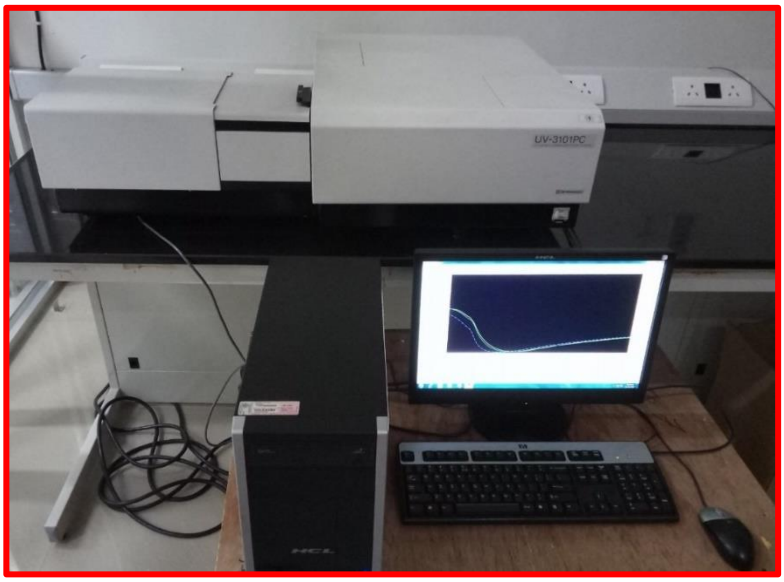

Figure 2.28: UV-Vis-NIR spectrophotometer used for the present thesis.

As the name suggests, this spectrometer can measure the surface reflectance in the wavelength range of 200 to 3200 nm. However, in the present thesis, all the reflectance spectra are recorded in the wavelength range of 300–800 nm according to the region of interest.

2.11 Field emission studies

According to quantum mechanical tunneling theory, an electron can penetrate through a potential barrier into the vacuum under an externally applied electric field which is called as field electron emission. Generally, this phenomenon occurs at high electric fields (10^7-10^8 V-cm^{-1}). To produce such a high field using reasonable potentials, the emitter is usually fabricated into a form of cone with a sharp apex where the radius of curvature of the apex lies in the range of tens of angstroms to several microns.

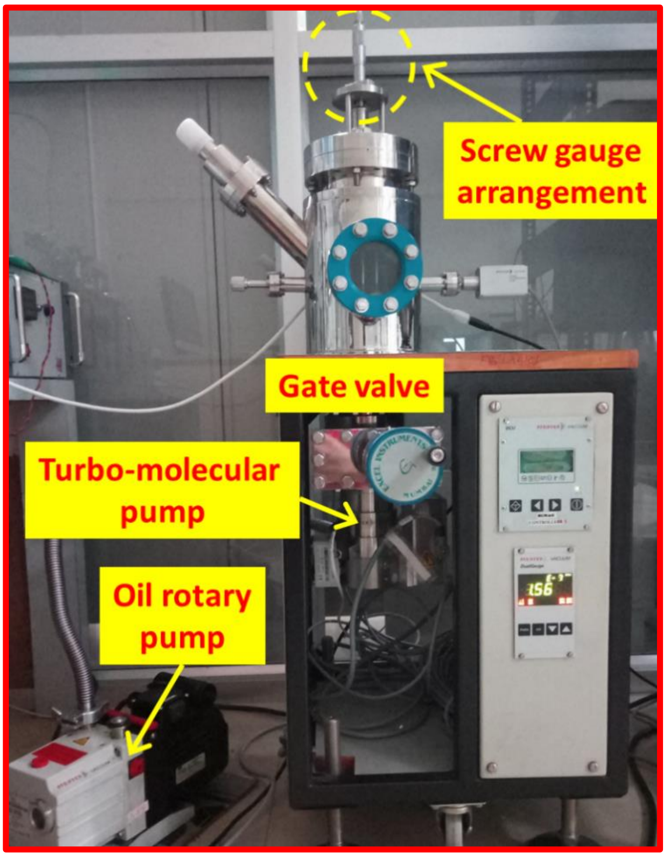

Figure 2.29: Field emission setup at SUNAG Laboratory.

The potential barrier (work function of material) is lowered down by an applied electric field to enable the tunneling of electrons from metal-vacuum interface which is called Fowler-Nordheim (F-N) tunnelling [61,62] and the corresponding Fowler-Nordheim (F-N) equation is given as:

$$J = A\left(\frac{\beta^2 E^2}{\Phi}\right) exp\left(\frac{-B\Phi^{\frac{3}{2}}}{\beta E}\right), \tag{2.12}$$

where J is the emission current density (A m^{-2}), E is the mean electric field between the electrodes (V μm^{-1}), Φ is the work function (eV), and β is the enhancement factor (which depends on geometry of the tip and sample which is 1 for a flat surface and higher for other geometries). The constants are A=1.56×10^{-10} A V^{-2} eV and B=6.83×10^{3} V $eV^{-1.5}$ μm^{-1} [61,62].

Field emission from semiconductors is a much more complicated process due to their low carrier concentrations in bulk emitter compare to metal emitter. In the presence of an external field, low carrier concentrations allow the field penetrating into a semiconductor, causing band bending and nonlinearity in the current-voltage characteristics in F-N coordinates. The intercept of F-N plot, $\ln(J\,E^{-2})$ versus E^{-1} contains electron emission related information about the effective emission area and the field enhancement factor. A vacuum chamber at a base pressure of 5×10^{-7} mbar is used for the field emission measurements reported in this thesis [Fig. 2.29]. The main chamber is equipped with a standard two-electrode configuration, where a known separation is maintained between two copper disks (serve as anode and cathode) by using a standard screw gauge arrangement (Mitutoyo, Japan). Sample is electrically stacked to the cathode using a conductive copper tape (sheet resistance ~0.004 Ω/□).

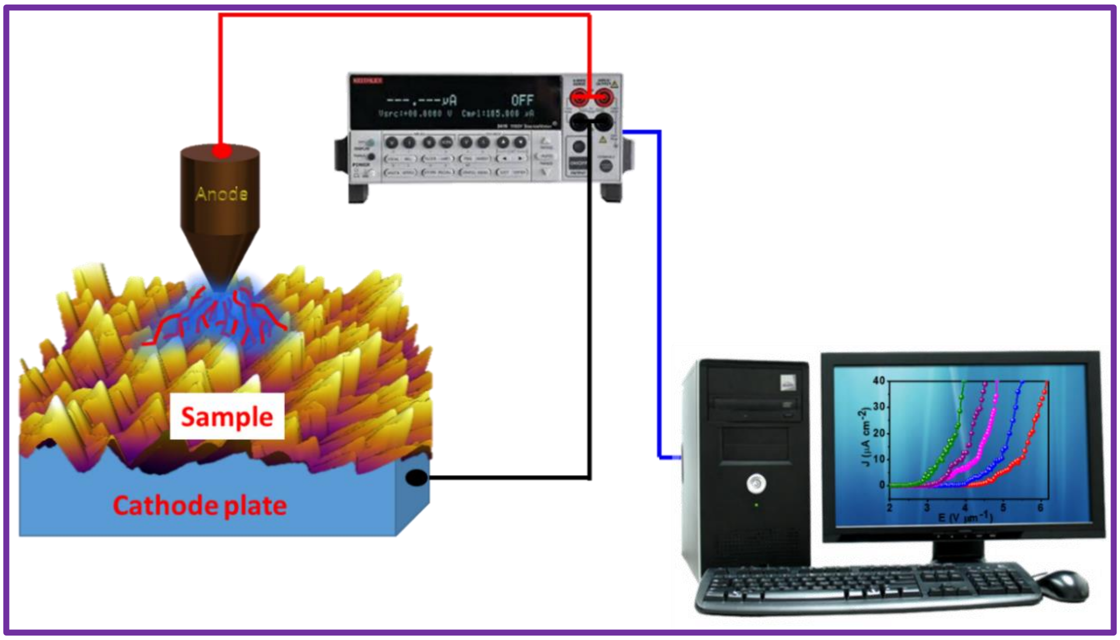

Figure 2.30: Schematic representation of field emission measurement.

A Keithley 2410 source meter, interfaced with a computer, is used to supply the desired voltage to the anode (with respect to the cathode) and measures the corresponding current where *I-V* characteristics are recorded by the LabTracer program [63]. A schematic representation of the field emission measurement setup used in the present thesis is depicted in Fig. 2.30.

Bibliography

[1] M.A. Herman, H. Sitter, *"Molecular beam epitaxy"*, Springer-Verlag Berlin Heidelberg, Berlin, Heidelberg, 1996.

[2] M. Henini, "*Molecular beam epitaxy from research to mass-production"*, Springer-Verlag Berlin Heidelberg, 2013.

[3] A.Y. Cho, J.R. Arthur, Prog. Solid State Chem. 10 (1975) 157.

[4] J.R. Arthur, Surf. Sci. 500 (2002) 189.

[5] P. Frigeri, L. Seravalli, G. Trevisi, S. Franchi, "*Molecular beam epitaxy: An overview"*, Elsevier Ltd., 2011.

[6] https://www.prevac.eu/

[7] X. Qiao, X. Zhang, Y. Tian, Y. Meng, Appl. Phys. Rev. 3 (2016) 031106.

[8] C.A. Bishop, Vac. Depos. onto Webs, Film. Foils, Elsevier (2011) 125.

[9] J.E. Mahan, K.M. Geib, G.Y. Robinson, R.G. Long, J. Vac. Sci. Technol. A Vacuum, Surfaces, Film. 8 (1990) 3692.

[10] N. Masud, J.B. Pendry, J. Phys. C Solid State Phys. 9 (1976) 1833.

[11] S. Nagano, Phys. Rev. B, 1990, 7363.

[12] Y. Horio, "*Reflection high-energy electron diffraction"*, John Wiley & Sons, Inc., USA, 2018.

[13] K.G. Wagner, Vacuum 34 (1984) 743.

[14] A.K. Shukla, S. Banik, R.S. Dhaka, C. Biswas, S.R. Barman, H. Haak, Rev. Sci. Instrum. 75 (2004) 4467.

[15] K.S. Sree Harsha, "*Principles of vapor deposition of thin films"*, Elsevier, 2006.

[16] Y. Lin, X. Chen, Eds. "*Advanced nano deposition methods"*, Wiley-VCH Verlag GmbH & Co. KGaA, Weinheim, Germany, 2016.

[17] R. Anton, T. Wiegner, W. Naumann, M. Liebmann, C. Klein, C. Bradley, Rev. Sci.

Instrum. 71 (2000) 1177.

[18] B.H. Wolf, "*Characterization of ion sources*", CRC Press, 1995.

[19] R. Stuart, "*Vacuum technology, thin films, and sputtering*", Elsevier, 2016.

[20] K.J. Klabunde, Ed., "*Thin films from free atoms and particles*", Elsevier, 2016.

[21] D.H. Lee, N.G. Cho, Meas. Sci. Technol. 23 (2012) 105601.

[22] http://www.rochester.edu/urnano/facilities/Ambios_profilometer/index.html

[23] J.W. Wood, R.D. Redin, Rev. Sci. Instrum. 64 (1993) 2405.

[24] C. Parigger, Handb. Phys. Med. Biol. 56 (2010) 34.

[25] J.G. Kushmerick, P.S. Weiss, "*Scanning probe microscopes*", Springer Berlin Heidelberg, Berlin, Heidelberg, 2016.

[26] M. Fujii, "*Scanning probe microscopy*", Springer New York, New York, 2011.

[27] S. Morita, "*Roadmap of scanning probe microscopy-nanoscience and technology*", Springer Berlin Heidelberg, Berlin, Heidelberg, 2007.

[28] W. Melitz, J. Shen, A.C. Kummel, S. Lee, Surf. Sci. Rep. 66 (2011) 1.

[29] R. Fuji, "*Conductive atomic force microscopy*", Ed. M. Lanza, Springer Singapore, Singapore, 2018.

[30] A. Avila, B. Bhushan, Crit. Rev. Solid State Mater. Sci. 35 (2010) 38.

[31] L. Jiang, J. Weber, F.M. Puglisi, P. Pavan, L. Larcher, W. Frammelsberger, G. Benstetter, M. Lanza, Materials (Basel). 12 (2019) 459.

[32] http://www.asylumresearch.com/Applications/ElectricalCharacterization/ElectricalSuite.pdf

[33] http://www.asylumresearch.com/Applications/Orca/Orca.shtml

[34] T. Basu, M. Kumar, M. Saini, J. Ghatak, B. Satpati, T. Som, ACS Appl. Mater. Interfaces 9 (2017) 38931.

[35] V. Chatterjee, R. Harniman, P.W. May, P.K. Barhai, Appl. Phys. Lett. 104 (2014) 171907.

[36] W. Han, H. Jiao, D. Fox, in: Springer Tracts Mod. Phys., Springer US, Boston, MA, 2018, pp. 35.

[37] P.S. Turner, C.E. Nockolds, S. Bulcock, *"Electron microscope techniques for surface characterization"*, Springer, Berlin, Heidelberg, 2013.

[38] https://www.zeiss.com/corporate/int/home.html

[39] N. Yao, Z.L. Wang, Eds. *"Handbook of microscopy for nanotechnology"*, Kluwer Academic Publishers, Boston, 2005.

[40] B. Satpati (Ph. D. Thesis, Institute of Physics, Bhubaneswar)

[41] B. Fultz, J.M. Howe, *"Transmission electron microscopy and diffractometry of materials"*, Springer Berlin Heidelberg, Berlin, Heidelberg, 2008.

[42] https://www.wikiwand.com/en/Transmission_electron_microscopy

[43] B.D. Cullity, *"Elements of x-ray diffraction"*, Addison-Wesley Publishing Co., Boston, 1978.

[44] A.L. Patterson, Phys. Rev. 56 (1939) 978.

[45] K. Siegbahn, K. Edvarson, Nucl. Phys. 1 (1956) 137.

[46] H. Fujiwara, *"Spectroscopic ellipsometry"*, John Wiley & Sons Ltd, Chichester, UK, 2007.

[47] M. Schubert, *"Infrared ellipsometry on semiconductor layer structures"*, Springer Berlin Heidelberg, Berlin, Heidelberg, 2012.

[48] H.G. Tompkins, E.A. Irene, *"Handbook of ellipsometry"*, Springer-Verlag Berlin Heidelberg, Berlin, Heidelberg, 2005.

[49] D. Goldstein, Polariz. Light. Third Ed. (2011) 117.

[50] K. Levenberg, Q. Appl. Math. 2 (1944) 164.

[51] D.W. Marquardt, J. Soc. Ind. Appl. Math. 11 (2005) 431.

[52] H.G. Tompkins, *"A user's guide to ellipsometry"*, Elsevier, 2016.

[53] R. Clark Jones, J. Opt. Soc. Am. 32 (2008) 486.

[54] P. Yeh, C. Gu, *"Optics of liquid crystal displays"*, John Wiley & Sons Ltd, UK, 2007.

[55] V.C. Chen, F. Li, S.S. Ho, H. Wechsler, IEEE Trans. Aerosp. Electron. Syst. 42 (2006) 2.

[56] M. Schubert, Phys. Rev. B - Condens. Matter Mater. Phys. 53 (1996) 4265.

[57] G.B. Arfken, H.J. Weber, F.E. Harris, *"Mathematical methods for physicists"*, Elsevier, 2013.

[58] https://www.jawoollam.com/

[59] https://www.jawoollam.com/products/vase-ellipsometer

[60] F.L. Forgerini, R. Marchiori, Biomatter 4 (2014) 28871.

[61] R.H. Fowler, L. Nordheim, Proc. R. Soc. A Math. Phys. Eng. Sci., 119 (1928) 173.

[62] P.A. Chatterton, Proc. Phys. Soc. 88 (1966) 231.

[63] https://www.tek.com/source-measure-units/2400-software/labtracer-29-unsupported

CHAPTER 3

Theoretical Background: Pattern formation and growth kinetics of nanoparticles

3.1 Ion-beam induced pattern formation

Self-organization of patterns fabricated under bombardment of energetic ions is an important area and is being studied extensively studied due to their potential in creating large scale surface patterns (wafer scale: 2 inch diameter) in a single processing step. Initial studies lead to a common belief that sputter erosion plays a major role in creating such nanoscale patterns [1,2]. As a matter of fact, sputter erosion can lead to different effects on the surface of a material, depending on different experimental parameters, such as incident ion energy, angle of incidence, mass, substrate temperature and material composition, and the presence of impurity also. However, subsequent studies indicate that self-organized periodic nanostructures originate due to a dynamic balance among various fundamental kinetic processes under ion bombardment like surface roughening via curvature-dependent sputtering (in which erosion rate is enhanced for concave surfaces rather than convex surfaces), smoothing via surface diffusion, and atomic mass redistribution which solely depend on the experimental conditions [2–5].

Thus, no single theory is able to describe ion-induced pattern formation, albeit for materials which get amorphized under ion bombardment the same can be explained well in light of continuum models [6]. This framework describes ion-bombarded surface at a length scale much higher than the atomic scale. Generally, the roughness or smoothness of a surface under ion exposure is described by fluctuations in the surface height with respect to a mean height. In this chapter, we briefly introduce some basic parameters which are used to characterize a surface and later on, we present a brief review of the theoretical models developed for the understanding of surface evolution under ion-bombardment.

3.1.1 Ion-solid interaction

The interaction of charged atomic particles with solid surfaces is the basis of many experimental techniques and it plays an important role in fundamental and applied research. The ability to sculpt the smooth material surfaces in the form of nanostructures using ion-beams are critically dependent on the nature of interactions between an incident ion-beam and the material under consideration.

Figure 3.1 shows a schematic diagram illustrating some of the possible processes that occur during ion-matter interaction. When ions are bombarded on a solid target, a major fraction of incident ions enters the solid after penetrating the target surface. In this process, energetic ions lose their kinetic energy by transferring it to the target atoms and electrons via elastic and inelastic collisions, respectively. The energy transferred directly to the target atoms is further propagated to stationary neighbouring atoms and electrons which results in a high degree of mobile target atoms and electrons. Therefore, this successive collision processes lead to a region dominated by the mobile atoms within the target material which is known as collision cascade. When an ion completely loses its kinetic energy inside the target after consecutive collisions with target atoms and electrons and comes to rest, the process is termed as ion-implantation and the ions get implanted in the material. However, if target atoms from the near-surface region of the material, get sufficient energy to overcome the potential barrier and are knocked out from the target surface, then the process is identified as sputtering. Hence, the combination of knocked out target atoms and backscattered species is called as sputtered atoms. The sputtering yield is the number of sputtered atoms per incident ion upon irradiation of a sample.

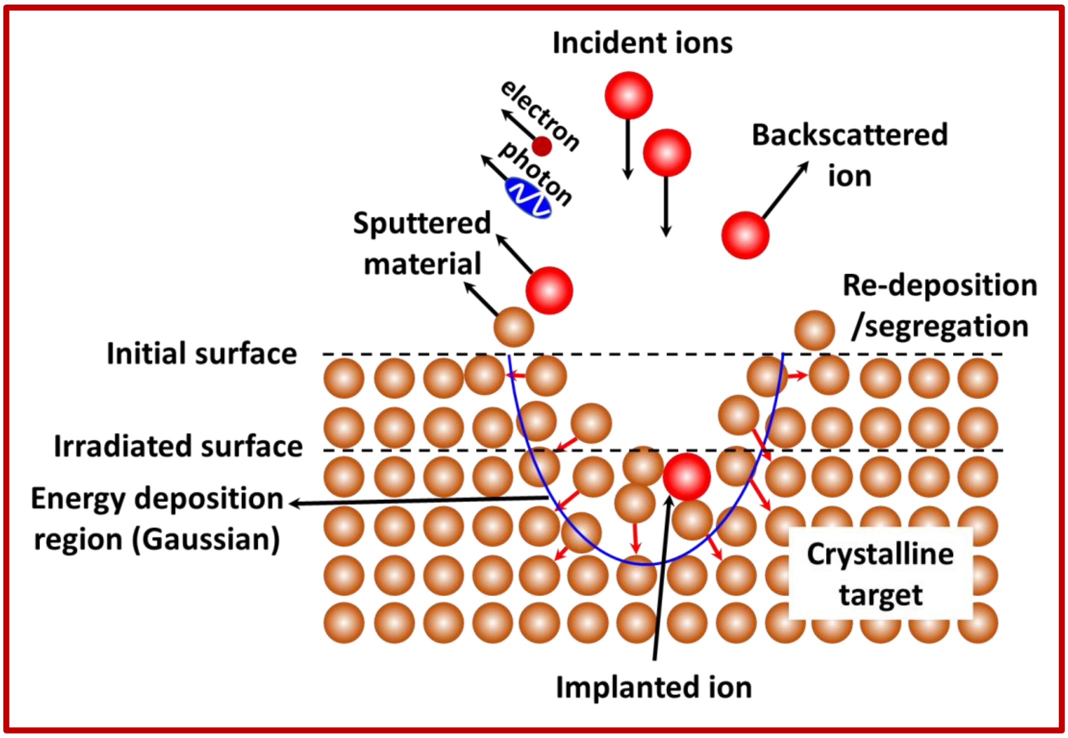

Figure 3.1: Schematic of ion-solid interaction.

In addition, there is a large angle scattering of ions upon colliding with target atoms which results in the reflection of ions (in case of a lighter projectile mass compared to target atomic mass). This process is termed as backscattering and the ions (charged or neutralized by charge exchange with target atoms) are called backscattered species. Further, the interaction of energetic ions with target electrons can give rise to emission of optical x-rays, optical photons, and secondary electrons. If the displacement of target atoms from their lattice positions can give rise to highly disordered zones along the path of the incident ions which is known as radiation damage. However, the disordered zones, which are initially isolated, may overlap with each other at sufficiently high ion fluences and therefore, give rise to the formation of a complete amorphous layer. The region of the solid target which is affected by the impact of energetic ions, is called as the region of deposited energy. In the following sections, we will briefly introduce the terminology exploited to describe the interaction of ions with matter.

Ion stopping

As the name suggests, ion stopping is the rate of energy lost by energetic ions while travelling inside a target. It can be described by the stopping power *dE/dx*, where the energy lost by the incident energetic ion is *dE* in traversing a distance *dx* which is measured from a reference frame parallel to the ion-beam direction. As mentioned above, energetic ions can lose their energy either by elastic (nuclear) or inelastic (electronic) collisions, therefore, the stopping power can be represented as the summation of both nuclear and electronic energy losses as:

$$\frac{dE}{dx} = \left(\frac{dE}{dx}\right)_n + \left(\frac{dE}{dx}\right)_e, \tag{3.1}$$

where nuclear and electronic energy losses are represented by $\left(\frac{dE}{dx}\right)_{\mathrm{n}}$ and $\left(\frac{dE}{dx}\right)_{\mathrm{e}}$, respectively. The stopping cross-section (effective impact area) is an important parameter which can describe the energy losses as:

$$S(E) = \frac{1}{N}\frac{dE}{dx} = \frac{1}{N}\left(\frac{dE}{dx}\right)_n + \frac{1}{N}\left(\frac{dE}{dx}\right)_e = S_n(E) + S_e(E), \tag{3.2}$$

where *N* is the atomic density of the target [7].

Nuclear stopping

To describe nuclear stopping, one can start with the interaction potential *V*(*r*) between an energetic ion and the target atom as:

$$\begin{aligned} V(r) &= 0 \qquad \text{for } r > r_0 \\ &= \frac{Z_1 Z_2 e^2}{r^2}\chi(r) \quad \text{for } \ a_0 < r < r_0, \end{aligned} \tag{3.3}$$

where *r* is the distance between the incident ion and the target atoms, a_0 and r_0 are the Bohr radius of hydrogen atom and equilibrium distance of atoms in a solid, respectively. Z_1 and Z_2 are atomic number of the incident ion and the target atom, respectively and *e* is the electronic charge. On the other hand, $\chi(r)$ is the electrostatic screening of nuclear charges by the bound electrons to the target atoms. To get the expression for nuclear stopping, both, the interatomic potential and screening function can be approximated in power forms as $V(r) \sim r^{-1}$ and $\chi(r/a_{\mathrm{TF}})$

= $(k_s/s)(a_{TF}/r)^{s-1}$, respectively where, s=1, 2….k$_s$, is an indexing constant, and a_{TF} is the Thomas-Fermi screening radius defined as:

$$a_{TF} = \frac{0.88534 a_0}{\left(Z_1^{1/2} + Z_2^{1/2}\right)^2} . \tag{3.4}$$

Using these power forms of interatomic potential and screening function, the nuclear stopping can be written as [7]:

$$S_n(E) = \frac{C_m E^{1-2m}}{1-m} \left[\frac{4M_1M_2}{(M_1+M_2)^2}\right], \tag{3.5}$$

where, $$C_m = \frac{\pi}{2} \lambda_m a_{TF}^2 \left(\frac{Z_1Z_2e^2}{a_{TF}}\right)^{2m} \left(\frac{M_1}{M_2}\right)^m . \tag{3.6}$$

Here, m=1/s and λ_m is a fitting variable having the functional form:

$$\lambda_m = 2m \left(\frac{k_s \Gamma(1/2)\Gamma(s+1/2)}{4\Gamma(s/2+1)}\right)^{2m} . \tag{3.7}$$

The compact form of the stopping cross-section can be shown by introducing reduced energy (ε) and reduced length (ρ) as:

$$S_n(\varepsilon) = \frac{d\varepsilon}{d\rho_L} = \frac{\lambda_m}{2(1-m)} \varepsilon^{1-2m}, \tag{3.8}$$

where $$\varepsilon = \frac{M_2}{M_1+M_2} . \frac{a_{TF}}{Z_1Z_2e^2} E \qquad and \qquad \rho_L = 4\pi L N a_{TF}^2 \left[\frac{M_1M_2}{(M_1+M_2)^2}\right]. \tag{3.9}$$

The exponent m depends upon the reduced energy (ε) in the following manner:

$$m = \left\{\begin{matrix} 1/3 & \text{for } \varepsilon \leq 0.2 \\ 1/2 & \text{for } 0.08 \leq \varepsilon \leq 2 \\ 1 & \text{for } \varepsilon > 2 \end{matrix}\right\}. \tag{3.10}$$

This approximation of screening function applicable to nuclear stopping was provided by Ziegler, Biersack, and Littmark (ZBL) [8].

Electronic stopping

When energetic ions traverse inside the target matrix, the electronic energy loss of energetic ions inside a solid is strongly dependent on the velocity of the ions. Lindhard and Scharff derived the cross-section corresponding to the electronic stopping of energetic ions inside a solid. It is valid for ion velocity $v<v_0 Z_1^{2/3}$, where v_0 is the Bohr velocity. The electronic stopping cross-section can be expressed as:

$$S_e(E) = 3.83 \frac{Z_1^{7/6} Z_2}{\left(Z_1^{2/3}+Z_2^{2/3}\right)^{3/2}} \left(\frac{E}{M_1}\right)^{1/2} = K_L E^{1/2}. \tag{3.11}$$

The compact from of the electronic stopping cross-section can also be shown in terms of reduced energy (ε) and reduced length (ρ) as:

$$S_e(\varepsilon) = \left(\frac{d\varepsilon}{d\rho}\right)_e = \frac{Z_1^{2/3} Z_2^{2/3} \left(1+\frac{M_2}{M_1}\right)^{3/2}}{12.6\left(Z_1^{2/3}+Z_2^{2/3}\right)^{3/4} M_2^{1/2}} \epsilon^{\frac{1}{2}} = k\varepsilon^{1/2}. \tag{3.12}$$

The interaction of high energy ions (velocity $v>v_0 Z_1^{2/3}$) with target electrons is out of the scope of this thesis and not discussed here.

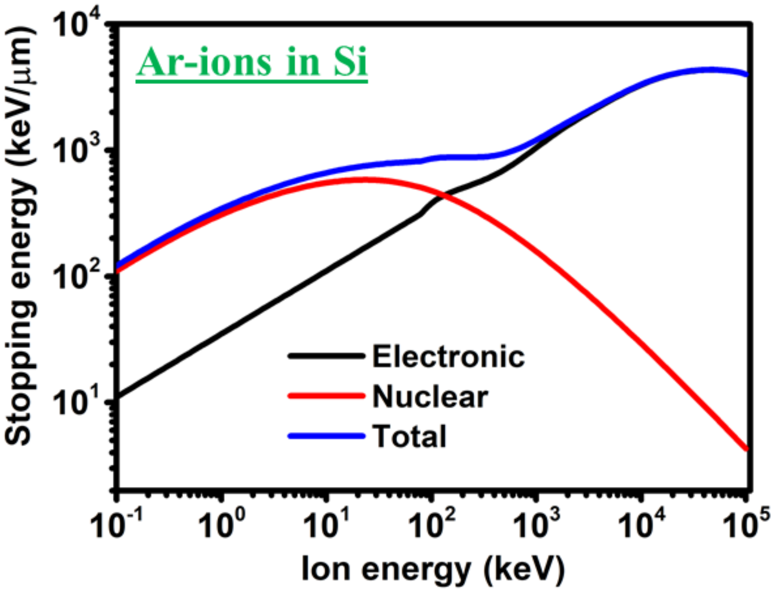

Figure 3.2: Nuclear, electronic, and total energy losses extracted from SRIM 2013 Monte Carlo simulation code [8]. Energy losses are plotted as a function of incident energy of Ar-ions.

Let's take an example of Ar-ion bombardment of Si target. As mentioned above, when energetic Ar-ions travel inside the silicon matrix, ions continuously lose their energy via nuclear (elastic) and electronic (inelastic) energy loss processes. To identify the energy regimes for the nuclear and electronic energy loss, SRIM simulation is performed on Ar-ion irradiated of Si system (Fig. 3.2) and is found that nuclear energy loss process is dominant in the low energy (0.1–10 keV) regime. However, in the medium energy (10–500 keV) regime, the dominant energy loss process starts to deviate from nuclear to electronic energy loss. Moreover, the electronic energy loss processes dominate at sufficiently higher energies (≥1 MeV to GeV).

Ion range and straggling

As mentioned above, when energetic ions travel through a solid, there are collisions of ions with the target atoms/electrons and therefore, ions lose their energy by the velocity-selective energy loss mechanisms. During this process, energetic ions undergo successive scattering of ions with target atoms and change their direction of motion. Thus, the trajectory of the ions becomes random instead of a straight line. A 3D representation of the process is shown in Fig. 3.3, where the origin of the coordinate system is considered at the target surfaces. The positive *x*-axis is normal to the surface pointing into the solid, while *y*- and *z*-axes are considered to be orthogonal to each other in the target surface plane.

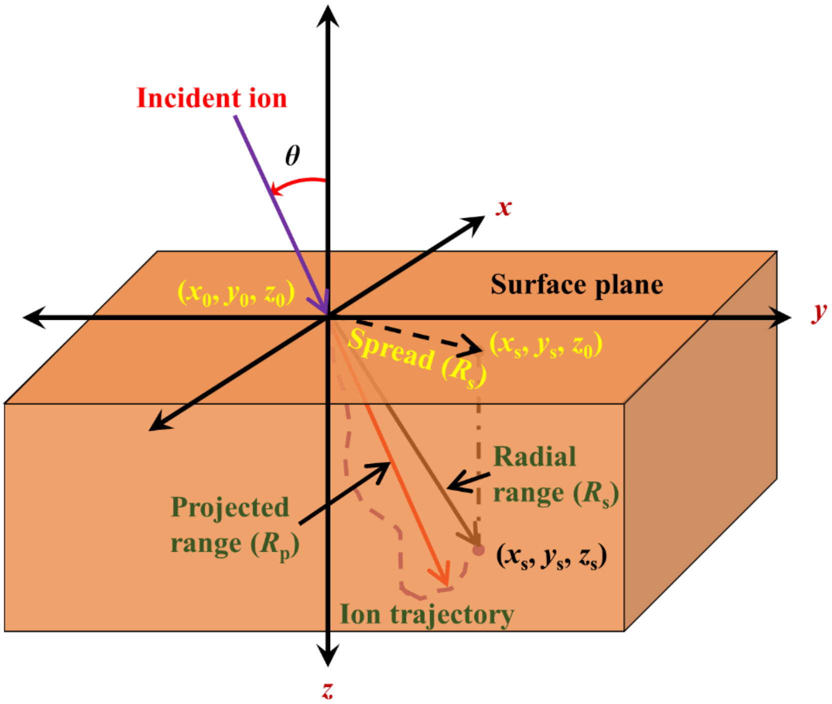

Figure 3.3: Schematic diagram clarifying the definitions of penetration depth, spread, radial range, and projected range.

As shown in the schematic, an ion incident at an angle of θ (with respect to the surface normal) hits the surface at a point (x_0, y_0, z_0) and follows the zigzag trajectory (shown by the blue line) after successive scattering with stationary target atoms and electrons. Finally, the energetic ion completely loses its kinetic energy and comes to rest at a point (x_S, y_S, z_S). The distance along the trajectory of the ion is called the range (R) of the ion. However, the projected range (R_p) is defined by the net penetration depth of the projectile measured along the initial ion trajectory. The net depth of ion-penetration along the z-axis (z_s) is equivalent to the projected range corresponding to the normal incidence of ions (θ=0°). The distance between the point of entrance (x_0, y_0, z_0) and the end point of ion path (x_S, y_S, z_S) is called the radial range (R_r). The distance between (x_0, y_0, z_0) and (x_S, y_S, z_0) is called the lateral spread (R_s). Since, the stopping of ions in a target is a stochastic process, it is not necessary for all the ions with same energy and angle of incidence to come in rest at the same depth below the surface. Hence, a statistical distribution of projected range is observed, which is referred as the range distribution. Generally, the ion-range distribution is roughly a Gaussian for low ion fluences where the distance of the Gaussian peak from the surface and FWHM of the distribution are called the average range of ions and the range straggling, respectively. The ion range (R) in terms of incident ion energy (E_0) [7] can be expressed as:

$$R(E_0) = \left(\frac{1-m}{2m}\right)\frac{\gamma^{m-1}}{NC_m}E_0^{2m}, \tag{3.13}$$

where $\gamma = 4M_1M_2/(M_1+M_2)^2$ is the reduced mass, C_m and m are defined earlier in Eq. 3.6 and 3.10, respectively.

Sputtering

Sputtering is a phenomenon in which atoms from a target are knocked out under the bombardment of energetic ions. Sputtering can be quantitatively described by the sputtering yield (Y) [7] as:

$$Y = \frac{\text{Number of sputtered atoms}}{\text{Number of incident ions}} = \mathit{\Lambda} F_{\mathrm{D}} = \frac{\alpha N S_n(E)}{E_{\mathrm{B}}}. \tag{3.14}$$

Here, $\mathit{\Lambda}$ is a material-specific constant, F_{D} is the deposition of nuclear energy per unit length, α is the correction factor depending on the ratio of ion and target atomic masses, N, and E_{B} are the atomic density and surface binding energy of the target, respectively. The sputtering of light mass ions is independent of temperature, while the heavy-ion sputtering is highly influenced by the near melting temperature of the target [9]. The maximum value of the sputtering yield can be achieved by the bombardment of medium energy ions. However, higher energy ions can penetrate deeper into the target and less number of atoms are removed from the surface which result in lower sputtering yields. On the other hand, the sputtering yield is maximum when the mass of ions equals the mass of the target atoms. An empirical formula can be given for the sputtering yield (Y_{E}) as a function of the ion energy (E), as:

$$Y_{\mathrm{E}} = 0.42 \frac{\alpha_{\mathrm{s}} Q_{\mathrm{s}} S_{\mathrm{n}}(E)}{E_{\mathrm{B}}[1+0.35 E_{\mathrm{B}} S_{\mathrm{e}}(\varepsilon)]} \chi^{2.8}, \tag{3.15}$$

where $\chi = 1 - \sqrt{(E_{\mathrm{th}}/E)}$, Q_{s} and α_{s} are empirical parameters evaluated from experimental sputtering yield data, and E_{th} is the threshold energy for sputtering.

The angular sputtering yield (Y_{θ}) can be approximated in terms of sputtering yield for normally incident ions (Y_0) as:

$$\frac{Y_{\theta}}{Y_0} = (\cos\theta)^{-f}, \tag{3.16}$$

where f is a function of M_2/M_1 [7].

Equation 3.16 predicts that the sputtering yield increases with increasing angle of incidence θ (with respect to surface normal). However, the experimentally observed sputtering yield starts to deviate from the behavior predicted in Eq. 3.16 at very grazing angles of incidence where incident ions are mostly reflected from the target surface. An empirical relation has been provided by Yamamura *et al.* [10] to consider the deviation in the sputtering yield at grazing incidences:

$$Y_\theta = Y_0 \left(\frac{1}{\cos\theta}\right)^f \exp\left(-\Sigma\left(\frac{1}{\cos\theta} - 1\right)\right), \tag{3.17}$$

where f is an energy dependent function: $f = 1.85\left(1 + 1.25\left(\frac{1-\chi}{\chi}\right)\right)$ and $\Sigma = f \cos\theta_{opt}$.

θ_{opt} is the angle of ion incidence corresponding to the maximum sputtering yield. Eq. 3.17 provides a more realistic description of angular sputtering yield compared to the one obtained by using Eq. 3.16.

3.1.2 Continuum theory based simulation of self-organized pattern formation

Continuum theories or models can explain a variation involved in a continuous sequence in which neighbouring elements are correlated with each other without any abrupt change or discontinuity. At the same time, the extreme elements are quite distinct. For example, the space-time continuum model explains space and time as a part of the same continuum rather than as separate entities. A spectrum in physics (e.g. light) is often termed either as a continuous spectrum (energy at all wavelengths) or discrete spectrum (energy at only certain wavelengths). Continuum models of a surface can be described at lengths more than the atomic scale. A solid surface can be assumed as a continuum of points expressed by a surface height function h (x, y, t) in a laboratory frame, where x- and y-axes are parallel to the initial flat surface and z-axis is normal to the surface. On the basis of Sigmund's theory of ion sputtering [11] of an amorphous solid surface, Bradley and Harper (BH) introduced the continuum theory of pattern formation [3] upon ion bombardment in 1988. According to BH theory, for a slowly undulating surface, the sputtering yield depends on the local surface curvature which makes surface unstable. The ripple-like sinusoidal modulations yields from the competition between the curvature-dependent sputter erosion and smoothening of surfaces by relaxation processes which results in the growth of a range of sinusoidal perturbations on the surface. In the following section, we introduce the continuum theories to describe ion-induced surface evolution.

3.1.2.1 Sigmund's Theory of sputtering

Upon considering only physical sputtering process, the ion-bombardment of solid surfaces leads to increase in the surface roughness as a function of fluence. According to Sigmund, the sputtering yield is proportional to the deposited energy in elastic collisions for an amorphous material. Sigmund [11] showed that the nuclear stopping of ions is the dominant energy loss process in the lower ion energy regime and the spatial distribution of the ion energy deposition inside an amorphous solid is approximated by a Gaussian distribution, as is shown in Fig. 3.4. According to this, the average ion energy deposited at the point p' due to the elastic collision inside the target is expressed by:

$$E(r) = \frac{\varepsilon}{(2\pi)^{3/2}\sigma\mu^2}\exp\left[-\frac{(z'+a)^2}{2\sigma^2} - \frac{x'^2+y'^2}{2\mu^2}\right] \quad , \tag{3.18}$$

where $r'=(x', y', z')$ is the origin of the coordinate system considered at the ion impact point p', ε is the total energy deposition by the ion, and a is the average depth of the energy deposition. Here z' is measured along the direction of the incident ion trajectory, while x' and y' are measured perpendicular to the z' direction. As depicted in Fig. 3.4, the point O is considered as the maximum energy deposition at a distance a below the surface, where the width of the Gaussian distribution in the direction parallel and perpendicular to the incident ion beam are σ and μ. The sputtering yield at any surface point p can be expressed in terms of surface recession velocity (v) at point p which is proportional to the total energy deposited at point p by all ions incident on the surface:

$$v = p\int_{\Re}\phi(r')E(r')dr' \tag{3.19}$$

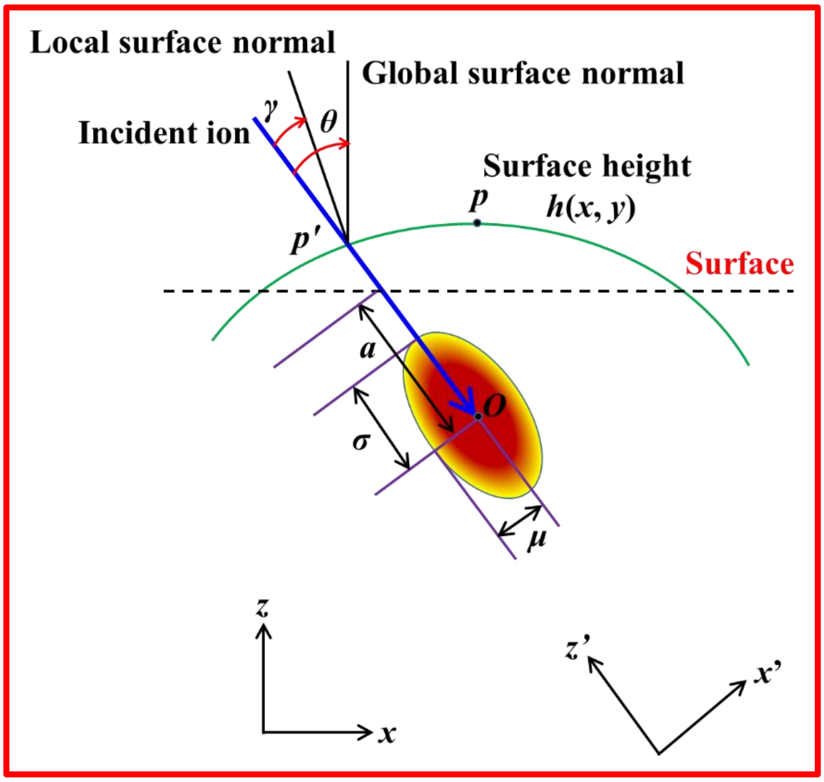

Figure 3.4: Schematic demonstration of Gaussian energy deposition of an incoming ion inside a target. θ: global angle of incidence; γ: local angle of incidence.

The integral extends over the region ($\mathfrak{R}$), where the impact of ions (anywhere on the surface) contributes significantly to the energy deposition at point p. Here, $\phi(r')$ is the ion flux corrected due to the difference between local angle of incidence γ and angle of incidence θ with respect to flat surface normal (z-direction). The proportionality constant p is the characteristic of the substrate and depends on the target atomic density N, surface binding energy U_0, and a constant C_0 related to the square of the radius of the effective potential due to the interaction of incident ion with target atom and is given by:

$$p = \frac{3}{4\pi} \frac{1}{NU_0C_0} \tag{3.20}$$

It is noteworthy that the curvature-dependent sputter erosion rate of target surfaces can be calculated using Eq. 3.19, which is discussed in the following section.

3.1.2.2 Bradley-Harper theory

A linear partial differential equation was derived by Bradley and Harper (BH) [3] using Eq. 3.19 which is able to describe the dynamics of a slowly undulating surfaces. It was considered that the radius of curvature (*R*) at any surface point is much larger compared to the mean depth of energy deposition (*a*), which was termed as the small slope approximation. Hence, in the laboratory coordinate system (*x*, *z*), one can express the surface height near the point *p* on the basis of small slope assumption as:

$$h(x) = -\frac{1}{2}\left(\frac{x^2}{R}\right) \quad , \tag{3.21}$$

where *R* is the radius of curvature of the surface. The surface evolution governed by linear partial differential equation can be expressed as:

$$\frac{\partial h}{\partial t} \cong -v_0 + \gamma\frac{\partial h}{\partial x} + \frac{fa}{N}Y_0(\theta)\left[\Gamma_1(\theta)\frac{\partial^2 h}{\partial x^2} + \Gamma_2(\theta)\frac{\partial^2 h}{\partial y^2}\right] - B\nabla^4 h. \tag{3.22}$$

The expressions for $\Gamma_1(\theta)$ and $\Gamma_2(\theta)$, used in Eq. 3.22, are written as:

$$\Gamma_1(\theta) = \frac{A}{B_1}sin\theta - \frac{B_2}{2B_1}\left(1+\frac{A^2}{B_1}\right)cos\theta - \frac{AC}{B_1^2}\left(3+\frac{A^2}{B_1}\right)cos\theta$$

and

$$\Gamma_2(\theta) = -\frac{\mu^2}{a^2}\left(\frac{B_2}{2}+\frac{AC}{B_1}\right)cos\theta, \tag{3.23}$$

where $A = \left(\frac{a}{\sigma}\right)^2 sin\theta,\ B_1 = \left(\frac{a}{\sigma}\right)^2 sin^2\theta + \left(\frac{a}{\mu}\right)^2 cos^2\theta, B_2 = \left(\frac{a}{\sigma}\right)^2 cos\theta,$

$C = \frac{1}{2}\left[\left(\frac{a}{\mu}\right)^2 - \left(\frac{a}{\sigma}\right)^2\right]sin\theta cos\theta$, and $D = \frac{1}{8}\left[\left(\frac{a}{\mu}sin\theta\right)^2 + \left(\frac{a}{\sigma}cos\theta\right)^2\right]$.

The curvature depends sputter erosion rate can be evaluated from Eq. 3.19 and 3.21 as:

$$v(\theta,R) \cong \frac{\mathrm{p}Efa}{\sqrt{2\pi\sigma\mu}}B_1^{-\frac{1}{2}}exp\left(-\frac{a^2}{2\sigma^2}+\frac{A^2}{2B_1}\right)\left[\cos\theta + \Gamma_1(\theta)\frac{a}{R}\right], \tag{3.24}$$

where *A*, B_1, and Γ_1 are the functions of angle of incidence *θ*, incident ion-flux *f*, *a*, *σ*, and *μ*. Let us now evaluate the sputtering yield of a flat surface by considering *R*=∞. In this case, the sputtering yield is $Y_0(\theta) = v(\theta, R{=}\infty)N/f \cos(\theta)$, where N is the target atomic density in the amorphous solid. Hence, Eq. 3.24 can be rewritten as:

$$Y_0(\theta) \cong \frac{\mathrm{p}Efa}{\sqrt{2\pi\sigma\mu}} B_1^{-\frac{1}{2}} exp\left(-\frac{a^2}{2\sigma^2}\right) exp\left(\frac{A^2}{2B_1}\right), \tag{3.25}$$

In the case of $\sigma>\mu$, parameters A and B_1 become increasing functions of the angle of incidence θ (which indicates that the sputtering yield of a flat surface), while $Y_0(\theta)$ also becomes an increasing function with angle of incidence. However, it is experimentally known that the sputtering yield begins to decrease when reflection of ions comes into picture after a critical angle θ. Equation 3.24 can be rewritten in terms of $Y_0(\theta)$ with the help of Eq. 3.25 as:

$$v(\theta, R) \cong \frac{f}{N} Y_0(\theta) \left[\cos\theta + \Gamma_1(\theta)\frac{a}{R}\right], \tag{3.26}$$

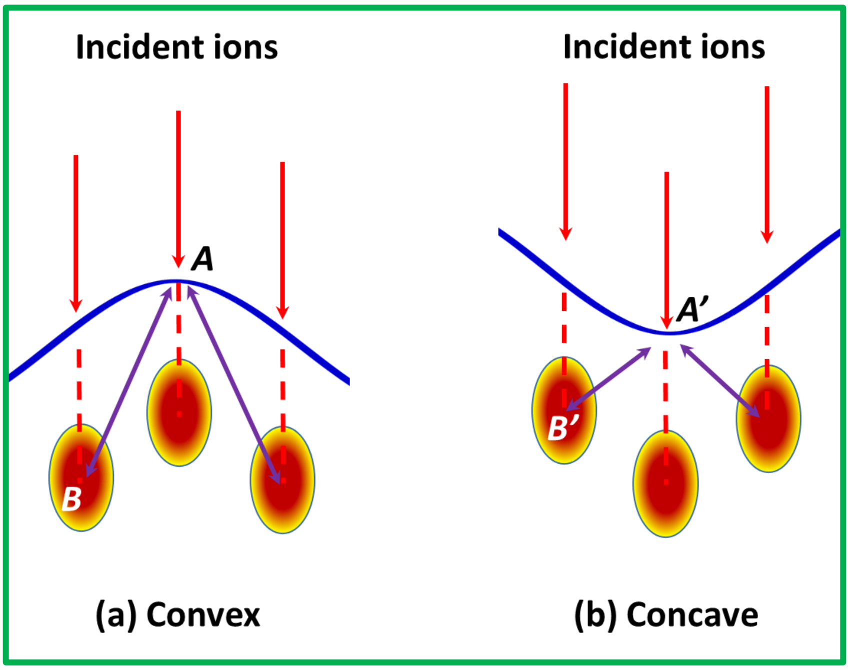

Figure 3.5: Schematic illustration of the origin of the curvature dependent sputtering induced by ion beam erosion of non-planar surfaces.

In Eq. 3.26, the term $a\Gamma_1(\theta)/R$ represents the curvature-dependent erosion velocity. At normal incidences ($\theta=0°$), $\Gamma_1(\theta)$ becomes negative. However, the radius of curvature (R) of the surfaces becomes negative in trough regions only. Therefore, Eq. 3.26 suggests that the velocity of erosion is greater in surface troughs than their crests and it can be concluded that under ion-bombardment, the valley parts of a surface will be eroded faster than their peaks. Thus, curvature dependent sputtering increases the amplitude of the perturbation and leads to a surface instability under bombardment of ions. The depth of the energy deposition by the incident ions is assumed to be constant for both the convex [Fig 3.5(a)] and concave [Fig 3.5(b)] surfaces. However, due to geometry of convex and concave surfaces, the distance $A'B'$ is smaller in case of a concave surface compared to the distance AB for a convex surface. Therefore, a higher amount of energy is deposited at point A' (the concave surface), leading to a greater erosion of the valleys compared to less energy deposition at A for the convex surface.

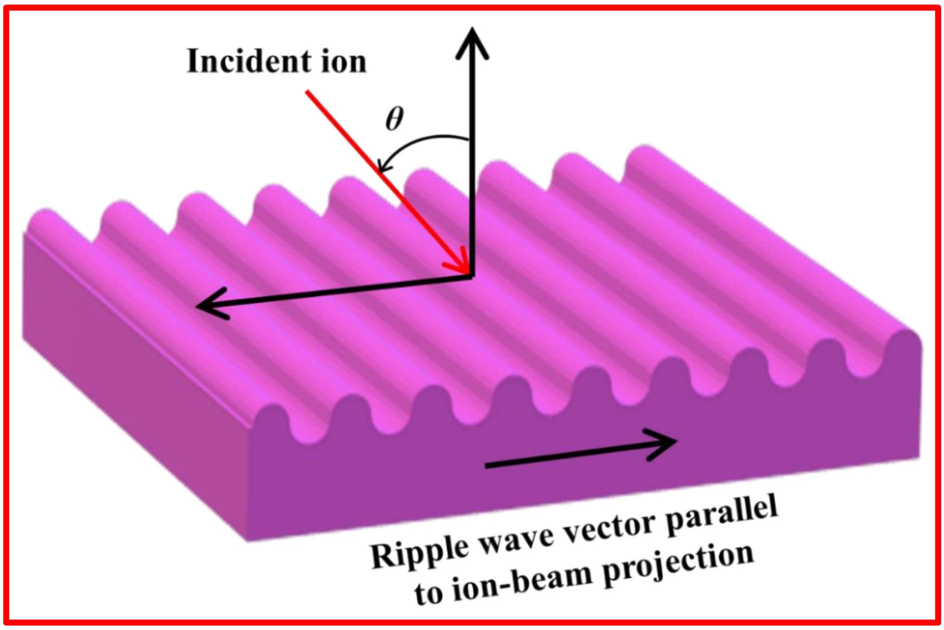

Figure 3.6: Schematic illustration of the parallel-mode ripples.

According to BH theory, the formation of periodically modulated structures like ripples are the consequence of two competing processes: one is the surface roughening due to curvature-dependent erosion rate and another is the thermally induced surface smoothing process. This theory can predict that below a critical angle (θ_c), parallel-mode ripples (wave vector of ripples parallel to the projection of ion-beam on the surface) are formed. However, ripples get rotated by 90° beyond the critical angle θ_c. A schematic of parallel-mode ripples is shown in Fig. 3.6. Due to reflection of ions at very grazing angles (close to 90º), BH model becomes inappropriate to describe the morphology of ion-bombarded surfaces.

Non-linear extension to BH theory

According to BH theory, when the slope of slowly undulating surfaces is small enough (small slope approximation), there is an exponential increase in the ripple amplitude under ion bombardment and therefore, the increased surface slopes become an important factor in the evolution of the surfaces, i.e. non-linear effects start to come into the picture. An extension of the BH theory, Makeev, Cuerno, and Barabási (MCB) [12] incorporated the effect of increasing surface slopes by considering higher order terms in the Taylor series expansion of surface height. The derived equation of surface height evolution can be represented as:

$$\frac{\partial h}{\partial t} \cong -v_0 + \gamma \frac{\partial h}{\partial x} + \nu_x \frac{\partial^2 h}{\partial x^2} + \nu_y \frac{\partial^2 h}{\partial y^2} - D^{\mathrm{T}} \nabla^4 h - D_{xx} \frac{\partial^4 h}{\partial x^4} - D_{yy} \frac{\partial^4 h}{\partial y^4} + \frac{\lambda_x}{2} \left(\frac{\partial h}{\partial x}\right)^2 + \frac{\lambda_y}{2} \left(\frac{\partial h}{\partial y}\right)^2 + \eta(x, y, t), \tag{3.27}$$

where, $\lambda_{\mathrm{x}} \left(\frac{\partial h}{\partial x}\right)^2$, $\lambda_{\mathrm{y}} \left(\frac{\partial h}{\partial y}\right)^2$ are the non-linear terms depending on slopes, D_{xx} and D_{yy} are ion induced effective surface diffusion terms along *x*- and *y*-direction, respectively, and $\eta(x, y, t)$ is added as a noise term to mimic the stochastic nature of ions on the surface. All the coefficients are functions of ion energy (ε), angle of incidence (θ), ion-flux (J), as well as a, σ, and μ except the thermal diffusion term $D^{\mathrm{T}} \nabla^4 h$ and the noise term η. These coefficients can be expressed as:

$$v_0 = Fc,$$

$$\gamma = F \frac{s}{f^2} \left[a_\sigma^2 a_\mu^2 c^2 (a_\sigma^2 - 1) - a_\sigma^4 s^2\right],$$

$$\nu_x = Fa \frac{a_\sigma^2}{2f^3} \left[2a_\sigma^2 s^4 - a_\sigma^4 a_\mu^2 c^2 s^2 + a_\sigma^2 a_\mu^2 c^2 s^2 - a_\mu^4 c^4\right],$$

$$\nu_y = -Fa \frac{c^2 a_\sigma^2}{2f},$$

$$D_{xx} = F \frac{a^3}{24 f^5} \left[-4(3a_\sigma^2 s^2 f + a_\sigma^6 s^4) f^2 + a_\sigma^2 c^2 (3f^2 + 6a_\sigma^4 s^2 f + a_\sigma^8 s^2) f + 2\left(a_\sigma^2 - a_\mu^2\right) c^2 (15 a_\sigma^2 f^2 s^2 + 10 a_\sigma^6 s^2 f + a_\sigma^{10} s^2)\right],$$

$$D_{yy} = F \frac{a^3}{24f^5} \frac{3a_\sigma^2}{a_\mu^2} (f^4 c^2),$$

$$\lambda_x = F \frac{c^2}{2f^4} \Big[a_\sigma^8 a_\mu^2 s^4 (3 + 2c^2) + 4a_\sigma^6 a_\mu^4 c^4 s^2 - a_\sigma^4 a_\mu^6 c^4 (1 + 2s^2)$$

$$- f^2 \left(2a_\sigma^2 s^2 - a_\sigma^2 a_\mu^2 (1 + 2s^2) \right) - a_\sigma^8 a_\mu^4 c^2 s^2 - f^4 \Big],$$

$$\lambda_y = \tfrac{c}{2f^2} \left[a_\sigma^4 s^2 - a_\sigma^2 a_\mu^2 c^2 - f^2 \right], \tag{3.28}$$

where,

$$F = \frac{J\epsilon p a}{\sigma\mu\sqrt{2\pi f}} e^{-a_\sigma^2 a_\mu^2 c^2 / 2f},$$

$$a_\sigma = a/\sigma, \;\; a_\mu = a/\mu, \;\; f = a_\sigma^2 s^2 + a_\mu^2 c^2, \;\; s = \sin\theta, \;\; c = \cos\theta.$$

The presence of nonlinear terms is the main difference between BH equation (Eq. 3.22) and MCB equation (Eq. 3.27). However, the analytic solutions of MCB equation is not possible due to the incorporation of these nonlinear terms. Therefore, numerical integration is the best solution of the same.

3.1.2.3 Carter-Vishniyakov Theory

According to BH theory, periodic ripple patterns can evolve for any off-normal incidence of an ion-beam. However, experimental results show that there is a critical angle of ion-incidence beyond which formation of ripples takes place. This critical angle varies between 45°-55° for Si substrates. Hence, to fill the gap between the theoretical predictions and experimental observations, Carter and Vishniyakov (CV) [13] introduced the ion-induced lateral mass redistribution as the reason behind the formation of these modulated topography. According to CV, the impact of energetic ions on surfaces leads to a displacement of the generated recoils, which on an average, is parallel to the initial direction of the incident beam. However, for off-normally incident ion-beams, the average displacement of the target atoms has a component parallel to the surface, which is parallel to the direction of ion-beam projection onto the surface.

Figure 3.7 presents a schematic diagram to demonstrate the CV mechanism where the incident ion lies in the plane parallel to the initial flat surface (*xz*) plane of the laboratory frame. However, in the local coordinate system, x'-axis is defined to be perpendicular to the local surface and *z*'-axis is perpendicular to *x*'.

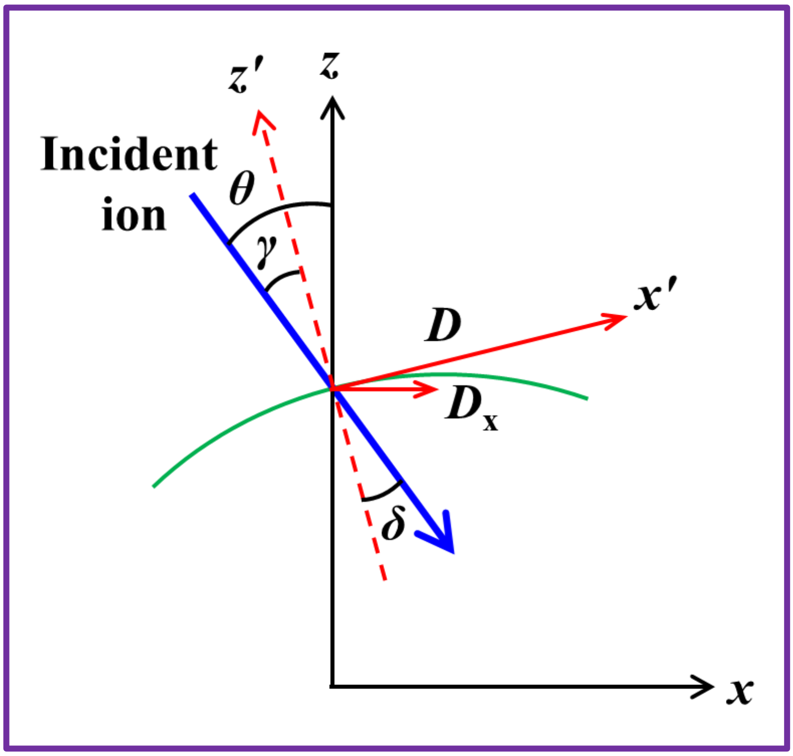

Figure 3.7: Schematic diagram of the laboratory coordinate frame (*x*, *z*) along with the local coordinate frame (x', z') to represent the CV mechanism. The local surface normal is represented by the unit vector z'.

The incident ion makes an angle θ and γ with the *z*- and z'-axis, respectively. The local misorientation of the surface can be represented as: $(\theta - \gamma) = \tan^{-1}(\partial h/\partial x) \approx \partial h/\partial x$. The recoil displacement vector can be defined as $\delta = f(E)d$, where *f(E)* is the total generated recoil atoms and the mean recoil displacement distance (*d*) is defined as the average movement of the recoils parallel to the ion-beam direction. However, the projection of δ on the surface is *D*. Moreover, under the present surface geometry, the normal component of the surface velocity is defined as: $v_n = -\cos(\theta - \gamma)\frac{\partial h}{\partial t}$. Therefore, with the above mentioned information, some identities can be obtained [14] as:

$$|D| = \delta \sin(\gamma)\,; \;\; D_{\mathrm{x}} = \delta \sin(\gamma)\cos(\gamma), \tag{3.28}$$

where Dx (component of D) is defined as the projection of δ along the x-axis. In addition to this, the projection of the ion flux along the x-axis can also be defined as $J_{\mathrm{x}}=J\cos(\gamma)/\cos(\theta-\gamma)$. Therefore, the net number of generated recoil displacements due to ion flux in the x-direction (J_{x}) is $J_{\mathrm{x}}\times D_{\mathrm{x}}$ and the equation of motion can be written as a continuum equation [15]:

$$\frac{\partial h}{\partial t} = -\frac{1}{N}\frac{\partial}{\partial x}(J_{\mathrm{x}}D_{\mathrm{x}}) = \frac{J\delta a \cos 2\theta}{N}\frac{\partial^2 h}{\partial x^2}. \tag{3.29}$$

Hence, the growth of surface height is also governed by the recoil displacements generated by the ion flux. The ion flux induced recoil displacements was first introduced by CV [13] and later elaborated by Madi *et al.* [4]. Hence, the effective surface tension term (coefficient of $\frac{\partial^2 h}{\partial x^2}$ term), which is responsible to evolve sinusoidal perturbations on materials surfaces, can be rewritten as the contribution from both BH and CV as:

$$\nu_{\mathrm{x}} = \frac{Ja}{N}[\delta \cos 2\theta + Y_0(\theta)\Gamma_1(\theta)] \tag{3.30}$$

where N is atomic density of the target. Hence, it is noteworthy that Eq. 3.30 includes the contribution of the recoil displacement and the sputter erosion as given by CV and BH, respectively. In addition to this, the magnitude of δ is higher than the sputtering yield $Y(\theta)$ by two or more orders of magnitude since the number of recoils generated [$f(E)$] and the energy deposition depth (a) also exceed the mean recoil displacement distance (d). Therefore, it can be concluded that the angle-dependent effective surface tension in y-direction (ν_{y}) will be similar to the one provided in Eq. 3.30.

As stated above, the incorporation of ion-induced lateral mass redistribution in the existing BH theory can explain the presence of critical angle above which ripple formation can take place. For ion bombardment at normal (θ=0°) and near-normal incidences, ν_{x} becomes positive and smoothening of surfaces dominates over roughening. As θ increases, the roughening term plays an increasingly important role and for some critical angle ($\theta=\theta_c$), ν_x becomes negative and roughening starts to dominate over surface smoothening.

3.1.2.4 Relaxation mechanisms

As discussed earlier, there are various relaxation processes to smooth out the surface features which get amplified during the roughening processes. There are various relaxation mechanisms depending on the experimental conditions such as substrate temperature, their crystallinity, and ion-beam parameters, etc. In this section, we will briefly introduce the possible relaxation processes applicable to the pattern formation during ion irradiation.

Thermal Diffusion: BH theory explains ripple formation by considering the interplay of curvature-dependent sputtering as roughening and thermal diffusion as smoothening parameter. There is a gradient in the chemical potential which urge the mass transport to wash out the ion-beam induced patterns on any amorphous surface. A simple description of the process can be provided by considering the variation in the surface profile, $h(x, y)$, only along the x-direction. When mass transport takes place for a random surface with varying curvature from 0 to R, the chemical potential can be expressed as $G = R\gamma\Omega$, where γ and Ω are the surface free energy per unit area and the atomic volume, respectively. Thus, due to the gradient in surface curvature, there will be a net drift of surface atoms with a surface current [16,17] given by:

$$j = \frac{D_S\gamma\Omega v}{k_BT}\frac{\partial R}{\partial s}, \tag{3.31}$$

where D_s is diffusivity of surfaces, v is the atomic areal density, k_B is Boltzmann constant, and s is the length of the arc along the profile. D_s shows an Arrhenius-type behaviour with temperature: $D_s \sim e^{-\Delta E/kt}$, where ΔE is the activation energy for the surface diffusion. The divergence of the surface current j is defined as the flow of atoms from unit area in unit time which can be rewritten in terms of surface height evolution by multiplying with the atomic volume (Ω):

$$\frac{\partial h}{\partial t} = -\Omega \frac{\partial j}{\partial s} = \frac{D_{\mathrm{S}} \gamma \Omega^2 \nu}{kT} \frac{\partial^2 R}{\partial s^2}. \tag{3.32}$$

Using small slope approximation: $R \sim -\frac{\partial^2 h}{\partial x^2}$ and $\partial s \sim \partial x$, Eq. 3.31 reduces to:

$$\frac{\partial h}{\partial t} = -D^{\mathrm{T}} \frac{\partial^4 h}{\partial x^4} = -D^{\mathrm{T}} \nabla^4 \mathrm{h}, \tag{3.33}$$

where $D^{\mathrm{T}} = \frac{D_{\mathrm{S}} \gamma \Omega \nu}{kT}$ is the surface diffusion constant. For a two-dimensionally varying surfaces, the Eq. 3.33 can be rewritten as:

$$\frac{\partial h}{\partial t} = -D^{\mathrm{T}} \left(\frac{\partial^4 h}{\partial x^4} + \frac{\partial^4 h}{\partial y^4} \right). \tag{3.34}$$

Effective surface diffusion (ESD): Makeev *et al.* [18] introduced the ion-induced effective surface diffusion as a reminiscent to surface diffusion which does not imply mass transport along the surface. The essence of ESD is the preferential erosion of surface hills faster than their valleys. Since the ESD does not depend on temperature, it can be successful in explaining the pattern formation at lower temperatures as well where thermal diffusion is negligible. Equation of motion can be expressed as:

$$\frac{\partial h}{\partial t} \cong -v_0 + \gamma \frac{\partial h}{\partial x} + \nu_x \frac{\partial^2 h}{\partial x^2} + \nu_y \frac{\partial^2 h}{\partial y^2} + \frac{\lambda_x}{2} \left(\frac{\partial h}{\partial x} \right)^2 + \frac{\lambda_y}{2} \left(\frac{\partial h}{\partial y} \right)^2 - D^I_{x_x} \frac{\partial^4 h}{\partial x^4} - D^I_y \frac{\partial^4 h}{\partial y^4}. \tag{3.35}$$

Here v_0 is the erosion rate, the second term accounts for uniform motion of the surface features along the *x*-direction, ν_x and ν_y represent ion-induced surface tension terms, λ_x and λ_y characterize the slope-dependence of the erosion rate, and D_x^I and D_y^I are ion-induced ESD coefficients. A fourth order expansion is used to obtain the ion-induced ESD constants D_x^I and D_y^I. While the calculations are performed for arbitrary σ and μ, to simplify the discussion we restrict ourselves to the symmetric case i.e. $\sigma = \mu$.

$$D_x^I = \frac{Fa^2}{24 a_\sigma} \{ a_\sigma^4 s^4 c^2 + a_\sigma^2 (6c^2 s^2 - 4s^4) + 3c^2 - 12s^2 \} \tag{3.36}$$

$$D_y^I = \frac{Fa^2}{24a_\sigma} 3c^2, \tag{3.37}$$

where,

$$F = \frac{J\epsilon p}{\sqrt{2\pi}} e^{\left(-a_\sigma^2/2 + a_\sigma^2 s^2/2\right)},$$

$$a_\sigma = a/\sigma\,, s = \sin\theta,\ and\ c = \cos\theta$$

The consequences of Eq. (3.36) and (3.37) can be summarized as follows:

A. If the system is viewed from a coordinate frame moving together with the average height of the surface, this preferential erosion appears as a re-organization of the surface corresponding to a surface diffusion like mechanism. ESD leads to relaxations which are different along *x*- and *y*-directions, implying an anisotropy in diffusion on the surface.

B. D_y^I is positive and independent of the sign of the angle of incidence. However, the sign of D_x^I depends on both *θ* and a_σ.Thus, while for *θ*=0°, ion bombardment enhances the surface diffusion in *x*-direction (since, $D_x^I > 0$). However, surface diffusion can be suppressed for large *θ* values.

C. Ion-enhanced diffusion can be defined in terms of effective temperature (T_{eff}) using the following relation:

$$D^I + D_0 e^{E_a/kT} = D_0 e^{E_a/kT_{eff}}. \tag{3.38}$$

3.1.3 Dynamic simulation studies behind self-organized silicon pattern formation

Rigorous and quantitative simulation of ion-matter interaction is essential not only to have an in-depth understanding on the topic, but also for the development of various applications of ion-beams in smoothening, treatment or sculpting of surfaces, etc. In this context, ion-beam induced self-organized pattern formation is of special interest. As discussed above, there are various competing smoothening and roughening processes which govern the pattern formation and their self-organization. Therefore, implementing the fundamentals of ion-solid interactions and gathering a vast and reliable informative data is the essence of a simulation studies. There are three popular Monte Carlo simulation programs named as SRIM [8], TRIDYN [19], and SDTrimSP [20,21], which are based on binary collision approximation. In the following sections, a brief introduction of these simulation programs is provided.

3.1.3.1 SRIM

SRIM (Stopping and Range of Ions in Matter) is a computer program which is used to calculate interaction of energetic ions with matter [8,20,22,23]. The core part of this program is TRIM (Transport of ions in matter) [8], which itself is a group of programs based on binary collision approximation to calculate the stopping and range of ions (10 eV – 2 GeV/amu) into matter (using a quantum mechanical treatment of collisions between energetic ions and target atoms). Some statistical algorithms are used to efficiently simulate the collisions in the presence of a screened Coulomb potential including exchange and correlation interactions between the overlapping electron shells. The charge state of the ions within the target is described by the concept of effective charge including a long range screening and velocity-dependent charge state due to the collective electron sea of the target.

It is used to calculate many features of the transport of energetic ions in matter. For example, it is capable to calculate energy loss of ions in matter and provides tables of stopping powers, range, and straggling distributions for any ion species in any target material. It is used to calculate most of the kinetic effects to simulate ion implantations such as damage statistics, doping profiles, etc. In case of sputtering process, it provides the sputtering yield of individual atomic species. TRIM accepts complex targets made of any compound materials with up to eight layers. It calculates both final 3D distribution of the ions and also all kinetic phenomena associated with the energy loss of ions such as target damage, sputtering, ionization, and phonon production. There are some limitations of this code that it does only static calculations, i.e. the damage or changes in the target made by previously irradiated ions are not considered upon bombardment of subsequent ions. In addition, ion-induced thermal diffusion, annealing, and damage are not implemented. Moreover, the effect of ion fluence is also not included in this program.

3.1.3.2 TRIDYN

TRIDYN code is used to simulate the dynamic changes in the thickness and/or composition of a multicomponent target during high-fluence ion implantation or ion-beam-assisted deposition [19,23]. It is based on TRIM code and makes use of the binary collision approximation (BCA) model for ballistic transport. This code can be used to simulate high fluence ion implantation, ion beam synthesis, sputtering and ion mixing of multicomponent atomic solids, and ion-beam or plasma-assisted etching. It computes the ballistic effects such as projectile deposition and reflection, sputtering, and ion mixing for a target, albeit radiation damage is not taken into account. Each simulated projectile (called pseudoprojectile) impinging on a surface represents a physical increment of incident ion fluence (number of incident ions per unit area). It provides versatile description of initially homogeneous as well as initially inhomogeneous or layered target, considering it to be amorphous and having maximum up to 5 different atomic species in the target and/or in the ion-beam with different ion-beam energies and angles of incidences.

TRIDYN allows to calculate the depth profiles of all atomic species in the target as a function of the incident fluence. Additionally, sputtering yields, total areal densities, surface concentrations, and re-emitted amounts are calculated as a function of ion fluence as well as the surface erosion under sputter conditions. It provides an option that allows to diffuse the interacting ions in the host matrix and after accumulating certain concentration it starts to re-emit the same. In this case, a simple diffusion procedure can be included along with ballistic transport of atoms. However, for non-reactive ions, re-emission of ion-species can be considered from the initial stages of the simulation. There are some limitations of this code that its lower energy limit is of the order of 10 eV due to binary collision approximation and it covers only non-thermal processes. In addition, this code is less suitable for energies in the MeV range (and above) as it does not consider the reduction in the collision frequency such as it is implemented in TRIM for higher energies. Nevertheless, it exhibits collisional processes with slightly lower characteristic energies, such as sputtering, are predicted quite accurately.

3.1.3.3 SDTrimSP

SDTrimSP [21,23] is a binary collision approximation based dynamic Monte Carlo simulation program which takes advantages of static capabilities of TRIM and dynamic mode of TRIDYN simulation codes to take advantages of both the programs. The binary collision approximation is used to handle the atomic (nuclear) collisions. This means the change in flight direction due to the collision is given by the asymptotes of the real trajectory. It assumes an amorphous target structure divided into layers with infinite lateral size and at zero temperature as shown in Fig. 3.8. SDTrimSP (where S stands for static and D for dynamic) can also work with dynamic targets. In the static mode, the target is kept perfect after the ion bombardment, while in the dynamic mode, the composition and thickness of target changes as more ions are incident on it by keeping the track of every single ion incident and all the target atoms displaced or sputtered due to this interaction. The atoms are distinguished in projectiles (incident atoms) and recoils (target atoms). For each traced atom the important physical quantities such as energy, spatial coordinates, and direction of motion are recorded along its path using general data structures. Moreover, the path length and the number of collisions are stored for the projectiles, while for the recoils the collision number in which they are generated is stored (generation). Besides the information about the single projectile there are also quantities integrated over all projectiles to save memory. For projectiles, the inelastic (electronic) energy loss and the total elastic and the elastic loss larger than the displacement energy are stored.

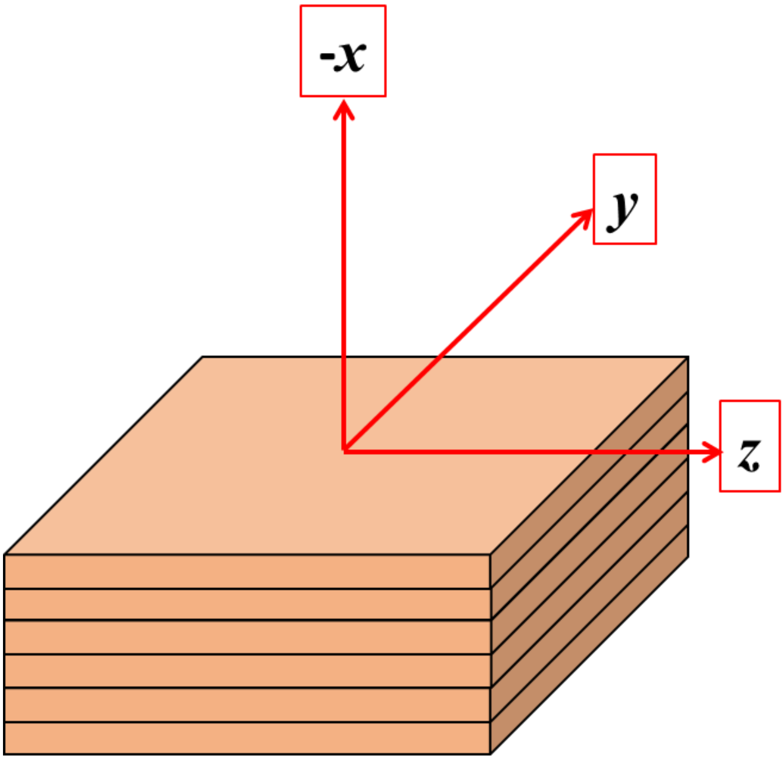

Figure 3.8: Geometry of the target and its axes representation.

Other values derived from these basic quantities can be determined according to the users' interests. SDTrimSP program can provide trajectories of projectiles and their respective recoils, angular distribution of scattered and sputtered atoms, backscattering coefficient, sputtering yield and atomic fraction, dynamic changes of the target composition, etc. In addition, ion fluence can be defined during the SDTrimSP run and hence, fluence-dependent changes in different physical parameters can be studied with good accuracy. Temperature, which is an important parameter to drive the ion-beam interaction in different direction, is also defined in this program to take care of ion-beam induced thermal diffusion and annealing effects along with thermal energy externally supplied to target (substrate temperature) also.

Now, we briefly describe the SDTrimSP simulation performed for 500 eV Ar-ion bombardment at several angles of incidence on the silicon surface. This simulation needs an input file named "tri.inp", where different ion-matter combinations and their relevant parameters can be defined. In the present case, we use ion-energy ($e0$) = 500 eV, total number of projectile (*nh*) = 50000, and ion-fluence (*flc*) = 50 (in units of 1×10^{16} ions/cm^2). A Linux shell script is written to vary the angle of ion incidence (*alpha*0) from 0^o to 85^o in the input file. The cut-off energy (*e_cutoff*) of all the components is chosen as 1 eV for limited generation of the recoils atoms. The bulk binding energy (*e_bulkb*) is related to the energy required for vacancy generation and it is applicable for crystalline targets only and is therefore considered to be zero. The surface binding energy (*e_surfb*) is mainly dependent on the local surface composition and for Si it is found to be 4.72 eV from the tables of the SDTrimSP code. The minimum ion-energy needed for the displacement of atoms is called the displacement energy. In this simulation, displacement energy (*e_displ*) of Ar and Si is taken to be 10 eV for each. After completion of SDTrimSP run, a huge informative data corresponding to sputtered, backscattered, stopped, transmitted projectiles, and recoils along with their areal density, surface composition, and energetics are generated. Some of the important results are discussed in the following sections:

Sputtering yield: It is straightforward to extract sputtering yield from the SDTrimSP output data file, "backsputt_f_31.dat", which provides the ion-fluence dependent sputtering rate of individual component and therefore, the angular sputtering yield can be extracted for a desired fluence (≤ input/maximum fluence) from SDTrimSP data corresponding to each incident angle. As shown in Fig. 3.9(a), the sputtering yield of Ar decreases with increasing angle of incidence, which is quite expected due to dominating momentum of recoiled ions parallel to surface over normal to the surface component. On the other hand, sputtering yield of Si increases monotonically for lower angles of incidence and achieves its maximum value at ~70^o and further starts to decrease for even higher angles of incidence. The observed sputtering yield of Si can be attributed to the momentum transferred to target atoms. In fact, upon increasing the angle of incidence, the component of momentum transfer parallel to the surface dominates over the one which is normal to the surface and therefore, near surface atoms get sufficient energy to overcome the surface binding energy and knocked out from the surface. However, at very glancing angles (> 85º), reflection of ions starts to come into picture.

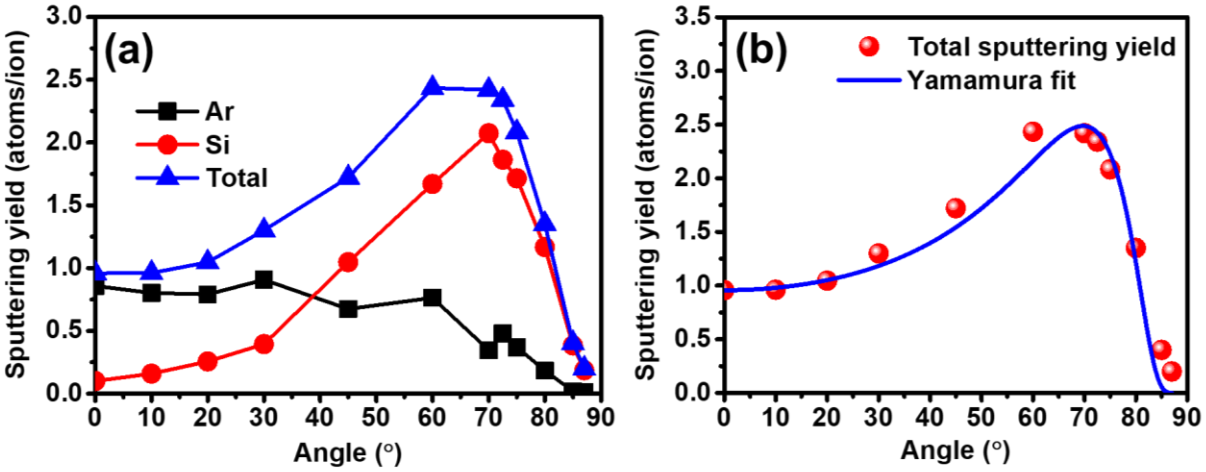

Figure 3.9: (a) Angular sputtering yields of Ar and Si and (b) total sputtering yield with Yamamura fitting for 500 eV Ar-ion bombardment on a Si surface.

Displacements per atom: Basically, displacement per atom (DPA) is defined as the ratio of the total number of knock-on atoms by total number of incident ions. It is an important parameter to characterize the interaction of ions with a matter. The DPA can be extracted from the file "output.dat", where total knock-on atoms having their energy more than the displacement energy is mentioned along with total incident projectiles. The DPA is extracted for each angle and is depicted in Fig. 3.10.

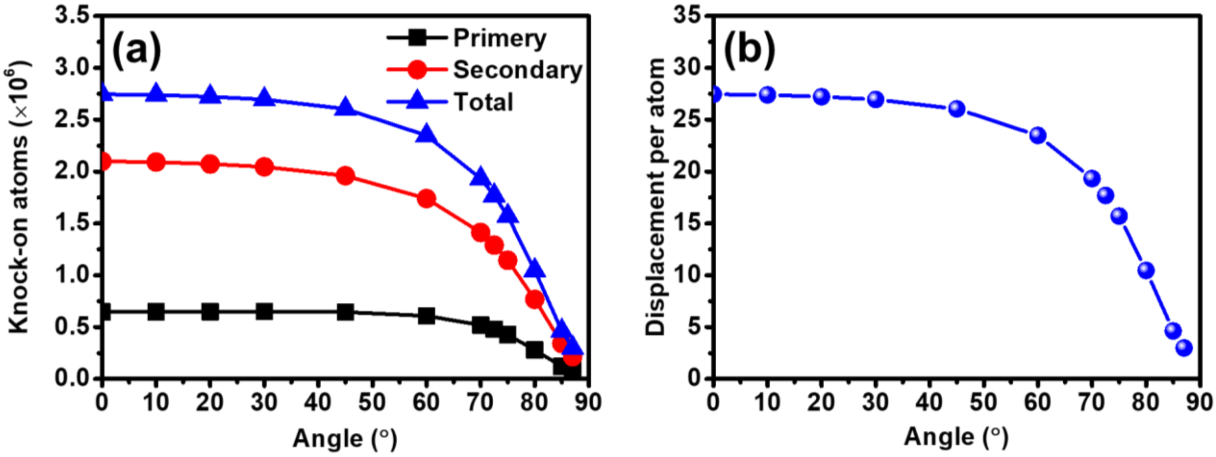

Figure 3.10: (a) Angle-dependent primary and secondary knock-on atoms and (b) displacement per atom (DPA) for 500 eV Ar-ion impact on a Si surface.

Range and straggling: The axis representation of SDTrimSP in Fig. 3.8 depicts that thickness of the target is along the *x*-axis, however *y*- and *z*-axis represents the surface plane of the target. Hence, the projected range (R_p) and longitudinal straggling (σ) can be calculated using the *x*-coordinates of recoiled particles i.e. "x_end" data of "partic_stop_r.dat" file. The peak value and FWHM for the Gaussian fitting of frequency counted "x_end" data are equivalent to the range and longitudinal straggling of ions.

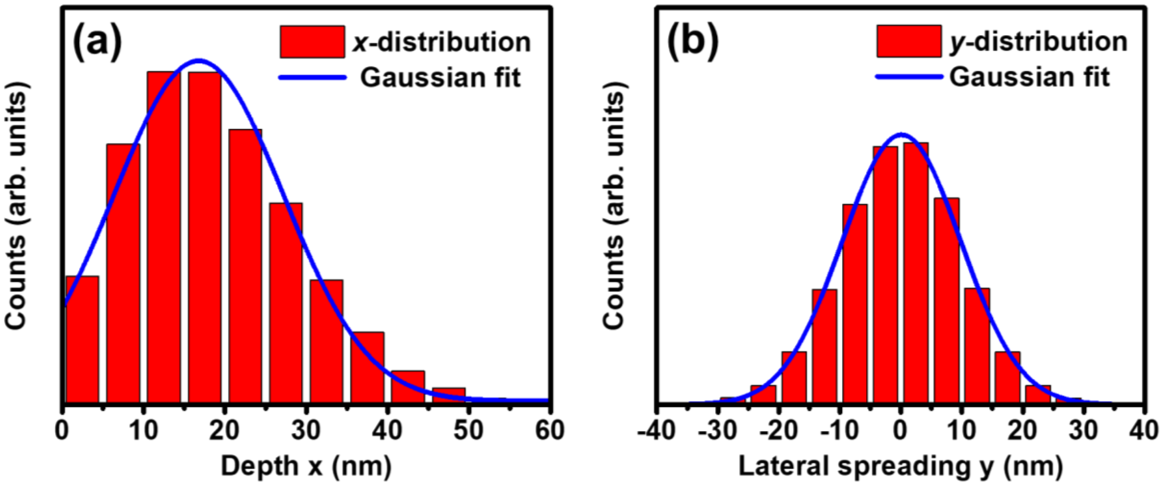

Figure 3.11: Gaussian fitting for recoils in *x*- and *y*-directions for estimation of ion-range, longitudinal, and lateral straggling.

However, the lateral straggling (μ) can be estimated from FWHM of the Gaussian fit of frequency counted "y_end" or "z_end" data. As presented in Fig. 3.11, The Gaussian fits for R_p, σ, and μ of 500 eV Ar-ions in a Si target are provide values of 1.68, 0.52, and 0.48 nm, respectively. In addition to this, longitudinal recoil displacement (δ) can be expressed as: $\delta = N_D(E > E_D)\frac{\sum_i \left|x_{end}^i - x_{start}^i\right|}{\sum_i (i)}$, where N_D ($E > E_D$) is the number of knock-on atoms (including primary and secondary) having energy more than their displacement energy (E_D) provided as an input in SDTrimSP simulation. Thus, δ can be extracted by taking the average of absolute difference between "x_end" and "x_start" columns and multiplying it with the number of knock-on atoms having energy more than their displacement energy. For 500 eV Ar-ion bombardment on Si, δ is found to be 7 nm.

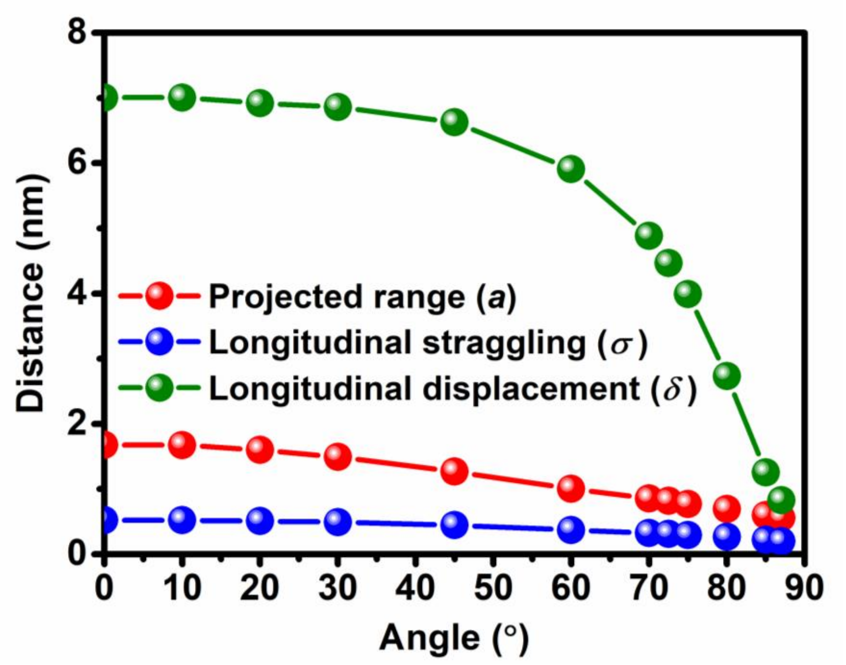

Figure 3.12: Angle-dependent projected range (a), longitudinal straggling (σ), and longitudinal displacement (δ) extracted from SDTrimSP simulation.

Sputtering coefficients: As discussed in sections 3.1.2.2 and 3.1.2.3, the effective coefficients of sputtering can be described as the contribution from ion-beam induced erosion (BH term) and atomic mass redistribution (CV term) of surfaces. These sputtering coefficients can be calculated using different parameters (viz. a, σ, δ, etc.) extracted from SDTrimSP data analysis. Moreover, the value of μ is considered to be half of the longitudinal straggling (σ). In this process, $Y(\theta)$ is the angular sputtering yield extracted (corresponding to the maximum ion-fluence) from the SDTrimSP output data file "backsputt_f_31.dat" for each angle. The angle corresponding to maximum sputtering yield, $\theta_{th} = \theta_{Y \rightarrow max}$ can be obtained by fitting $Y(\theta)$ with Yamamura equation (Eq. 1.17). The longitudinal recoil displacement (δ) can be calculated by multiplying the displacement per atom (DPA) value and average longitudinal mass transport distance per ion. DPA is the ratio of total knock-on atoms (having their energy more than the displacement energy) with total incident projectiles extracted from "output.dat" file.

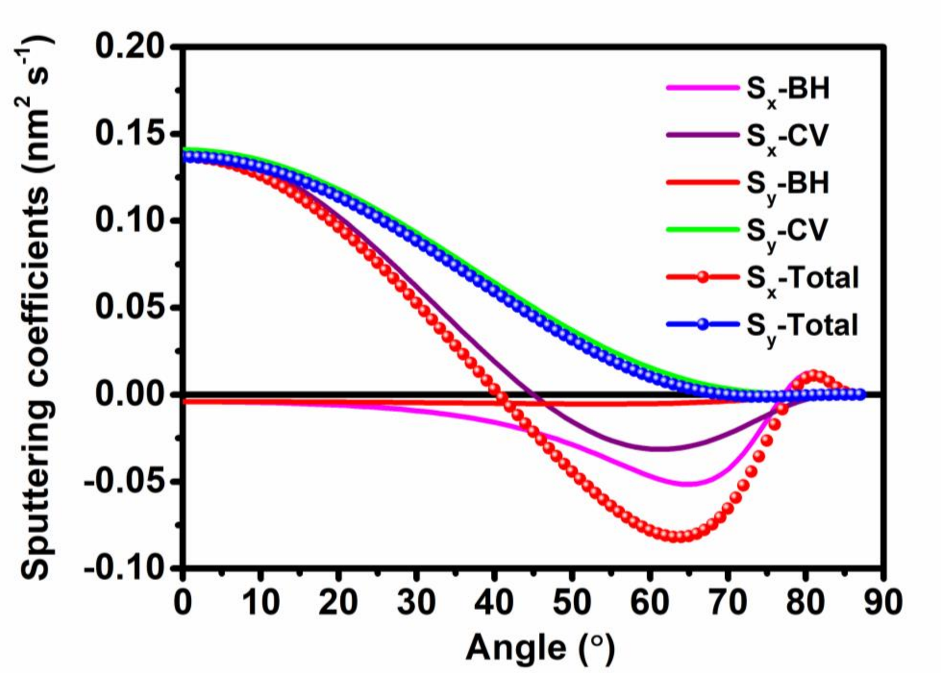

Figure 3.13: Sputtering coefficients including the sputter erosion (BH-term) and mass redistribution (CV-term) along the *x*- and *y*-directions.

The average longitudinal mass transport distance per ion is the average of the absolute differences between "*x_start*" and "*x_end*" columns extracted from "*partic_stop_r.dat*" file. The sputtering coefficients (BH and CV term) as a function of ion-beam incidence angle for 500 eV Ar-ions on a Si surface are presented in Fig. 3.13. Few inferences can be made on the basis of the sputtering coefficients calculated using the SDTrimSP code which are briefly described below.

3.1.3.4 Nanoscale ripples formation

According to the experimental findings on 500 eV Ar-ion irradiation on Si substrates, there is no pattern formation up to θ=50°, parallel-mode ripples emerge in the range of $51° \leq \theta < 80°$, rotation of ripples from parallel-mode to perpendicular-mode takes place for $80° \leq \theta < 82.5°$, and finally flat surface appears at very grazing angles (θ>82.5°) [24]. These experimental results are explained in light of both BH theory and CV model (explained earlier in sections 3.1.2.2 and 3.1.2.3) by supplying essential parameters as input from SDTrimSP simulation.

In this quest, it is observed that the S_x-BH remains negative [Fig. 3.13] for an angular range of $0° \leq \theta < 77°$ with $|S_x\text{-BH}| > |S_y\text{-BH}|$, which suggests that if BH model is applicable alone then parallel-mode ripples should evolve up to 77° and beyond this angle perpendicular-mode ripples should appear. On the other hand, S_x-CV remains negative for $\theta \geq 46°$ with $|S_x\text{-CV}| > |S_y\text{-CV}|$, which indicates that if CV model is operative alone then parallel-mode ripples are present for more than 46° angle of ion-incidence and no perpendicular-mode ripples should appear since S_y-CV remains always positive. BH theory predicts the ripple formation at any off-normal incidence, although experimental observations show that there is a critical angle above which ripple pattern starts to emerge. Thus, it cannot explain the experimentally observed results on the basis of curvature dependent sputtering alone. On the other hand, CV model suggests only parallel mode ripple formation till θ=90°, which is also not observed in experiments. Thus, CV model is also unable to explain all the experimental findings alone. However, synergetic effects of curvature dependent sputtering (BH theory) and ion-induced atomic mass redistribution (CV model) can predict the angular window of pattern formation and the angle for ripple rotation. In this quest, a composite model of BH and CV predicts that both S_x-Total and S_y-Total remain positive up to an angle of $\theta < 40.5°$, revealing no pattern formation in this angular window and the S_x-Total remains negative for an angular window of $40.5° \leq \theta < 77°$ leading to parallel-mode ripple formation along with a transition from parallel- to perpendicular-mode ripples beyond an incidence angle of 77°. Hence, it is found that the synergetic effects of BH and CV predicts the critical angle for pattern formation and ripple-rotation to be 40.5° and 77° (while it is observed experimentally to be 51° and 80°), respectively. This difference may be attributed to an underestimation of the erosive contribution from Sigmund's ellipsoidal energy distribution-based BH theory (compared to CV model). To some extent, it can compensate for missing thickness-dependent contribution from a stabilizing layer.

3.1.3.5 Nanoscale facets formation

It is observed experimentally that 500 eV Ar-ion bombardment on Si surfaces leads to the formation of nanoscale cone-like structures in a narrow angular window of 70°-75°. This is in fact, a transition angle from parallel-mode ripples to nanoscale faceted structures.

Ion-beam shadowing effect

It is predicted from the BH theory that the amplitude of ripple patterns (developed on the surface with sputtering) increases exponentially under oblique angle incidences of the ion-beam on surface. Apart from the inception of nonlinear effects, an exponential increase in the ripple amplitude gives rise to a situation where ion-beams are prohibited to irradiate the upstream face of a ripple by the foregoing ripple peak. This phenomenon is called *ion-beam shadowing* effect, which can be understood from the geometrical argument proposed by Carter [25]. Figure 3.14 presents a schematic diagram to illustrate Carter's argument in *xz* surface plane described by $h = h_0 \cos(2\pi x/\lambda)$, where h_0 is the ripple amplitude and λ is the ripple wavelength. The incidence angle of ion-beam on the surface is θ with respect to the normal to the mean surface plane. The gradient of surface slope is defined by $tan(\alpha)=\partial h/\partial x$, where α is angle between local surface normal (z') and the z-axis. It is interesting to note that when the ratio of ripple amplitude and ripple wavelength, h_0/λ, increases, the maximum gradient of the sinusoidal ripple pattern, $2\pi x/\lambda$, becomes too large. As a consequence, the local angle of ion-beam incidence (θ-α) decreases which ultimately reaches to a limiting condition for incident ion-beam parallel to the back slope of the ripple pattern. However, a further increase in the h_0/λ ratio leads to the shadowing of upstream part of the ripples from the incident ion-beam due to the preceding sinusoidal peak. The limiting condition for non-shadowing regime is expressed by:

$$tan\left(\frac{\pi}{2} - \theta\right) \geq \frac{2\pi h_0}{\lambda}. \qquad (3.39)$$

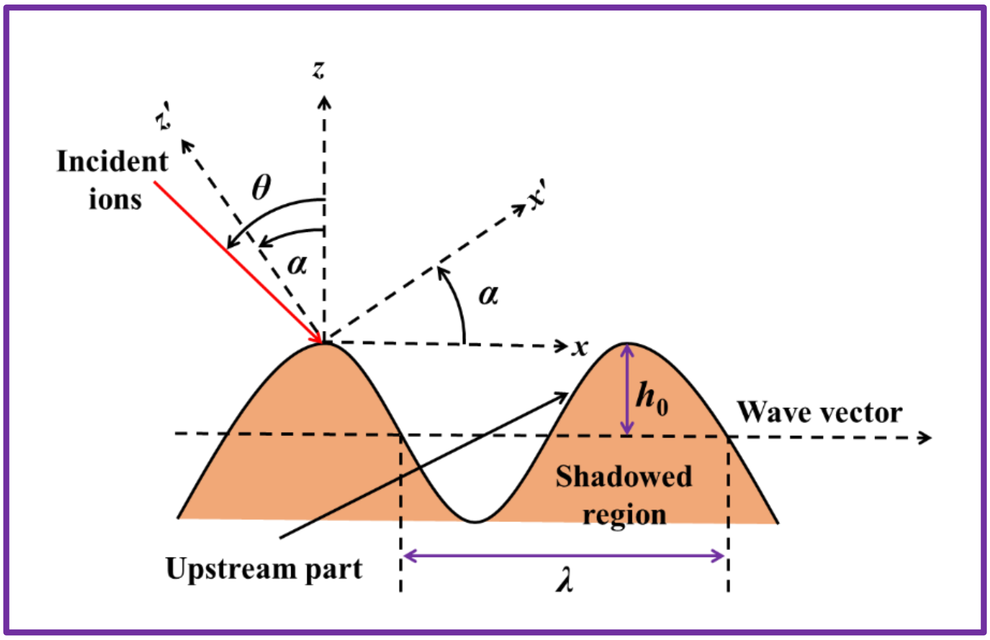

Figure 3.14: Illustration of geometry for ion bombardment on a sinusoidal profile.

This condition poses an upper limit on the ratio h_0/λ for any angle of ion incidence θ. According to this condition, ripple crests are eroded by ion-beams, but not their valleys and hence, it is expected to see a transition from ripples to a sawtooth-like waveform for prolonged ion sputtering.

3.2 Growth kinetics of thin films and nanoparticles

3.2.1 Thin film growth modes

Deposition of thin films is basically condensation of impinging particles (atoms or molecules) on host matrix of atoms (substrate). The mutual interaction of particles in a system is governed by thermodynamics which is the most common macroscopic approach to study the physics of thin films. Indeed, the macroscopic shape and orientation of a particular type of surface or interface of a solid are governed by some rules imposed by thermodynamics. In thermodynamic equilibrium, all the processes should occur in opposite direction with equal rate to satisfy the principle of detailed balance. However, growth of thin films is a non-equilibrium kinetic process where the rate of particle condensation is always higher than the re-evaporation of the same. From the kinetic theory of gases, the growth of thin films is described by the condensation of materials with an impinging rate $r = p(2\pi M k_B T_0)^{-1/2}$, where p is the vapour pressure, M is the molecular weight of the evaporating species, k_B is Boltzmann's constant, and T_0 is the source temperature. A particle condensed from the vapour phase has a finite probability to immediately re-evaporate or diffuse along the surface. However, diffusion processes have some adsorption probability mostly at special sites like defects or edges. Moreover, there is a chance of nucleation of two or more adsorbed particles. The successive nucleation of particles leads to the formation of islands and thereafter forms a thin film for prolonged nucleation. During the growth of a thin film, interdiffusion of particles with substrate is also an important process which results in a smooth film-substrate interface. In addition, a sufficiently high surface mobility of diffusing species can be achieved at elevated temperatures to obtain smooth film surfaces during the growth of thin films. To realize all these processes, particles have to overcome the characteristic activation energies. The fraction of total impinging particles being able to participate in a particular process is described by an Arrhenius-type exponential law: $\nu \propto \exp(E_a/k_B T)$ where E_a is the activation energy for desorption.

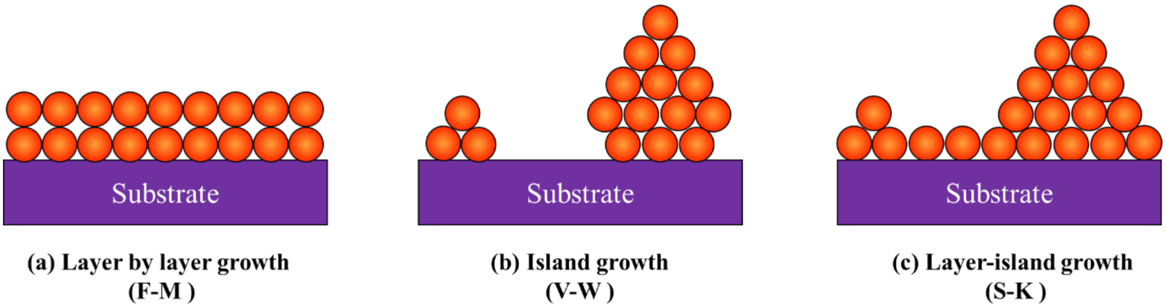

Figure 3.15: Schematics of different growth modes: (a) layer by layer growth, (b) island growth, and (c) layer plus island growth.

Hence, it can be inferred that surface/interface energy, lattice constant, and substrate temperature are crucial for the growth of thin films. In the case of hetero-epitaxial systems, the nucleation of particles depends critically on the interaction strength between adatoms and the surface, which is strongly influenced by the surface free energy of the substrate (γ_s), the free energy of film (γ_f), and the interfacial energy (γ_i). On the basis of surface energy, growth of thin films is phenomenologically classified into three main growth modes [26,27] as shown in Fig. 3.15. In the Volmer-Weber (V-W) growth mode [28], small clusters start nucleating directly on the substrate surface and work as seed to subsequently grow into islands of the condensed phase.

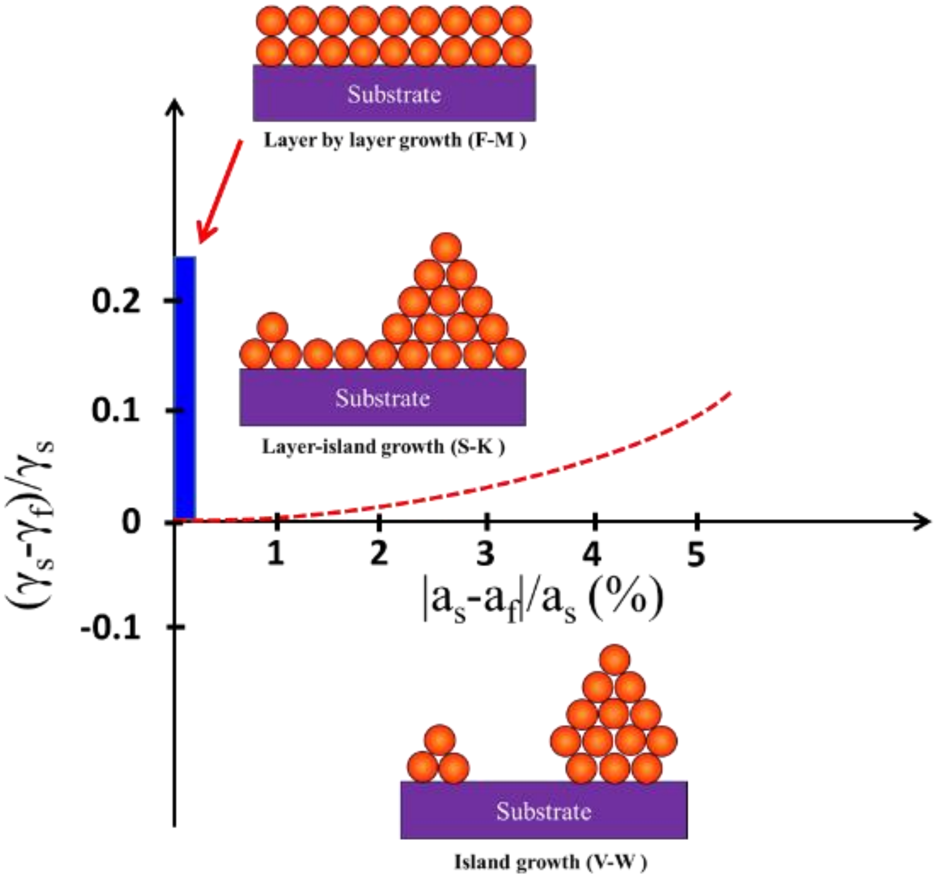

Figure 3.16: Surface energy-lattice misfit plot and regions for different growth modes.

The island or V-W growth mode appears when the adatoms (or molecules) are more strongly bound to each other than to the substrate ($\gamma_i + \gamma_f > \gamma_s$). This mode is exhibited by the growth of metals on insulators, alkali halides, graphite, and layered compounds [29,30].

Another growth mode is the layer-by-layer one or Frank-van der Merwe (F-M) growth mode [31], which exhibits the opposite characteristics of V-W growth. In this mode, atoms are more strongly bound to the substrate than to each other ($\gamma_i + \gamma_f < \gamma_s$) and adatoms attach preferentially to surface sites resulting in atomically smooth and fully formed layers. This layer-by-layer growth is two-dimensional, indicating that complete films form prior to the growth of subsequent layers. It is observed in several rare gases on graphite or metals, in some metal-metal systems, and in semiconductor growth on semiconductors [29,30]. The third growth mode is the Stranski-Krastanov (S-K) growth mode which is an intermediate one of V-W and F-M growth modes. In this mode, first the adatoms condense in layer-by-layer growth mode. However, after forming the first few monolayers, the layer-by-layer growth becomes unfavourable and it switches to island growth on top of the subsequent layers. The lattice strain is responsible for the change in surface energies during the deposition of films. In fact, strain relaxation can take place at the step edges of a strained system. Atoms at the edges are displaced from their positions and maintain the bulk-like atomic separation at the edges and corners of the islands. Hence, the nucleation of the subsequent layers often take place at the edges and corners, which results in S-K growth mode [32]. The trade-off between strain and surface energies is a microscopic concept. The thin film growth modes can be identified by plotting the surface energy ratio $\left(\gamma_s - \gamma_f/\gamma_s\right)$ and lattice mismatch $\left(|a_s - a_f|/a_s\right)$ as depicted in Fig. 3.16.

3.2.2 Nucleation and coalescence

Like other natural processes, phase transformation of matter takes place following the easiest path governed by thermodynamics [33]. A phase of matter is characterized by its entropy, volume, and composition. The supersaturation is the driving force for phase transformation which corresponds to the favourable balance in Gibbs energy [33]. However, a system needs to overcome the energy barriers to transform into a new phase. This is the process flow involved in the formation of thin films [Fig. 3.17]:

- **Old phase**: Thermal accommodation of vapour atoms

- **Nucleation**: Binding on the substrate surface
- **Growth aggregation**: Surface diffusion and cluster formation
- **Coalescence**: Growth of islands
- **New phase**: Growth of continuous film

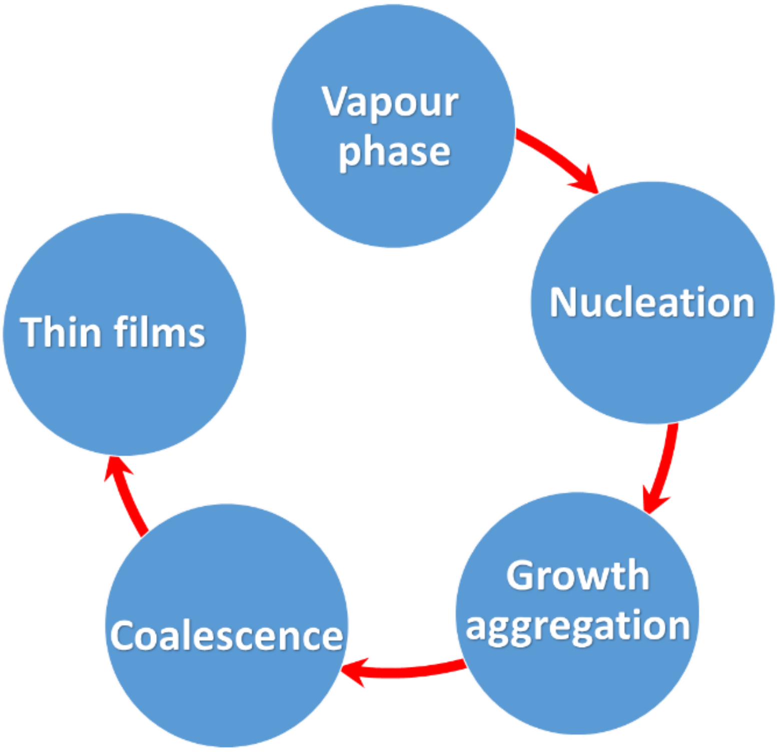

Figure 3.17: The process flow of phase transformation from vapour phase to growth of nanoparticles and thin films.

Nucleation is the primary stochastic process for a material to condense which is defined as the process by which extremely small (nanoscale) aggregates of the new phase are formed irreversibly. Nucleated clusters can then start to form in old phase as well as surface of the substrate. After the substrate is completely covered with particles, no further nucleation occurs. Islands grow by incorporation of adatoms diffusing across the substrate. Particularly, the stage where islands grow together is of prime interest. The islands minimize their surface energy by changing the shape mainly to single cap-shaped aggregates especially when they are still very small. The coalescing islands show a behaviour similar to liquid droplets. After the island get a proper form, the grain boundary separating it with the former ones is able to move. In contrast, paths with energetically less favourable orientations are swallowed. Finally many islands have grown together giving a coverage of the substrate which changes to a continuous film by taking up further atoms.

3.3 Statistical characterizations of surfaces

While analyzing randomly rough surfaces, we often require a statistical approach to determine some set of representative quantities. In a continuum description, the surface height at a given point (x, y) can be described by a height function $h(r) \equiv h(x, y)$ in a fixed frame of reference. The nature of the surface can be characterized using some statistical parameters which may be defined as a variation in height function $h(r)$ as described below:

Average surface roughness

The basic characterization of a surface can be described by average or mean surface height $\bar{h}$. In a surface area of dimension $L\times L$, it can be defined as:

$$\bar{h} = \frac{1}{L^2}\int_{-L/2}^{L/2}\int_{-L/2}^{L/2} h(x,y)dxdy. \tag{3.40}$$

RMS Roughness

The fluctuations in the surface height with respect to the mean surface height can be described by the rms (root mean square) roughness w, which is defined as:

$$w = \frac{1}{L}\left[\int_{-L/2}^{L/2}\int_{-L/2}^{L/2}[h(x,y)-\bar{h}]^2 dxdy\right]^{\frac{1}{2}}. \tag{3.41}$$

Correlation functions and correlation length

The spatial correlation of distinct surface points can be determined by the height-height correlation (autocorrelation) function where the maximum distance up to which height of two surface points is considered to be correlated, is called as the *correlation length*.

Autocorrelation

The autocorrelation function *R(r)* can be defined as:

$$R(r) = \frac{1}{w^2}\frac{1}{L^2}\int_{-L/2}^{L/2}\int_{-L/2}^{L/2}\left[\{h(x,y)-\bar{h}\}\{h(x+x',y+y')-\bar{h}\}\right]dxdy. \tag{3.42}$$

Here the spatial separation between two arbitrary surface points $r_1 = (x, y)$ and $r_2 = (x+x', y+y')$ is represented by r. For a truly random rough surface, $R(r)$ decays to zero with increasing r. However, the decay rate depends on the randomness of the surface. Moreover, the lateral correlation length (ξ) is defined as a length scale over which the magnitude of $R(r)$ decreases to $1/e$ of its value at $r=0$, i.e, $R(\xi)=(1/e)R(0)$. Two surface points are considered to be correlated if the distance r between two surface points is within lateral correlation length $r < \xi$ otherwise they are independent of each other.

Power spectrum

So far we have discussed the statistical characterizations of a rough surface in the real space. However, Fourier transformations can be used to visualize the collective behaviour of the surface in reciprocal space by defining power spectrum or structure factor of the surface. Power spectrum, $S(k)$, is the square of the Fourier transformation of the surface height profile, $h(x, y)$ and it can be expressed as:

$$S(k) = \frac{1}{L^2}\left|\int_{-L/2}^{L/2}\int_{-L/2}^{L/2}\left[\{h(x+x',y+y')-h(x,y)\}e^{-i(k_x x+k_y y)}\right]dxdy\right|^2. \tag{3.43}$$

If the surface height fluctuation is periodic with a repetition length, l, then the periodicity is reflected in the power spectrum $S(k)$ as a peak at the wave number $k = 2\pi/l$.

Measurement of ripple wavelength using AFM images

The autocorrelation image is the two-dimensional autocorrelation function defined by Eq. 3.42. For an ion-beam patterned rippled-Si substrate, the ripple wavelength is determined from the autocorrelation image of the AFM micrographs which shows bright strips (similar intensity) on both the sides of a central bright strip (maximum intensity). In fact, the distance between any of two side bright regions to the central bright region gives the wavelength of the ripple pattern [34].

Surface bearing area curve

Surface bearing area (Abbott) curves are basically defined as the accumulation of height distribution histogram of surface nanostructures along with the percentage of area covered by the same [35]. This curve can be obtained by plotting the successive height of nanostructure against the integrated cross-sectional area of the same that lies within the plane drawn at successive heights.

Bibliography

[1] M. Navez, C. Sella, D. Chaperot, CR Académie Des Sci. . Paris. 254 (1962) 240–243.

[2] W.L. Chan, E. Chason, J. Appl. Phys. 101 (2007) 1–46.

[3] R.M. Bradley, J.M.E. Harper, J. Vac. Sci. Technol. A Vacuum, Surfaces, Film. 6 (1988) 2390–2395.

[4] C.S. Madi, E. Anzenberg, K.F. Ludwig, M.J. Aziz, Phys. Rev. Lett. 106 (2011) 1–4.

[5] T. Basu, D.P. Datta, T. Som, Nanoscale Res. Lett. 8 (2013) 289.

[6] T. Lohner, E. Kótai, N.Q. Khánh, Z. Tóth, M. Fried, K. Vedam, N. V. Nguyen, L.J. Hanekamp, A. van Silfhout, Nucl. Inst. Methods Phys. Res. B 85 (1994) 335–339.

[7] M. Nastasi, J. Mayer, J.K. Hirvonen, Ion–Solid Interactions, Cambridge University Press, Cambridge, 1996.

[8] J.F. Ziegler, M.D. Ziegler, J.P. Biersack, Nucl. Instruments Methods Phys. Res. Sect. B Beam Interact. with Mater. Atoms 268 (2010) 1818–1823.

[9] R. Behrisch, W. Eckstein, eds., "*Sputtering by Particle Bombardment*", Springer Berlin Heidelberg, Berlin, Heidelberg, 2007.

[10] Y. Yamamura, C. Mössner, H. Oechsner, Radiat. Eff. 103 (1987) 25–43.

[11] P. Sigmund, Phys. Rev. 184 (1969) 383–416.

[12] M.A. Makeev, R. Cuerno, A.L. Barabási, Nucl. Instruments Methods Phys. Res. Sect. B Beam Interact. with Mater. Atoms 197 (2002) 185–227.

[13] G. Carter, V. Vishnyakov, Phys. Rev. B. Condens. Matter 54 (1996) 17647–17653.

[14] C.S. Madi, H. Bola George, M.J. Aziz, J. Phys. Condens. Matter 21 (2009) 224010.

[15] A.-L. Barabasi, H.E. Stanley, Fractal Concepts in Surface Growth, Cambridge University Press, Cambridge, 1995.

[16] C. Herring, J. Appl. Phys. 21 (1950) 301–303.

[17] W.W. Mullins, J. Appl. Phys. 30 (1959) 77–83.

[18] M.A. Makeev, A.L. Barabási, Appl. Phys. Lett. 71 (1997) 2800–2802.

[19] W. Möller, W. Eckstein, Nucl. Instruments Methods Phys. Res. Sect. B Beam Interact. with Mater. Atoms 2 (1984) 814–818.

[20] J.P. Biersack, W. Eckstein, Appl. Phys. A Solids Surfaces 34 (1984) 73–94.

[21] W. Eckstein, Computer Simulation of Ion-Solid Interactions, Springer Berlin Heidelberg, Berlin, Heidelberg, 1991.

[22] J.P. Biersack, L.G. Haggmark, Nucl. Instruments Methods 174 (2002) 257–269.

[23] H. Hofsäss, K. Zhang, A. Mutzke, Appl. Surf. Sci. 310 (2014) 134–141.

[24] T. Basu, J.R. Mohanty, T. Som, Appl. Surf. Sci. 258 (2012) 9944–9948.

[25] G. Carter, J. Appl. Phys. 455 (1999) 455–459.

[26] E. Bauer, Zeitschrift Für Krist. 110 (1958) 395–431.

[27] R. Lacmann, Berichte Der Bunsengesellschaft Für Phys. Chemie 85 (1981) 462–462.

[28] M. Volmer, A. Weber, Zeitschrift Für Phys. Chemie 119U (1926) 11927.

[29] D.L. Smith, D.W. Hoffman, Phys. Today 49 (1996) 60–62.

[30] M. Ohring, Materials Science of Thin Films, Elsevier, 2002.

[31] F.C. Frank, J.H. Van Der Merwe, Proc. R. Soc. London. Ser. A. Math. Phys. Sci. 198 (1949) 216–225.

[32] J.E. Prieto, I. Markov, Surf. Sci. 664 (2017) 172–184.

[33] A. Wagendristel, Y. Wang, An Introduction to Physics and Technology of Thin Films, World Scientific Publishing Co. Pte. Ltd., 1994.

[34] S.K. Garg, D.P. Datta, D. Kanjilal, T. Som, Nucl. Instruments Methods Phys. Res. Sect. B Beam Interact. with Mater. Atoms 409 (2017) 181–186.

[35] E. Abbot, F. Firestone, ASME Mech. Eng 55 (1933) 569.

CHAPTER 4

Nanoscale functionalization of rippled-Si substrates

4.1 Introduction

Noble metal nanoparticles have attracted a lot of attention of researchers in recent years due to their unique physical and chemical properties suitable for different technological applications, viz. plasmonic circuits including waveguides, switches [1–3], metamaterials [4–6], SERS-based detection of complex molecules [7–11], solar cells [12–15], etc. In particular, noble metal nanoparticles demonstrate novel optical properties due to local surface plasmons which is a collective oscillation of coherent conduction electrons present in isolated metallic objects under the presence of the electromagnetic field of light [1]. There is a characteristic oscillation frequency of these conduction electrons at which electromagnetic field of light resonantly interacts with them and in turn, optical absorption and scattering cross-sections are greatly enhanced [1]. This phenomenon is called localized surface plasmon resonance (LSPR) and the characteristic frequency is the LSPR frequency which greatly relies on the geometrical and optical aspects of metal nanoparticles and their surrounding medium [1,16,17], viz. shape, size, refractive index, etc. For instance, tuning the size of nanoparticles in the range of 10-100 nm can tune the LSPR in the visible and near-infrared region of the electromagnetic spectrum of light. Moreover, the interparticle gap also plays an important role in tuning the LSPR frequency and their plasmonic coupling strength [18,19]. In the quasi-static regime, nanoparticles are much smaller in size compared to the wavelength of the incident light and therefore, the distribution of electric field remains homogeneous along the whole nanoparticle which helps in exciting pure dipolar oscillations of conduction electrons. Thus, the interaction of light with matter can be manipulated in terms of plasmonic anisotropy by aligning the size-tunable nanoparticles in an ordered manner with the directional-dependent tunable interparticle gap, i.e. 1D or 2D arrays of nanoparticles.

From the technological point of view, precise control over the growth process is exigent towards achieving tunable plasmonic properties and their direction-dependent plasmonic anisotropy. It is noteworthy that the plasmonic coupling strength of nanoparticles drastically improves with decreasing interparticle gap below 25 nm, which is helpful in achieving optical anisotropy with a large plasmon resonance shift [20]. In this quest, self-organized growth of metal nanoparticles on ion-beam patterned substrates has proven its strength in fabricating metal nanoparticle arrays with tunable size and interparticle gap. For instance, Ranjan *et al.* have reported tunable plasmonic coupling of Ag-NPs arrays on nanoscale rippled-Si substrates, characterized their optical anisotropy, and demonstrated their efficacy towards SERS-based detection of rhodamine 6G [7]. Gkogkou *et al.* have characterized the anisotropy in Ag-NPs arrays via spectroscopic ellipsometry and explored the polarization- and wavelength-dependent SERS sensing [21,22]. Similarly, Sooraj *et al.* have demonstrated SERS-based detection of glucose (with a lower concentration than blood glucose level) using plasmonic nanoparticle arrays of Ag-NPs on nanoscale *R*-Si substrates [9].

Although Ag-NPs exhibit better plasmonic properties than other noble metal nanoparticles, these NPs are prone to get oxidized and thus suffer from a challenge in terms of device stability issue [23,24]. On the other hand, Au-NPs demonstrate pretty stable LSPR for a longer time due to their excellent device stability due to their oxidation-resistant nature. In this direction, Barelli *et al.* have demonstrated infrared plasmonics properties of self-organized Au/PDMS nanoarrays [25]. Giordano *et al.* have shown plasmon hybridization engineering in self-organized anisotropic Au-silica-Au dimers on rippled glass substrates [26]. Likewise, Schreiber *et al.* have reported SERS-based detection of 1 nm-thick cobalt phthalocyanine film using Au-NP arrays on *R*-Si substrates corresponding to a growth angle of 80° for different nominal thicknesses of Au [27]. However, in-depth investigations on growth angle-dependent tunability in shape and size of Au-NPs to understand the anisotropic nature of dielectric functions and their optical simulations to strengthen the experimental findings as well as to identify the potential application of such systems for SERS-based detection of complex molecules are still lacking.

In this work, we demonstrate the anisotropic plasmonic properties and excellent SERS-based detection efficiency of oblique angle deposited self-organized Au-NPs on *R*-Si substrates. In particular, Au-NPs are deposited under three growth angles (in the range of 65°, 70°, and 80°) on ripple patterned-Si (having a periodicity of ~30 nm) fabricated using 500 eV Ar-ion bombardment at an oblique angle of 65° (with respect to the sample normal). A simple variation in the growth angle, θ_g, from 65° to 80° leads to the self-organization of Au-NPs into plasmonic arrays (having a separation, approximately equivalent to the periodicity of the ripples) with decreasing size of Au-NPs and their shape-tuning from elongated to spherical nanoparticles. Optical reflection measurements exhibit a large red shift of LSPR peak for plasmonic excitation along the Au-NP arrays, indicating a strong plasmonic anisotropy. A biaxial model is developed to fit the Jones matrix elements (measured using generalized ellipsometry) by considering Au-NP arrays as an effective medium. The anisotropic dielectric functions determined from the biaxial fit reveal the LSPR excitations along *x*- and *y*-axis, whereas metallic nature is obviously along the *z*-axis. From the application point of view, strong near field enhancement between the Au-NP arrays is utilized in the SERS-based detection of ultralow concentration (10 μM) of crystal-violet dye. In addition, finite-difference time-domain (FDTD) simulations divulge the strong near-field enhancement between Au-NPs due to their lesser inter particle gap along the NP-arrays. Thus, the direction-dependent near-field coupling produces optical anisotropy via LSPR tuning and improves the Raman scattering cross-section of complex molecules to enable their detection via SERS.

4.2 Experimental detail

In the present work, *p*-Si (100) samples (1×1 cm^2) were subjected to low energy Ar-ions at an oblique angle incidence for the fabrication of nanoscale self-organized ripple patterns followed by the deposition of Au towards the formation of 2D Au-NPs arrays under various θ_g. For instance, an ultra-high vacuum (UHV) compatible experimental chamber (Prevac, Poland) equipped with an electron cyclotron resonance (ECR)-based broad-beam (3 in. dia.) ion-source (GEN-II, Tectra GmbH, Germany) and a 5-axes sample manipulator was used for irradiation of Si surfaces. The base pressure of the experimental chamber was below 8×10^{-9} mbar and the working pressure was kept fixed at 2.5×10^{-4} mbar by controlled injection of ultrapure (99.999%) Ar gas through a mass flow controller. Prior to loading into the experimental chamber, Si samples were ultrasonically cleaned using trichloroethylene, isopropyl alcohol, acetone, and deionized water for 5 min. each and thereafter bombarded with 500 eV Ar-ions obliquely incident at an angle of 65° to the fluence of 5×10^{17} ions cm^{-2} at room temperature (RT). This leads to the fabrication of nanoscale ripple patterns onto them and is identified as *R*-Si substrate [Fig. 4.1(a)]. The average ripple-wavelength and -amplitude are observed to be 30 nm and 3 nm, respectively. To avoid the incorporation of sputtering-induced impurities (originating from the sample-platen) in Si, a bigger piece of Si from the same wafer was used in between the specimen and the sample-platen. The measured constant ion-flux was found to be 1.3×10^{14} ions cm^{-2} s^{-1} with a beam diameter of 3.5 cm. Several Si substrates were exposed to Ar-ions in a simultaneous fashion to ensure the uniformity in the evolved surface morphology. Thereafter, Au-NPs were deposited on *R*-Si substrates under three different θ_g values in the range of 65°-80° (with respect to the surface normal) [Fig.4.1(b)] and at a constant deposition rate of 0.1 nm/min for 90 min using electron beam evaporation technique. During Au evaporation, the working pressure was maintained at 2×10^{-8} mbar. Further, the size and shape of Au-NPs were tailored by their postgrowth annealing at 573 K for 1 h under vacuum

($<1\times10^{-6}$ mbar). To maintain a clarity, as-deposited Au-NPs on *R*-Si substrates at 65°, 70°, and 80° are named as R65-R80, whereas, their postgrowth annealed counterparts are identified as R65A-R80A, respectively.

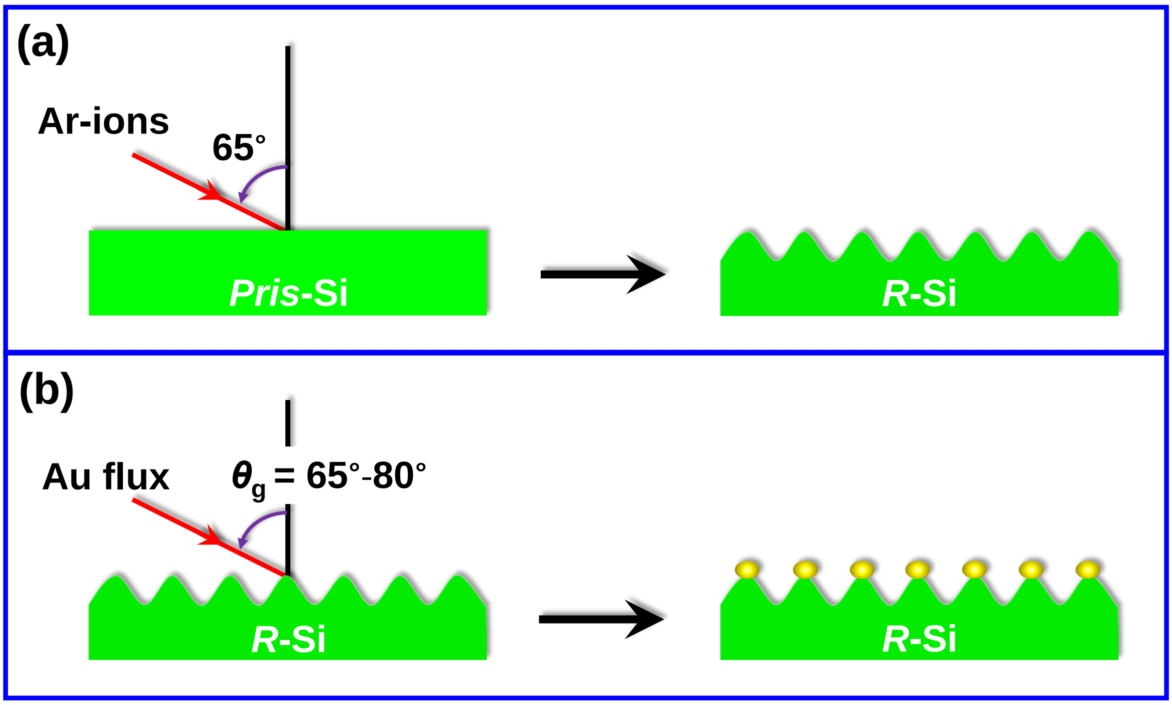

Figure 4.1: Schematic diagram: (a) Process flow for ion-beam fabrication of *R*-Si substrates and (b) self-organized growth of Au-NPs on *R*-Si substrates at θ_g=65°-80°.

The morphological characterizations were carried out using atomic force microscopy (AFM) (MFP3D, Asylum Research, USA) and scanning electron microscopy (SEM) (Carl Zeiss Merlin VP). In order to investigate the crystallinity of Au-NPs, (GIXRD) (Bruker D8 Advance, Germany) measurements were carried out on as-deposited and postgrowth annealed Au-NP arrays on *R*-Si substrates. A glancing angle geometry was used where the incident Cu-K_α (λ=0.154 nm) x-ray beam was made to fall at an incidence angle of θ=0.5°. The optical characterizations including reflection (*pristine*-Si as the reference) and generalized ellipsometry measurements were performed using an ellipsometer (V-VASE, J. A. Woollam Inc., USA). Subsequently, SERS spectra were recorded using a confocal Raman spectrometer (Alpha 300 R, WITec GmbH, Germany) at a laser wavelength of 532 nm (laser power: 9.2 mW and laser spot size: 2.5 mm) for an accumulation time of 1 s. Further, FDTD simulations were carried out to compute the electric field enhancement between Au-NPs arrays grown on *R*-Si substrates.

4.3 Results and discussion

Figures 4.2(a) and (b) depict the AFM images of *pristine*- and as-prepared *R*-Si, respectively where the arrow on (b) indicates the direction of ion-beam projection onto the Si surface. The corresponding insets show the fast Fourier transformation (FFT) of the respective image, revealing the isotropic surface morphology of the *pristine*-Si [inset, Fig. 4.1(a)] which transforms into an anisotropic surface morphology for an as-prepared *R*-Si substrate [inset, Fig. 4.1(b)]. Analysis using WSxM software [28] reveals that ripples have an average wavelength of 30 nm and an amplitude of 3 nm.

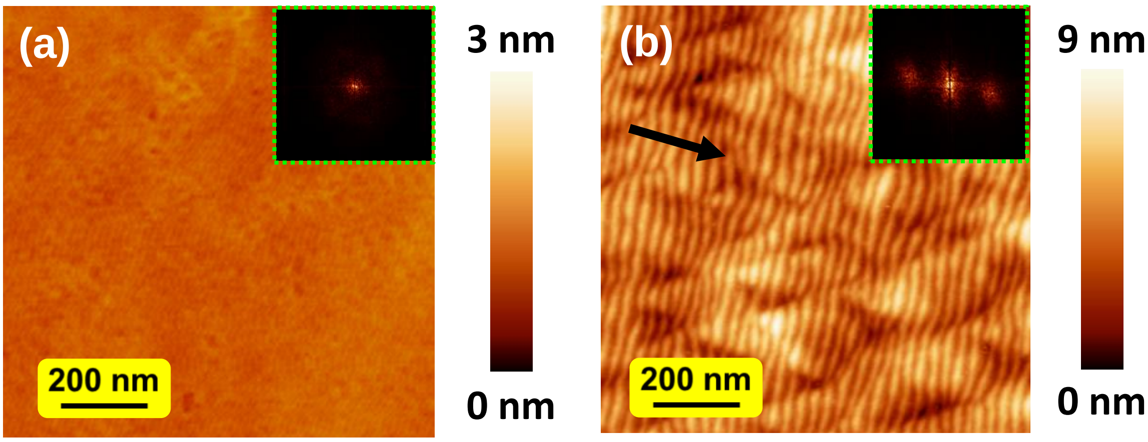

Figure 4.2: AFM micrographs: (a) *Pristine*-Si and (b) *R*-Si substrates. Respective inset shows the 2D FFT image of the corresponding AFM micrograph. The black arrows indicate the direction of ion-beam bombardment.

On the other hand, Figs. 4.3(a)-(c) depict the SEM images of as-deposited Au-NPs on *R*-Si substrates (R65-R80) at various oblique angles corresponding to θ_g=65°, 70°, and 80°, respectively, where the presence of Au-NPs suggests that gold deposition follows the island (Volmer-Weber) growth mode on silicon substrates. It is interesting to note that the Au-NPs are elongated for 65° and 70° growth angles, however, 80° growth angle leads to the formation of spherical nanoparticles. Moreover, it is observed from the SEM images that oblique angle growth of Au-NPs leads to their decoration along the ripple patterns which in turn gives rise to arrays of Au-NPs on the same. In addition, Au-NPs are elongated along the ripples with an aspect ratio (major to minor axis ratio of Au-NPs fitted with an ellipse) of approx. 1.6 and their coverage area decreases from 39% to 22% with increasing growth angle from 65° to 80° (for a constant growth time of 90 min). It is important to note that for increasing θ_g value (i.e. from 65°-80°), the average dimension of Au-NPs reduces systematically. In order to improve the alignment of Au-NPs along the ripple patterns, their postgrowth thermal annealing is carried out at 573 K for 1 h under high vacuum ($<1\times10^{-6}$ mbar) condition.

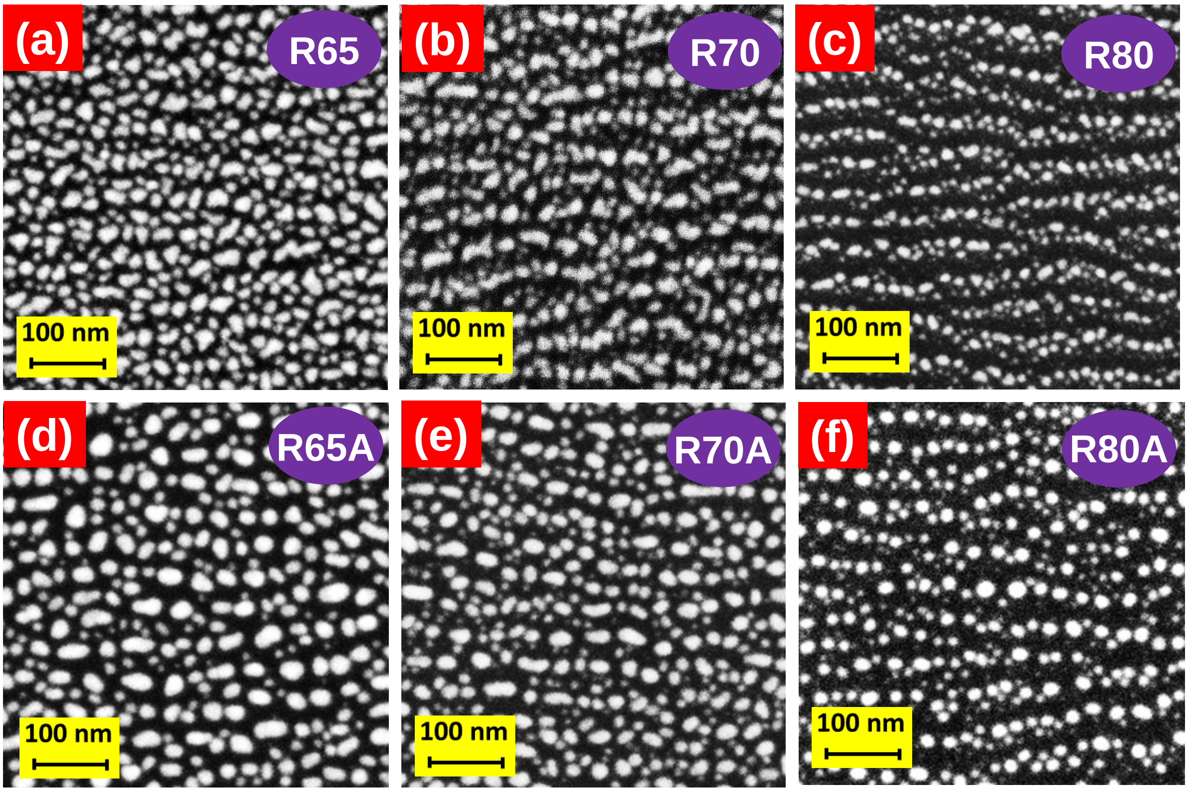

Figure 4.3: (a)-(c) SEM images of as-deposited Au-NPs on *R*-Si surfaces grown at θ_g=65°, 70°, and 80° (R65, R70, and R80) and (d)-(f) their postgrowth annealed counterparts (i.e. R65A, R70A, and R80A).

It may be mentioned that the choice of annealing temperature is made in a way that it remains well below the eutectic temperature of Au-Si system (i.e. 636 K). Likewise, Figs. 4.3(d)-(f) show the SEM images of postgrowth annealed Au-NPs on *R*-Si substrates corresponding to θ_g=65°, 70°, and 80°, respectively.

These images clearly reveal that the average dimension of Au-NPs increases upon postgrowth thermal annealing. It is interesting to note that Au-NPs get sufficient thermal energy and tend to attain thermodynamically favoured spherical shape upon their postgrowth annealing. However, the expansion of nanoparticles across the ripple patterns is restricted by the ripple modulation itself. Therefore, it is expected that during the annealing process, small NPs in their close proximity (along the ripples) may undergo Ostwald ripening and grow bigger in dimension [29]. Analysis of the SEM images indeed reveals that the average dimension of Au-NPs increases, whereas their coverage area and the aspect ratio decrease upon annealing which support the Ostwald ripening of small Au-NPs [29]. A further decreasing trend in the average dimension and coverage area of Au-NPs is observed with increasing θ_g after postgrowth annealing as well. Some useful parameters, extracted from SEM data analysis, viz. average dimension of Au-NPs, their coverage area, and aspect ratio of Au-NPs are summarized in Table 4.1.

Sample	**Major axis (nm)**	**Minor axis (nm)**	**Coverage area (%)**	**Aspect ratio**
R65	20.3±9.2	13.1±3.8	39	1.6
R70	19.2±8.2	12.4±2.7	36.6	1.8
R80	13.8±4.4	11.2±2	22	1.6
R65A	23.2±10.2	13.5±3.8	32	1.5
R70A	22.3±9.8	13.5±3.6	31.1	1.5
R80A	15.7±7.8	10.1±2	18.5	1.2

Table 4.1: Some useful parameters (i.e. the average dimension of Au-NPs, percentage coverage area, and aspect ratio of Au-NPs) from the analyses of SEM images.

Figure 4.4(a) presents the GIXRD data of as-deposited and postgrowth annealed Au-NPs grown on *R*-Si substrates at θ_g=65° (i.e. R65 and R65A), whereas Fig. 4.4(b) exhibits the same for as-deposited and postgrowth annealed Au-NPs grown on *R*-Si substrates at θ_g= 80° (i.e.

R80 and R80A). These two distinct Bragg reflection peaks appear at 2θ values of 38.22 and 44.3 in the GIXRD spectra which correspond to Au(111) and Au(200), respectively. From the GIXRD data, it becomes evident that Au-NPs are polycrystalline in nature and the peak intensity improves after their postgrowth annealing along with a reduction in the FWHM of both the peaks due to increasing dimension of Au-NPs upon annealing (grain growth) as is evident from the SEM images described earlier [Figs. 4.3(a)-(f)].

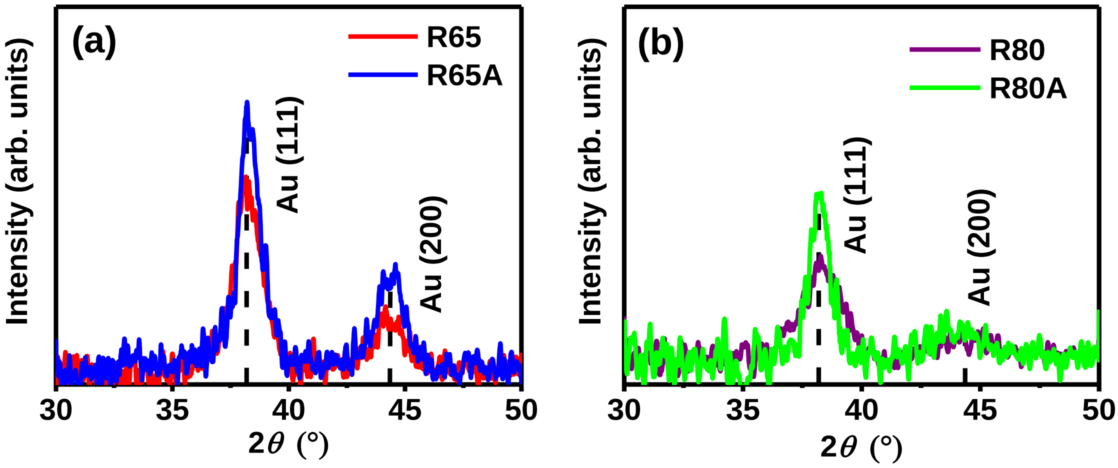

Figure 4.4: GIXRD data of as-deposited and postgrowth annealed Au-NPs grown on *R*-Si substrates: (a) θ_g=65° (i.e. R65 and R65A) and (b) θ_g=80° (i.e. R80 and R80A).

In order to characterize the plasmonic anisotropy of as-prepared and postgrowth annealed Au-NPs deposited on *R*-Si substrates, reflection measurements are performed using linearly polarized light incident at an angle of 70° (with respect to the sample normal), where the in-plane optical anisotropy is probed by providing a 90° azimuthal sample rotation to align the *E*-field parallel ($E \| k$) and perpendicular ($E \perp k$) to the ripple wavevector (k), as presented in the schematic diagram [Fig. 4.5]. In fact, reflection measurements are carried out with respect to a *pristine*-Si wafer to directly capture the plasmonic response of Au-NPs and measure the plasmonic anisotropy in terms of LSPR peak shifting. It is reported that noble metal nanoparticles grown on a *pristine*-Si substrate have a random distribution and in turn do not show any direction-dependent shift in the LSPR peak for both $E \| k$ and $E \perp k$ due to their isotropic near-field coupling, whereas metal nanoparticles deposited on *R*-Si substrates exhibit anisotropic plasmonic response [18].

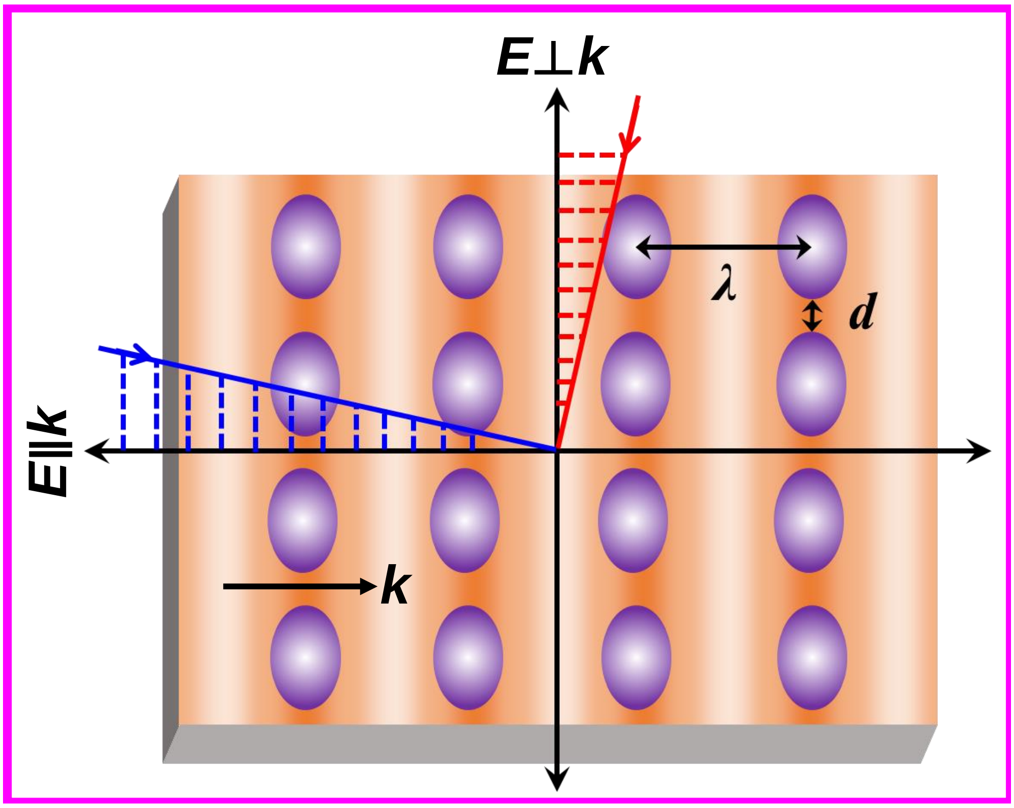

Figure 4.5: Schematic representation of the reflection measurements with azimuthal sample rotation by 90°, i.e. the electric field of light is parallel (*E*‖*k*) and perpendicular (*E*⊥*k*) to the ripple wavevector (*k*).

For instance, Fig. 4.6(a) presents the reflection data corresponding to as-deposited Au-NPs (θ_g=65°) on *R*-Si substrate (R65) where the plasmonic peak appears at 578 nm while measuring reflection along the ripple wavevector (*E*‖*k*). However, upon a 90° sample-rotation (*E*⊥*k*), the plasmonic peak shifts to 708 nm with a peak shift of 130 nm (ΔE=0.39 eV) which can be attributed to the stronger near-field coupling between Au-NPs due to smaller inter-particle gaps along the ripple patterns. Similarly, as shown in Fig. 4.6(b), as-deposited Au-NPs corresponding to θ_g=70°, on *R*-Si substrates (R70) exhibit the plasmonic peak at 570 nm and 886 nm corresponding to *E*‖*k* and *E*⊥*k*, respectively which yields a shift in the plasmonic peak by 316 nm (ΔE=0.78 eV). Moreover, Au-NPs grown at θ_g=80° (R80) reveal the occurrence of plasmonic peaks at 611 nm ($E\|k$) and 701 nm ($E\perp k$) with a peak shift of ΔE=0.26 eV [Fig. 4.6(c)].

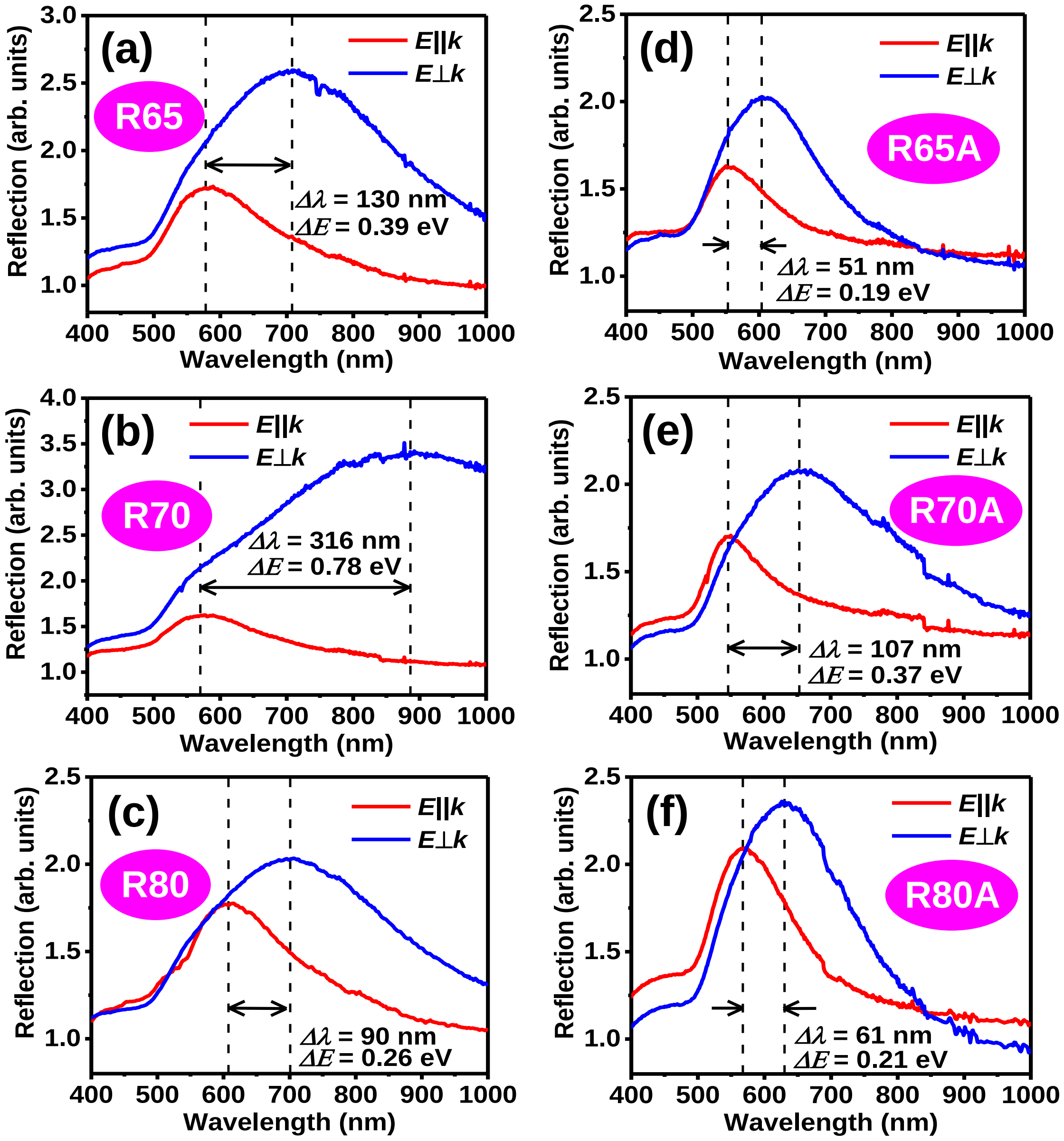

Figure 4.6: Anisotropic reflection measurements (with respect to *pristine*-Si) on (a)-(c) R65, R70, and R80 and (d)-(f) their annealed counterparts R65A, R70A, and R80, respectively.

By comparing the plasmonic peak positions corresponding to Au-NPs grown at θ_g=65° and 70°, it is observed that the latter shows a red shift in the plasmonic peak for compared to $E\|k$ which is likely due to an enhanced near-field coupling strength due to an inter-particle gap. In contrast, for Au-NPs grown at θ_g=80°, a blue shift in the plasmonic peak corresponding to $E\perp k$ is observed in comparizon to Au-NPs grown at θ_g=70° which is attributed to an enhanced interparticle gap via a shape transition from elongated to spherical nanoparticles as is evident from the SEM images [Fig. 4.3(d)-(f)]. On the other hand, postgrowth annealing of R65 shows the plasmonic peaks at 553 nm and 604 nm (ΔE=0.19 eV) corresponding to $E \| k$ and $E \perp k$ [Fig. 4.6(d)], respectively. Similarly, the reflection plot of R70A exhibits the plasmonic peak at 546 nm and 653 nm (ΔE=0.37 eV) corresponding to $E \| k$ and $E \perp k$ [Fig. 4.6(e)], respectively. However, postgrowth annealed Au-NPs grown at θ_g=80° (R80A) exhibit the plasmonic peaks at 565 nm ($E \| k$) and 626 nm ($E \perp k$) with a peak shift of ΔE=0.21 eV [Fig. 4.6(f)]. These observations reveal that there is a blue shift in the plasmonic peak of Au-NPs for postgrowth annealed sample (i.e. R65A) which is attributed to their enhanced inter-particle gap upon annealing [30]. In addition, the plasmonic peak becomes sharper due to the size-distribution of annealed Au-NPs via Ostwald ripening [30]. It is interesting to note that the growth angle-dependent shape transition from elongated to spherical Au-NPs leads to a blue shift in both the plasmonic peaks ($E \| k$ and $E \perp k$) due to increased inter-particle gap. The wavelength of plasmonic peaks arising in the reflection spectra corresponding to $E \| k$ and $E \perp k$ are summarized in Table 4.2.

Sample	**λ (nm) ($E \| k$)**	**λ (nm) ($E \perp k$)**	**$\Delta\lambda$ (nm)**
R65	578	708	130
R70	570	886	316
R80	611	701	90
R65A	553	604	51
R70A	546	653	107
R80A	565	626	61

Table 4.2: Peak shift in the plasmonic resonance of Au, measured from the optical reflection (with respect to *pristine*-Si) using a linearly polarized light where electric field remains parallel ($E \| k$) and perpendicular ($E \perp k$) to the ripple wavevector (k).

It is worth mentioning that the oblique angle growth of noble metal nanoparticles on *pristine*-Si substrates leads to their deposition in an isotropic manner (images not shown) and it does not possess any strong anisotropy in the reflection peak unlike the ones observed for Au-NPs deposited on *R*-Si substrates [18]. The reduction in the plasmonic anisotropy upon thermal annealing of Au-NPs can be governed by the increased interparticle gap between Au-NPs due to thermal energy-mediated merging of small Au-NPs, located somewhere in the interparticle gap. As it is mentioned previously that the wavelength of ripple patterns is observed to be 30 nm and their amplitude is 3 nm, the center to center distance between two adjacent arrays of Au-NPs is approximately equal to the wavelength of ripple patterns. However, interparticle separation is dependent on their deposition-time, and postgrowth annealing temperature [7,31]. For detail investigations on the plasmonic response of annealed Au-NPs on *R*-Si substrates, generalized ellipsometry (GE) measurements are carried out on postgrowth annealed samples in the wavelength range of 400 nm to 1000 nm where complex reflection coefficients are measured using polarized light with the electric field directed parallel (*p*) and perpendicular (*s*) to the plane of incidence. These complex-valued reflection coefficients can be expressed as three independent normalized reflection matrix elements represented by a 2×2 Jones matrix, which are written as:

$$R_{pp} \equiv \frac{r_{pp}}{r_{ss}} = tan\left(\Psi_{pp}\right)e^{i\Delta_{pp}}, \tag{1}$$

$$R_{ps} \equiv \frac{r_{ps}}{r_{pp}} = tan\left(\Psi_{ps}\right)e^{i\Delta_{ps}}, \tag{2}$$

$$R_{sp} \equiv \frac{r_{sp}}{r_{ss}} = tan\left(\Psi_{sp}\right)e^{i\Delta_{sp}}, \tag{3}$$

where Ψ_{ij} and Δ_{ij} are the parameters measured using GE and r_{ij} are the elements of the Jones matrix (*i*=*s*, *p*; *j*=*s*, *p*) which are able to explain the entire complex reflection phenomenon for a non-depolarizing specimen [19]. It may be mentioned that the standard ellipsometry measurements are enough to determine the dielectric function of an isotropic material due to vanishingly small off-diagonal components (r_{ps} and r_{sp}) of the Jones matrix [19,31]. However, for an anisotropic system, a fraction of the incident *p*-polarized light is converted into *s*-

polarized light and vice versa, which give rise to off-diagonal components of the Jones matrix (determined using GE) [19,31]. It is also observed that the off-diagonal components of the Jones matrix are maximized for light incident at 45° (azimuthally rotated sample) with respect to the ripple direction [19,31].

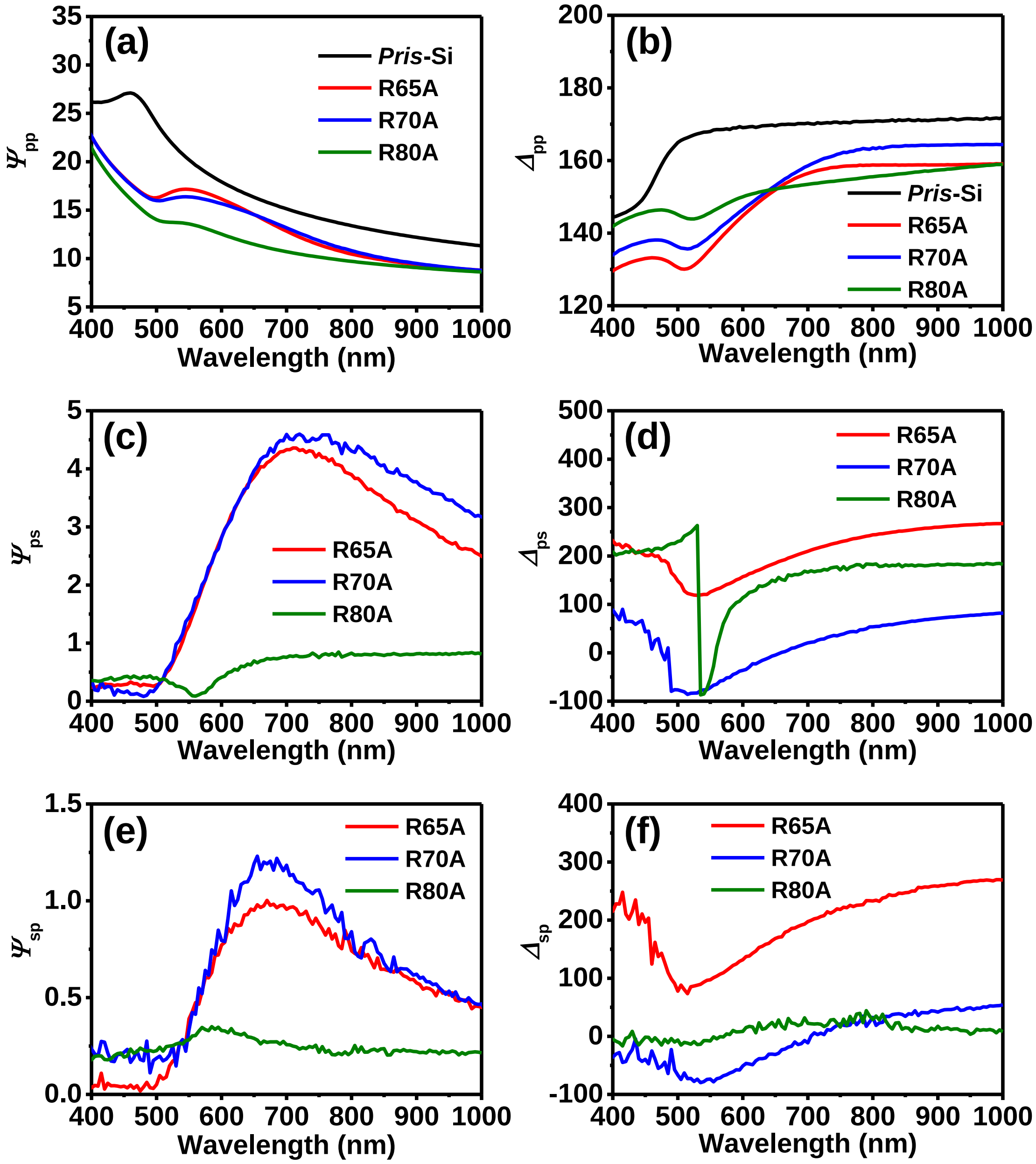

Figure 4.7: Anisotropic ellipsometry measurement as a function of θ_g: (a) Ψ_{pp}, (b) Δ_{pp}, (c) Ψ_{ps}, (d) Δ_{ps}, (e) Ψ_{sp}, and (f) Δ_{sp} plots for Au-NPs grown on R-Si substrates and annealed at 573 K for 1 h.

In the present context, a biaxial generalized oscillator model is developed to account the substrate morphology-mediated anisotropy in the growth of Au-NPs along the ripple patterns. The biaxial model is defined using three independent orthogonal optical axes (*x*, *y*, *z*) in such a way that Au-NPs get aligned ripple patterns are parallel to the *y*-axis.

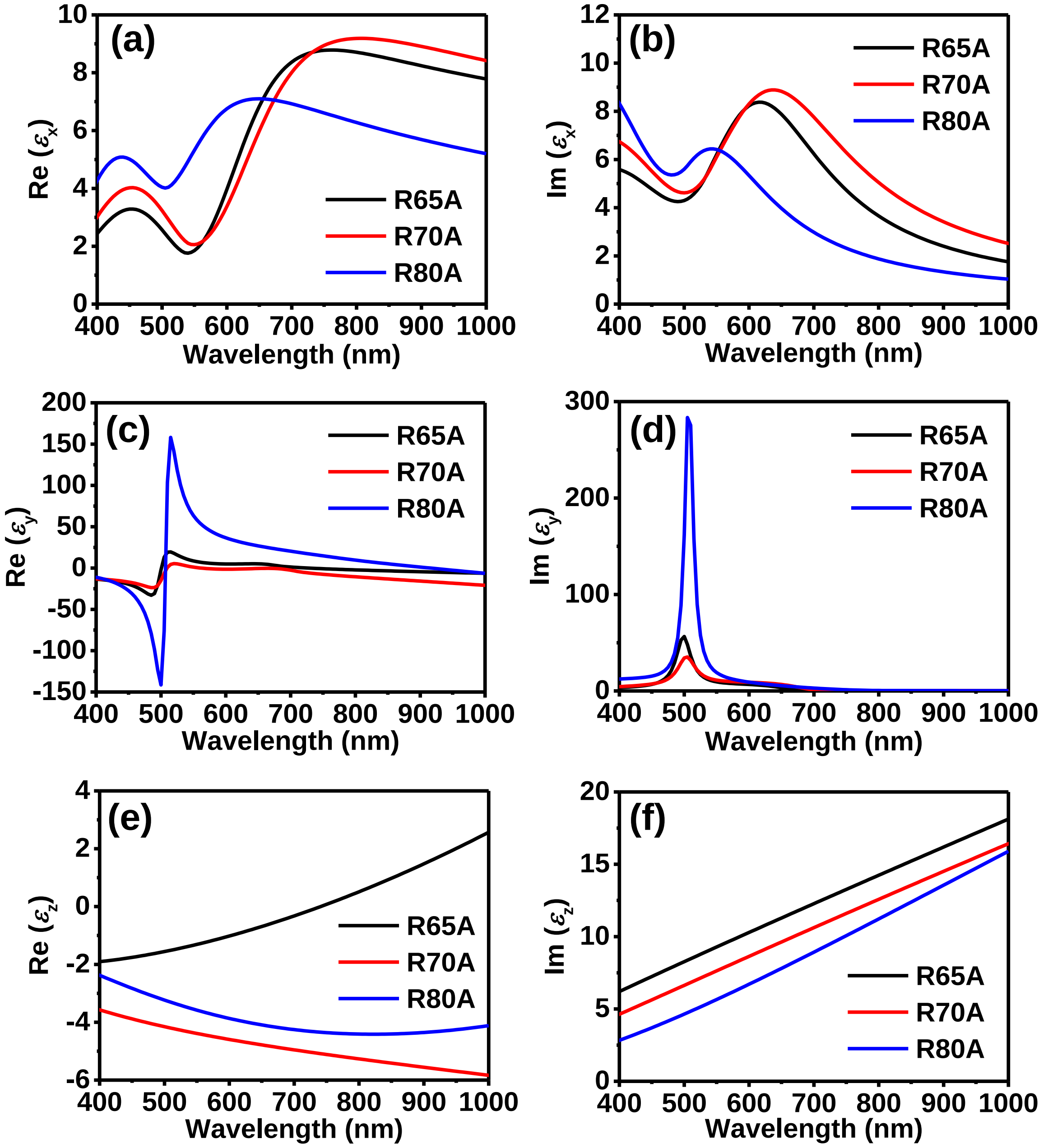

Figure 4.8: Dielectric functions obtained from biaxial generalized oscillator model fit as a function of θ_g: (a) Re(ε_x), (b) Im(ε_x), (c) Re(ε_y), (d) Im(ε_y), (e) Re(ε_z), and (f) Im(ε_z). The data are presented for postgrowth annealed samples.

This generalized oscillator model is composed of Lorentz and Tauc-Lorentz [32] oscillators along x- and y-axes, and a Drude oscillator along the z-axis. A Drude oscillator accounts for the contribution of free electrons for a bulk-like optical response with the help of concentration, mobility, and the effective mass of free electrons. However, the Lorentz oscillator accounts for the plasmonic response of Au-NPs and their interband transition from 5d valance state to hybridized 6sp state (band-edge at 2.5 eV and first peak at ~3 eV) [33,34] are represented by Tauc-Lorentz oscillator with the help of internal parameters, viz. amplitude, broadening, energy, bandgap, etc. The figure of merit for a biaxial model fit is characterized by a mean-square error (MSE) minimization algorithm. Figures 4.7(a)-(b) show the measured Ψ_{pp} and Δ_{pp} plots for *pristine*-Si and postgrowth annealed Au-NPs on *R*-Si substrates at various growth angles, viz. θ_g=65°, 70°, and 80° (R65A, R70A, and R80A), respectively. Upon fitting the Jones matrix elements, the nominal thickness of Au-NPs are found to be 9.1, 7.8, and 5.5 nm corresponding to θ_g=65°, 70°, and 80°, respectively. This observation is well supported by our SEM results on decreasing diameter and coverage area with increasing θ_g. By comparing Ψ_{pp} and Δ_{pp} of Au-NPs on *R*-Si with the ones obtained from the *pristine*-Si substrates, it is clear that a hump is observed with an overall reduction in the wavelength range of 500-750 nm for R65A-R80A which may be attributed to the plasmonic response of Au-NPs. Similarly, the cross-components obtained from the GE measurements, viz. Ψ_{ps}, Δ_{ps}, Ψ_{sp}, and Δ_{sp} are presented in Figs. 4.7(c)-(f), respectively which also manifest the presence of plasmonic anisotropy in self-organized Au-NPs on *R*-Si substrates. Figures 4.8(a)-(f) depict the direction-dependent orthogonal complex dielectric functions (ε_x, ε_y, ε_z) of postgrowth annealed Au-NPs on *R*-Si substrates (corresponding to θ_g=65°-80°) determined by biaxial model fitting of GE data. The real part of ε_x remains positive in the wavelength range of 400-1000 nm, suggesting the insulating behaviour of Au-NPs along the x-axis due to their interparticle gap approximately equal to the ripple wavelength. From Fig. 4.8(a), it is observed that the real part of dielectric function along the *x*-axis yields a similar trend for θ_g=65° and 70° due to the self-organized growth of elongated Au-NPs along the ripple patterns. However, it deviates for θ_g=80° due to their spherical shapes. Moreover, the imaginary part of dielectric function along the *x*-axis exhibits a LSPR peak at 621 nm, 642 nm, and 545 nm for R65A, R70A, and R80A, respectively [Fig. 4.8(b)]. It is interesting to note that the stronger LSPR peak with lowest FWHM (136 nm) is observed for R80A possibly due to the spherical shape of Au-NPs. Figure 4.8(c) shows the real part of ε_y which reveals the metallic behaviour in the wavelength range of 300-520 nm and beyond this, a transition from metal to insulator is observed at wavelengths beyond 520 nm. Since there is a strong LSPR coupling of Au-NPs due to the less inter-particle gap along the ripple patterns, the imaginary part of ε_y exhibits a sharp resonance peak at 499 nm, 504 nm, and 507 nm corresponding to R65A, R70A, and R80A, respectively. Interestingly, a most intense LSPR peak with lowest FWHM (12 nm) is exhibited by Au-NPs deposited at θ_g=80° possibly due to the spherical shape of Au-NPs [Fig. 4.8(d)].

Sample	**λ (nm) | E_x**	**FWHM | E_x**	**λ (nm) | E_y**	**FWHM | E_y**
R65A	621	149	499	24
R70A	642	179	504	29
R80A	545	136	507	12

Table 4.3: The LSPR wavelength and FWHM extracted from the LSPR peak appearing in the imaginary part of dielectric functions along *x* and *y*-axes obtained from the biaxial model fit of generalized oscillators for Au-NP arrays on *R*-Si substrates.

Similarly, it is observed from Fig. 4.8(e) that the real part of ε_z remains negative in the wavelength range of 400-1000 nm for θ_g=70° and 80° which exhibits the metallic nature of Au-NPs along the *z*-axis. However, Au-NPs deposited at θ_g=65° shows the metallic nature up to a wavelength of 750 nm and then switches to an insulating nature. Moreover, Drude-like response is evident from the imaginary part of dielectric function along the *z*-axis [Fig. 4.8(f)]. The LSPR wavelength and FWHM extracted from the LSPR peak appearing in the imaginary part of dielectric functions along *x* and *y*-axes– obtained from the biaxial model of generalized oscillators for 2D Au-NP arrays on *R*-Si substrates– are summarized in Table 4.3. Thus, it is manifested from the reflection measurements that Si substrate morphology-driven self-organized growth of Au-NP arrays exhibit anisotropic field-coupling between them upon providing an azimuthal rotation (i.e. in-plane anisotropy). It is also illustrated by the proposed optical model based on GE measurements that there is a LSPR peak shift in the imaginary part of dielectric functions along *x*- and *y*-axes which substantiate the presence of strong in-plane anisotropy in the plasmonic response of Au-NP arrays. The fitting parameters obtained from the proposed biaxial optical model based on GE measurements are summarized in Table 4.4.

Sample	**Effective thickness of Au layer (nm)**	**Resistivity (Ω.cm)**	**Scattering time (fs)**	**MSE**
R65A	11.2	1.5×10^{-4}	0.2	0.35
R70A	10.4	1.7×10^{-4}	0.25	0.47
R80A	8.1	2.5×10^{-4}	0.3	0.25

Table 4.4: Fitting parameters obtained from biaxial optical model based on GE measurements.

Moreover, a strong field coupling between Au-NPs should be useful in improving the Raman scattering cross-section of complex molecules in the vicinity of the strong field coupling regions via SERS. In addition, Au-NPs exhibit an excellent stability even in harsh environments due to its oxidation-resistant nature, unlike the silver nanoparticles. These merits of Au-NP arrays on *R*-Si substrate make it suitable for an efficient and longevous SERS sensing of complex molecules.

Following this, the SERS-based crystal violet detection efficacy of as-deposited and annealed Au-NPs on *R*-Si substrates is investigated and the role of growth angle-dependent anisotropy in the deposition of Au-NPs on *R*-Si substrates (i.e. 2D arrays of Au-NPs) is explored. Figure 4.9 depicts the schematic representation of SERS-based detection of crystal violet dye molecules spread over Au-NPs decorated on *R*-Si substrates (3D view).

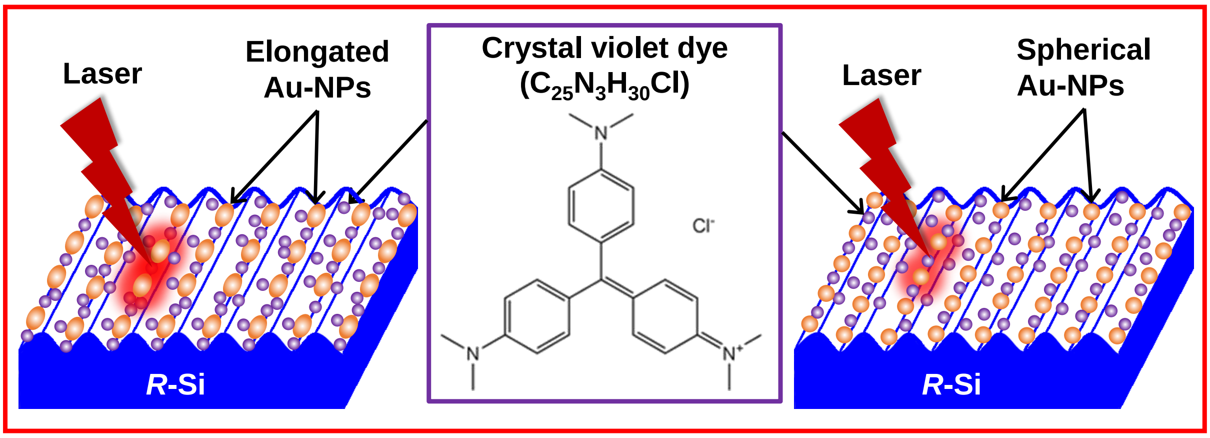

Figure 4.9: Schematic diagram (cross-section view) for SERS-based detection of crystal violet dye molecules on elongated and spherical Au-NP arrays along the ripple patterns.

A 10 μM concentration of crystal violet dye is prepared, pipetted out on 2D arrays of Au-NPs on *R*-Si substrates, and allowed to dry before the acquisition of SERS spectra. Figures 4.10(a) and (b) present the SERS-based Raman spectra of crystal violet dye solution drop-casted on as-prepared *R*-Si, as-deposited (R65-R80), and postgrowth annealed (R65A-R80A) Au-NPs on *R*-Si substrates. The observed SERS peaks for crystal violet dye appearing at 795.3, 902.7, and 1169.5 cm^{-1} which correspond to the bending vibration of the radial aromatic ring in the plane of C-H bond, whereas SERS peaks at 1378.4, and 1645.2 cm^{-1} correspond to C-C bond stretching vibration of the aromatic ring [35]. From the comparison of SERS spectra of *R*-Si and Au-NP decorated *R*-Si substrates, it becomes evident that the peak intensity enhances by a large extent after the growth of Au-NPs and it further improves after the postgrowth annealing. A noticeable improvement in the SERS detection efficacy upon postgrowth annealing can be attributed to an improved occupancy of CV molecules in the increased inter-particle gap between Au-NPs. In addition, it is observed that the SERS peak intensity decreases with increasing θ_g from 65° to 80° for both as-deposited and postgrowth annealed conditions [Figs. 4.10(a) and (b)] which is governed by the reduced dimension of Au-NPs with increasing growth angle.

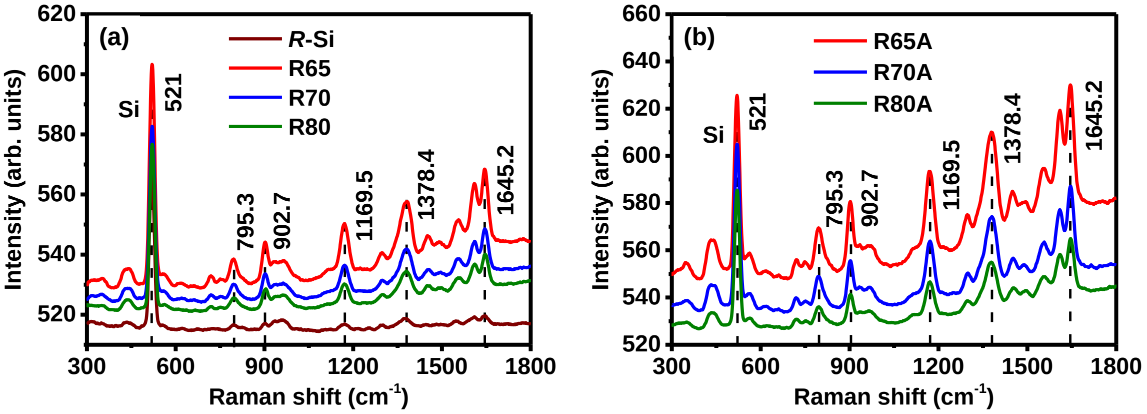

Figure 4.10: SERS spectrum for crystal violet dye detection efficacy of Au-NP on *R*-Si substrates: (a) *R*-Si and as-deposited Au-NPs on *R*-Si substrates θ_g=65°, 70°, and 80° (R65, R70, and R80) and (b) their postgrowth annealed counterparts (R65A, R70A, and R80A).

Therefore, postgrowth annealed Au-NPs decorated *R*-Si substrate corresponding to θ_g=65° exhibits superior SERS detection efficiency compared to Au-NPs grown at θ_g=70° and 80°. The enhancement in the SERS peak intensities corresponding to 1378.4 and 1645.2 cm^{-1} is quantified by normalizing with respect to their respective Si peak, appearing at 521 cm^{-1} in the respective Raman spectra and are summarized in Table 4.5.

Sample	**Normalized peak intensity**	
	I (1378.4 cm^{-1})	**I (1645.2 cm^{-1})**
R-Si	0.91	0.91
R65	0.92	0.94
R70	0.93	0.94
R80	0.93	0.94
R65A	0.98	1
R70A	0.95	0.97
R80A	0.95	0.96

Table 4.5: SERS intensity normalized with respect to the Si peak intensity, corresponding to crystal violet characteristic peaks (1378.4 and 1645.2 cm^{-1}), for Au-NPs deposited on *R*-Si substrates along with their annealed counterparts.

In order to explain the experimentally observed strong in-plane plasmonic anisotropy in the optical reflection and ellipsometry measurements, the near-field coupling strength between Au-NPs is computed using FDTD method-based simulations. As depicted in Fig. 4.11, three orthogonal axes (*x*, *y*, *z*) are considered in such a way that Au-NPs aligned on ripple patterns are parallel to the *y*-axis. However, *R*-Si substrate with a ripple-wavelength of 30 nm and ripple-height of 3 nm is modeled by alternatively arranging Si and void (air) elliptical cylinders (major axis: 15 nm; minor axis: 3 nm) half-buried in the *pristine*-Si substrate and further Au-NPs placed along the void cylinders. An FDTD domain with periodic boundary conditions for *x*- and *y*-axes is used to account for the periodic effects, whereas, a perfectly matched layer (PML) is used for the *z*-axis. A plane-wave source is used with an *E*-field strength of 1 V m^{-1} in the wavelength range of 400-700 nm.

The *E*-field and the refractive index are obtained from field profile and refractive index monitors situated at the center of Au-NPs in the *xy*-plane, respectively. Comparizon of both these cases reveals that there is a stronger near-field coupling between Au-NPs corresponding to *E*-field parallel to Au-NP arrays compared to the perpendicular one which can be attributed to the lesser inter-particle gap between Au-NPs along the NP-arrays.

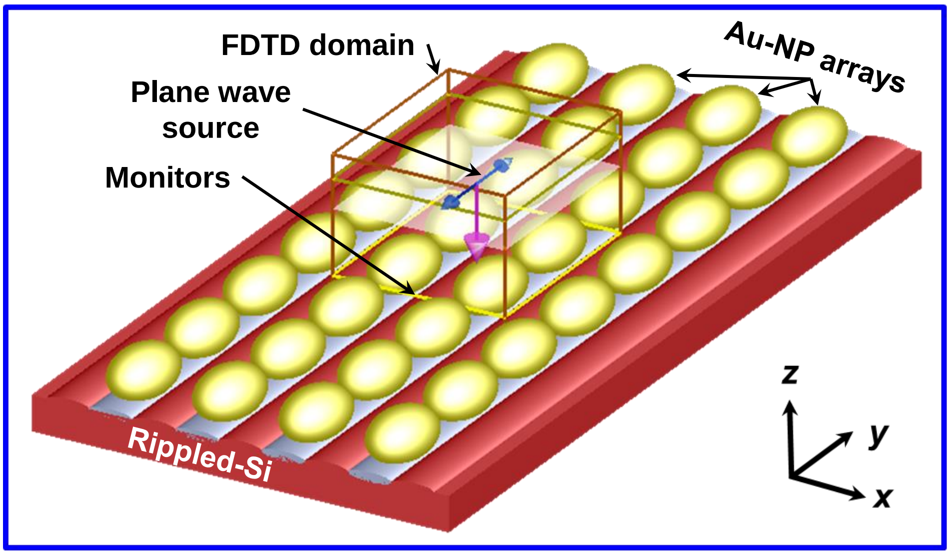

Figure 4.11: FDTD model (3D view) to evaluate the near field coupling between Au-NPs on a *R*-Si substrate.

Thus, it is evident that direction-dependent near-field coupling strength can produce optical anisotropy via LSPR tuning which corroborates well with our experimental findings on reflection and GE measurements and anisotropy observed in the SERS measurements. In addition, from the FDTD simulations, it is inferred that Raman spectroscopy-based detection of complex molecules, having low Raman scattering cross-section, can be efficiently performed due to strong near-field coupling-induced manifold enhancement in their Raman scattering cross-section. To have a better understanding of the spectral dependence of *E*-field, maximum field values are obtained from their respective |*E*| color maps corresponding to wavelength of light in the range of 400 to 700 nm. The *E*-field and the refractive index are obtained from field profile and refractive index monitors situated at the center of Au-NPs in the *xy*-plane, respectively. Figure 4.12(a) presents the refractive index profile of air and Au at 533 nm where elliptical Au-NPs are modeled with their major and minor axes as 15 nm and 10 nm, respectively along with an inter-particle gap of 5 nm along the major axis. Figure 4.12(b) shows the |*E*| color map at a wavelength of 590 nm exhibiting maximum *E*-field corresponding to the *E*-field parallel to the ripple wavevector ($E \| k$), where color contrast represents the strength of the *E*-field. Similarly, Fig. 4.12(c) demonstrates the color map of |*E*| at 590 nm corresponding to *E*-field perpendicular to the ripple wavevector ($E \perp k$). Comparizon of both these cases reveals that there is a stronger near-field coupling between Au-NPs corresponding to *E*-field parallel to Au-NP arrays compared to the perpendicular one which can be attributed to the lesser inter-particle gap between Au-NPs along the NP-arrays. Thus, it is evident that direction-dependent near-field coupling strength can produce optical anisotropy via LSPR tuning which corroborates well with our experimental findings on reflection and GE measurements and anisotropy observed in the SERS measurements. In addition, from the FDTD simulations, it is inferred that Raman spectroscopy-based detection of complex molecules, having low Raman scattering cross-section, can be efficiently performed due to strong near-field coupling-induced manifold enhancement in their Raman scattering cross-section.

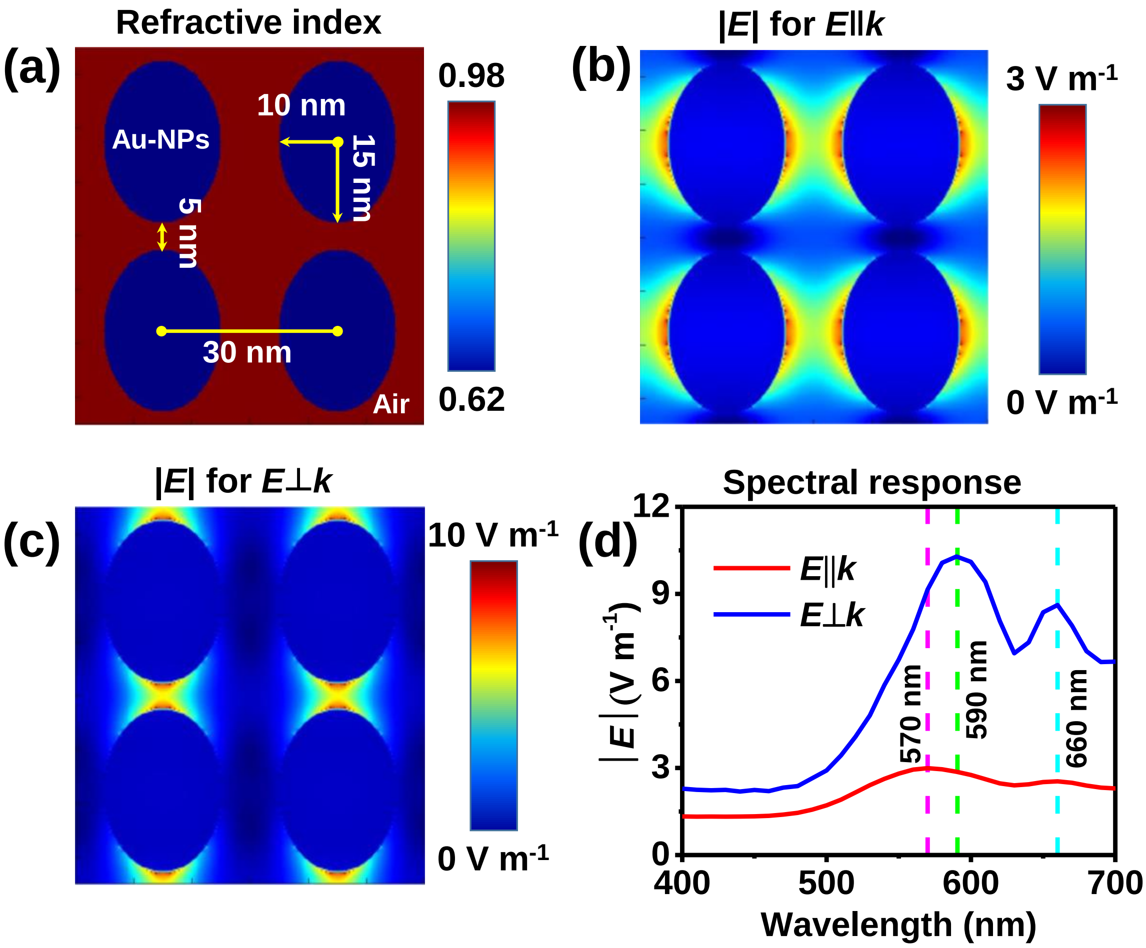

Figure 4.12: (a) Simulated refractive index profile marked with different dimensions of modeled Au-NPs on a *R*-Si substrate, (b) corresponding |*E*|-map when the electric field is parallel to the ripple wavevector (*k*), (c) |*E*|-map when the electric field is perpendicular to the ripple wavevector, and (d) spectral response of the near-field coupling when electric field is directed parallel and perpendicular to the ripple wavevector.

To have a better understanding of the spectral dependence of *E*-field, maximum field values are obtained from their respective |*E*| color maps corresponding to wavelength of light in the range of 400 to 700 nm. Figure 4.12(d) presents the spectral response of *E*-field computed for *E*∥*k* and *E*⊥*k* which exhibit sharper plasmonic peaks arising at 590 nm and 660 nm for the latter one, whereas it is observed at 570 nm and 660 nm for the former one (i.e. *E*∥*k*). These observations qualitatively explain the appearance of sharp and red-shifted reflection peak for

$E \perp k$ compared to $E \parallel k$ and thus, the higher near-field coupling between Au-NPs along the NP arrays results in an improved SERS intensity.

4.4 Conclusions

In conclusion, Au-NPs are deposited on low energy ion-beam patterned nanoscale rippled-Si surfaces using electron beam evaporation technique. Oblique angle growth of Au-NPs leads to their self-organization along the ripple patterns, resulting in 2D arrays of Au-NPs on *R*-Si substrates which exhibit strong near field coupling between Au-NPs along the NP-arrays confirmed by GE measurements and FDTD simulations. Therefore, a red shift in the wavelength corresponding to the LSPR peak (in-plane plasmonic anisotropy) is observed while measuring the reflection of *p*-polarized light incident parallel and perpendicular to the Au-NP arrays. A LSPR peak gets blue-shifted upon thermal annealing of Au-NPs due to their increasing inter-particle gap. Spectroscopic ellipsometry measurements reveal the anisotropic dielectric function along *x*-, *y*-, and *z*-axes where a strong LSPR coupling is observed along the Au-NP arrays. In addition, SERS-based detection efficacy of crystal violet dye is examined on these 2D Au-NPs arrays demonstrating an excellent sensing efficiency of the same. FDTD simulation of 2D arrays of Au-NPs on *R*-Si surface reveals a stronger near-field coupling between Au-NPs for *E*-field parallel to the NP arrays. Thus, the directional dependence of near-field coupling explains the experimentally observed optical anisotropy. Therefore, the substrate morphology-induced plasmonic anisotropy in 2D arrays of Au-NPs on *R*-Si surfaces can be utilized in intriguing plasmonic-based applications and it also provides a way towards extremely stable SERS-based sensors for detection of complex molecules in chemical and biological systems with ease in operation and excellent efficiency.

Bibliography

[1] S.A. Maier, "*Plasmonics: Fundamentals and applications*", Springer US, New York, NY, 2007.

[2] E. Ozbay, Science 311 (2006) 189–193.

[3] T.J. Davis, D.E. Gómez, A. Roberts, Nanophotonics 6 (2017) 543–559.

[4] F. Monticone, A. Alù, Chinese Phys. B 23 (2014) 047809.

[5] Z. Li, S. Butun, K. Aydin, ACS Photonics 1 (2014) 228–234.

[6] V.G. Bordo, Phys. Rev. B 97 (2018) 115410.

[7] M. Ranjan, S. Facsko, Nanotechnology 23 (2012) 485307.

[8] M. Bhatnagar, M. Ranjan, S. Mukherjee, J. Nanoparticle Res. 17 (2015) 1–13.

[9] K.P. Sooraj, M. Ranjan, R. Rao, S. Mukherjee, Appl. Surf. Sci. 447 (2018) 576–581.

[10] J. Reguera, J. Langer, D. Jiménez De Aberasturi, L.M. Liz-Marzán, Chem. Soc. Rev. 46 (2017) 3866–3885.

[11] Y. Li, Q. Wei, F. Ma, X. Li, F. Liu, M. Zhou, Acta Pharm. Sin. B 8 (2018) 349–359.

[12] K.R. Catchpole, A. Polman, Opt. Express 16 (2008) 21793.

[13] P. Mandal, S. Sharma, Renew. Sustain. Energy Rev. 65 (2016) 537–552.

[14] Y.H. Jang, Y.J. Jang, S. Kim, L.N. Quan, K. Chung, D.H. Kim, Chem. Rev. 116 (2016) 14982–15034.

[15] F. Enrichi, A. Quandt, G.C. Righini, Renew. Sustain. Energy Rev. 82 (2018) 2433–2439.

[16] A. Agrawal, I. Kriegel, D.J. Milliron, J. Phys. Chem. C 119 (2015) 6227–6238.

[17] J. Katyal, R.K. Soni, J. Mod. Opt. 60 (2013) 1717–1728.

[18] M. Ranjan, S. Facsko, M. Fritzsche, S. Mukherjee, Microelectron. Eng. 102 (2013) 44–47.

[19] M. Ranjan, T.W.H. Oates, S. Facsko, W. Mller, Opt. Lett. 35 (2010) 2576.

[20] P.K. Jain, W. Huang, M.A. El-Sayed, Nano Lett. 7 (2007) 2080–2088.

[21] D. Gkogkou, T. Shaykhutdinov, T.W.H. Oates, U. Gernert, B. Schreiber, S. Facsko, P. Hildebrandt, I.M. Weidinger, N. Esser, K. Hinrichs, Appl. Surf. Sci. 421 (2017) 460–464.

[22] D. Gkogkou, B. Schreiber, T. Shaykhutdinov, H.K. Ly, U. Kuhlmann, U. Gernert, S. Facsko, P. Hildebrandt, N. Esser, K. Hinrichs, I.M. Weidinger, T.W.H. Oates, ACS Sensors 1 (2016) 318–323.

[23] J. Liu, P. Chai, J. Tang, H. Wen, Y. Shi, C. Xue, Anal. Methods 4 (2012) 2381–2387.

[24] Y. Han, R. Lupitskyy, T.M. Chou, C.M. Stafford, H. Du, S. Sukhishvili, Anal. Chem. 83 (2011) 5873–5880.

[25] M. Barelli, D. Repetto, F.B. de Mongeot, ACS Appl. Polym. Mater. 1 (2019) 1334–1340.

[26] M.C. Giordano, S. Longhi, M. Barelli, A. Mazzanti, F. Buatier de Mongeot, G. Della Valle, Nano Res. 11 (2018) 3943–3956.

[27] B. Schreiber, D. Gkogkou, L. Dedelaite, J. Kerbusch, R. Hübner, E. Sheremet, D.R.T. Zahn, A. Ramanavicius, S. Facsko, R.D. Rodriguez, RSC Adv. 8 (2018) 22569–22576.

[28] I. Horcas, R. Fernández, J.M. Gómez-Rodríguez, J. Colchero, J. Gómez-Herrero, A.M. Baro, Rev. Sci. Instrum. 78 (2007) 013705.

[29] M. Bhatnagar, M. Ranjan, K. Jolley, A. Lloyd, R. Smith, S. Mukherjee, Nucl. Instruments Methods Phys. Res. Sect. B Beam Interact. with Mater. Atoms 393 (2017) 5–12.

[30] H. Sun, M. Yu, G. Wang, X. Sun, J. Lian, J. Phys. Chem. C 116 (2012) 9000–9008.

[31] M. Ranjan, M. Bhatnagar, S. Mukherjee, J. Appl. Phys. 117 (2015) 103106–103113.

[32] G.E. Jellison, F.A. Modine, Appl. Phys. Lett. 69 (1996) 371–373.

[33] M. Losurdo, M.M. Giangregorio, G. V. Bianco, A.A. Suvorova, C. Kong, S. Rubanov, P. Capezzuto, J. Humlicek, G. Bruno, Phys. Rev. B - Condens. Matter Mater. Phys. 82

(2010) 155451.

[34] A. Derkachova, K. Kolwas, I. Demchenko, Plasmonics 11 (2016) 941–951.

[35] E.J. Liang, X.L. Ye, W. Kiefer, J. Phys. Chem. A 101 (1997) 7330–7335.

CHAPTER 5

Nanoscale functionalization of faceted-Si substrates

5.1 Introduction

Advancement in modern electronic device technology is based on the manipulation of matter at nanoscale by achieving precise control over the dimension of nanomaterials to obtain fascinating physical properties with their exceptional performances [1]. For instance, slicing down the dimensions of matter from bulk (3D) to layers (2D) and further into nanowires (1D) and nanodots (0D), the density of states and in turn the charge transport drastically changes due to confinement effects [2,3]. One such important property is field induced tunneling of electrons from nanoscale materials to vacuum which is governed by their shape, dimension, and physical properties of nanomaterials where electrons near to the Fermi level can escape from the surface of a material by tunneling due to a lowering of the surface potential barrier with the help of an externally applied electric field [4].

Cold cathode electron emission from materials has attracted the attention of researchers due to its applications in high brightness flat panel displays, high power strategically important nanoscale electronic devices, microwave power amplifiers, space technology, electron microscopes, and sensors [5–9]. However, issues of heating and stability always pose a challenge for devices based on thermionic emission. Consequently, a lot of effort has been put for exploring materials which exhibit enhanced and highly stable field induced electron emission with low turn-on fields, high emission current densities, and superior electronic conduction at room temperature (RT) [4,10–12]. Most of these observations are explained in light of Fowler-Nordheim (F-N) tunneling [13]. Following F-N theory, one can enhance the field emission (FE) from a material either by enhancing the field enhancement factor (ratio of local to the applied electric field), β, or by reducing its work function, ϕ (i.e. the potential barrier at the interface of the material and vacuum). In principle, β can be enhanced by tuning the radius of curvature and the aspect ratio of nanostructures [11,14–19], whereas ϕ can be tuned by doping [20–23].

In addition to β *and* ϕ, the density of electron emitting sites also plays a crucial role towards enhancing FE performance at RT [24,25]. Recently, hierarchical development of field emitters (i.e. the decoration of high aspect ratio nanostructures with tiny nanoparticles) is recognized to be an effective way to further boost the FE performance by simultaneously increasing the density of field emitting sites and decreasing their resistance [19,24–26]. For instance, there are reports on lowering down of turn-on fields from 2.1 to 1.14 V μm^{-1} by decorating SiC nanowires with Au-NPs [24,25]. In another report, Das *et al.* have demonstrated a reduction in the turn-on field from 3.83 to 2.03 V μm^{-1} after attachment of Ag-NPs with Bi_2Se_3 nanoflakes [27]. Likewise, it has been demonstrated that turn-on fields can be significantly lowered down for oxide-based semiconducting nanostructures as well by decorating them with Au- and Ag-nanoparticles [19,26]. However, if the density of Au-NPs becomes very high, the field screen effect can reduce the influence of Au-NPs [24].

In particular, Si nanostructures-based cold cathode emitters are considered to be important for easy integration with the existing micro- and nanoelectronics due to their low power consumption and other applications [28,29]. In view of these facts, a plethora of attempts have been made towards preparing cold cathode emitters based on Si nanostructures [15,30,39–41,31–38]. It is well-known that the formation of an ultrathin native oxide layer hampers the tip emission from Si-based cold cathode emitters, restricting the number of electron emitting sites. In spite of this, Basu *et al.* have reported a fascinating low turn-on field (0.67 V μm^{-1}) for Si nanofacets (average dimension ~80 nm) and explained the results in light of curvature-dependent degree of native oxide formation and crystallographic orientation-dependent work function of silicon nanofacets [11]. In another work, Chang *et al.* have demonstrated that turn-on field for Si nanocones improves from 4.2 V µm^{-1} to 3.65 and 2.90 V µm^{-1} by depositing Pt and Au, respectively on these nanocones [42].

Among various available techniques for fabricating nanostructures of Si, self-organization by low energetic ion-beams offers the advantages of single step processing over a large surface area (up to 3-4 cm^2) and at RT [36]. In addition, one can tune the size and shape of Si nanostructures by varying the experimental parameters, viz. angle of incidence of ions, ion -fluence, -energy, and -species [36,37,41,43]. As a consequence, their structural and optoelectronic properties (e.g. optical reflectance, crystallographic orientation, and work function) can also be tuned [44,45].

These studies make it evident that there is a room to further enhance the FE performance of Si-based nanostructures by tuning their size and shape towards improving the field enhancement factor, reducing the work function, limiting the field screening effects and/or increasing the density of field emitters (effective electron emitting area) by choosing a controlled fabrication method of nanostructures and decorating them suitably with nanoparticles of noble metals.

The present study reports a combinatorial study on tunable cold cathode electron emission from Au-NP decorated self-organized Si-NFs with hitherto unseen low turn-on fields. In the first step, low energy ion-beam fabrication of silicon nanofacets is carried out [37,41]. Subsequently, the Si-NFs are decorated by self-assembled gold nanoparticles using oblique angle growth geometries (65°-85°). Bulk field emission measurements exhibit a very low threshold field (0.6 V µm^{-1}) for cold cathode electron emission from as-prepared Si-NFs (average height: 23 nm and base width: 196 nm) which reduces significantly after decorating these nanofacets by Au-NPs, resulting in an ultralow low turn-on field of 0.27 V µm^{-1}

(corresponding to the growth angle of 70º for Au-NPs) with an excellent stability and an impressive enhancement factor of 24157. However, due to the inability of these measurements to identify the cold cathode electron emitting sites on Si-NFs, it becomes exigent to employ local probe characterization techniques to probe the same. In doing so, Kelvin probe force microscopy (KPFM) and local probe-based dual pass tunneling current microscopy (DPTCM) are used to probe the same from Si-NFs before and after Au-NP decoration as well as their subsequent annealing. In conjunction to this, local probe-based dual pass tunneling current microscopy (DPTCM) is employed to probe the cold cathode electron emission sites from Si-NFs before and after Au-NP decoration and after annealing. Our investigations on the spatial distribution of electron emission sites (based on DPTCM) suggest that the main contribution towards the improvement in observed cold cathode electron emission can be attributed to the decoration of Au-NPs at the apexes and sidewalls of Si-NFs. This is fortified by our electrostatic field-based simulation studies which reveal that self-organized Au-NPs at the apexes of Si-NFs serve as nanoscale field emitters and therefore, improve the FE performance manifold by local field enhancement. The present combinatorial study paves a way to increase the density of free electrons on the Si-NFs and in turn tune their work function by decorating them with Au-NPs which is manifested by their excellent performance enhancement in terms of cold cathode electron emission with ultralow turn-on field.

5.2 Experimental detail

5.2.1 Sample preparation

A UHV-compatible experimental chamber (Prevac, Poland) equipped with an electron cyclotron resonance (ECR)-based filament less, broad beam ion source (GEN-II, Tectra GmbH, Germany) and a 5-axes manipulator was used for Ar-ion exposure. The manipulator offers a fully automated software controlled sample rotation with a precision of 0.01º. The chamber base pressure was below 8×10^{-9} mbar and the working pressure was maintained at

2.5×10^{-4} mbar. A bigger Si piece (e.g. 3×3 cm^2) cut from the same wafer was used as a sacrificial wafer and placed in between the sample and the sample platen to prevent the incorporation of sputtering-induced contaminations (originating from the stainless steel sample platen) [37]. The beam spot was observed to be circular with a diameter of 3.5 cm, leading to a constant ion flux of 1.2×10^{14} ions cm^{-2} s^{-1}. The Si samples used in the present study were cut into slices (1×1 cm^2) from a commercially available *p*-type (B-doped, ρ=0.01-0.05 Ω cm) Si (100) wafer. These pieces were ultrasonically cleaned in trichloroethylene, isopropyl alcohol, acetone, and deionized water for 5 min. each and exposed to 500 eV Ar^+ ions at RT at an oblique incidence angle of 71° (with respect to the sample normal) for an ion fluence of 5×10^{17} ion cm^{-2} (equivalent to 3300 s). It is expected that the present experimental conditions would lead to the fabrication of self-organized Si-NFs due to ion-beam shadowing [41].

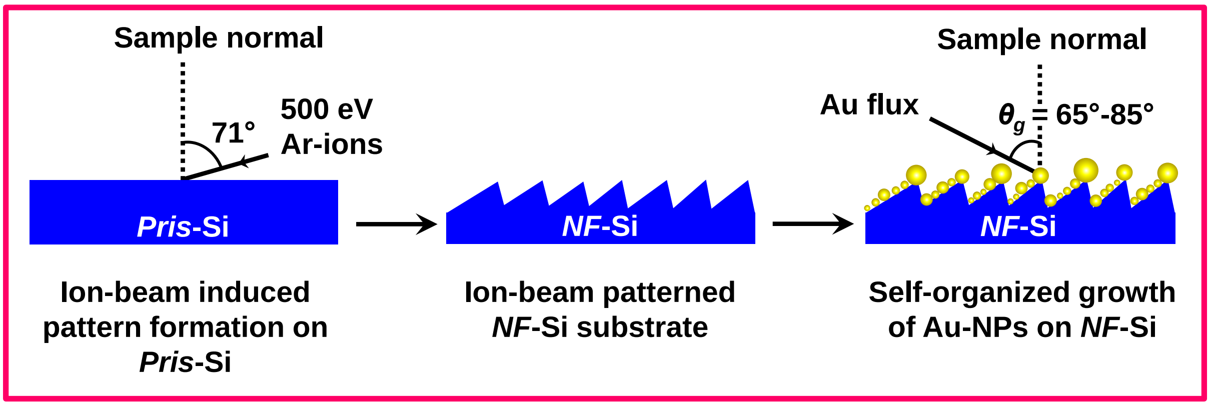

Figure 5.1: Schematic diagram of the process flow for the fabrication of ion-beam induced Si-NFs followed by oblique angle (65º-85º) growth of Au-NP on them.

Following this, Au-NPs were deposited on patterned-Si substrates under different oblique angles of incidence (in the range of 65º to 85º). For this purpose, a constant deposition rate of 0.1 nm/min was used for 90 min (for all the growth angles) using electron beam evaporation technique (working pressure: 2×10^{-8} mbar). All the samples were subjected to post-growth annealing in vacuum (< 1×10^{-6} mbar) at 573 K for 1 h to tailor the size and/or shape of Au-NPs. In addition, as-prepared Si-NFs were also annealed for the sake of comparison. Figure 5.1 depicts the process flow for the fabrication of ion-beam induced self-organized Si-NFs on

Si substrates and further growth of self-organized Au-NPs on these substrates. Hereinafter, as-prepared and annealed NF-Si substrates would be named as S1 and S1', respectively. On the other hand, Au-NP decorated Si-NFs corresponding to the growth angle (of Au), θ_g=65°, 70°, 80°, and 85° were named as S2, S3, S4, and S5, respectively, whereas these annealed samples were named as S2', S3', S4', and S5', respectively.

5.2.2 Sample characterization

The surface morphology and nanoscale electrical transport properties of Si-NFs before and after their decoration with Au-NPs as well as after annealing were simultaneously investigated using an *ex-situ* atomic force microscopy (AFM) (MFP 3D, Asylum Research, USA). In addition, Kelvin probe force microscopy (KPFM) and dual pass tunneling current microscopy (DPTCM) studies were also carried out on self-organized Si-NFs before and after decorating the same with Au-NPs and their subsequent annealing to measure the change in the work function and tunneling current, respectively. A Pt-coated Si conductive tips (AC240TM, Electric-Lever, Olympus) with ~70 kHz of resonance frequency, ~30 nm radius of curvature, and ~2 N m^{-1} stiffness were used for electrical measurements. AFM micrographs were analyzed using WSxM software [46].

Microstructural studies on nanofaceted-Si substrates and their Au-NPs decorated counterparts before and after vacuum annealing were performed using a high-resolution scanning electron microscope (HRSEM) (Carl Zeiss, Germany) under the plan-view geometry. The spatial uniformity of Au-NP decorated Si-NFs was confirmed by collecting several images from a large number of randomly chosen places on all samples. In addition, cross-sectional transmission electron microscopy (XTEM) measurements were carried out on selected samples using a high-resolution transmission electron microscope (HRTEM) (FEI, Tecnai G2 F30, S-Twin microscope operated at 300 kV and equipped with a GATAN Orius CCD camera). The specimen for XTEM measurements were prepared by standard mechanical thinning followed by double dimpling and final sample thinning using a precision ion polishing system (PIPS, Gatan, Pleasanton, CA). A high-angle annular dark field (HAADF) imaging based on scanning transmission electron microscopy (STEM) was carried out using the same HRTEM setup equipped with a HAADF detector (Fischione, Model 3000). Further, elemental analysis was performed using energy-filtered TEM (EFTEM) (GIF Quantum SE, Model 963) measurements. Glancing incidence x-ray diffraction (GIXRD) measurements were performed for phase identification using a Cu-K_α (λ=0.154 nm) radiation (Bruker D8 Advance, Germany). Compositional analysis of Si-NFs before and after Au-NP decoration were carried out using x-ray photoelectron spectroscopy (XPS) system (PHI 5000 Versa Probe II, ULVAC–PHI, Japan) equipped with a microfocused (100 μm, 15 KV, 25 W) monochromatic Al-K_α source ($h\nu$=1486.6 eV), a multichannel detector, and a hemispherical analyzer.

For cold cathode electron emission experiments, a high vacuum (3×10^{-7} mbar) chamber (Excel Instruments, India), equipped with a two-electrode configuration was used where a copper plate served as the cathode on which samples were loaded using a conductive copper tape (sheet resistance ~0.004 Ω/□). On the other hand, a copper anode metallic probe (kept normal to the cathode plate) was attached to a microgauge arrangement for adjusting the inter-electrode spacing. A computer-interfaced source meter (Keithley 2410, USA) was employed to apply bias voltage between the copper anode and NF-Si samples (with and without Au-NP decoration and their subsequent annealing) mounted on the copper cathode and the current-voltage (*I-V*) characteristics were recorded using a commercially available software (Lab Tracer 2.0). Further, to address the origin of electron emitting sites for all the samples under investigation, we have used AFM-based dual pass tunneling microscopic (DPTCM) measurements. Further to this, electrostatic field-based simulations were performed using Agros2D software[47] to simulate the electrostatic field distribution between the NF-Si sample surface and the anodic probe before and after its decoration with Au-NPs.

5.3. Results and discussion

5.3.1 Microstructure and compositional analyses

Prior to cold cathode electron emission measurements, Au-NPs decorated NF-Si substrates are analyzed by SEM, XRD, and XPS to look for its possible correlation with microstructural and compositional properties. Figures 5.2(a)−(h) show the plan-view SEM images of as-prepared and Au-NP decorated NF-Si substrates before and after annealing at 573 K for 1 h. The direction of the ion-beam projection is marked with a red arrow on all the SEM images. As a result of stochastic nature of ion-beams, *pristine*-Si surfaces evolve into an ensemble of randomly distributed Si-NFs under obliquely incident 500 eV Ar-ions at room temperature [Fig. 5.2(a)]. A vacuum annealing of self-organized Si-NFs substrates does not yield any visible change in the microstructure [Fig. 5.2(b)]. The SEM images of Au-NP decorated (in the range of 65°-85°) NF-Si substrates before and after annealing are depicted in Figs. 5.2(c)-(h). For instance, Fig. 5.2(c) reveals that Au-NPs (average dimension: 20±3 nm) grow uniformly around the sidewalls of Si-NFs, although the apexes of the facets are decorated by conformally grown bigger nanoclusters. In addition, self-organized Au-NPs are seen to form ordered chain-like microstructures (extended from apexes to the base of Si-NFs) at several places on the sidewalls of Si-NFs. Upon annealing the sample in vacuum for 573 K for 1 h, more Au-NPs get organized into vertically aligned chain-like microstructures on the sidewalls of Si-NFs followed by a clear signature of a grain growth [Fig. 5.2(d)]. An increase in the Au-growth angle of 70° yields the self-assembly of Au-NPs all around the Si-NFs [Fig. 5.2(e)], albeit the coverage reduces compared to the growth angle of 65°.

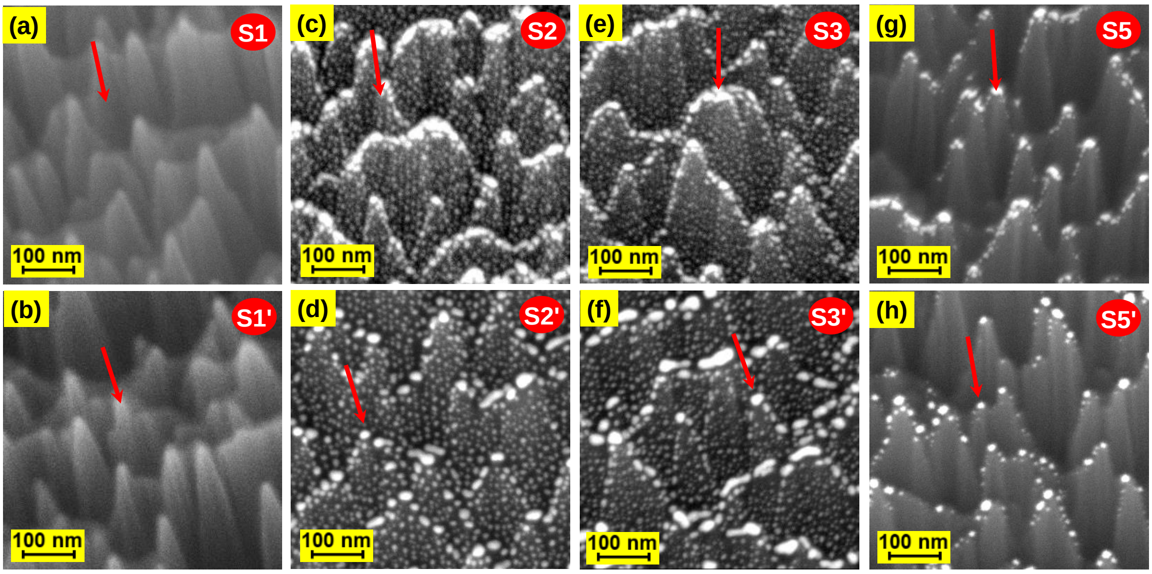

Figure 5.2: (a)–(b) SEM images of as-prepared NFs before and after annealing (i.e. S1 and S1'), respectively. SEM images of Au-NPs decorated Si-NFs at (c)–(d) θ_g=65° (i.e. S2 and S2'), (e)–(f) θ_g=70° (i.e. S3 and S3'), and (g)–(h) θ_g=85° (i.e. S5 and S5') before and after annealing, respectively.

In contrast, the apexes of the facets get decorated by bigger and more randomly assembled flower-like Au-nanostructures. Such a change in the microstructure and a relatively lower coverage in Au Au-NP decorated Si-NF samples can be understood in light of growth at a higher oblique angle where shadowing starts playing an important role [48]. It is interesting to note that after annealing the sample at 573 K for 1 h, grain growth (due to Ostwald ripening) becomes evident [Fig. 5.2(f)] [49]. In particular, the apexes and their surrounding get decorated with bigger nanostructures compared to the one shown in Fig. 5.2(e). Similar trend is observed for growth of Au-NPs at 80° (images not shown) with a further reduction in the coverage of Au-NPs. As the growth angle is further increased to 85°, the coverage area of Au-NPs reduces drastically and mostly the apexes of Si-NFs get decorated by the same [Fig. 5.2(g)]. Interestingly, upon annealing of these samples under similar conditions mentioned above, there is a marginal rearrangement of Au-NPs around the apexes become evident [Fig. 5.2(h)]. The above mentioned changes in the microstructure of as-grown Au-NP decorated Si-NFs fortify the role of shadowing with increasing growth angle. Quantitative analyses of SEM images corresponding to post-annealed Au-NP decorated Si-NFs is carried out using ImageJ software [50] leading to the coverage area of Au-NPs and the areal density which are summarized in Table 5.1. However, the same is difficult to extract for as-prepared Au-NP decorated Si-NFs (corresponding to different growth angles).

Sample description	Growth angle (°)	Coverage area (%)
S2'	65	38.9
S3'	70	28.6
S4'	80	22.8
S5'	85	9.4

Table 5.1: Coverage area of Au-NPs obtained from the analyses of SEM images corresponding to Au-NP decorated Si-NFs upon postgrowth annealing. It is noteworthy that the above mentioned parameters could not be extracted for as-prepared samples (S2-S5) due to their undistinguishable nature.

Further, to strengthen the results obtained from SEM measurements, we have also carried out XTEM measurements on selective samples, viz. an as-prepared Si-NFs (i.e. S1) and Au-NP decorated (growth angle: 70°) Si-NF annealed at 573 K for 1 h in vacuum (i.e. S3'). Figure 5.3 shows a low-magnification XTEM image of an as-prepared Si-NF sample showing the presence of self-organized nanofacets on Si. The inset in this image depicts a HRTEM image of the same, revealing clear signature of lattice fringes. Thus, it can be inferred that facets are single crystalline in nature. It is interesting to note that although the ion-beam fabricated small faceted structure (shown in the inset) is devoid of native oxide formation, there are randomly observed small patches of native oxide at some other places of the samples. In fact, the lack of formation of native oxide around the apexes of Si-NFs can be attributed to the curvature-dependent native oxide formation in Si [11]. This justifies our choice of experimental parameters to fabricate smaller Si nanofacets than the ones reported in the literature [11,41,51]. Figure 5.4(a) represents a low-magnification XTEM image of an annealed (573 K; 1 h) Au-NP decorated (growth angle of Au: 70°) Si-NF sample where the presence of Au-NPs (with wide size distribution in the range of 17 to 33 nm) surrounding the apexes of Si-NFs and the valley regions is evident.

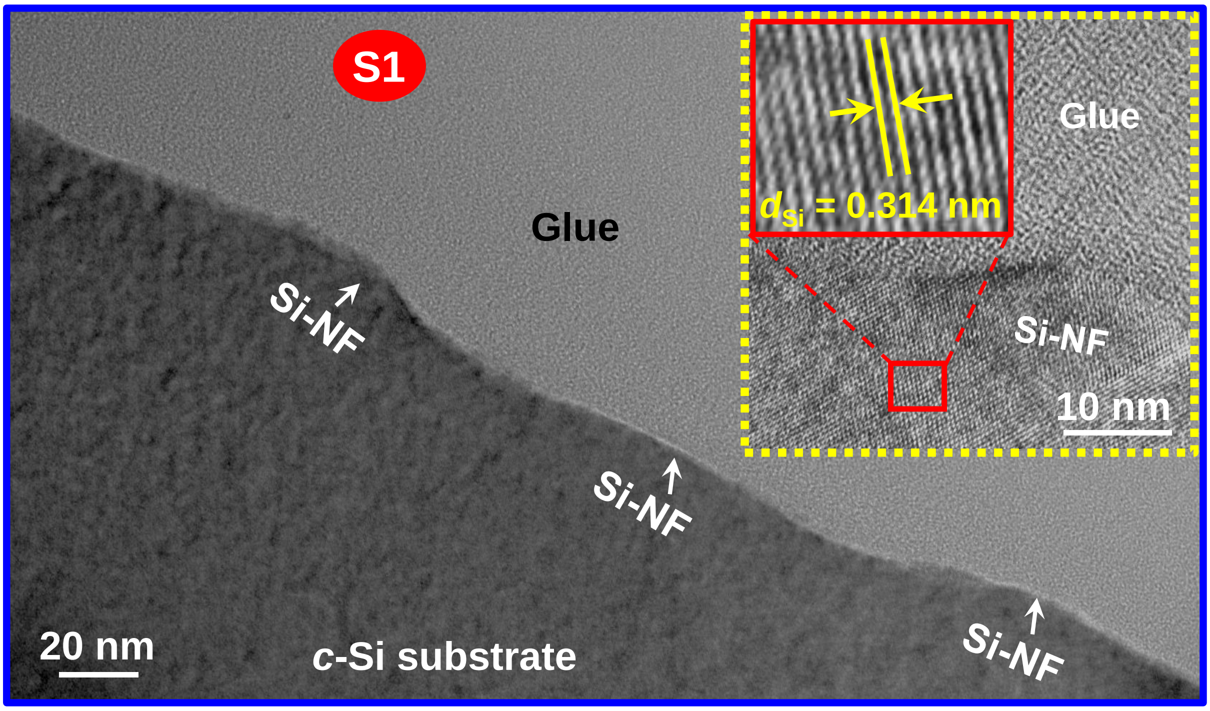

Figure 5.3: Low-magnification XTEM images of as-prepared NF-Si sample (i.e. S1) where inset depicts the corresponding HRTEM image and lattice fringe image of Si.

This image further confirms the presence of randomly formed native oxide patches on the as-prepared Si-NF substrate, albeit to a very less extent. On the other hand, Fig. 5.4(b) and (c) present HRTEM images, showing the presence of self-organized Au-NPs in the valley region next to a Si facet and the presence of Si lattice fringes is also evident. Analysis of lattice fringes obtained from the HRTEM image of nanofacets and the NPs grown on them as depicted in inset of Fig. 5.4(b) and (c), reveals that *d*-spacing match well with that of Si(111) and Au(111) planes. It is also important to note that HRTEM studies do not show any signature of gold silicide formation which is quite expected since Au-Si system has an eutectic temperature of 636 K [52]. However, a small amount of atomic diffusion of Au in Si may not be ruled out completely [53].

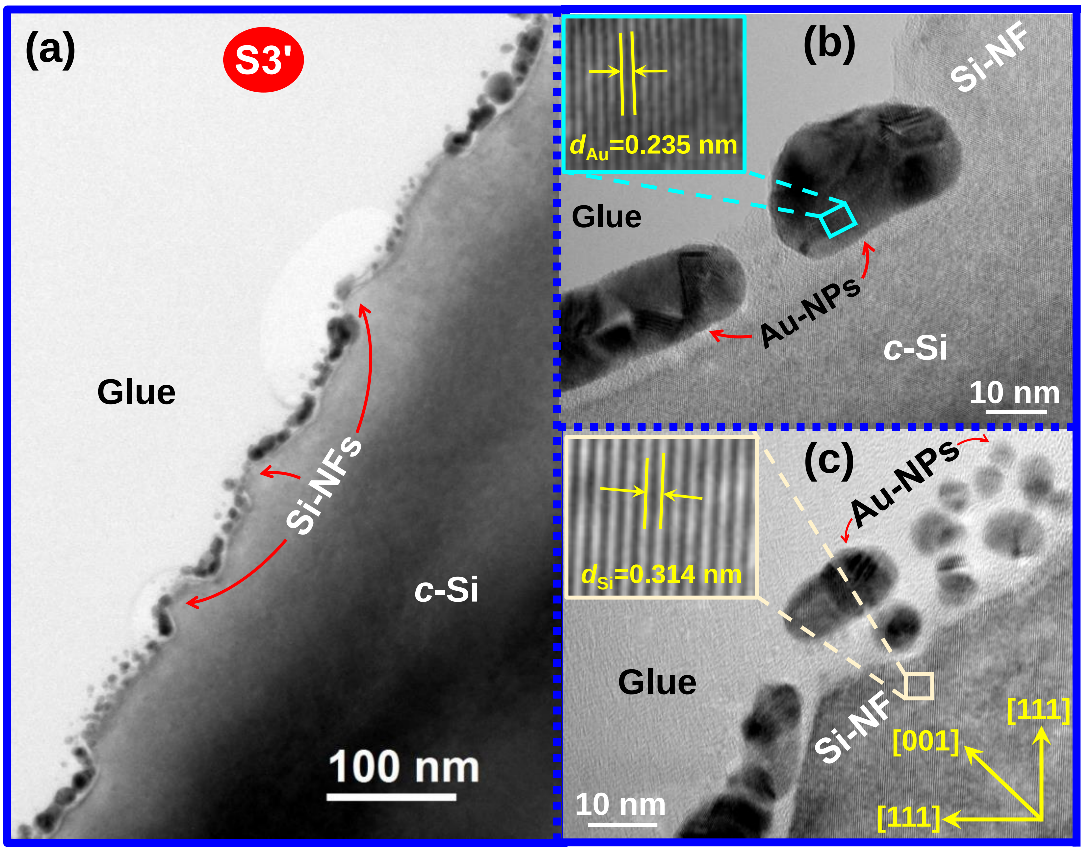

Figure 5.4: (a) low-magnification XTEM images of as-prepared NF-Si sample (i.e. S1) where inset depicts the corresponding HRTEM image and lattice fringe image of Si. Likewise, (b) low-magnification XTEM image of postgrowth annealed Au-NPs self-organized on Si-NFs at θ_g=70° (i.e. S3'), (c)-(d) corresponding HRTEM images of S3' where inset depicts the lattice fringe image of Au and Si.

Besides probing the microstructures of NF-Si and Au-NP decorated NF-Si samples, the spatial distribution of Au atoms on Si-NFs is studied by energy filtered TEM (EFTEM) measurements at randomly chosen places on Au-NP decorated self-organized Si-NFs. Figure 5.5(a) presents a low-magnification STEM-HAADF image of self-organized Au-NPs grown on Si-NFs (corresponding to a growth angle of 70°), whereas the EFTEM images corresponding to Si-K, Au-L, and Au-M, obtained from the marked region (by a red colored rectangle) of the STEM-HAADF image are shown in Figs. 5.5(b)-(d), respectively. In fact, the EFTEM image corresponding to Si-K signal [Fig. 5.5(b)] clearly reveals the presence of ion-beam fabricated NFs on the Si substrate.

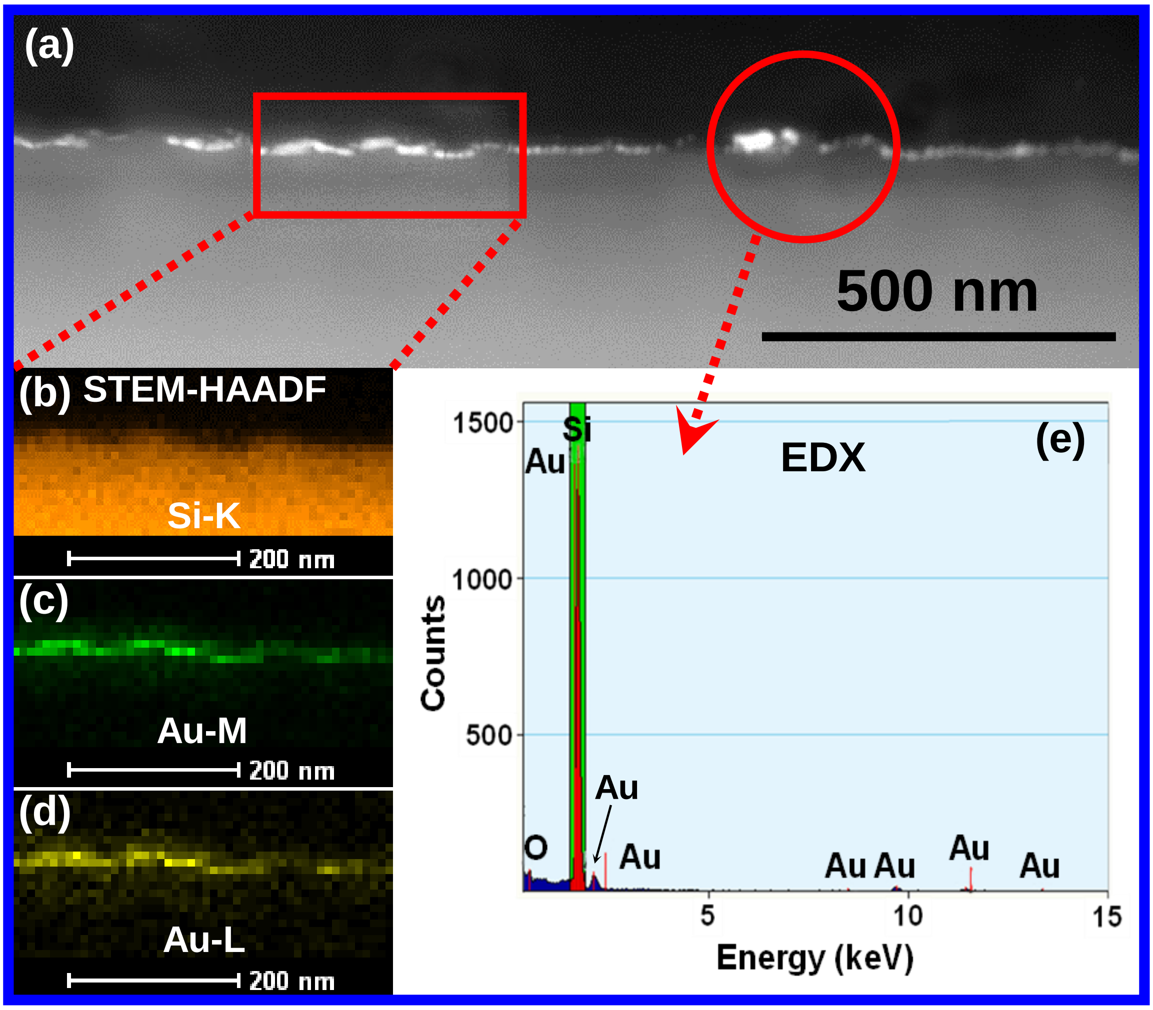

Figure 5.5: (a) low-magnification STEM-HAADF image of Au-NPs decorated Si-NFs at θ_g=70° (i.e. S3'), (b)-(d) EFTEM images corresponding to Si-K, Au-L, and Au-M, respectively obtained from red colored rectangle marked on the STEM-HAADF image, and (e) EDX profile obtained from red colored circle marked on the STEM-HAADF image.

On the other hand, a careful observation of the elemental color maps corresponding to Au-L and Au-M signals [Figs. 5.5(c)-(d)] shows the growth of Au-NPs on Si-NFs which corroborates well with our SEM [Fig. 5.2(c)-(h)] and XTEM [Fig. 5.4(a)] results. In addition, EDX measurement is also carried out from a region marked with red colored circle in Fig. 5.5(a) which reveals the presence of Si and Au besides a very small amount of O, arising from the random patches of native oxide present on Si-NFs as confirmed by the XTEM and XPS investigations. From the peak area analysis of the EDX spectra [Fig. 5.5(e)], the concentrations of Si, Au, and O are observed to be 93.6%, 5.3%, and 1.1%, respectively.

The presence of Au becomes further evident in all Au-NP decorated Si-NFs before and after annealing from the GIXRD measurements corresponding to a glancing angle of θ=1°. Figures 5.6(a) and (b) present GIXRD spectra obtained from all Au-NP decorated NF-Si substrates before and after annealing at 573 K for 1 h, albeit a similar trend is observed for all other growth angles of Au-NPs. GIXRD data before and after annealing of Au-NP decorated Si-NF samples reveal the polycrystalline nature of Au-NPs. In addition, annealing leads to increase in the peak intensity for all growth angles, indicating a grain growth of Au-NPs after annealing. This is followed by a reduction in the intensity of Au peaks with increasing growth angle before and after annealing. This clearly indicates a reduction in the coverage of Au-NPs at higher growth angles.

The presence of Au atoms were further confirmed from the XPS measurements on selective samples. For instance, XPS analysis of as-prepared Si-NFs reveal the presence of Si, Si-O, and Si-OH related bonds (spectrum not shown) which can be attributed to the formation of native oxide. On the other hand, appearance of Au 4*f* core level signals show the Au decorations of Si-NF samples [Fig. 5.6(c)]. Au-NPs were grown at an oblique angle of incidence of 70° (i.e. S3) and a representative one. A similar nature of Au 4*f* core level spectrum is observed for all other growth angles (data not shown towards maintaining the clarity). It may be mentioned that Fig. 5.6(c) presents the XPS data obtained from the specimen where a Gaussian fitting of this spectrum reveals that the two peaks correspond to binding energy for Au $4f_{7/2}$ and Au $4f_{5/2}$ located at 83.96 eV and 87.66 eV, respectively. The ratio of the peak area of $4f_{7/2}$ and $4f_{5/2}$ is found to be 1.37 with a characteristic difference of 3.7 eV in binding energy. In addition, a systematic reduction in the peak areas of Au core level signals with increasing growth angle of Au (spectra not shown) corroborate well with our SEM and XRD data described above.

In order to evaluate the effect of thermal annealing on the composition of Au-NP decorated Si-NF samples, XPS measurements are also carried out on the annealed samples.

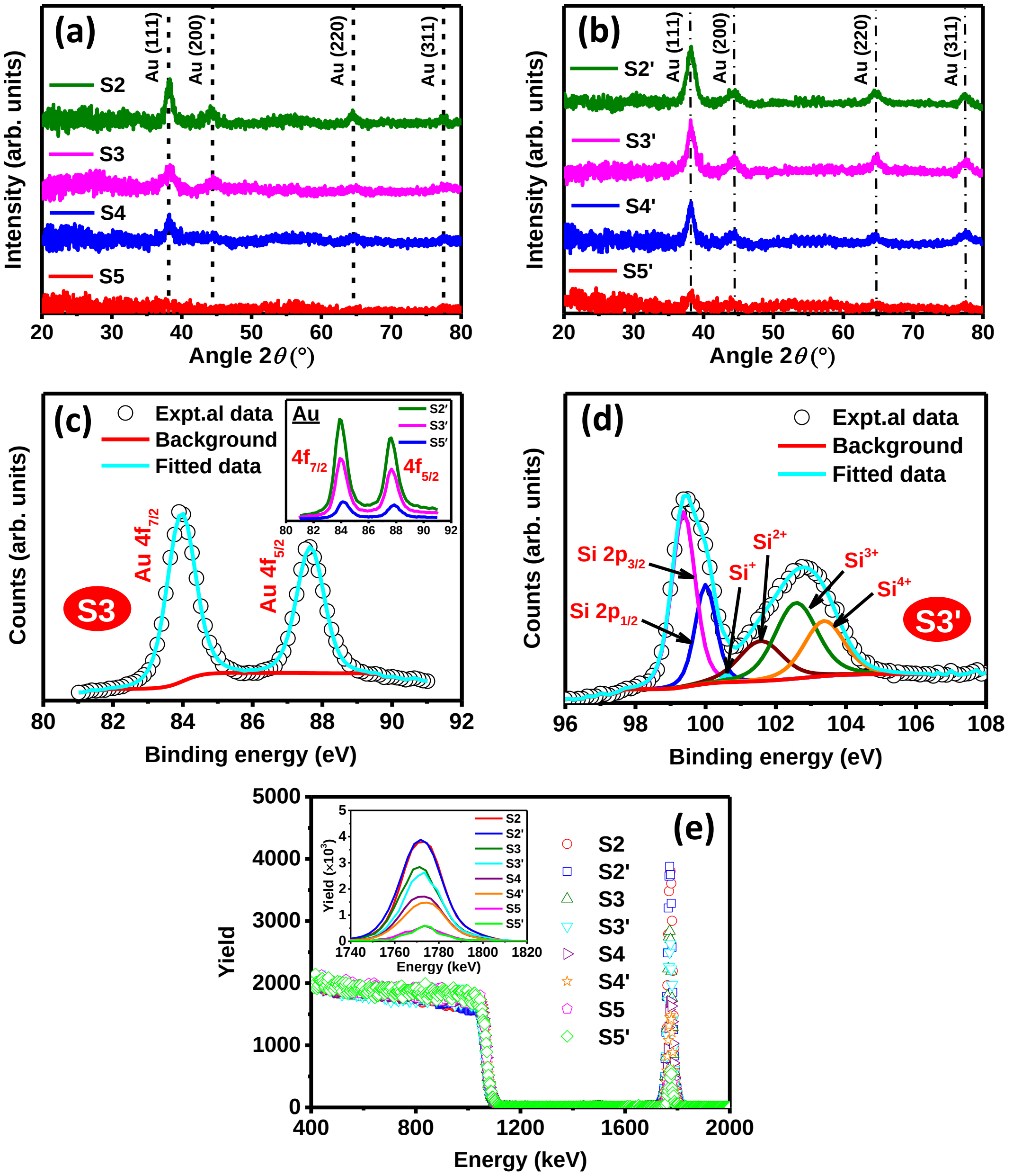

Figure 5.6**:** (a)-(b) GIXRD spectra of all Au-NP decorated NF-Si samples at θ_g=65°-85° before and after annealing (i.e. S2-S5 and S2'-S5'), respectively. (c) XPS spectrum of Au 4*f* core level obtained from S3 where inset depicts the comparative plot of Au 4*f* core level for S2', S3', and S5'. (d) Si 2*p* core level spectrum for S3'. (e) RBS spectra of all as-grown and annealed Au-NP decorated Si-NF samples grown at θ_g=65°, 70°, 80°, 85° (i.e. S2-S5 and S2'-S5').

For instance, the inset of Fig. 5.6(c) shows the overlapped Au $4f_{7/2}$ and $4f_{5/2}$ core level spectra corresponding to S2', S3', and S5'. It becomes evident that nature of the spectra and the peak positions remain the same after annealing. However, a systematic reduction in the peak intensity (area) reveals a decrease in the coverage of Au-NPs with increasing growth angle which is also seen for the as-grown samples and is in complete agreement with the SEM and XRD results described earlier (Table 5.1). On the other hand, Fig. 5.6(d) depicts the Si 2*p* spectrum corresponding to the specimen, S3' which is deconvoluted into five different peaks centred around binding energies of 99.37, 99.99, 100.6, 101.57, 102.58, and 103.38 corresponding to elemental Si, SiO_3, Si_2O_3, SiO_2, and Si-OH, respectively [45,54]. Similar trend in Si 2*p* spectrum is observed for all other samples as well (data not shown). Results obtained from the XPS measurements are summarized in Table 5.2.

Sample description	Growth angle (°)	State	Binding energy (eV)	FWHM (eV)
S3'	70	$4f_{5/2}$	87.66	0.94
		$4f_{7/2}$	83.96	0.97
S4'	80	$4f_{5/2}$	87.71	0.97
		$4f_{7/2}$	84.00	0.97
S5'	85	$4f_{5/2}$	87.87	1.02
		$4f_{7/2}$	84.17	0.98

Table 5.2: Binding energy and FWHM of XPS peaks corresponding to Au $4f_{7/2}$ and $4f_{5/2}$ are presented from the fitting of XPS spectra.

In order to have a quantitative measure of growth angle-dependent decoration of Au atoms on NF-Si substrates, we have also carried out RBS measurements. For instance, Fig. 5.6(e) depicts the RBS spectra of all as-grown and annealed Au-NP decorated Si-NF samples grown at θ_g=65°, 70°, 80°, 85°. The spectra of Au-NP decorated (corresponding to Au-growth angle of 65°) Si-NF samples before and after annealing are nearly identical and show the presence of Au and Si. Upon analyzing the spectra, the areal density of Au atoms turns out to be nearly same (2×10^{16} at. cm^{-2}) before and after annealing. Likewise, RBS data of Au-NP decorated (corresponding to θ_g=85°) Si-NF samples before and after annealing are demonstrated in Fig. 5.6(e). Simulation of these data also provides the nearly same areal density of Au (8×10^{14} at.

cm^{-2}) before and after annealing. These observations show 25 times less amount of Au atoms present in the case of highest growth angle i.e. θ_g=85° compared to the lowest growth angle (θ_g=65°). Likewise, areal density of Au atoms deposited on Si-NFs corresponding to the Au-growth angles of 70° and 80° turn out to be 1.5×10^{16} and 7.1×10^{15} at. cm^{-2}, respectively. In addition, there is hardly any change in the Au content (within the detection limit) of these two samples as well after postgrowth annealing. Therefore, RBS analyses show a systematic reduction in Au content with increasing θ_g, albeit postgrowth annealing expectedly does not influence the same [Fig. 5.6(e)]. Thus, RBS data qualitatively matches our SEM and XPS results where a systematic reduction in the amount of Au with increasing θ_g due to the shadowing effect, originating under an oblique angle geometry.

5.3.2 Work function mapping

It is known that work function of materials plays an important role in determining the electron emission current from cold cathode electron emitters [4,11,17,19,26,55]. At the same time, there can be a spatial variation in the work function of a nanostructured material which can effectively bring around changes in electron tunneling sites [4]. Therefore to address the cold cathode electron emission from NF-Si substrates and their Au-NP decorated counterparts (before and after annealing) local variation in the work function of these specimen are investigated using KPFM. This is a scanning probe microscopy (e.g. AFM)-based non-destructive tool where contact potential difference, V_{CPD} between a specimen and the metal-coated AFM tip is measured. Thus, the work function of a specimen (W_{sample}) can be written as: $W_{sample} = W_{tip} - eV_{CPD}$, where W_{tip} is the work function of metal-coated tip used during KPFM measurements and e is electronic charge [56]. Figures 5.7(a) and (b) depict the magnified topographic height images and the corresponding work function map of as-prepared Si-NFs (i.e. S1), respectively.

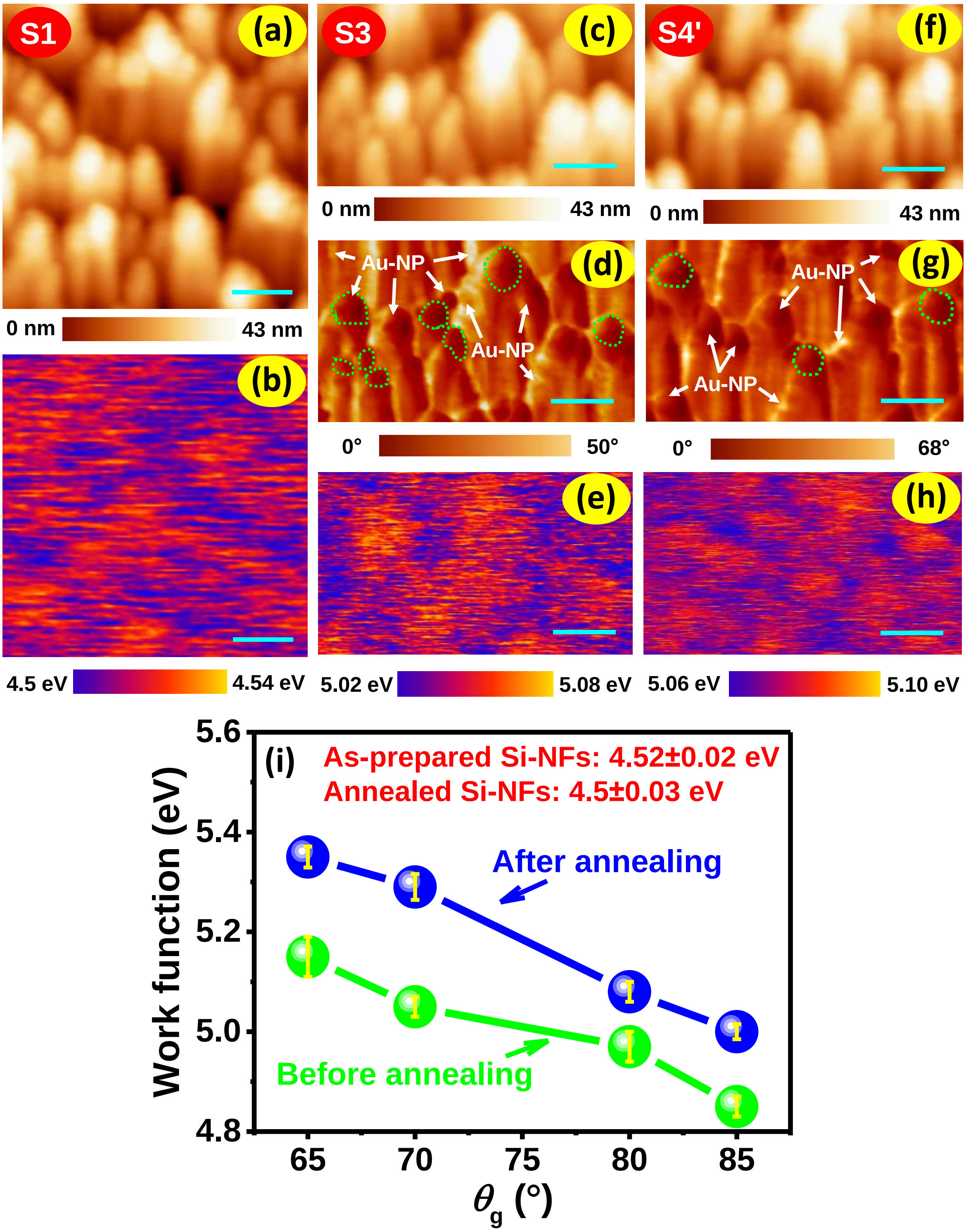

Figure 5.7: (a)-(b) Topography and corresponding work function map of as-prepared Si-NFs (i.e. S1),respectively. (c) Topography, (d) corresponding phase image, and (e) work function map obtained from as-deposited Au-NP decorated on Si-NFs at θ_g=70° (i.e. S3). Similarly, (f) Topography, (g) corresponding phase image, and (h) work function map obtained from postgrowth annealed Au-NP decorated on Si-NFs at θ_g=80° (i.e. S4'). (i) Plot of work function values (along with their spatial variation) against the Au-growth angle.

As a matter of fact, an experimentally measured V_{CPD} map (not shown) is converted into a work function map and in doing so, the work function, W_{tip}, of the Pt/Ir tip is measured to be ~4.85 eV with respect to a clean highly oriented pyrolytic graphite (HOPG) (SPI Supplies, USA) [57]. Accordingly, work function of the as-prepared Si-NF sample (i.e. S1) turns out to be 4.52 eV. In doing so, several randomly chosen spots on S1 are scanned (over large areas) to acquire the V_{CPD} maps. Subsequently, Si-NFs are decorated with Au-NPs corresponding to different growth angles, θ_g=65°, 70°, 80°, and 85°. Figure 5.7(c) depicts an AFM topographic height image corresponding to Au-NP decorated (θ_g=70°) NF-Si substrate (as a representative one). However, this image does not reveal the presence of smaller features like Au-NPs on and around Si-NFs. To overcome this problem, we present the corresponding AFM phase image in Fig. 5.7(d) which expectedly offers a better resolution [58] and thus enables us to observe the decoration of Au-NPs on the apexes and sidewalls of Si-NFs (some of which are marked with green dashed loops) which corroborates well with our SEM and XTEM results described above. On the other hand, Fig. 5.7(e) depicts the work function map of this sample (i.e. S3) which provides a work function of 5.05 eV. Likewise, Figs. 5.7(f) and (g) depict the surface topography and the phase image of S4' (i.e. postgrowth annealed counterpart of sample S4 corresponding to θ_g=80°), respectively. In this case also the AFM phase image helps to realize the presence of Au-NPs at the facet apexes and their sidewalls (marked by green closed loops) which otherwise remain hidden within the topographic height image [Fig. 5.7(f)]. Further, Fig. 5.7(h) presents the work function map of S4' which provides work function value of 5.08 eV. It is interesting to note that for all Au-NP decorated samples (including S4'), apexes of Si-NFs show relatively higher work function values, indicating the higher probability of Au-NP coated apexes to yield higher electron emitting current. The work function values of all other samples under investigation are also extracted in a similar fashion (images and work function maps not shown in order to maintain the clarity). Figure 5.7(i) demonstrates the plot of variation in work function of Au-NP decorated Si-NFs (as-deposited and postgrowth annealed) with θ_g (i.e. the growth angle of Au). From this figure, it is interesting to note that the work function of Au-NP decorated Si-NFs corresponding to θ_g=65° (i.e. S2) is the highest, viz. 5.15 eV, whereas it turns out to be the lowest (4.85 eV) for S5 (i.e. θ_g=85°). Upon annealing the samples at 573 K for 1 h, it is observed that work function of all Au-NP decorated NF-Si samples (corresponding to θ_g=65°, 70°, 80°, and 85°) increase, albeit a similar growth angle-dependent monotonically decreasing trend persists, viz. from 5.35 eV (for S2') to 5 eV (for S5'). This observation of decreasing trend in work function with increasing θ_g can be attributed to the presence of lesser amount of Au atoms at higher growth angles (as observed from our RBS measurements described earlier). On the other hand, an enhancement in the work function of all annealed Au-NP decorated NF-Si specimen (i.e. S2' to S5') compared to their as-deposited counterparts (i.e. S2-S5) can be attributed to an average increase in average dimension of Au-NPs during annealing through Ostwald ripening (Table 5.3). Such enhancements in the work function value with increasing dimension of Au-NPs are reported earlier [25,59,60] and are attributed to electrostatic effects like charge transfer between the substrate and the Au-NPs because of the mismatch in their work functions [60]. In order to further elucidate the relation between Au-NP size and the measured work function, it is important to note that in the present case, growth of uniform particle size does not take place on the facet apexes vis-à-vis their sidewalls of facets and edges [Figs. 5.2(c)-(h)], leading to a spatial variation in the work function of facets in these regions for each sample (data not shown). For instance, the average work function of S2 turn out to be 5.15 eV, whereas the same is found to be 5.05 eV for S3. In contrast, the average Au-NP diameter (~27 nm extracted from a large number of SEM images) at the apexes of Si-NFs corresponding to S3 turns out to be higher than the ones (~23 nm) seen to decorate the facet apexes of S2, albeit the average diameter of Au-NPs sitting on the sidewalls and edges of those facets turn out to be bigger for S2 in comparison to those in S3. As a result, the overall average diameter of Au-NPs for S2 turns out to be higher than that of S3. A similar trend is observed in their annealed counterparts (i.e. S2' and S3') as well. On the other hand, with further increase in θ_g, average diameter of Au-NPs reduces steadily on the facet apexes, sidewalls, and edges leading to reduced average work function of these samples. Such changes in work function values should in turn lead to changes in the cold cathode electron emission from these samples which is described later.

5.3.3 Electron field emission characteristics

In the quest of improving the efficacy of cold cathode electron emission from Si-NFs, smaller facets are fabricated than those reported in the literature [44]. In addition, NF-Si samples (S1) are decorated with self-organized Au-NPs deposited under several oblique angles of growth (in the range of 65°-85°) and all these samples are vacuum annealed at 573 K for 1 h.

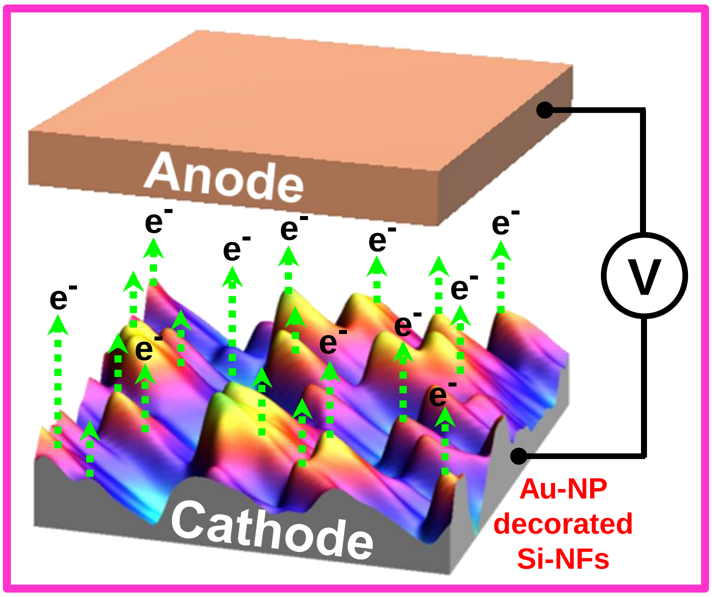

Figure 5.8: Schematic diagram of the cold cathode field electron emission from Au-NP decorated Si-NFs.

Subsequently, field emission characteristics are recorded from all the specimen before and after annealing. Figure 5.8 shows a schematic diagram of the cold cathode electron emission measurement geometry, whereas Figs. 5.9(a) and (b) show the plots for the current density (J)

versus applied electric field (E) for as-prepared and Au-NP decorated Si-NFs before and after annealing, respectively.

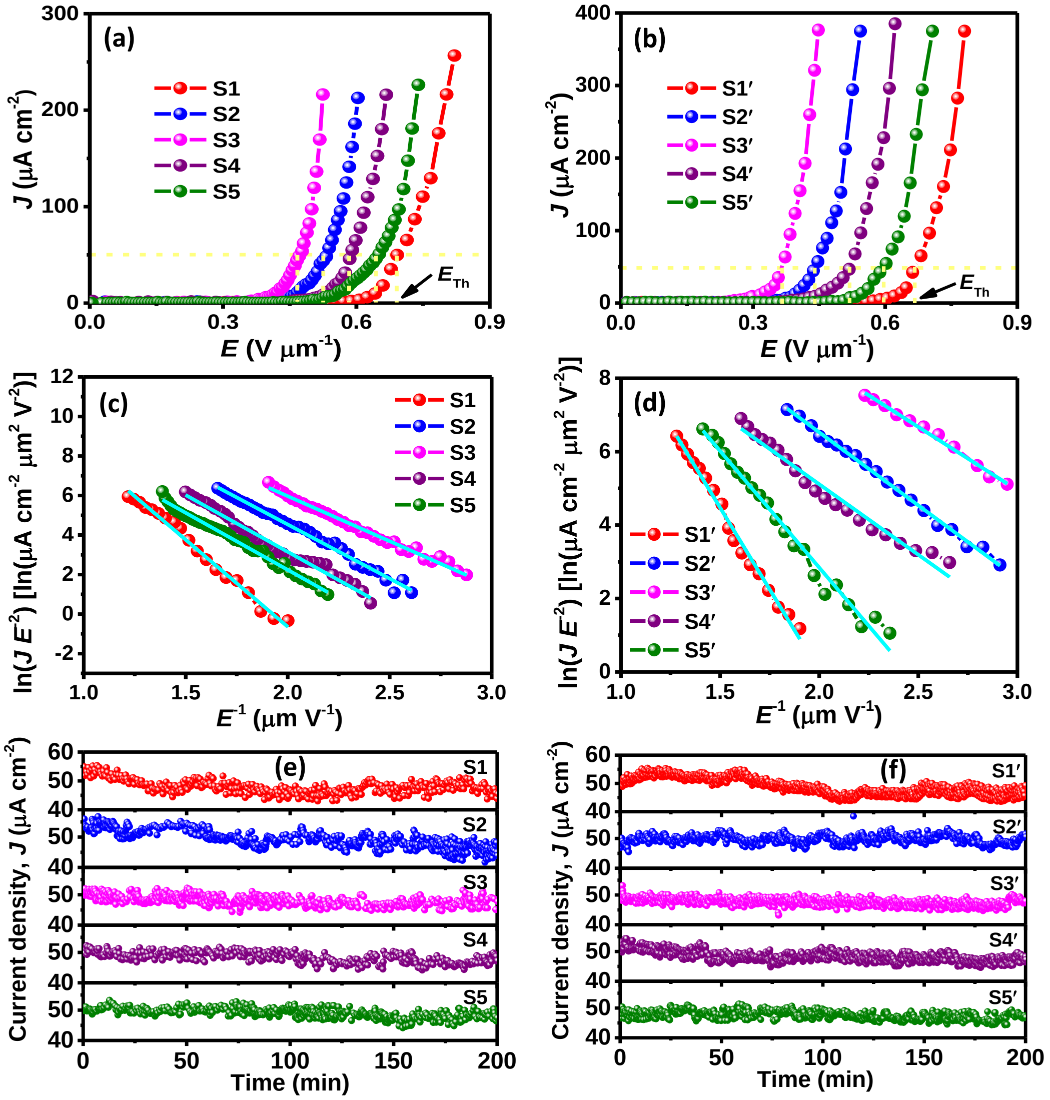

Figure 5.9**:** (a) Electron emission current density (J) versus applied electric field (E) plots corresponding to as-prepared Si-NFs and as-deposited Au-NPs on Si-NFs (i.e. S1-S5). Likewise, (b) J-E plots corresponding to annealed bare Si-NFs and as-deposited Au-NPs on Si-NFs (i.e. S1'-S5'). (c)-(d) FN plots [i.e. ln (J E^{-2}) versus E^{-1}] corresponding to as-prepared Si-NFs and Au-NP decorated NF-Si samples before and after annealing, respectively. Best linear fits to the data are presented with green lines. (e)-(f) Stability plots: Behaviour of electron emission current density as a function of time corresponding to before and after annealing of samples, respectively.

From Fig. 5.9(a), it becomes evident that turn-on field (E_{TO}, at which J becomes higher than the background) for as-prepared Si-NFs is 0.6 V μm^{-1} which, to the best of our knowledge, is by far the best-known for any Si-based nanostructures fabricated at RT. On the other hand, turn-on field reduces for Au-NP decorated NF-Si samples, viz. 0.44 and 0.39 V μm^{-1} for Au-NPs grown under θ_g=65° and 70°, respectively (i.e. S2 and S3). However, beyond θ_g=70°, it starts increasing (up to a growth angle of 85°) (Table 5.3). A similar trend is observed for all the specimen (S1'-S5') after annealing [Fig. 5.9(b)]. Moreover, a distinct reduction in the turn-on field is observed for all Au-NP decorated Si-NF samples as well as the bare Si-NFs specimen (viz. 0.58 V μm^{-1}). Indeed, the NF-Si specimen (i.e. S3') decorated with Au-NPs (corresponding to θ_g=70°) shows the lowest turn-on field (0.27 V μm^{-1}) which, to the best of our knowledge, is the lowest among all Si-based nanostructured materials. The values of turn-on field for Au-NP decorated Si-NFs (at all growth angles) after annealing are summarized in Table 5.3. It may be mentioned that the threshold field (E_{Th}, at which J becomes 50 $\mu A\ cm^{-2}$) for as-prepared and Au-NP decorated Si-NFs before and after annealing follow the similar trend as E_{TO} (Table 5.3).

To the best of our knowledge, the observed ultralow turn-on field (E_{TO}) values of as-prepared and Au-NP decorated Si-NFs (before and after annealing) are the best among Si-based nanostructures like Si nanowires (1.3 V μm^{-1}) [61], Si nanocones (4.2 V μm^{-1}) and its subsequent coating with Pt (3.65 V μm^{-1}) and Au (2.9 V μm^{-1}) [42], Si nanowires (5.01 V μm^{-1}) and annealed Au-coated Si nanowires (1.95 V μm^{-1}) [62], and silicon facets (0.67 V μm^{-1}) [11] besides these, the present results also offer better figure of merit compared to most of the well-established electron emitters such as vertically aligned carbon nanotubes (1.3 V μm^{-1}) [63], carbon nanowalls (0.9 V μm^{-1}) [64], WS_2 nanotubes (1.1 V μm^{-1}) [65], MoS_2 sheets (2.7 V μm^{-1}) [66], WS_2-RGO nanocomposites (2 V μm^{-1}) [67], free standing graphene sheets (2 V μm^{-1}) [68], Cu-O nanostructures (0.8 V μm^{-1}) [4].

Sample description	θg (°)	E_{TO} (V μm^{-1})	E_{Th} (V μm^{-1})	Work function Φ (eV)	β (using experimentally measured work function)
S1	As-prepared Si-NFs	0.60	0.69	4.52	8024
S2	65	0.44	0.53	5.15	16029
S3	70	0.39	0.47	5.05	18152
S4	80	0.51	0.59	4.97	13184
S5	85	0.52	0.64	4.85	12709
S1'	Annealed Si-NFs	0.58	0.66	4.5	7326
S2'	65	0.36	0.44	5.35	21236
S3'	70	0.27	0.37	5.29	24157
S4'	80	0.39	0.52	5.08	20365
S5'	85	0.51	0.59	5.0	12025

Table 5.3: Useful parameters i.e. turn-on field, threshold field, and field enhancement factor (β) (calculated using experimentally measured work function and the slope of respective FN-plots) obtained from bulk field emission and KPFM measurements of as-prepared Si-NFs and Au-NP decorated Si-NFs before and after annealing (S1-S5 and S1'-S5').

According to Fowler and Nordheim (FN) cold cathode electron emission is a quantum mechanical tunneling phenomenon where electrons tunnel from a material (cathode) to the anode (through vacuum) under an applied electric field. This can modulate the height of potential barrier at the interface of emitter surface and vacuum which can be described as the work function (φ) of the cathode (i.e. material under consideration) [Fig. 5.7(i)]. The FN equation is given by [13]:

$$J = \left(\frac{AE_f^2}{\phi}\right) \exp\left(\frac{-B\phi^{3/2}}{E_f}\right), \tag{1}$$

Where, J is the electron emission current density, E_f is the effective electric field felt on the localized apex area of the emitter surface, A=1.56×10^{-10} A V^{-2} eV and B=6.83×10^{3} V eV$^{-1.5}$

μm^{-1}, respectively [13]. Here $E_f = \beta E = -\beta(V/d)$ where d is the distance between anode and cathode, V is the applied voltage between the electrodes, and E is the corresponding external field. On the other hand, β is the field enhancement factor and is dependent on the emitter geometry. β plays a crucial role in enhancing the effective electric field on the apex area of the nanostructures, resulting in higher emission current. Following this, Figs. 5.9(a) and (b) are converted to plots between E^{-2} versus ln(JE^{-2}) [Fig. 5.9(c) and (d), respectively] and are fitted linearly, revealing FN tunneling phenomenon to be operative in both the cases (i.e. for as-deposited and annealed) Au-NP decorated NF-Si substrates as well as bare Si-NFs. The respective enhancement factor, β, extracted from the slope of these linear fits and using average work function obtained from KPFM measurements, turns out to be quite high for all samples (Table 5.3). For instance, as-prepared Si-NFs show a field enhancement factor, β, of 8024 which gets nearly doubled after Au-NP decoration corresponding to θ_g=65° which further increases for Au-NP decoration under a growth angle of 70° (β =18152), beyond which (i.e. θ_g>70°) it decreases. Subsequent postgrowth annealing gives rise to a further enhancement in β for all θ_g values in the range of 65°-85° which also depends on dimensions of Au-NPs, decorating the apexes of Si-NFs (besides sidewalls and edges). For instance, β is found to be maximum (β =24157) for θ_g=70° and minimum (β =12025) corresponding to θ_g=85°. Besides low turn-on field, the stability of field induced electron emission is an important issue from the viewpoint of display devices because an emitter surface get damaged due to localized thermal energy, originating from electronic collision. Thus, we have studied the stability of all the as-prepared and annealed samples under investigation. For instance, Fig. 5.9(e) and (f) present the behaviour of J for a continuous operation of 200 min for all the samples. It is interesting to note that all these plots demonstrate very good stability (at 50 μA cm^{-2}) with fluctuations within ±10% of the average value in each case. In addition, there being no further degradation in fluctuation over a significantly long period. It can be inferred that the Au-NP decorated Si-NFs as well as bare Si-NFs show very good potential for use in field emission-based devices.

In general, an enhanced FE performance of cold cathode electron emitter is attributed to the sharp tip and enhanced aspect ratio of nanostructures [69]. However, the Si-NFs presented in this work do not have so sharp apexes [Fig. 5.2(a)], compared to the ones reported in the literature [70–72]. In the present case, Au-NPs decoration on Si-NFs can serve as individual field emitters, which in turn, can increase the effective area of the electron emission and hence, contribute towards enhancing the FE performance of Au-NP decorated Si-NFs in comparison to as-prepared Si-NFs. Thus, to have a better understanding on the observed ultralow turn-on fields for cold cathode electron emission from Au-NP decorated Si-NFs, we employ local probe-based dual pass tunneling current microscopy technique to probe the electron emitting sites on Si-NFs as well as Au-NPs decorated Si-NFs.

5.3.4 Dual pass tunneling current microscopy

It is observed from the bulk FE measurements that the decoration of Si-NFs with Au-NPs leads to the tunneling of electrons at relatively lower turn-on fields compared to bare Si-NFs which suggests that Au-NPs promote the tunneling of electrons under externally applied electric fields. In addition, the observed growth angle-dependent self-organization of Au-NPs also plays a vital role in the observed FE performance. However, bulk FE measurements cannot provide any information on the electron emitting sites on Si-NFs (with and without Au-NP decorated ones). Hence, in order to probe the electron emitting sites for the bare and Au-NP decorated Si-NFs, DPTCM technique is employed [11]. In this case, during first pass, the AFM tip records the surface morphology (in contact mode), whereas in the second pass, the tip is raised at a constant height (lift height: 50 nm) over the surface by following the morphology data.

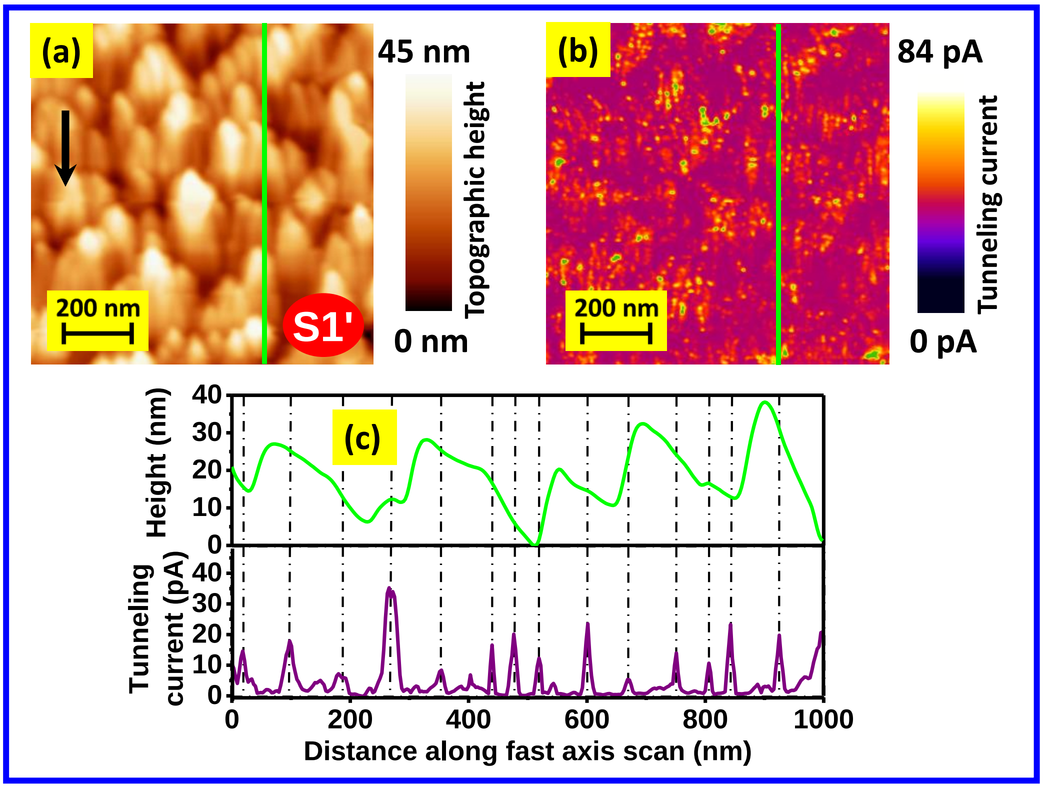

Figure 5.10: (a) AFM topography collected during the first pass and (b) corresponding tunneling current map obtained during the second pass from DPTCM measurement of S1'. (c) Corresponding profiles of topographic height and respective tunneling current obtained from the green lines marked on topography and tunneling current map.

However, during the second pass, a constant dc bias is applied to the tip with respect to the sample [17] which stimulates the electrons to tunnel from the sample and travel a certain distance (equal to the lift height) through the air. It is important to note that although all the samples are probed by DPTCM technique, to maintain the clarity in the presented data, tunneling current maps corresponding to the post-annealed bare (S1') and Au-NPs decorated Si-NFs with lowest observed threshold field (S3') are demonstrated. Several images were collected from various randomly chosen places on the sample to confirm the measured tunneling current to be a true reflection of the emission properties of Au-NPs decorated on NF-Si substrates and not an artefact arising out of the surface topography. Figures 5.10(a) and (b) depict the surface topography and corresponding tunneling current map of S1' (i.e. annealed bare Si-NFs) recorded during the first and second scan of DPTCM measurements, respectively.

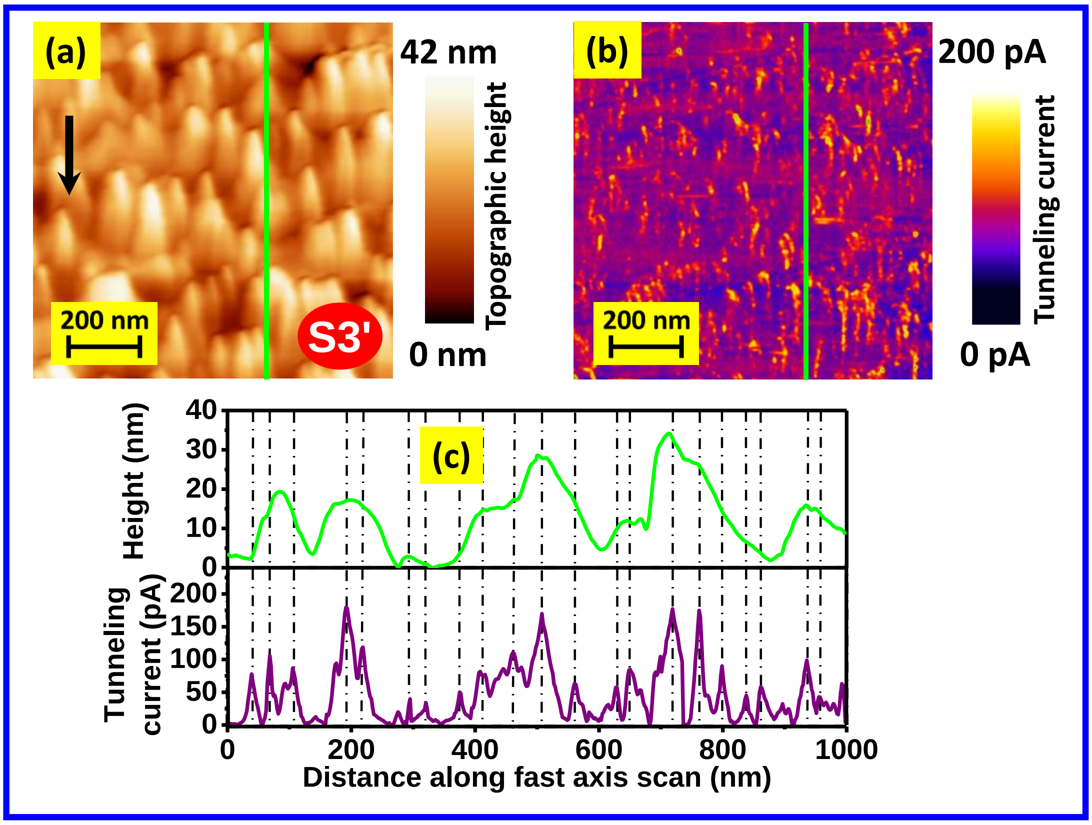

Figure 5.11: (a) AFM topography collected during the first pass and (b) corresponding tunneling current map obtained during the second pass from DPTCM measurement of S3'. (c) Corresponding profiles of topographic height and respective tunneling current obtained from the green lines marked on topography and tunneling current map.

The color contrast in the topographic height image is the measure of the height of the apexes and sidewalls with those of its valleys, however, the color contrast with bright spots in the tunneling current map [Fig. 5.10(b)] depicts the origin of tunneling current emitting sites. A plot of line profiles extracted from the marked green lines drawn across the topographic height image and the tunneling current map corresponding to S1' is shown in Fig. 5.10(c). It becomes evident from the line profile obtained from the tunneling current map that the sidewalls and valleys of Si-NFs are the prominent electron emitting sites rather than their apexes, which is further confirmed by the corresponding line profile [Fig. 5.10(c)]. This observation can be attributed to curvature-dependent coverage of native oxide predominantly on apexes of Si-NFs compared to their sidewalls and valleys, which give rise to an additional potential barrier to hinder/limit the tunneling of electrons [11]. Similarly, the topographical height image and the corresponding tunneling current map of S3' are shown in Figs. 5.11(a) and (b), respectively. The line profiles of the height image and the corresponding tunneling current map are extracted from the marked green lines [in Figs. 5.11(a) and (b)] and plotted in Fig. 5.11(c). From a careful observation of tunneling current map, it is revealed that mostly the apexes and sidewalls of Si-NFs are the preferential sites for electron emission (for an applied tip voltage of 5 V). Albeit, there is no significant emission current from their valleys. In fact, apexes of Si-NFs contribute the most in electron emission current compared to their sidewalls which happens for all other Au-NP decorated Si-NF samples. This is corroborated well with the SEM image shown in Fig. 5.2(g) where the apexes of Si-NFs are decorated with bigger Au-NPs in contrast to smaller Au-NP occupying their sidewalls. It is interesting to note that the tunneling currents obtained from S3 and S3' (corresponding to θ_g=70°) is the highest compared to all other samples under investigation. While it is understandable for Au-NPs grown under θ_g>70° (due to reduced areal density of Au and the reduced average diameter of Au-NPs for θ_g=80° and 85°), a reduction in the tunneling current for θ_g=65° (data not shown) can be attributed to the reduced average diameter of Au-NPs at the apexes of Si-NFs (as discussed earlier), though RBS data reveal that areal density of Au atoms is little higher in S2 and S2' compared to S3 and S3'. These observations corroborate well with our results obtained from SEM, GIXRD, and bulk field emission data discussed in the preceding sections. Therefore, it can be inferred that the tiny Au-NPs on Si-NFs individually work as cold cathode electron emission sites which in turn improves the effective electron emitting area (compared to bare Si-NFs), offering enhanced FE performances. To strengthen the above inference, the simulation studies are carried out to map the electrostatic field between the anode and the sample (electrically attached to cathode) is quite adequate to investigate the same.

5.3.5 Electrostatic field simulation

In order to have a complete picture on the role of Au-NPs and their size at the apexes of Si-NFs, quantum mechanical tunneling of electrons from a nanostructured cold cathode emitter under externally applied bias is revisited. Ease of electron emission relies on the potential barrier which depends on the emitter material. In the present case, emission of electrons from the Si-NFs is subjected to the tunneling of conduction band electrons via field-induced band bending of Si as depicted in Fig. 5.12(a). However, in case of metallic field emitters, free electrons of metal contribute in the field emission process unlike the semiconductors. For Au-NP decorated Si-NFs, Au-NPs assists the cold cathode electron emission as it is evident from the DPTCM measurements. However, to understand the role of Au-NPs and their size at the apexes of Si-NFs in field emission process, a model for Au-NPs assisted enhancement in the cold cathode electron emission performance of Si-NFs is proposed [Fig. 5.12(c)]. To facilitate the proposed model, electrostatic simulations are performed using finite element method (FEM)-based electrostatic field simulation between the anode (kept at a constant DC bias of +300 V) and the sample (electrically coupled to the grounded cathode) using a freely available Agros2D software [47]. Figures 5.12(d) and (e) present the electric field maps of Si-NFs decorated with small and relatively bigger Au-NPs, respectively. From the electric field mapping, it is observed that the field enhancement takes place at the apexes of Si-NFs decorated with Au-NPs. However, the sidewalls of Si-NFs also contribute in the field enhancement significantly. It is interesting to note that the Si-NFs decorated with relatively bigger Au-NPs [Fig. 5.12(e)] exhibit better field enhancement compared to the ones with small Au-NPs [Fig. 5.12(d)]. Hence, it can be concluded that mostly the apexes and sidewalls of Si-NFs decorated by Au-NPs contribute to the cold cathode electron emission. In addition, we also demonstrate the effects of increasing average diameter of Au-NPs on the apexes and their sidewalls of Si-NFs (due to postgrowth annealing), resulting in an enhanced electrostatic field intensity.

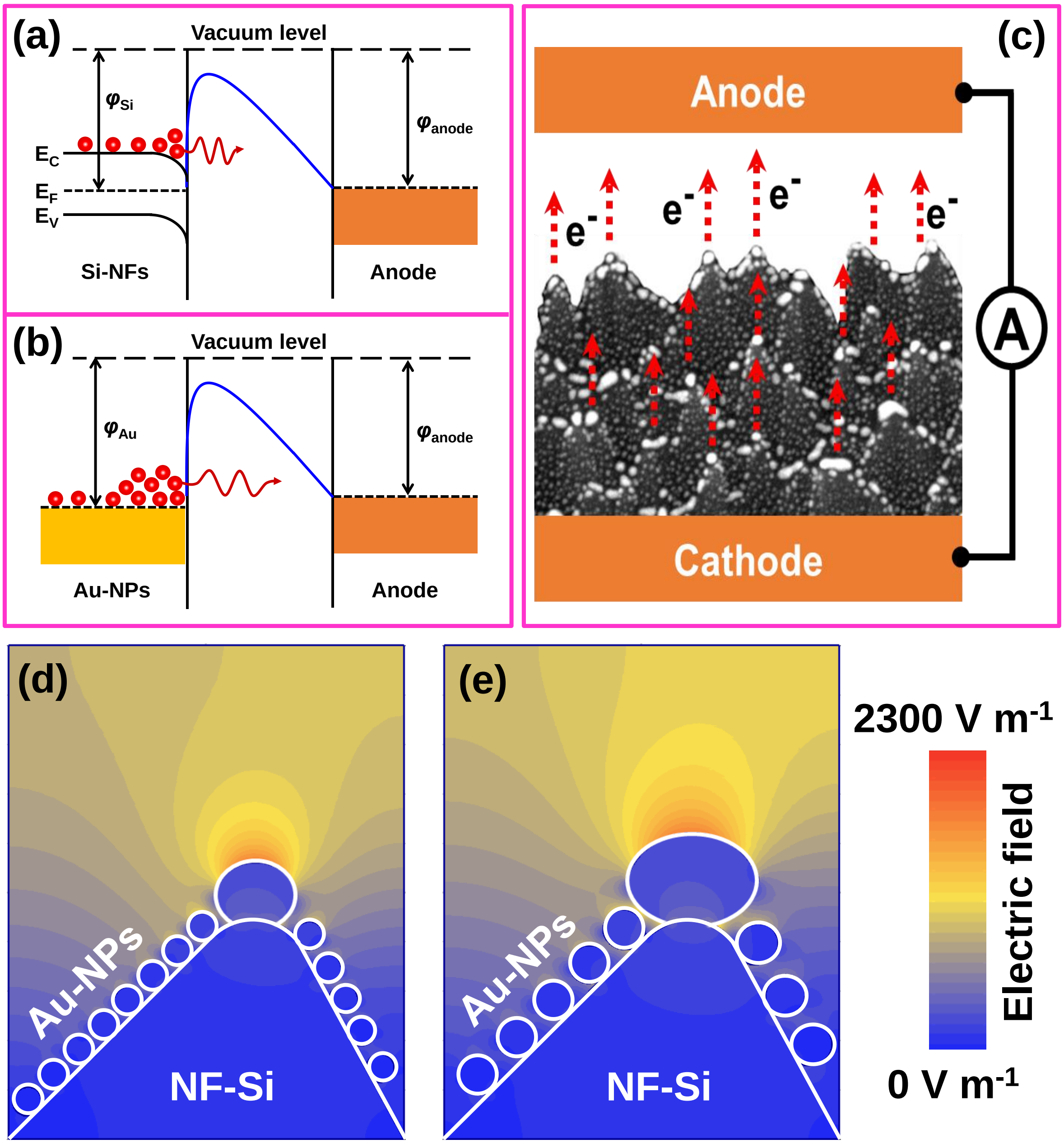

Figure 5.12: (a)-(b) Band alignment and presence of potential barrier for cold cathode electron emission process from Si and Au (cathode materials), respectively. (c) Proposed model for Au-NPs assisted enhancement in the cold cathode electron emission performance of Si-NFs. (d)-(e) Simulated electric field map of Si-NFs decorated with small and relatively bigger Au-NPs, respectively.

This suggest that the field enhancement and low threshold field emission is mainly governed by the Au-NP decoration of Si-NFs and in particular samples where bigger Au-NPs decorate the facet apexes should lead to a better field emission.

5.4. Conclusions

In conclusion, we demonstrate fascinating ultralow turn-on field for cold cathode electron emission from Au-NP decorated self-organized Si-NFs fabricated by 500 eV Ar ions at room temperature. We also demonstrate that the size and self-assembly of Au-NPs on Si-NFs can be easily altered by varying the growth angle of Au-NPs. This leads to a remarkable tunability in the turn-on field (in the range of 0.39─0.52 V μm^{-1}) and corresponding field enhancement factor (18152-12709). The turn-on field and β can be further tuned in the ranges of 0.27-0.51 V μm^{-1} and 24157-12025, respectively upon vacuum annealing at 573 K for 1 h. The SEM images demonstrate that self-organized Au-NPs get decorated both on the apexes and sidewalls of NFs. SEM analyses also reveal that the overall (average) diameter of Au-NPs reduce with increasing growth angle of Au on NF-Si substrates, albeit the average diameter of Au-NPs decorating the apexes of NFs is highest corresponding to the growth angle of 70°. This is followed by a grain growth for Au-NPs after annealing (for all growth angles). In addition RBS studies show that the areal density of Au atoms decreases with increasing growth angle. GIXRD data depict the polycrystalline nature of Au-NPs and grain growth take place after annealing. The growth angle-dependent reduction in the Au atoms is further confirmed by XPS measurements. KPFM-based work function measurements divulge a monotonically decreasing work function with increasing growth angle for both as-prepared and annealed samples, although annealing leads to an increase in the work function of NF-Si samples corresponding to all growth angles. This is attributed to an increase in diameter of Au-NPs after annealing. AFM-based DPTCM measurements provide a direct evidence on the electron emission sites, viz. the apexes and sidewalls of Au-NP decorated Si-NFs (in contrast to sidewalls and valleys for bare Si-NFs), albeit Au-NPs sitting on the apexes of Si-NFs contribute more in the electron emission process. Furthermore, our electrostatic field based simulation results reveal that Au-NPs sitting on the facet apexes serve as better individual field emitters and the FE performance enhances for bigger Au-NPs formed after postgrowth annealing through an enhancement in the local electrostatic field. Thus we conclude that our experimental results manifest a direct and novel way to address the origin of cold cathode electron emission from self-organized Au-NP decorated Si-NFs by employing a combination of bulk and local probe techniques that are further supported by the electrostatic field simulation studies. The present study also paves the way to fabricate Si nanostructure-based efficient field emitters with tunable and ultralow turn-on fields.

Bibliography

[1] K. Ariga, "*Manipulation of nanoscale materials*", Royal Society of Chemistry, Cambridge, 2012.

[2] S.E. Hunyadi Murph, G.K. Larsen, K.J. Coopersmith, eds., "*Anisotropic and shape-selective nanomaterials*", Springer International Publishing, Cham, 2017.

[3] F. Priolo, T. Gregorkiewicz, M. Galli, T.F. Krauss, Nat. Nanotechnol. 9 (2014) 19–32.

[4] S. Nandy, R. Thapa, M. Kumar, T. Som, N. Bundaleski, O.M.N.D. Teodoro, R. Martins, E. Fortunato, Adv. Funct. Mater. 25 (2015) 947–956.

[5] N. Egorov, E. Sheshin, in: Springer Ser. Adv. Microelectron., 2017, pp. 427–538.

[6] Y. Fan, M. Rose, in: Handb. Vis. Disp. Technol., Springer Berlin Heidelberg, Berlin, Heidelberg, 2012, pp. 1071–1103.

[7] A. Basu, M.E. Swanwick, A.A. Fomani, L.F. Velásquez-García, J. Phys. D. Appl. Phys. 48 (2015) 225501.

[8] S. Cheng, F.A. Hill, E. V Heubel, L.F.V. Quez-García, J. Phys. Conf. Ser. 476 (2013) 012016.

[9] A.A. Fomani, A.I. Akinwande, L.F. Velásquez-García, J. Phys. Conf. Ser. 476 (2013)

012014.

[10] S. Chatterjee, M. Kumar, A. Pal, I. Thakur, T. Som, J. Mater. Chem. C 3 (2015) 6389–6394.

[11] T. Basu, M. Kumar, M. Saini, J. Ghatak, B. Satpati, T. Som, ACS Appl. Mater. Interfaces 9 (2017) 38931–38942.

[12] X. Fang, Y. Bando, U.K. Gautam, C. Ye, D. Golberg, J. Mater. Chem. 18 (2008) 509–522.

[13] R.H. Fowler, L. Nordheim, in: Proc. R. Soc. A Math. Phys. Eng. Sci., World Scientfic, 1928, pp. 683–691.

[14] M. Choueib, R. Martel, C.S. Cojocaru, A. Ayari, P. Vincent, S.T. Purcell, ACS Nano 6 (2012) 7463–7471.

[15] B. Zeng, G. Xiong, S. Chen, W. Wang, D.Z. Wang, Z.F. Ren, Appl. Phys. Lett. 90 (2007) 033112.

[16] C.S. Chang, S. Chattopadhyay, L.C. Chen, K.H. Chen, C.W. Chen, Y.F. Chen, R. Collazo, Z. Sitar, Phys. Rev. B 68 (2003) 125322.

[17] A. Singh, K. Senapati, M. Kumar, T. Som, A.K. Sinha, P.K. Sahoo, Appl. Surf. Sci. 411 (2017) 117–123.

[18] Y.-J. Hung, Y.-J. Huang, H.-C. Chang, K.-Y. Lee, S.-L. Lee, Nanoscale Res. Lett. 9 (2014) 540.

[19] A. Ghosh, P. Guha, R. Thapa, S. Selvaraj, M. Kumar, B. Rakshit, T. Dash, R. Bar, S.K. Ray, P.V. Satyam, Nanotechnology 27 (2016) 125701.

[20] U.A. Palnitkar, R. V. Kashid, M.A. More, D.S. Joag, L.S. Panchakarla, C.N.R. Rao,

Appl. Phys. Lett. 97 (2010) 063102.

[21] S. Chen, M. Shang, F. Gao, L. Wang, P. Ying, W. Yang, X. Fang, Adv. Sci. 3 (2015) 1500256.

[22] C.X. Xu, X.W. Sun, B.J. Chen, Appl. Phys. Lett. 84 (2004) 1540–1542.

[23] S. Sridhar, C. Tiwary, S. Vinod, J.J. Taha-Tijerina, S. Sridhar, K. Kalaga, B. Sirota, A.H.C. Hart, S. Ozden, R.K. Sinha, Harsh, R. Vajtai, W. Choi, K. Kordás, P.M. Ajayan, ACS Nano 8 (2014) 7763–7770.

[24] Q. Dong, S. Chen, Q. Chen, F. Gao, L. Wang, Z. Xie, W. Yang, Appl. Phys. Lett. 109 (2016) 082104.

[25] Q. Chen, S. Chen, F. Gao, L. Wang, Z. Xie, W. Yang, J. Mater. Chem. C 4 (2016) 1363–1368.

[26] P. Guha, A. Ghosh, R. Thapa, E.M. Kumar, S. Kirishwaran, R. Singh, P. V. Satyam, Nanotechnology 28 (2017) 415602.

[27] B. Das, D. Sarkar, S. Maity, K.K. Chattopadhyay, J. Mater. Chem. C 3 (2015) 1766–1775.

[28] X. Fang, Y. Bando, C. Ye, G. Shen, U.K. Gautam, C. Tang, D. Golberg, Chem. Commun. 7345 (2007) 4093.

[29] K.L. Aplin, C.M. Collingwood, B.J. Kent, J. Phys. D. Appl. Phys. 37 (2004) 2009–2017.

[30] J.D. Holmes, K.P. Johnston, R.C. Doty, B.A. Korgel, Science (80-.). 287 (2000) 1471–1473.

[31] G. Audoit, É.N. Mhuircheartaigh, S.M. Lipson, M.A. Morris, W.J. Blau, J.D. Holmes,

J. Mater. Chem. 15 (2005) 4809.

[32] T.F. Teepen, A.H. V. van Veen, H. van’t Spijker, S.W.H.K. Steenbrink, A. van Zuuk, C.T.H. Heerkens, M.J. Wieland, N.J. van Druten, P. Kruit, H. van’t Spijker, S.W.H.K. Steenbrink, A. van Zuuk, C.T.H. Heerkens, M.J. Wieland, N.J. van Druten, P. Kruit, J. Vac. Sci. Technol. B 23 (2005) 359–369.

[33] N.N. Kulkarni, J. Bae, C.-K.K. Shih, S.K. Stanley, S.S. Coffee, J.G. Ekerdt, Appl. Phys. Lett. 87 (2005) 1–3.

[34] G.S. Huang, X.L. Wu, Y.C. Cheng, X.F. Li, S.H. Luo, T. Feng, P.K. Chu, Nanotechnology 17 (2006) 5573–5576.

[35] C. Mu, Y. Yu, W. Liao, X. Zhao, D. Xu, X. Chen, D. Yu, Appl. Phys. Lett. 87 (2005) 1–4.

[36] T. Som and D. Kanjilal, eds., *"Nanofabrication by ion-beam sputtering: From fundamentals to applications"*, CRC Press, 2012.

[37] T. Basu, J.R. Mohanty, T. Som, Appl. Surf. Sci. 258 (2012) 9944–9948.

[38] C.S. Madi, B. Davidovitch, H.B. George, S.A. Norris, M.P. Brenner, M.J. Aziz, Phys. Rev. Lett. 101 (2008) 10–13.

[39] J.C. Perkinson, C.S. Madi, M.J. Aziz, J. Vac. Sci. Technol. A Vacuum, Surfaces, Film. 31 (2013) 021405.

[40] V. Chatterjee, R. Harniman, P.W. May, P.K. Barhai, Appl. Phys. Lett. 104 (2014) 171907.

[41] T. Basu, D.P. Datta, T. Som, Nanoscale Res. Lett. (2013).

[42] Y.M. Chang, P.H. Kao, H.M. Tai, H.W. Wang, C.M. Lin, H.Y. Lee, J.Y. Juang, Phys.

Chem. Chem. Phys. 15 (2013) 10761–10766.

[43] M. Engler, S. Macko, F. Frost, T. Michely, 245412 (2014) 1–14.

[44] T. Basu, T. Som, Appl. Surf. Sci. 418 (2017) 340–345.

[45] T. Basu, M. Kumar, A. Kanjilal, J. Ghatak, P.K. Sahoo, T. Som, J. Appl. Phys. 116 (2014) 114309.

[46] I. Horcas, R. Fernández, J.M. Gómez-Rodríguez, J. Colchero, J. Gómez-Herrero, A.M. Baro, Rev. Sci. Instrum. 78 (2007) 013705.

[47] P. Karban, F. Mach, P. Kůs, D. Pánek, I. Doležel, Computing 95 (2013) 381–408.

[48] M.M. Hawkeye, M.T. Taschuk, M.J. Brett, Glancing Angle Deposition of Thin Films, John Wiley & Sons, Ltd, Chichester, UK, 2014.

[49] M. Bhatnagar, M. Ranjan, K. Jolley, A. Lloyd, R. Smith, S. Mukherjee, Nucl. Instruments Methods Phys. Res. Sect. B Beam Interact. with Mater. Atoms 393 (2017) 5–12.

[50] C.T. Rueden, J. Schindelin, M.C. Hiner, B.E. DeZonia, A.E. Walter, E.T. Arena, K.W. Eliceiri, BMC Bioinformatics 18 (2017) 529.

[51] M. Engler, S. Macko, F. Frost, T. Michely, Phys. Rev. B - Condens. Matter Mater. Phys. 89 (2014) 1–14.

[52] J.B. Hannon, S. Kodambaka, F.M. Ross, R.M. Tromp, Nature 440 (2006) 69–71.

[53] K. Nakashima, M. Iwami, A. Hiraki, Thin Solid Films 25 (1975) 423–430.

[54] M.Y. Bashouti, J. Ristein, H. Haick, S. Christiansen, Hybrid Mater. 1 (2013).

[55] M. Kumar, D.Y. Park, R. Singh, M.S. Jeong, T. Som, J. Kim, ACS Appl. Mater. Interfaces (2019) acsami.9b08844.

[56] R. Singh, A. Dutta, P. Nandi, S.K. Srivastava, T. Som, Appl. Surf. Sci. 493 (2019) 577–586.

[57] L. Yan, C. Punckt, I.A. Aksay, W. Mertin, G. Bacher, Nano Lett. 11 (2011) 3543–3549.

[58] T. Basu, M. Kumar, S. Nandy, B. Satpati, C.P. Saini, A. Kanjilal, T. Som, J. Appl. Phys. 118 (2015).

[59] F. Ruffino, M.G. Grimaldi, F. Giannazzo, F. Roccaforte, V. Raineri, Appl. Phys. Lett. 89 (2006) 243113.

[60] Y. Zhang, O. Pluchery, L. Caillard, A.F. Lamic-Humblot, S. Casale, Y.J. Chabal, M. Salmeron, Nano Lett. 15 (2015) 51–55.

[61] S.L. Cheng, H.C. Lin, Y.H. Huang, S.C. Yang, RSC Adv. 7 (2017) 23935–23941.

[62] F. Zhao, G. an Cheng, R. ting Zheng, D. dan Zhao, S. long Wu, J. hua Deng, Nanoscale Res. Lett. 6 (2011) 176.

[63] A. Pandey, A. Prasad, J.P. Moscatello, M. Engelhard, C. Wang, Y.K. Yap, ACS Nano 7 (2013) 117–125.

[64] E. Stratakis, R. Giorgi, M. Barberoglou, T. Dikonimos, E. Salernitano, N. Lisi, E. Kymakis, Appl. Phys. Lett. 96 (2010) 043110.

[65] G. Viskadouros, a Zak, M. Stylianakis, E. Kymakis, R. Tenne, E. Stratakis, Small 10 (2014) 2398–403.

[66] R. V. Kashid, D.J. Late, S.S. Chou, Y.K. Huang, M. De, D.S. Joag, M.A. More, V.P. Dravid, Small 9 (2013) 2730–2734.

[67] C.S. Rout, P.D. Joshi, R. V. Kashid, D.S. Joag, M.A. More, A.J. Simbeck, M.

Washington, S.K. Nayak, D.J. Late, Sci. Rep. 3 (2013) 3282.

[68] J. Xu, G. Hou, H. Li, T. Zhai, B. Dong, H. Yan, Y. Wang, B. Yu, Y. Bando, D. Golberg, NPG Asia Mater. 5 (2013) e53–e53.

[69] C.J. Park, D.K. Choi, J. Yoo, G.C. Yi, C.J. Lee, Appl. Phys. Lett. 90 (2007) 98–101.

[70] M.E. Swanwick, P.D. Keathley, A. Fallahi, P.R. Krogen, G. Laurent, J. Moses, F.X. Kärtner, L.F. Velásquez-García, Nano Lett. 14 (2014) 5035–5043.

[71] S. Ravipati, C.-J.J. Kuo, J. Shieh, C.-T.T. Chou, F.-H.H. Ko, Microelectron. Reliab. 50 (2010) 1973–1976.

[72] S.A. Guerrera, A.I. Akinwande, Nanotechnology 27 (2016) 295302.

CHAPTER 6

Broadband antireflection of ZTO thin films on patterned-Si substrates

In this chapter, we have demonstrated the sputter-grown ZTO film thickness dependent broadband antireflection (AR) property of ion-beam patterned-Si substrates. In particular, low energy ion-beam patterned (rippled- and faceted-Si) silicon substrates were used as templates for the growth of ZTO thin films. Furthermore, the antireflection efficacy of ZTO thin films grown on patterned-silicon substrates is compared with their *pristine*-Si counterparts.

6.1 Introduction

Zinc oxide (ZnO) is an important multifunctional II-VI semiconductor with a wide bandgap of 3.37 eV (at room temperature) and a large excitonic binding energy of ~60 meV, which is suitable for wide range of emerging applications such as transparent electrode, AR coatings, light emitting diodes (LEDs), solar cells, and transparent thin film transistors (TFTs) and so on [1–10]. It is highly transparent for visible light and offers *n*-type conductivity which can be enhanced up to three to four orders of magnitude after doping with Al and Sn [11,12]. For instance, in case of Sn-doping in ZnO, the ionic radius of Sn^{4+} (0.069 nm) is smaller than Zn^{2+} (0.074 nm) and thus, Sn^{4+} substitutes Zn^{2+} site in the ZnO crystal structure, resulting in two more free electrons to contribute to the electric conduction [11]. Hence, zinc tin oxide has emerged with improved electron mobility and high transparency in the visible spectrum for applications based on transparent conductive oxides (TCOs).

Recently, ZTO is being used as a window layer and top electrode for next-generation highly efficient Si-based heterojunction solar cells [13–15]. Reduced front surface reflection is an essential criterion to enhance the efficiency of silicon-based solar cells. As a matter of fact,

~35% of the incident light is lost through Fresnel reflection due to a large and abrupt change in the RI at the interface of Si (n_{Si}~3.4) and air (n_{air}=1). Therefore, AR plays an important role to enhance light absorption towards fabricating silicon-based heterojunction solar cells having higher efficiencies [16–18]. An efficient AR coating, preferably in the form of a TCO, is required to improve the performance of a silicon solar cell via an increased light coupling. In fact, these AR coatings reduce the intensity of reflected waves on the basis of thin film interference property. In particular, the growth of a single layer AR coating on micro/nano-patterned surfaces is helpful in reducing the reflection losses over a broad spectral range [19–22].

In this study, we show the efficacy of ion-beam fabricated self-organised *R*-Si and *F*-Si in prompting light trapping through a significant reduction in reflection losses when ZTO thin films are grown on them. For instance, we demonstrate the broadband (in the wavelength range of 300-800 nm) AR property in conformally grown ZTO thin films on ion-beam patterned Si substrates and compare the same with the one grown simultaneously on a *P*-Si substrate. This study will be useful to explore the role of patterned surfaces for the growth of conformal TCO overlayers as single layer AR coatings for broadband light harvesting which is essential for fabrication of efficient photovoltaic devices.

6.2 Experimental detail

An ultrahigh vacuum (UHV)-compatible experimental chamber (Prevac, Poland) was used which is equipped with an electron cyclotron resonance (ECR)-based broad-beam ion-source (GEN-II, Tectra GmbH, Germany) and a five-axes sample manipulator. A sacrificial wafer of *p*-type Si (2×2 cm^2) was used in between the sample (1×1 cm^2) and the sample-holder to avoid the sputtering induced impurities on the sample [23]. The measured beam diameter and the fixed ion flux is 3 cm and 1.3×10^{14} ions cm^{-2} s^{-1}, respectively. Ultrasonically cleaned *p*-type Si(100) substrates were exposed to 500 eV Ar$^+$ ions at room temperature (RT) and two oblique angles of incidence viz. 65° and 72.5° (with respect to the surface normal) for an ion fluence of 5×10^{17} ions cm^{-2} towards the fabrication of nanoscale ripples and facets, respectively on Si surfaces [23,24].

Following this, an RF magnetron sputtering system (Advanced Energy, USA) was used with commercially available $ZnO:SnO_2$ (1:1 molar ratio) target (MTI corporation, USA) for the deposition of ZTO films of different thickness values in the range of 15-120 nm at RT on *P*-, *R*-, and *F*-Si substrates at 30 sccm of Ar gas flow rate, resulting in an working pressure of 5×10^{-3} mbar in the growth chamber. An RF (13.56 MHz) power of 100 W was used for the growth of ZTO thin films where the target-to-substrate distance was kept at 10 cm. The deposition was performed under normal incidence using a constant substrate rotation of 3 rpm. For the sake of comparison, ZTO thin films were simultaneously grown on a *P*-Si substrate along with *R*-Si and *F*-Si substrates. Film thickness measurement on all ZTO films were carried out by a thickness profilometer (XP 200, Ambios, USA). Figure 6.1 shows the process flow for fabrication of ion-beam induced ripples and facets on Si-substrates at various angles of incidence and further deposition of ZTO overlayers on them.

Surface morphology was studied using atomic force microscopy (AFM) (MFP3D, Asylum Research, USA). Several images were collected from various randomly chosen places to confirm the pattern and film uniformities. AFM images were analyzed by employing WSxM software [25]. X-ray diffraction (XRD) measurements were performed under the Bragg-Brentano geometry using a Cu-K_α (λ=0.154 nm) radiation (Bruker D8 Discover, Germany). Compositional analyses on selective ZTO-coated samples were performed using x-ray photoelectron spectroscopy (XPS) system (PHI 5000 Versa Probe II, ULVAC–PHI, Japan) with a microfocused (100 µm, 25 W, 15 KV) monochromatic Al-K_α source ($h\nu$=1486.6 eV), a hemispherical analyzer, and a multichannel detector. Reflectance measurements were performed using a UV-Vis spectrophotometer (3101PC, Shimadzu, Japan) in the wavelength range of 300 to 800 nm with the help of unpolarized light.

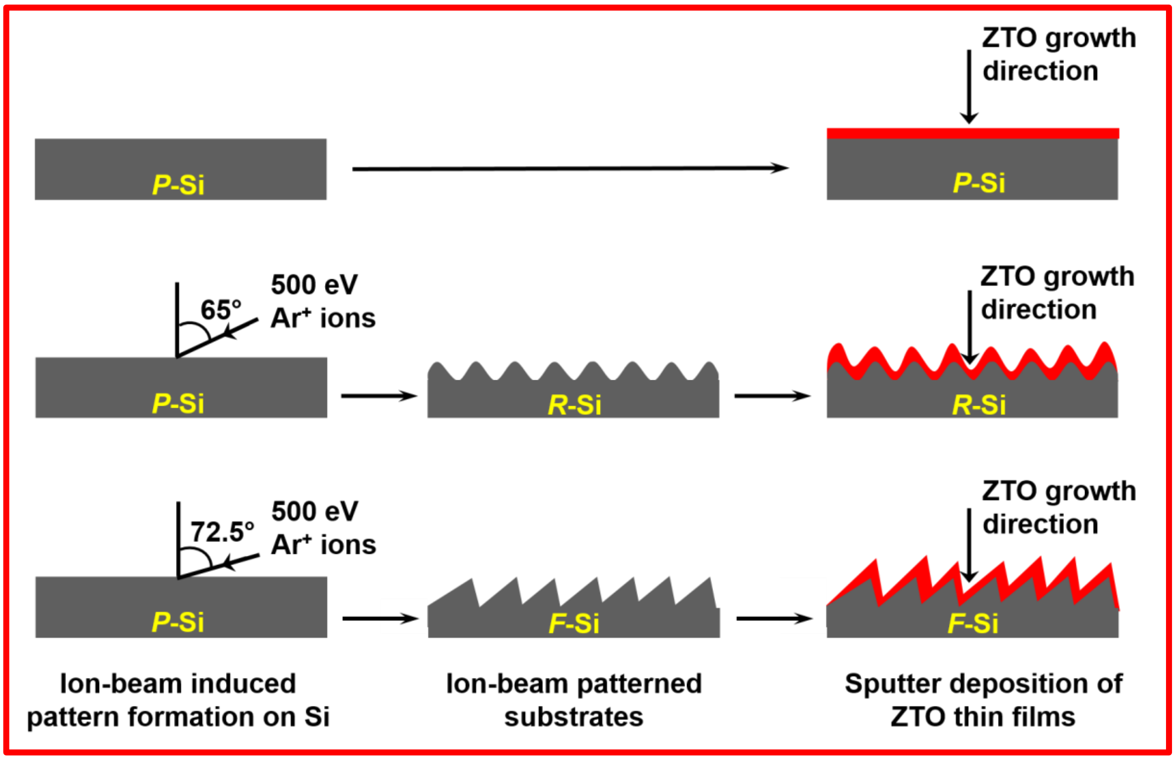

Figure 6.1: Schematic diagram of the process flow for ion-beam fabrication of *R*- and *F*-Si substrates followed by conformal growth of ZTO films on them along with *P*-Si.

6.3 Results and discussion

Figures 6.2(a)-(o) show the AFM micrographs of *P*-, *R*-, and *F*-Si substrates before and after the growth of ZTO overlayers of different thicknesses. For instance, Fig. 6.2(a) shows the AFM image of a *P*-Si substrate having an rms roughness of 0.12 nm where the corresponding two-dimensional (2D) fast Fourier transform (FFT), in the inset, shows an isotropic surface. However, Figs. 6.2(b) and (c) present the AFM topographic images of ion-beam fabricated nanostructures on silicon surfaces followed by their exposure to Ar-ions at an incidence angle of 65° and 72.5° (with respect to the surface normal), respectively. Here the former one manifests a ripple-patterned Si substrate [Fig. 6.2(b)] where the ripples are found to have an average wavelength of 30±1 nm with an amplitude of 3.2 nm (rms roughness is found to be 1.2 nm). In addition, the corresponding 2D-FFT image, as is depicted in the inset of Fig. 6.2(b), clearly illustrates the presence of anisotropy in the surface morphology across the ion-beam projection onto the surface. On the other hand, the AFM image shown in Fig. 6.2(c) depicts nanofacets which mostly point towards the direction of incident ion-beam. From the topographical analysis, it is observed that the rms roughness of this nanostructured surface is 15.3 nm with an average facet height of 39.3 nm and average base-width of 200 nm. A 2D-FFT image of the same is presented in the inset of Fig. 6.2(c), showing a clear signature of anisotropic surface morphology. It is well-known that self-organized periodic nanostructures originate due to a dynamic balance among various fundamental kinetic processes under ion bombardment [26]. According to the classical linear stability theory proposed by Bradley and Harper (B-H) [27], formation of ripples occurs at oblique angles by the dynamic balance of surface roughening via curvature-dependent sputtering (in which erosion rate is enhanced for concave surfaces rather than convex surfaces) and smoothing via surface diffusion. However, later on the role of atomic mass redistribution has also been shown to play an important role in pattern formation [28–30]. At certain higher oblique angles of incidence~~,~~ the ratio of ripple height (h_0) to ripple wavelength (λ) increases with continuous ion bombardment and hence, the local angle of incidence along the ripple pattern eventually becomes so large that the upstream part of ripples gets shadowed from the ion-flux by the preceding peak. The limiting condition to avoid such shadowing of ion-beam is: $\tan(\pi/2 - \theta) \geq 2\pi(h_0/\lambda)$, where θ is the angle of incidence. According to this condition, as the ratio (h_0/λ) exceeds a threshold value, erosion takes place at the crests of a sinusoid instead of its troughs which in turn gives rise to nanofaceted structures [23,24,29–31].

Let us now describe the evolution of surface morphology upon growing a 15 nm-thick ZTO overlayer on *P*-, *R*-, and *F*-Si substrates (images not shown to maintain the clarity) which exhibit conformal growth of ZTO film in all three cases followed by increase in the rms roughness values compared to the respective substrates. Figure 6.2(d) shows the AFM topography of a 30 nm-thick ZTO-coated *P*-Si substrate (rms roughness of 0.2 nm) which reveals an isotropic surface (as is clear from the corresponding 2D-FFT image shown in the inset) and in turn its conformal nature. By comparing the AFM micrographs of *P*-Si substrates before and after the growth of ZTO overlayer, it is observed that rms roughness increases in the latter case.

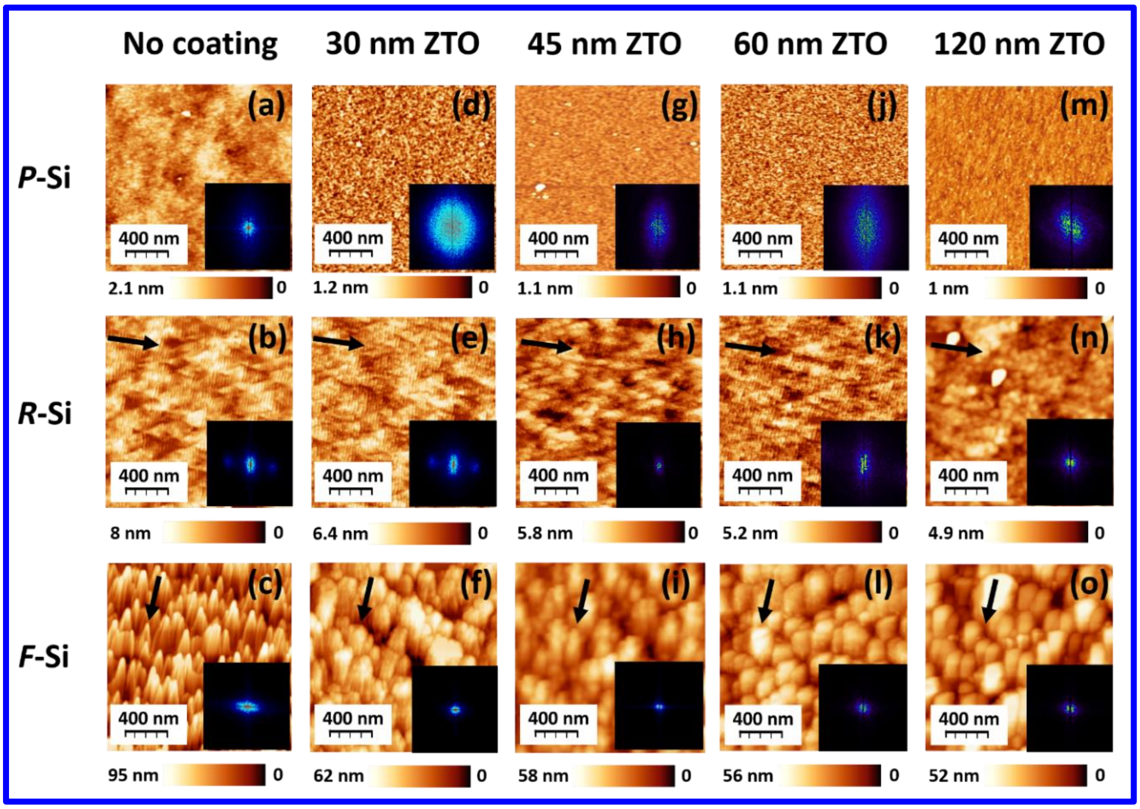

Figure 6.2: AFM topographic data: (a) *P*-Si, (b) *R*-Si, (c) *F*-Si, selective thicknesses of ZTO grown on *P*-, *R*-, and *F*-Si substrates namely 30 nm [(d)-(f)], 45 nm [(g)-(i)], 60 nm [(j)-(l)], and 120 nm [(m)-(o)], respectively, where the insets in (a)-(o) show the corresponding 2D FFT images. The black arrows indicate the direction of ion-beam bombardment.

On the other hand, Fig. 6.2(e) presents the topography of a 30 nm-thick ZTO film grown on an *R*-Si substrate where the signature of ripple patterns is clearly visible, confirming the conformal growth of ZTO. The rms roughness of this film is found to be 1.42 nm, and the corresponding 2D-FFT image in the inset also shows an anisotropic nature of the film morphology [as is the case in Fig. 6.2(b)]. Figure 6.2(f) shows the AFM image of a 30 nm-thick conformally grown ZTO film on an *F*-Si template where the rms roughness is 16.4 nm, and the average facet height turns out to be 36 nm. The inset in Fig. 6.2(f) depicts a 2D-FFT image, showing an anisotropic nature of the ZTO film morphology [as is seen for an as-prepared *F*-Si substrate, Fig. 6.2(c)]. Thus, it is observed that the sharpness of the nanofacets decreases, whereas the rms roughness increases after the growth of a 30 nm-thick ZTO overlayer on an *F*-Si substrate as well. Likewise, Figs. 6.2(g)-(o) depict the AFM micrographs of ZTO-coated (for thicknesses in the range of 45-120 nm) *P*-, *R*-, and *F*-Si substrates from where it becomes evident that ZTO films grow conformally up to a thickness of 60 nm on *R*-Si substrates, whereas the signature of surface ripples become weaker with increasing film thickness (e.g. 120 nm). Thus, hereinafter we shall limit our discussion up to 60 nm-thick ZTO layers on *P*-, *R*-, and *F*-Si substrates due to the conformal nature of these films. It may be mentioned that in all these cases, rms roughness value increases with ZTO thickness for all types of substrates.

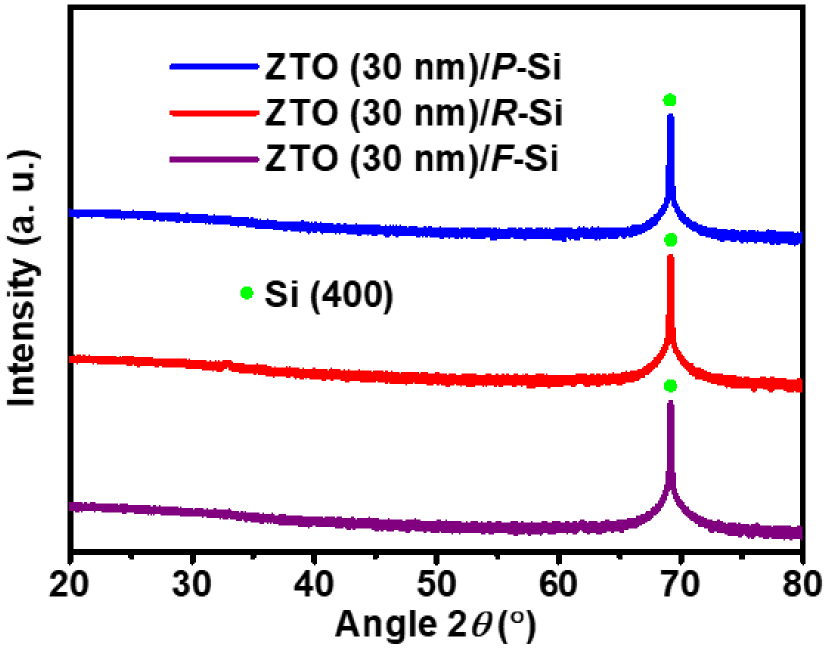

Figure 6.3: XRD spectra of 30 nm-thick ZTO films grown on *P*-, *R*-, and *F*-Si substrates. For a better clarity, the XRD spectrum intensity is plotted in logarithmic scale.

XRD measurements are carried out on all the samples (described above) to check the crystalline nature of deposited films and the absence of any peak in the representative XRD spectra [Fig. 6.3], corresponding to 30 nm-thick ZTO films grown on *P*-, *R*-, and *F*-Si substrates, indicate the amorphous nature of all the ZTO films. Similar is the trend for all other ZTO film thicknesses grown on all three types of substrates (spectra not shown). This is well supported by literature where RF sputter-grown ZTO thin films (at RT) are found to be amorphous in nature [32–34].

In order to perform a thorough compositional analysis, XPS measurements are carried out on selective samples. For instance, Figs. 6.4(a)-(c) depict XPS data for 30 nm-thick ZTO films grown on *P*-, *R*-, and *F*-Si substrates. XPS measurements are also carried out on all three substrates before the growth of ZTO films. Besides *P*-Si substrate, the XPS spectra of *R*-Si and *F*-Si substrates also do not reveal the presence of any impurity (spectra not shown) due to the chosen experimental geometry during ion-exposure where a sacrificial Si wafer is used to cover the entire sample platen to avoid impurity-induced pattern formation. Figures 6.4(a)-(c) show the Zn 2*p*, Sn 3*d*, and O 1*s* core level spectra, respectively for the ZTO overlayer grown on a *P*-Si substrate. Fitting of the XPS spectra presented in Fig. 6.4(a) reveals that Zn $2p_{3/2}$ and Zn $2p_{1/2}$ levels are centred around 1021.9 eV and 1044.98 eV, respectively. On the other hand, Sn $3d_{5/2}$ and Sn $3d_{3/2}$ energy levels are located [Fig. 6.4(b)] at 486.54 and 494.92 eV, respectively which correspond to the presence of SnO_2 phase in the film [35–37]. Likewise, the O 1*s* spectrum presented in Fig. 6.4(c) is deconvoluted into three distinct peaks located at 530.37, 531.65, and 532.51 eV which correspond to the presence of O atoms at regular lattice sites (O_L) associated with Zn-O or Sn-O bonds, the deficiency of O atoms (O_V) within the ZTO matrix, and the presence of loosely bound O atoms (O_H) at the surface with absorbed H atom-based compounds, respectively [37,38]. By calculating the area under the curves for these three peaks, the percent concentration of O_L, O_V, and O_H turns out to be 58.7%, 29.3%, and 12%, respectively, indicating an oxygen-deficient nature of the ZTO film grown on a *P*-Si substrate.

In case of the *R*-Si substrate [Fig. 6.4(d)], it is observed that the binding energy of Zn $2p_{3/2}$ and Zn $2p_{1/2}$ are centred at 1021.51 and 1044.63 eV, respectively. On the other hand, the binding energy corresponding to Sn $3d_{5/2}$ and Sn $3d_{3/2}$ energy levels [Fig. 6.4(e)] are located at 486.26 and 494.65 eV, respectively where the binding energy corresponding to Sn $3d_{5/2}$ peak confirms the presence of SnO_2 in the ZTO film on *R*-Si substrates.

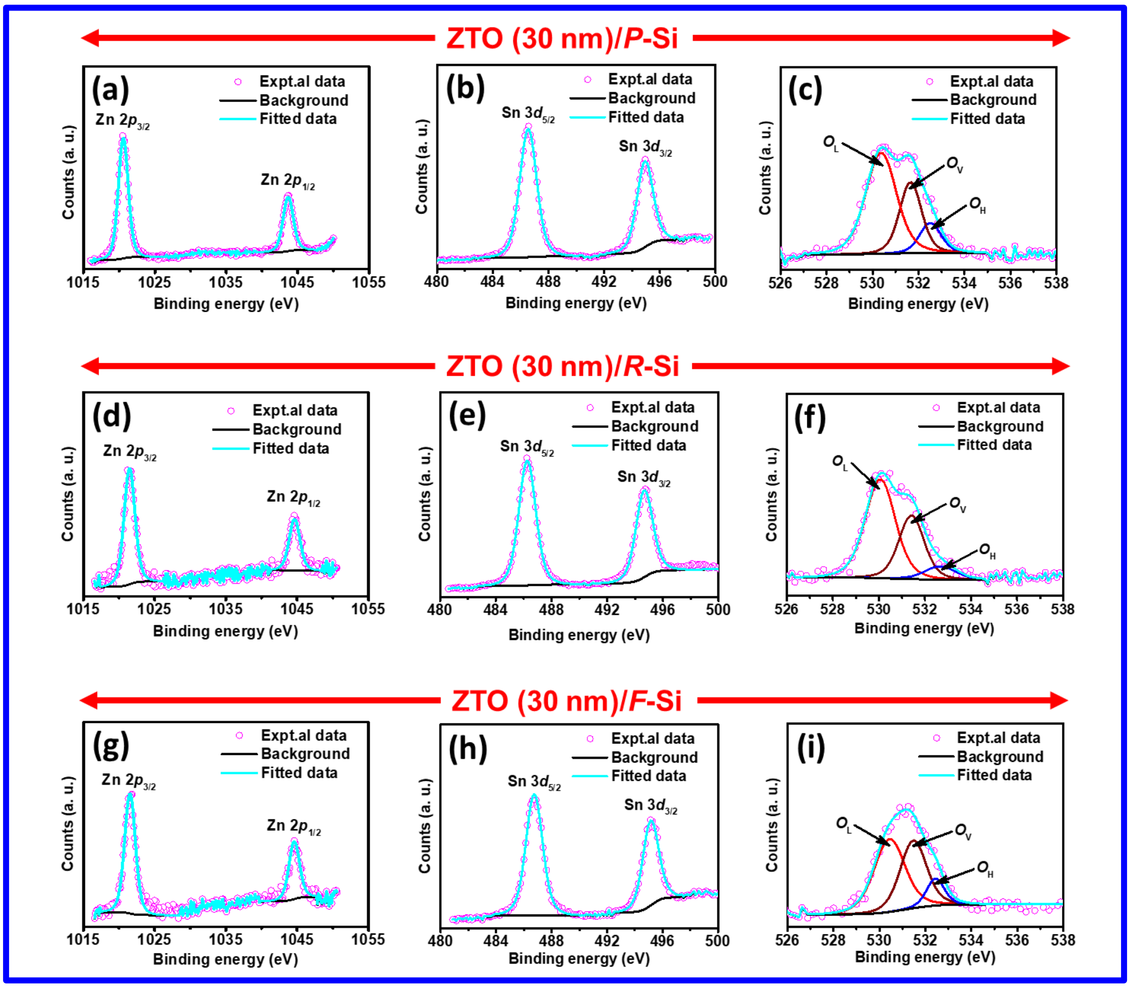

Figure 6.4: XPS spectra of Zn 2*p*, O 1*s*, and Sn 3*d* present in ZTO (30 nm)/*P*-Si (a)-(c), ZTO (30 nm)/*R*-Si (d)-(f), and ZTO (30 nm)/*F*-Si (g)-(i).

Following this, the O 1*s* spectrum [Fig. 6.4(f)] is deconvoluted into three distinct peaks located at 530.06, 531.41, and 532.66 eV which correspond to O_L, O_V, and O_H, respectively. It is observed that the relative percentage of O_L, O_V, and O_H are found to be 59.4, 32.3, and 8.3%, respectively. Upon performing a Gaussian fitting of the XPS data shown in Fig. 6.4(g), it is observed that the binding energy corresponding to the Zn $2p_{3/2}$ and Zn $2p_{1/2}$ signals are centred around 1021.48 and 1044.58 eV, respectively. Similarly, fitting of the data presented in Fig. 6.4(h) reveals that Sn $3d_{5/2}$ and Sn $3d_{3/2}$ signals are centred around the binding energy values of 486.75 and 495.14 eV, respectively, where the binding energy corresponding to Sn $3d_{5/2}$ confirms the presence of SnO_2 in ZTO/*F*-Si, too.

Sample description	Composition	Binding energy (eV)	Relative percentage (%)
ZTO/*P*-Si	Sn $3d_{5/2}$	486.54	61.1
	Sn $3d_{3/2}$	494.92	38.9
	O 1*s* O_L	530.37	58.7
	O 1*s* O_V	531.65	29.3
	O 1*s* O_H	532.51	12.0
	Zn $2p_{3/2}$	1021.9	68.0
	Zn $2p_{1/2}$	1044.98	32.0
ZTO/*R*-Si	Sn $3d_{5/2}$	486.26	59.1
	Sn $3d_{3/2}$	494.65	40.9
	O 1*s* O_L	530.06	59.4
	O 1*s* O_V	531.41	32.3
	O 1*s* O_H	532.66	8.3
	Zn $2p_{3/2}$	1021.51	69.6
	Zn $2p_{1/2}$	1044.63	30.4
ZTO/*F*-Si	Sn $3d_{5/2}$	486.75	59.9
	Sn $3d_{3/2}$	495.14	40.1
	O 1*s* O_L	530.44	50.1
	O 1*s* O_V	531.48	39.3
	O 1*s* O_H	532.44	10.6
	Zn $2p_{3/2}$	1021.48	68.0
	Zn $2p_{1/2}$	1044.58	32.0

Table 6.1 Compositional analyses of 30 nm-thick ZTO films on *P*-Si, *R*-Si, and *F*-Si substrates.

In a similar note, it is observed from Fig. 6.4(i) that the O 1*s* can be convoluted into three peaks namely O_L, O_V, and O_H which are positioned at 530.44, 531.48, and 532.44 eV, respectively. The extracted relative percentage of O_L, O_V, and O_H, in this case, turns out to be 50.1, 39.3, and 10.6%, respectively. All the results obtained from the XPS analyses of 30 nm-thick ZTO films grown on *P*-, *R*-, and *F*-Si substrates are summarised in Table 6.1.

From the above discussion, it is observed that there are nominal shifts in the binding energy values corresponding to Zn and Sn doublet peaks for 30 nm-thick ZTO films deposited on both *R*- and *F*-Si substrates with respect to the one deposited on a *P*-Si substrate which may originate due to differently patterned substrates. It is reported that the binding energy of Zn 2$p_{3/2}$ peak from ZTO is located at a slightly higher binding energy compared to that obtained from a ZnO film (~1021.1 eV) irrespective of the Sn content in a ZTO film [35] which matches well with our obtained results. A careful observation reveals that the oxygen-deficient nature progressively increases from ZTO/*P*-Si to ZTO/*R*-Si to ZTO/*F*-Si substrate.

Sample description	Reflectance (%*R*)
P-Si	43.9
R-Si	42
F-Si	32

Table 6.2 Reflectance (at 550 nm) of *P*-Si, *R*-Si, and *F*-Si substrates.

Figures 6.5 (a)-(c) show the optical reflectance spectra corresponding to different ZTO film thicknesses grown on *P*-, *R*-, and *F*-Si substrates, respectively. It is revealed from Fig. 6.5(a) that the surface reflectance reduces from ~43.9% (*P*-Si) to ~36% after deposition of a15 nm-thick ZTO film. It is interesting to note that the reflectance reduces to ~20% for a 30 nm-thick ZTO film on *P*-Si which further reduces to ~11% and 0.5% for 45 and 60 nm-thick films on *P*-Si substrate, respectively. Similarly for different thicknesses of ZTO films on *R*-Si, the surface reflectance reduces from 42% (*R*-Si) → ~35% → ~20% → 9.6% for 15, 30, and 45 nm-thick ZTO film, respectively, whereas it further reduces to 0.5% for a 60 nm-thick film. Likewise, the reflectance reduces from 32% (*F*-Si) to ~29%, 14%, 6%, and 0.4% for 15, 30, 45, and 60 nm-thick ZTO film, respectively grown on *F*-Si substrates. We have presented all the reflectance values in Table 6.2 and Table 6.3.

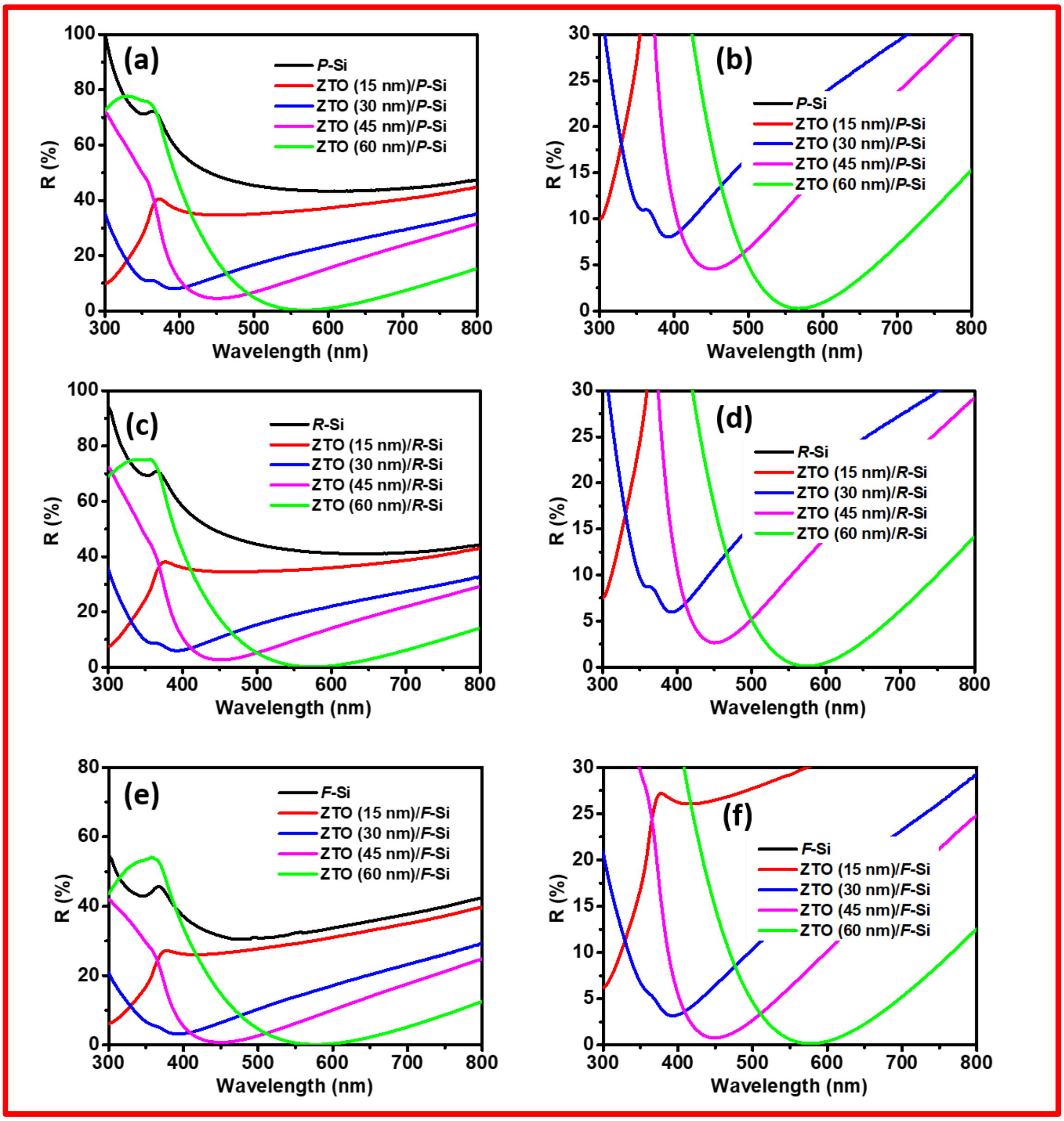

Figure 6.5: Reflectance spectra: (a) *P*-Si and ZTO/*P*-Si, (b) zoomed data on *P*-Si and ZTO/*P*-Si, (c) *R*-Si and ZTO/*R*-Si, (d) zoomed data on *R*-Si and ZTO/*R*-Si, (e) *F*-Si ZTO/*F*-Si, and (f) zoomed data on *F*-Si and ZTO/*F*-Si with varying ZTO film thickness, namely 15, 30, 45, and 60 nm.

A careful observation of the zoomed reflectance spectra [Figs. 6.5(b), (d), and (f)] corresponding to all thicknesses (except the 15 nm ones due to the low coverage) show reflectance minima which get red shifted with increasing thickness of ZTO film on *P*-, *R*-, and *F*-Si substrates. In fact, the reflection minima occurs upon satisfying the condition of destructive interference between light rays reflected from air/ZTO and ZTO/Si interfaces which is discussed later in detail. In view of the present reflectance data, one can infer that 60 nm-thick sputter-grown ZTO films on all three types of substrates show optimum antireflection. Thus, here onwards we shall discuss the reflectance data limited to 60 nm-thick ZTO films only.

ZTO film thickness (nm)	**Reflectance (%*R*)**		
	ZTO/*P*-Si	**ZTO/*R*-Si**	**ZTO/*F*-Si**
15	35.9	35.1	29.2
30	21.5	20.4	13.9
45	10.9	9.6	6.2
60	0.6	0.5	0.4

Table 6.3 Reflectance (at 550 nm) of *P*-Si, *R*-Si, and *F*-Si samples after the growth of different ZTO film thicknesses.

Let us now go on to explain the observed AR property of the ZTO films grown on *P*-, *R*-, and *F*-Si substrates. In doing so, it is important to note that the aspect ratio of the patterned nanostructures plays an important role to improve light trapping by maximizing absorption of photons via internal scattering [39,40]. In the present case, the aspect ratio of nanostructures for an *R*-Si substrate is defined as the ratio of ripple amplitude to its wavelength, while the aspect ratio of the facets on an *F*-Si substrate is defined as the ratio of facet height to its base-width. Accordingly, the calculated aspect ratios of ripples and facets turn out to be 0.13 and 0.25, respectively. Hence, the higher aspect ratio of facets leads to more internal scattering of light and in turn results in minimum surface reflectance for ZTO films grown on an *F*-Si template [16,41,42].

It may be mentioned that a 60 nm-thick ZTO film grown on a *P*-Si substrate shows reduced residual reflectance of 0.27% (at 568 nm), whereas the overall reflectance of the same is below 10% in the range of 474 to 742 nm. On the other hand, the overall surface reflectance of a 60 nm-thick ZTO film grown on an *R*-Si substrate reduces to less than 10% over a broad spectral range of 474-755 nm (with a residual reflectance of 0.1% at 574 nm), which amounts to a reduction in the same by ~37% and ~54% corresponding to *R*-Si and *P*-Si substrates, respectively.

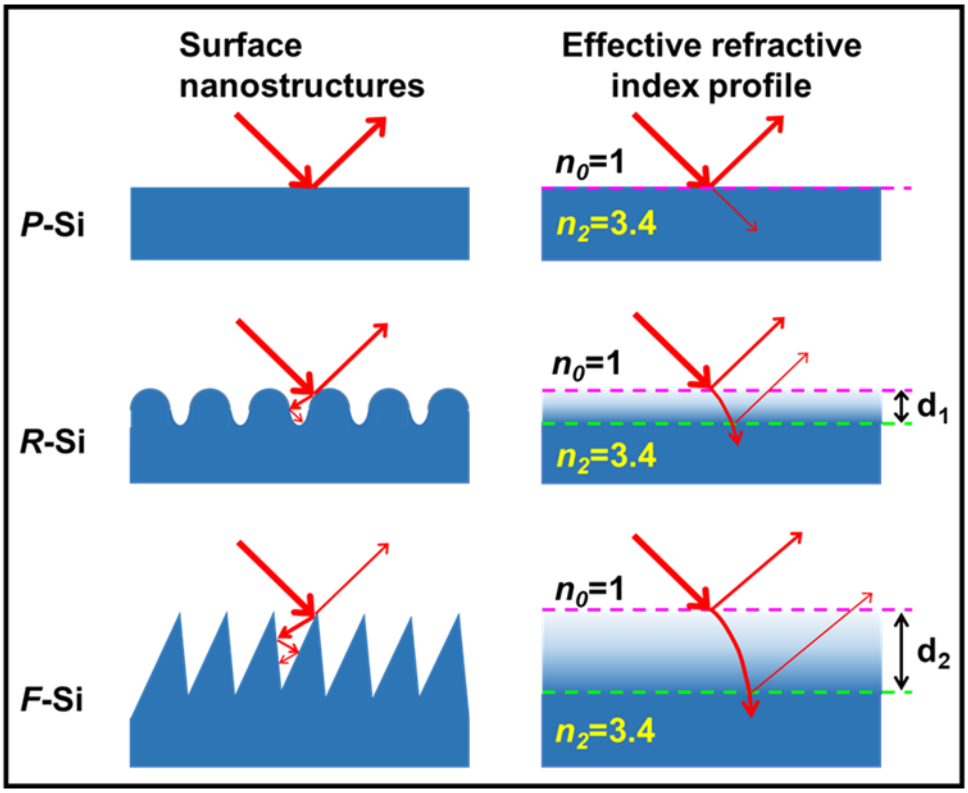

Figure 6.6: Optical ray diagrams for light propagation scheme in *P*-Si, *R*-Si, and *F*-Si substrates along with their equivalent effective RI representation where graded RI is represented by different colour contrasts.

In contrast, for a 60 nm-thick ZTO film grown on an *F*-Si substrate, the overall surface reflectance reduces further to less than 10% (over a broad spectral range of 467-773 nm), whereas the residual reflectance goes down to 0.16% (at 576 nm). Such a large reduction in surface reflectance in the case of 60 nm-thick ZTO/*F*-Si sample can be attributed to multiple light scattering events among the front and rear surfaces of neighbouring faceted structures [21]. All the results on reflectance measurements of *P*-, *R*-, and *F*-Si substrates and the conformally grown 60 nm-thick ZTO films on them are summarised in Table 6.2 and Table 6.3.

Basically, multiple scattering of light is the successive reflection events of light among front surfaces (exposed to the incident light) of nanofacets and rear surfaces (not exposed to incident light directly) of neighbouring facets. In this process, light is partially absorbed at the front (rear) surface and the remaining fraction of light intensity reflects towards the rear (front) surface of neighbouring nanofacets until light is either fully absorbed or some fraction is escaped from the nanofacets after a significant number of scattering events.

In order to explain these results, it is important to understand the role of surface patterns, which can be considered as analogous to grating structures. It is well-known that a grating on any surface can be used to achieve an arbitrary refractive index (RI) by tuning its geometry [43]. For instance considering a binary grating, its effective RI can be expressed as: $n_{eff} = (n_g - 1)d + 1$, where n_g is the RI of the grating and the duty cycle (d) is defined as ratio of the grating line width to the grating period [44]. If the grating material is considered to be the same as substrate and the surrounding medium is taken as air then the optimized duty cycle can be expressed as: $d = (\sqrt{n_2} - 1)/(n_2 - 1)$, where n_2 is the RI of the substrate [45]. Such binary gratings are expected to show AR property over a narrow spectral range. However, this range can be broadened by continuous tuning of the RI from the surrounding media to the substrate. In other words, a continuous change in d along the depth of the grating lines can lead to AR property over a broad spectral range which is possible to be achieved by sinusoidal or tapered/conical type gratings. In addition, when the grating is same as the substrate material then RI is matched at the substrate interfaces, leading to very good improvement in AR property

[45]. Hence, the gradual variation in RI can effectively eliminate the reflected light across a wide spectrum.

Zhu *et al*. have shown that sinusoidal gratings can also be used for enhancing AR for broadband spectrum by tuning their aspect ratio [46]. In this case of an *R*-Si substrate, which basically manifests surface modulation in a sinusoidal fashion, can be considered as a sinusoidal AR grating. On the other hand, an *F*-Si substrate can be realized as an ensemble of ion beam-fabricated self-organized conical nanofacets on Si surface. Thus, both *R*- and *F*-Si surfaces have gradually varying Si-fraction from top (100% air, 0% Si) to bottom (0% air, 100% Si) and the effective medium theory can be invoked for such cases (where the feature size is smaller than that of the incident wavelength of 300-800 nm) [47].

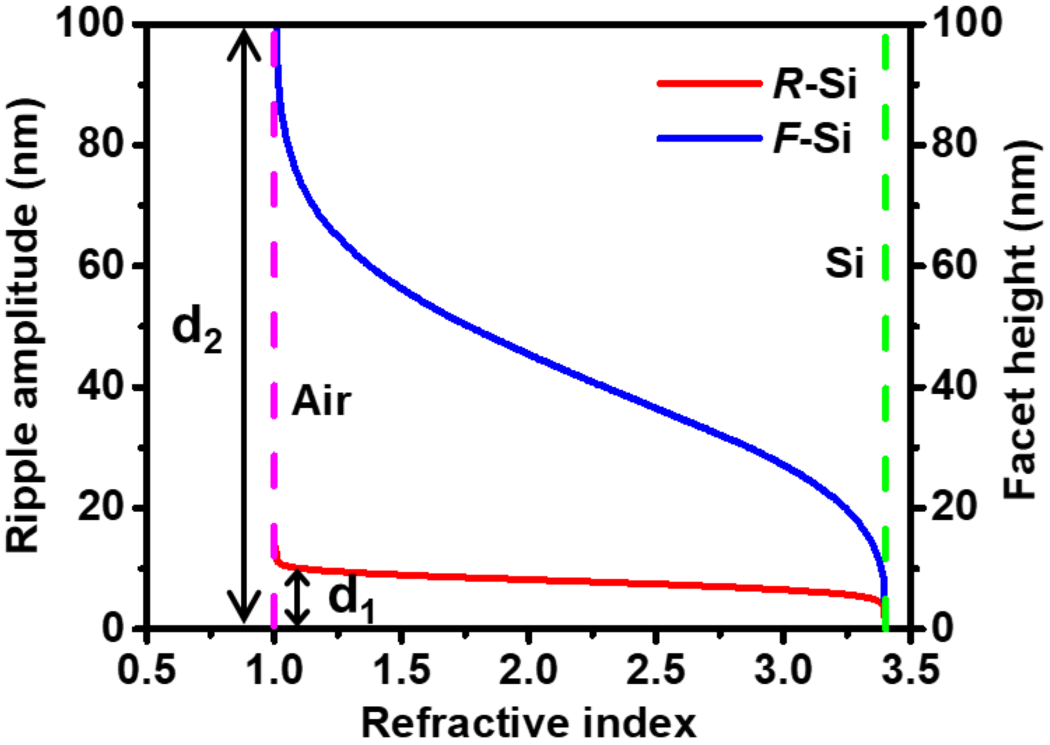

Figure 6.7: Graded RI profiles for *R*-Si and *F*-Si substrates from top (100% Air, 0% Si) to bottom (0% Air, 100% Si) of the nanostructures. In these figures distances shown are not to the scale.

Figure 6.6 shows the optical ray diagrams, illustrating reflection and transmission schemes for *P*-Si, *R*-Si, and *F*-Si substrates where patterned substrates are collectively represented by effective RIs which is basically proportional to the spatial distribution of the grating material. It may be mentioned that there is an abrupt change in the RI at the interface of air and *P*-Si which leads to Fresnel reflection losses. However, it reduces for *R*-Si and *F*-Si substrates due to gradually varying Si-fraction, which is manifested as graded RI between air and the substrate.

In order to correlate the change in AR property with the surface morphology observed for *R*- and *F*-Si substrates, the graded RI profiles of *R*- and *F*-Si surfaces are calculated. In doing so, first the surface bearing area curves (not shown) are calculated from the AFM images of *R*- and *F*-Si [Figs. 6.2 (b) and (c)] substrates using SPIP software [48]. As a matter of fact, surface bearing area (Abbott) curve is basically the accumulation of height distribution histogram of surface nanostructures along with percentage of area covered by the same [49–51]. This curve can be obtained by collecting height and crossectional area of a nanostructure that lies within the plane drawn at successive heights. In addition, effective RI (n_{eff}) profiles for *R*- and *F*-Si surfaces are calculated using: $n_{eff} = f\, n_{Si} + (1 - f)n_{Air}$ [52], where f is the coverage area of nanostructures taken from the surface bearing area curve after normalization with the area of corresponding AFM image, n_{Si} and n_{Air} are RIs of Si and air, respectively. From Fig. 6.7, it is observed that *R*- and *F*-Si surfaces have gradually varying Si-fraction from the top of nanostructures (100% air, 0% Si) to their bottom (0% air, 100% Si). From Fig. 6.7, it is quite evident that the *F*-Si surface reveals more prominent graded RI compared to the *R*-Si surface due to much higher aspect ratios of the facets.

To understand the role of ZTO thin films on patterned surfaces, first we start with a film grown on a *P*-Si surface. It is a well-known that when light passes from a low to a high RI medium it gets reflected with a 180° phase shift (with respect to the incident light) at the interface. Hence, to minimize the surface reflectance, reflected light from all the interfaces should have equal amplitude and 180º phase shift to vanish mutually, which is known as destructive interference.

For a thin film deposited on a substrate can be considered as an antireflective coating, if it satisfies $n_c = \sqrt{n_S}$ and $t = \lambda/4n_c$, where n_s is the RI of the substrate, λ is the incident wavelength of light, n_c is the RI of the film, and *t* is the required film thickness for minimizing the surface reflectance. In case of a *P*-Si substrate, two interfaces are formed namely air/ZTO and ZTO/*P*-Si where RI is successively higher as the RI of ZTO and Si are reported in literatures as 1.9-2.2 and ~3.5, respectively [32,53]. Hence, at air/ZTO and ZTO/Si interfaces, light is due to get reflected with a 180° phase shift, however the reflecting light from ZTO/Si interface retains it phase when incident on the ZTO/air interface. This way destructive interference takes place, leading to a reduction in the reflectance value. In addition, the angle at which light is incident, also gets affected due to variation in the local surface curvatures for ZTO-coated *R*- and *F*-Si surfaces, which help in AR by enhancing forward scattering of light significantly [55]. Hence, broadband antireflection property can be achieved depending on the deposited suitable thicknesses of ZTO overlayers on patterned surfaces [21]. It is interesting to note that light absorption is boosted by increasing the aspect ratio and in turn increasing the area of surface nanostructures. Thus, it can be inferred that tunable AR property can be achieved from ZTO-coated Si surfaces, although a 60 nm-thick ZTO film offers the most efficient AR property when it is deposited on an *F*-Si substrate.

6.4 Conclusions

In conclusion, we have fabricated ion-beam induced self-organized patterned silicon substrates and shown their efficacy to give rise to a significant reduction in the reflectance. Subsequently, 15, 30, 45, 60, and 120 nm-thick amorphous ZTO films are grown on these patterned substrates as well as on pristine-Si substrate. Atomic force microscopy reveals that films grow conformally up to a thickness of 60 nm on *R*-Si substrate. X-ray photoelectron spectroscopic data recorded from selective samples reveal the presence of zinc and tin atoms along with oxygen vacancies where the latter varies with the substrate morphology. In conjunction with the oxygen vacancy concentration, the anisotropic morphology of differently patterned substrates gives rise to different refractive indices and in turn different optical properties. We show that sputter deposited conformally grown ZTO overlayers exhibit AR property, although upon growing them on patterned surfaces (in particular the ones grown on *F*-Si substrates) can work as an tunable single layer AR coating over a broad range of the optical spectrum. Out of all the films studied here, 60 nm-thick ZTO-coated F-Si substrate offers the best AR property. Thus, it may be concluded that these self-organized light trapping nanoscale patterned Si substrates together with the overlayer of suitable materials, having lower refractive indices than Si, can work as broadband AR materials for next-generation highly efficient silicon-based heterojunction solar cells.

Bibliography

[1] A.K. Asvarov A S , Abduev A K, Bull. Lebedev Phys. Inst. 37 (2010) 18.

[2] S. Pearton, F. Ren, Curr. Opin. Chem. Eng. 3 (2014) 51.

[3] Y.-S. Choi, J.-W. Kang, D.-K. Hwang, S.-J. Park, IEEE Trans. Electron Devices 57 (2010) 26.

[4] D.K. Hwang, M.S. Oh, J.H. Lim, S.J. Park, J. Phys. D. Appl. Phys. 40 (2007) R387.

[5] K.A. Salman, K. Omar, Z. Hassan, Superlattices Microstruct. 50 (2011) 517.

[6] B. Hussain, A. Ebong, I. Ferguson, Sol. Energy Mater. Sol. Cells 139 (2015) 95.

[7] Y.H. Zhang, Z.X. Mei, H.L. Liang, X.L. Du, Chinese Phys. B 26 (2017) 047307.

[8] K. Ellmer, A. Klein, B. Rech, *"Transparent conductive zinc oxide"*, Springer Berlin Heidelberg, Berlin, Heidelberg, 2008.

[9] Ü. Özgür, Y.I. Alivov, C. Liu, A. Teke, M.A. Reshchikov, S. Doğan, V. Avrutin, S.-J. Cho, H. Morkoç, J. Appl. Phys. 98 (2005) 041301.

[10] A. Kołodziejczak-Radzimska, T. Jesionowski, A. Kołodziejczak-Radzimska, T. Jesionowski, Materials (Basel). 7 (2014) 2833.

[11] J.-H. Lee, B.-O. Park, Thin Solid Films 426 (2003) 94.

[12] M. Kumar, A. Kanjilal, T. Som, AIP Adv. 3 (2013) 092126.

[13] J. Werner, A. Walter, E. Rucavado, S.-J. Moon, D. Sacchetto, M. Rienaecker, R. Peibst, R. Brendel, X. Niquille, S. De Wolf, P. Löper, M. Morales-Masis, S. Nicolay, B. Niesen, C. Ballif, Appl. Phys. Lett. 109 (2016) 233902.

[14] X. Wu, S. Asher, D.H. Levi, D.E. King, Y. Yan, T.A. Gessert, P. Sheldon, J. Appl. Phys. 89 (2001) 4564.

[15] S.S. Shin, W.S. Yang, J.H. Noh, J.H. Suk, N.J. Jeon, J.H. Park, J.S. Kim, W.M. Seong, S. Il Seok, Nat. Commun. 6 (2015) 7410.

[16] J. Cai, L. Qi, Mater. Horizons 2 (2015) 37.

[17] F. Wang, Y. Jiang, T. Li, Y. Zhao, X. Zhang, J. Mater. Chem. A 3 (2015) 22902.

[18] A.K. Katiyar, S. Mukherjee, M. Zeeshan, S.K. Ray, A.K. Raychaudhuri, ACS Appl. Mater. Interfaces 7 (2015) 23445.

[19] C.P. Saini, A. Barman, M. Kumar, P.K. Sahoo, T. Som, A. Kanjilal, Appl. Phys. Lett. 105 (2014) 123901.

[20] R. Singh, M. Kumar, M. Saini, A. Singh, B. Satpati, T. Som, Appl. Surf. Sci. 418 (2017) 225.

[21] T. Basu, M. Kumar, P. Sahoo, A. Kanjilal, T. Som, Nanoscale Res. Lett. 9 (2014) 192.

[22] C. Martella, D. Chiappe, C. Mennucci, F.B. De Mongeot, J. Appl. Phys. 115 (2014).

[23] T. Basu, J.R. Mohanty, T. Som, Appl. Surf. Sci. 258 (2012) 9944.

[24] T. Basu, D.P. Datta, T. Som, Nanoscale Res. Lett. 8 (2013) 289.

[25] I. Horcas, R. Fernández, J.M. Gómez-Rodríguez, J. Colchero, J. Gómez-Herrero, A.M. Baro, Rev. Sci. Instrum. 78 (2007) 013705.

[26] W.L. Chan, E. Chason, J. Appl. Phys. 101 (2007) 1.

[27] R.M. Bradley, J.M.E. Harper, J. Vac. Sci. Technol. A Vacuum, Surfaces, Film. 6 (1988)

2390.

[28] C.S. Madi, B. Davidovitch, H.B. George, S.A. Norris, M.P. Brenner, M.J. Aziz, Phys. Rev. Lett. 101 (2008) 10.

[29] S.K. Garg, D.P. Datta, M. Kumar, D. Kanjilal, T. Som, Appl. Surf. Sci. 310 (2014) 147.

[30] D.P. Datta, S.K. Garg, T. Basu, B. Satpati, H. Hofsäss, D. Kanjilal, T. Som, Appl. Surf. Sci. 360 (2016) 131.

[31] G. Carter, J. Appl. Phys. 455 (1999) 455.

[32] P. Janicek, K.M. Niang, J. Mistrik, K. Palka, A.J. Flewitt, Appl. Surf. Sci. 421 (2017) 557.

[33] H.Q. Chiang, J.F. Wager, R.L. Hoffman, J. Jeong, D.A. Keszler, Appl. Phys. Lett. 86 (2005) 013503.

[34] D.L. Young, H. Moutinho, Y. Yan, T.J. Coutts, J. Appl. Phys. 92 (2002) 310.

[35] J.H. Han, B.K. Lee, E.A. Jung, H.-S. Kim, S.J. Kim, C.G. Kim, T.-M. Chung, K.-S. An, Appl. Surf. Sci. 357 (2015) 672.

[36] Y. Zhao, G. Dong, L. Duan, J. Qiao, D. Zhang, L. Wang, Y. Qiu, RSC Adv. 2 (2012) 5307.

[37] R.D. Chandra, M. Rao, K. Zhang, R.R. Prabhakar, C. Shi, J. Zhang, S.G. Mhaisalkar, N. Mathews, ACS Appl. Mater. Interfaces 6 (2014) 773.

[38] M. Kumar, S. Mookerjee, T. Som, Nanotechnology 27 (2016) 375702.

[39] H. Sai, Y. Kanamori, K. Arafune, Y. Ohshita, M. Yamaguchi, Prog. Photovoltaics Res. Appl. 15 (2007) 415.

[40] H. Kim, S. Park, B. Kang, S. Kim, S.J. Tark, D. Kim, S.S. Dahiwale, Appl. Surf. Sci. 284 (2013) 133.

[41] T. Basu, M. Kumar, A. Kanjilal, J. Ghatak, P.K. Sahoo, T. Som, J. Appl. Phys. 116 (2014) 114309.

[42] Y.-H. Pai, F.-S. Meng, C.-J. Lin, H.-C. Kuo, S.-H. Hsu, Y.-C. Chang, G.-R. Lin, Nanotechnology 20 (2009) 035303.

[43] W.H. Southwell, Opt. Lett. 8 (1983) 584.

[44] B. Päivänranta, P.K. Sahoo, E. Tocce, V. Auzelyte, Y. Ekinci, H.H. Solak, C.-C. Liu, K.O. Stuen, P.F. Nealey, C. David, ACS Nano 5 (2011) 1860.

[45] Y. Ono, Y. Kimura, Y. Ohta, N. Nishida, Appl. Opt. 26 (1987) 1142.

[46] H. Zhu, X. Jing, L. Chen, Y. Tian, Opt. Commun. 357 (2015) 78.

[47] L. Han, H. Zhao, Opt. Express 22 (2014) 31907.

[48] www.imagemet.com (Accessed: 21 June 2019)

[49] T. Basu, M. Kumar, A. Kanjilal, J. Ghatak, P.K. Sahoo, T. Som, J. Appl. Phys. 116 (2014) 114309.

[50] F. Firestone, E. Abbot, ASME Mech. Eng 55 (1933) 569.

[51] http://www.imagemet.com/WebHelp6/Default.htm (Accessed: 21 June 2019)

[52] J.M. Ha, S.H. Yoo, J.H. Cho, Y.H. Cho, S.O. Cho, Nanoscale Res. Lett. 9 (2014) 1.

[53] V. Ganesh, I.S. Yahia, S. AlFaify, M. Shkir, J. Phys. Chem. Solids 100 (2017) 115.

CHAPTER 7

Summary and future scope

In summary, we have fabricated self-organized nanoscale ripples and facets on Si surfaces by Ar-ion bombardment (energy: 500 eV) at different oblique incidences. Further, we make use of these nanoscale patterns as templates for different potential applications including field emitters, plasmonic anisotropy, surface-enhanced Raman spectroscopy (SERS) based detection of crystal violet dye, and antireflection coatings. Nanoscale ripple patterns were functionalized by oblique angle (65º-80º) growth of gold on them and observed the alignment of Au-NPs along the ripples. These one-dimensional arrays of Au-NPs aligned on Si nanoripples exhibit in-plane plasmonic anisotropy due to hotspot formation (enhancement of the electromagnetic field) in the gap between two adjacent Au-NPs in the array. The observed plasmonic anisotropy of Au-NPs aligned on silicon nanoripples is utilized for SERS-based detection of crystal violet dye. On the other hand, silicon nanofacets are employed as templates for the oblique angle (65º-85º) growth of Au-NPs which demonstrate fascinating ultralow threshold fields for cold cathode electron emission. Further, film thickness-dependent antireflection efficacy of sputter-grown ZTO films on nanorippled- and nanofaceted-Si substrates is investigated and results are compared with the ones obtained from ZTO films grown on *pristine*-Si.

In this thesis, the introduction part includes low energy (500 eV) ion-beam induced self-organized pattern formation, basics on the growth of thin films and nanoparticles, introduction to cold cathode electron emission process, and brief discussion on SERS detection of molecules followed by the motivation behind the organization of this thesis. The next chapter describes the experimental techniques and characterization tools used for the self-organized pattern formation on Si surfaces followed by their nanoscale functionalization and further characterizations on the same. In the third chapter, the ion-solid interaction is briefly introduced and the existing continuum theory-based models for ion-beam induced surface evolution are outlined. In addition to this, Monte Carlo based dynamic simulations are briefly introduced to understand the pattern formation under experimental conditions presented in the thesis work. Our in-depth study reveals that oblique angle (65º-80º) deposition of Au-NPs on rippled-Si (*R*-Si) substrates leads to the growth of Au-NPs along the ripples, resulting in the fabrication of two dimensional arrays of Au-NPs which is confirmed by the morphological studies. In the present scenario, growth angle is found to be a key parameter for self-organization and tunability in the sizes of Au-NPs besides their growth time. These 1D arrays of Au-NPs on *R*-Si substrates exhibit substrate morphology-driven in-plane anisotropy in the optical response due to their stronger local surface plasmon resonance (LSPR) coupling along the Au-NP arrays compared to the one across the ripples. The observed optical anisotropy enhances after annealing of the samples due to the merging of small Au-NPs. As an application of 2D Au-NP arrays, surface-enhanced Raman scattering (SERS)-based detection of crystal violet dye with its low concentration of 10 µM is demonstrated and it is observed that the detection efficiency decreases with the growth angle of Au-NPs due to their decreasing density and size. Moreover, the SERS peak intensity is maximum for 65º growth angle and it further improves upon annealing.

As an application of as-prepared and Au-NPs deposited Si-NFs, their cold cathode electron emission is systematically investigated. In this quest, we have fabricated small Si-NFs at ion-incidence angle of 71º (with respect to the surface normal) for an ion-fluence of 5×10^{17} ions cm^{-2}. The reason behind choosing the smaller Si-NFs is the lesser degree of native oxide formation at their apexes compared to the bigger ones, which imposes an additional barrier for electrons to tunnel from the surface.

Further, oblique angle (65º-80º) deposition of e-beam evaporated Au-NPs on nanofaceted-Si (NF-Si) substrate leads to the self-organization of Au-NPs predominantly at their apexes and sidewalls. However, it is noteworthy that for the growth angle of 85º, Au-NPs are selectively decorated at the apexes and near apex regions of Si-NFs due to shadowing of gold flux by neighbouring Si-NFs. As a matter of fact, Au-NPs at the apexes of Si-NFs are bigger in size corresponding to the growth angle of 70º compared to the ones formed at other growth angles. Subsequently, cold cathode electron emission from Au-NPs decorated Si-NFs is demonstrated. The turn-on field is measured to be 0.6 V μm^{-1} with β-value of 8104 for the as-prepared Si-NF sample which marginally reduces to 0.58 V μm^{-1} after their annealing at 573 K for 1 h. It is interesting to note that the turn-on field drastically reduces to 0.39 V μm^{-1} with an enhanced β-value of 18152 for a Si-NF substrate decorated with Au-NPs deposited at a growth angle of 70º. This further reduces to a fascinating low threshold field of 0.27 V μm^{-1} with improved β-value of 24157 after/upon post-growth annealing at 573 K for 1 h. It can be attributed to increased density and curvature of effective field-emitters. Hence, tunability in the turn-on fields from 0.6 V μm^{-1} to 0.27 V μm^{-1} is achieved by varying the growth angle of Au-NPs and the post-growth annealing. We have also surfed Au-NP decorated Si-NFs samples to identify the field emitting sites using AFM local probe based dual pass tunneling current microscopy (DPTCM) which suggests that tunneling current emerges predominately from the Au-NP decorated apexes and sidewalls of Si-NFs in contrast to emission of tunneling current mostly from the sidewalls and valleys (negligible contribution from apexes) of the as-prepared and annealed Si-NFs due to the curvature-dependent formation of native oxide mostly at their apexes. Moreover, finite element method (FEM)-based electrostatic field simulations are performed to address the underlying mechanism of field emission from Au-NPs decorated Si-NFs and it is observed from the electric field maps that the electric field is mostly enhanced at the apex of Si-NFs which improves manifold after their decoration with Au-NPs. Therefore, Au-NPs at the apexes of Si-NFs lead to electric field enhancement (improved β-values) and in turn lower down the turn-on field for cold cathode electron emission. The lowest observed turn-on field for 70º growth angle is governed by the electric field enhancement due to the presence of bigger Au-NPs at the apexes of Si-NFs.

In another study, ion-beam patterned-Si (NR- and NF-Si) substrates were used as templates for exploring film thickness-dependent antireflection of sputter-grown $ZnO:SnO_2$ (ZTO) overlayers at RT. It is observed that ZTO thin films grow conformally on NR-Si substrates up to a thickness of 60 nm and found to be amorphous in nature. A large reduction in the average surface reflectance is observed from 43.9% (for *pristine*-Si) to 42% and 32% for as-prepared *R*- and *F*-Si substrate, respectively. The observed reduction in the surface reflectance of patterned-Si substrates can be attributed to the multiple reflection of light and their graded refractive index. After depositing conformal ZTO overlayers (up to a film thickness of 60 nm) on patterned-Si substrates, a continuous reduction in the surface reflectance is observed over a broad spectral range of 300-800 nm. In this quest, 60-nm thick ZTO overlayers grown on *pristine*-, *R*-, and *F*-Si substrates exhibit the minimal surface reflectance of 0.6%, 0.5%, and 0.4% (at 550 nm), respectively. The reduced reflectance after depositing ZTO overlayers is governed by the destructive interference of reflected light from the air/ZTO and ZTO/Si interfaces. Hence, sputter deposited conformally grown ZTO films on patterned-Si substrates manifest a tunable single layer antireflecting coating over a broad spectral range in contrast to the elimination of surface reflectance only over a narrow wavelength range by single layer AR coating on flat surfaces.

Thus, a comprehensive study on nanoscale functionalization of low energy ion-beam fabricated self-organized patterns on silicon surfaces is carried out in this thesis by growing Au-NPs at oblique angles of incidence using both electron beam evaporation technique and sputter-grown ZTO films. Ion-beam patterned substrates can be used either in as-prepared condition or as templates where patterned surfaces can be functionalized at nanoscale through the growth of thin films or nanoparticles for studying morphology-driven anisotropic physical properties and their viable applications. Therefore, fabrication of highly ordered patterns with minimal defects is necessary. In this quest, bombardment of Kr- and Xe-ions at elevated substrate temperature can be helpful in improving the quality of patterns. Generally, the tunable size of Au-NPs on NR-Si substrates can be achieved by varying the growth angle (presented in this thesis) and the growth time. Therefore, there is a room for further studies on the growth time-dependent optical response of 2D Au-NP arrays on NR-Si substrates and their SERS-based detection efficacy of complex molecules. Since, the wavelength and amplitude of ripples increases with increasing ion-energy, therefore, ion-energy can be varied from 250 to 1000 eV for tunable size (by accumulating more gold-flux) and interparticle-gap of nanoparticles across the ripples and in turn, plasmonic coupling strength can be altered for efficient SERS. Moreover, during the SERS measurements, the optimization of the incidence angle of the laser beam (with respect to the sample normal) is also important for improved plasmonic coupling between Au-NPs during the same. Further, it is also interesting to note that SERS-based detection of complex molecules can be improved by choosing the wavelength of incident laser light equal to (or close enough) the wavelength of the plasmonic peak for any SERS substrate. Therefore, tunable wavelength of plasmonic peak for any SERS substrate can be achieved by alloying or making core-shell structures of noble metals and in turn enhanced SERS-based detection can be achieved.

Similarly, there is a room to study the growth time-dependent tunability in the turn-on fields for improving the cold cathode electron emission from any nanofaceted semiconducting substrates. In addition, self-organization of Au-NPs at 87º growth angle on nanofaceted semiconductors can be interesting for cold cathode electron emission as it is expected that Au-NPs may grow only at the apexes of Si-NFs for gold flux incident at grazing angles. Finally, it would also be interesting to study the role of native oxide on Si-NFs by *in-situ* Au deposition on as-prepared Si-NFs without exposing them to air.